igh Energy Particle Interactions in Large Targets

Volume 1

Hadronic Cascades, Shielding, Energy Deposition

A. Van Ginneken
and M. Awschalom

1975

Fermi National Accelerator Laboratory

Batavia, Illinois

Operated by Universities Research Association Inc. under contract
with the Energy Research and Development Administration

TABLE OF CONTENTS

PREFACE . . . . . -v-

I. INTRODUCTION . . . . . -1-

II. MONTE CARLO CALCULATION . . . . . -3-

A. Summary of the CASIM Approach . . . . . -3-

B. Particle Production Models . . . . . -5-

C. Particle Selection Schemes . . . . . -9-

D. Multi-Media and Complex Geometries. . . . . -10-

III. STAR DENSITY CALCULATIONS . . . . . -13-

A. Cases Analyzed . . . . . -13-

B. Results Obtained. . . . . -14-

C. Parameters of the Calculations . . . . . -16-

IV. ENERGY DEPOSITION DENSITY CALCULATIONS. . . . . -19-

A. Electromagnetic Showers . . . . . -19-

B. Other Mechanisms. . . . . -30-

V. SPECIAL CALCULATIONS. . . . . -33-

A. Biased Calculations. . . . . -33-

B. Other Outputs. . . . . -36-

C. Ionization Calorimeters . . . . . -36-

VI. RADIATION PROTECTION. . . . . -39-

A. Fluxes and Dose Rates . . . . . -39-

B. Exposure Rate from Induced Radioactivity. . . . . -57-

C. Environmental Protection . . . . . -57-

VII. REFERENCES . . . . . -59-

VIII. GRAPHS . . . . . -63-

APPENDIX. . . . . -151-

PREFACE

This manual is primarily a collection of calculations of the development of hadronic cascades in steel and concrete in some typical geometries for incident protons of momenta ranging from 30 GeV/c to 1000 GeV/c. It is hoped that they will be useful when designing and reviewing shielding of beam lines and experimental setups. The emphasis is placed on radiation safety. Some data pertaining to the design of ionization calorimeters are also presented.

Since the hadronic cascade is by nature a complicated process and since in real life shielding configurations are influenced by factors other than safety, it is impossible to provide anything but a rough guide. Of necessity it is left to the user to decide which of the idealized cases analyzed here may pertain to a particular situation. Hopefully, both the cases analyzed and the sample of results included here are sufficiently general to be useful for many applications.

A few more complex problems are also included to illustrate the computational capabilities and limitations of the computer program used in this work. Such detailed calculations naturally provide more information within the narrow limits where they apply. In many cases a complex configuration with potential weak spots will call for such detailed analysis. This is the most useful approach if the design is otherwise satisfactory or nearly so. It is presently uneconomical to solve problems by programming and computing for every contingency.

The results presented here are pure predictions. A comparison with data must await the outcome of the approved and scheduled Fermilab Experiment-108. However, comparisons of predictions for measured target yields are in acceptable agreement with experiment (see Appendix). Both the measurement and the interpretation will have to be performed with

sufficient care to yield quantitative insight. Field measurements are usually too crude and their interpretations too ambiguous to be decisive.

There may be other substantial omissions in this manual and readers' comments will be greatly appreciated. This work is being released before the completion of E-108 because the ever increasing number and intensity of secondary beams require convenient access to these data.

We are grateful to all of our colleagues at Fermilab and elsewhere for discussions on shielding and on related problems, and in particular to Peter J. Gollon for his critical reading of the manuscript. We wish to thank Angela Gonzales for the careful preparation of the figures and creation of the cover. Her attention for detail in every graph of this large collection will contribute greatly to its usefulness. Our thanks also to Nancy Holloway for typing of the manuscript and to R. Gabriel and R. Santoro of ORNL for permission to reproduce Fig. VI.1.

I. Introduction

II. Monte Carlo Calculations

III. Star Density Calculations

IV. Energy Deposition Density Calculations

V. Special Calculations

VI. Radiation Protection

VII. References

VIII. Graphs

APPENDIX

Introduction

I. INTRODUCTION

The main results shown here are obtained with the Monte Carlo (MC) program CASIM[1] which was expressly written for problems dealing with high energy incident hadrons and shields of large dimensions. This program also allows quite complicated hadron production models in the form of inclusive distributions to be used in shielding design. Practically all of the materials presented here is calculated with the Hagedorn-Ranft[2] thermodynamical model of hadron production. This model is presently the only one for which extensive quantitative predictions were made on particle yields from proton-nucleus interactions. While there is still considerable extrapolation involved from the 19 GeV/c momentum region where it is known to be approximately valid, to Fermilab momenta, this extrapolation is performed in a physically meaningful way and not as a mere mathematical convenience. In the Appendix, it is shown that thick target yield predictions agree in an acceptable manner with actual measurements made at 200 and 300 GeV. In addition, preliminary results of thermal heating at 300 GeV (to be published later) show good agreement between measurements and calculations.

In Section II the salient features of CASIM and of the Hagedorn-Ranft particle production model are briefly reviewed. Section III presents a description of the star (i.e., inelastic nuclear interaction) density calculations performed for different geometries, materials and incident proton energies. These form the main body of this manual. Sections IV and V deal respectively with energy deposition and with calculations for special situations. Section VI gives the information necessary to use these star density results to evaluate personnel and environmental radiation hazards. Section VIII contains the results of the calculations in graphical form along with

a table for easy reference. The results pertaining to calorimeter design are also in this section.

Some recent review articles may be consulted in order to place the present work in perspective.[3-5]

Monte Carlo Calculations

II. THE MONTE CARLO CALCULATION

The approach to internuclear cascade simulations implemented in CASIM has been described elsewhere.[1] This approach is briefly reviewed below. It is followed by a description of the hadron production model and particle selection techniques employed in generating the present results.

A. Summary of the CASIM Approach

In contrast to other calculations[5-7] of hadronic cascades, CASIM makes extensive use of weighting techniques. Each generation is represented by a single particle weighted in such a manner that the properties of the cascade are reproduced on the average, or, equivalently, over many incident particles. When a hadron is "born" from the nuclear interaction of the representative hadron of the previous generation, the relevant parameters, e.g., kind (i), momentum (p) and angles (Ω) are randomly chosen from a selection function $S(i, p, \Omega)$. The particle is weighted according to the inclusive distribution of the production model,

$$W(i, p, \Omega) = S^{-1}(i, p, \Omega) \frac{dN}{dp d\Omega} (i, p, \Omega) \qquad (1)$$

Since only one particle represents all outgoing secondaries,

$$\sum_i \int S(i, p, \Omega)\, dp d\Omega = 1 \qquad (2)$$

Repeated use of equation (1) will yield an estimate of the average multiplicity of a hadron-nucleus collision. Likewise when applied to an internuclear cascade it will yield the average multiplicity of each generation in the cascade. The choice of the selection function $S(i, p, \Omega)$ determines the sampling of the cascades under study. While this points to the need for care in the choice of a selection function, deliberate biasing can also be exploited in particular problems. Note also the direct use of inclusive distributions

in equation (1). This is again in contrast with other work [5-7] in which each nuclear event is represented in the fully exclusive sense. The direct use of inclusive distributions is not only more efficient but also more accurate since a fully exclusive description of particle production involves more approximations which are unnecessary for the present applications.

Weighting techniques are also useful in calculating the collision distance, r. In the case of a constant mean free path, λ, this distance is distributed according to $\lambda^{-1} \exp(-r/\lambda)$. If one wishes to study the cascade over large or small distances this distribution is not the most efficient. In CASIM, r is chosen from a selection function,

$$F(r) = (k\lambda)^{-1} e^{-r/k\lambda} \tag{3}$$

where k can be large or small according to the problem.

An additional feature of CASIM is the large degree of decoupling between cascade propagation and recording of information. In a star density calculation a "propagating particle" and one or more "recording particles" are generated when the propagating particle of the previous generation undergoes an inelastic collision. The propagating particle is chosen according to its efficiency in producing stars in all <u>subsequent</u> generations. Recording particles are selected according to their efficiency in producing stars in the <u>current</u> generation. The star density along the trajectory of the recording particle is computed at fixed intervals until the particle either (i) leaves the shielding configuration or (ii) the length of its trajectory exceeds its range, or (iii) its weight drops below a preset limit.

Some other examples of this decoupling are discussed in Section V.

B. Particle Production Models

The representation of inelastic hadron-nucleus interactions is of singular importance in cascade calculations. Previous calculations[5-7] relied on empirical production formulae or on extrapolations of intranuclear cascade simulations at much lower energy ($\leq$ 3 GeV).[6] Both schemes are mathematically more convenient than realistic. The Trilling formulae[8,9] used in Ranft's calculations[5] lead to gross overestimates in the particle multiplicity at Fermilab energies compared with recent nuclear emulsion measurements.[10] The extrapolation technique of Armstrong, et al.[6], fails when applied to p-p collisions.

While a proper comparison of the Hagedorn-Ranft (thermodynamical) model with experiment is as yet lacking, there are presently no compelling reasons to abandon it. Most results presented in this work are obtained with the thermodynamical model plus an additional component describing low energy "knock out" nucleons. The angular and momentum distributions of these low energy particles are taken from the parameterization by Ranft and Routti[11] of Bertini's intranuclear cascade calculations.[12]

So far the thermodynamical model has been formulated only for p-p collisions. A number of parameters in the model were determined by empirical fits to existing data. Subsequently Ranft[13] re-adjusted these parameters to match the 19.2 GeV/c p-nucleus data of Allaby et al.[14] Then he used the new parameters to predict particle yields at higher incident momenta. A discussion of the justification as well as the limitations of this procedure is included in Ranft's paper.[13] It must also be noted that regardless of the parameterization, the thermodynamical spectra are symmetric in the p-p center of mass. While this symmetry no longer holds in p-nucleus interactions, it appears that even for relatively heavy nuclei the spectra are largely hydrogen-like. Emulsion experiments with 200 GeV protons show this behavior at least qualitatively.[10] Theoretical interpretations can reconcile

this behavior with various models (other than the thermodynamical model) of the p-p interaction.[15] Nuclear effects seem to be significant only for low energy secondaries. It is for this reason that the low energy component representing knocked-out nucleons is included in the present work. In addition the effects of nuclear excitation and binding energy are approximately taken into account. Finally, energy conservation is enforced by introducing an extra factor (dependent on incident momentum) in the thermodynamical model predictions. This factor is typically within 20% of unity except at momenta below about 3 GeV/c.

The particles considered in the calculation are nucleons and pions. For the latter no distinction is made between π^+ and π^-. The π^0 are not considered in propagating the cascade; however, they are very important in calculating energy deposition. (See Section IV). Less frequently produced particles (kaons, hyperons, nuclear fragments, etc.) are not explicitly included. Their effects are not completely neglected since energy conservation is forced among the few dominant mechanisms. The input data needed to describe particle production are then the nine inclusive distributions: $pA \rightarrow p$, $pA \rightarrow n$, $pA \rightarrow \pi$, $nA \rightarrow p$, $nA \rightarrow n$, $nA \rightarrow \pi$, $\pi A \rightarrow p$, $\pi A \rightarrow n$, $\pi A \rightarrow A$, where A represents any nucleus (H through Pb) and π represents $\pi^+ + \pi^-$. The thermodynamical model has presently been explicitly formulated only for the first and third interactions, i.e., $pA \rightarrow p$ and $pA \rightarrow \pi^{\pm}$. The following assumptions are made to represent the remaining processes:

1. Neutrons act much like protons. They yield the same π^+ and π^- spectra as incident protons.

2. Neutrons produced by any incident particle have the same relative spectra as protons but differ in total number. The fractions of protons among all nucleons are assumed to be:

$$F(pA) = 0.5\ (1 + Z/A)$$
$$F(nA) = 0.5Z/A \qquad (4)$$
$$F(\pi^{\pm}A) = Z/A$$

This takes into account to first order the leading particle effect and relative proton and nucleon abundances in the target nucleus.

3. To represent pion induced reactions in the same manner as for incident nucleons would entail a reformulation of the model for incident bosons plus the necessary data fitting to fix the free parameters. Since no such a prescription is as yet available the (πA) spectra are generated in analogy with pA spectra:

a. The incident pion is replaced by a proton having the same center of mass momentum as the π in the πp frame.

b. Only backward moving fireballs are considered to contribute to $\pi A \rightarrow p$ (or n). To balance momentum, nucleons from forward fireballs are assumed to be pions.

Using Hagedorn's notation[2] and for the incident pion moving left to right:

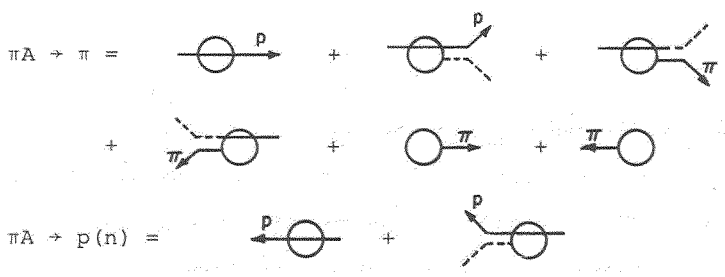

(5)

Briefly, represents an incident particle emerging from the collision, is a newly created particle, and are the decay products of low lying resonances (the label and arrow indicate the particle for which the differential cross section is calculated). For more details, see Reference 2.

4. The parameters for pion (and neutron) induced reactions are assumed to be the same as for proton induced reactions. The preceeding assumptions permit the necessary (nine) inclusive distributions to be derived from four "basic" reactions: $pA \rightarrow p$, $pA \rightarrow \pi$, $\pi A \rightarrow p$, $\pi A \rightarrow \pi$. Of these four, the last two are derived by a rearrangement of the contributions of the first two.

5. For nucleon induced reactions π^o production is assumed to equal one half the charged π production at any angle or secondary momentum. Likewise for π induced reactions except that here the leading particle component is excluded from contributing to π^o production.

6. The parameters for target nuclei other than those given by Ranft (Be, Al, Cu, Pb) are obtained by interpolation.

7. For each inelastic interaction a certain amount of nuclear excitation energy is included in the energy balance. This excitation energy (E*) is determined from a modified version of the formula used by Ranft[5],

$$E^* = E' \qquad E_{inc} \geq 5 \text{ GeV}$$

$$E^* = 0.05 + \frac{(E_{inc}-0.05)}{4.95}(E'-0.05) \qquad 0.05 \leq E_{inc} < 5 \text{ GeV}$$

$$E^* = E_{inc} \qquad E_{inc} \leq 0.05 \text{ GeV}$$

where $E' = \text{Max}(.005A, 0.05)$ and E_{inc} is the incident kinetic energy (for nucleons) and total energy (for pions). A binding energy correction of 8 MeV per (net) nucleon emitted is applied.

8. Even with the presence of the low energy nucleon component a threshold of 0.3 GeV/c was introduced in the calculations reported here. This limit is well below the commonly assumed range of validity of the model. Nevertheless, due in large part to the forcing of energy conservation, the multiplicities at these low energies are not unreasonable.

9. At the other extreme the highest momentum accepted by the program is 1000 GeV/c. This encompasses present Fermilab

momenta and includes the projected momentum of the "energy doubler".

Some results are also included which are based on the Trilling hadron production formulae.[8,9] This is essentially the same calculation as described by Ranft and Borak[9] but performed in the CASIM scheme.

C. Particle Selection Schemes

In principle the selection function is arbitrary, except that is should not vanish for physically meaningful values of the parameters. In practice the choice of selection function is very important since it will determine the rate of convergence of the calculation; therefore, its optimum choice is problem dependent. Most results presented here are derived with a selection scheme suited for a general calculation. This scheme should yield valid star density information for the entire shielding configuration and for the complete range of secondary particle momenta. The selection of recording particles and of propagating particles are performed differently.

The selection of a recording particle is made much in the fashion of conventional calculations, i.e., the selection function resembles the differential cross section. (If the selection function were identical to the differential cross section all particles emerging from a collision would carry equal weight.) First, the selection of the kind of particle i.e., p, n, or π and (for nucleons) whether it belongs to the thermodynamical or knock-out distribution is made by the usual comparison of a random number to the respective probabilities of these events, viz., $\int_{p_t}^{p_i} \frac{dN}{dpd\Omega} dpd\Omega$, where p_i, p_t are respectively the incident and threshold momenta. In the case of the thermodynamical spectra for each of the four basic reactions, from which all others are derived ($pA \rightarrow p$, $pA \rightarrow \pi$, $\pi A \rightarrow p$, and $\pi A \rightarrow \pi$), the values of the double differential cross section are represented in tables for ten logarithmically spaced incident

momenta. The variables of the outgoing particles are $\exp(-kp_T^2)$, where $k(\simeq 4)$ is optional, and p^c/p^c_{max} · where c denotes the center of mass of the colliding particle with a nucleon at rest. For every simulated collision the table nearest in incident momentum is referenced and the variables are randomly chosen by interpolation between the adjacent tabular values. The weight is then determined according to equation (1) with the differential cross section being evaluated for the actual incident momentum, outgoing variables, and nuclear target species. For the knock-out component the selection functions of angles and momenta are equal to the assumed differential cross sections.

The selection function for propagating particles reflects the rather well established fact that the total number of stars produced in a large block is essentially proportional to the energy of the incident particle. Thus, the selection of the species of propagating particles is made by comparing a random number with the normalized inelasticity distributions, $\int_{p_t}^{p_i} E_o \frac{dN}{dpd\Omega}\, dpd\Omega$, where E_o is the outgoing kinetic (or total) energy in the case of nucleons (or pions). The remaining variables are selected similarly: For the thermodynamical spectrum these are derived from tabular values of $E_o \frac{dN}{dpd\Omega}$, while for the knock-out component they are derived from an analytical procedure based on this principle. Again the particle weight is calculated using only the actual differential cross section.

The selection function used with the Trilling formula is a simple analytical formula which approximates the more detailed expression of the differential cross section.

Some examples of other selection schemes may be found in Section V.

D. Multi-Media and Complex Geometry Calculations

The description of the geometry and composition of the shielding is entirely confined to a relatively simple subroutine of CASIM. For most applications this routine merely

determines the material at any point in the shield from the cartesian coordinates of the point. The subroutine also indicates if the point is outside the boundaries of the configuration. This subroutine is used both in determining the location of the collisions of the propagating particle and in recording star densities. When a new particle is selected, the distance to its subsequent interaction is determined in units of interaction lengths. The particle is then propagated in a series of steps of constant length $\Delta\ell$ through the shield. After each step the geometry subroutine is called and the particle's cumulative track length ($\sum_{\ell}\Delta\ell/\lambda_{mat}$) is compared with the collision distance and with the range in the case of charged particles. To avoid bias, the length of the first step is determined randomly on the interval $(0, \Delta\ell)$. Similar techniques are used to track the recording particle.

For some applications it is advantageous to make $\Delta\ell$ a function of position. This is the case whenever important fine structure is present in the shielding configuration. For example, in the case of a narrow collimator in a large block, the region near the collimator should be examined with a smaller $\Delta\ell$ than is necessary elsewhere. The geometry subroutine also performs this task.

Star Density Calculations

III. STAR DENSITY CALCULATIONS

This section contains a summary of the geometry, composition and dimensions of the different shielding configurations analyzed for this manual. A brief description of the general results obtained and of the parameters used in the calculations is also included. The particular results included in this manual appear in Section VIII all in graphical form. Some special cases are discussed in Sections IV and V.

A. Cases Analyzed

Six cases (numbered 1 through 6) are considered here. In all cases:

(i) the incident particles are protons;

(ii) the beam is uniformly distributed over a 0.3 cm x 0.3 cm area except in case (5);

(iii) cylindrical symmetry prevails and the beam is centered on the axis of revolution of the configuration and travels parallel to it except in case (5);

(iv) the threshold momentum is 0.3 GeV/c. The incident momenta are standardized to 30, 100, 300, and 1000 GeV/c for ease of intercomparison.

1. Solid Iron Cylinder

Length = 1000 cm

Radius = 250 cm

To provide information on the hadron albedo the beam is assumed to travel 100 cm into the cylinder before starting to interact.

2. Solid Concrete Cylinder

Length = 1500 cm

Radius = 250 cm

The beam travels 150 cm before starting to interact.

3. Target in Iron Cave

This is an idealized version of a frequently encountered experimental layout, viz. that of a target in a shielded cave.

Overall length = 1500 cm

Cave length = 900 cm

Radius of shielding = 250 cm

Radius of cave = 100 cm

The beam strikes a copper target 15 cm long (about one interaction length) and 1 cm in radius located at 150 cm downstream from the entrance to the cave.

4. Target in Concrete Cave

This is similar to case 3.

Overall length = 2500 cm

Cave length = 1500 cm

Radius of shield = 500 cm

Radius of cave = 100 cm

The target geometry is as in case (3). It is located 250 cm downstream from the entrance to the cave.

5. Iron Pipe with Beam Grazing Inner Wall

This represents a beam interacting with the wall of a vacuum pipe inside a steel close-in shield.

Overall length = 1000 cm

Outer radius of pipe = 100 cm

Inner radius of pipe = either 10 cm or 1 cm

The beam strikes the pipe wall 100 cm downstream from the entrance, travelling parallel to the axis at an infinitesimal distance from the inner surface.

6. Iron Pipe with Center Target

Dimensions of the pipe are the same as in case (5). The beam strikes a copper target as in cases (3) and (4), placed 100 cm downstream from the entrance. This represents the beam striking an obstacle inside a steel, close-in shield. The results can be compared with those of cases (3) and (5).

B. Results

The main results are presented in terms of star densities and momentum specrta of the particles producing the stars. These are directly derived from the CASIM results. Some information on the conversion of star densities to other quantities of practical interest may be found in Section VI.

In general the outputs of the calculations include:

1. Star (nuclear interaction) density obtained in 2500 volume bins delineated by 50 equally spaced depths and 50 equally spaced radii. For all geometries except case (5) this is recorded separately for protons, neutrons and pions. In case (5) (a beam grazing the inner wall of a cylindrical shell), the volumes are further divided into three azimuthal regions, viz., $(-\pi/4, \pi/4)$, $(3\pi/4, 5\pi/4)$ and $(\pi/4, 3\pi/4)$ combined with $(5\pi/4, 7\pi/4)$ measured with respect to the incident beam. In this case only the sum over all particle types are recorded.

2. For the solid cylinders the smallest radial bin is further subdivided into five equally spaced radial bins. This yields a 5 x 50 array of star densities near the beam axis where the radial dependence is expected to be strongest.

3. Radial and longitudinal integrals of star density and total number of stars.

4. Momentum spectra of particles producing stars in 12 larger regions (3 longitudinal x 4 radial bins). For all cases except (5) these spectra are recorded separately for each particle species. In case (5) they are recorded for each of the three azimuthal regions.

5. Although of less practical value, the average number of stars per generation is recorded. In Fig. III.1. this is plotted as a function of generation number for the case of a solid iron beamstop bombarded by 30 to 1000 GeV/c protons. This illustrates dramatically the extent to which the cascade grows with incident energy.

The results presented here do not include any error analysis. For many cases, the results of more than one computer run are included. These runs are generally performed with different collision distance selection functions, i.e., a different value for k in equation (3). Agreement is generally quite satisfactory, typically within 10%. However, in certain locations of low star density, the agreement is considerably poorer. Thus the results in the

backward region or at very large radii may be off by factors of three or more. Deviations of more than one order of magnitude between two typical "production" runs are seldom encountered. In the plots of Section VIII duplicate runs are combined and statistical fluctuations are smoothed over by hand as much as possible. A certain amount of the remaining structure in the plots may still be statistical in origin. For most applications, the magnitude of the star density at a given location is much more important than its rate of change, with distance so any fine structure present should not unduly influence practical conclusions. But for the same reason care must be taken in extrapolating results.

The typical result of Section VII is based on about 4×10^5 pseudostars (i.e., interactions of propagating particles) and about 4×10^4 incident particles. Throughout the calculation an energy balance is kept. This energy balance usually agrees with the energy supplied by the original particles to within 5%.

C. Parameters of the Calculation

For most calculations only the inelastic interactions of the hadrons are considered (see Section II.B). In a few cases such as the "target in a cave", Coulomb scattering and nuclear elastic scattering of the primary beam are also included. The material parameters are taken from the compilation of Shaw.[16] The small variations of interaction length with energy observed at low energy are roughly included by means of transparency factors based on results of intranuclear cascade calculations.[17] The slowing down of charged particles is evaluated by means of range-momentum tables based on the compilations of Barkas and Berger[18] and of Theriot.[19] Decay of charged pions and of neutrons is neglected.

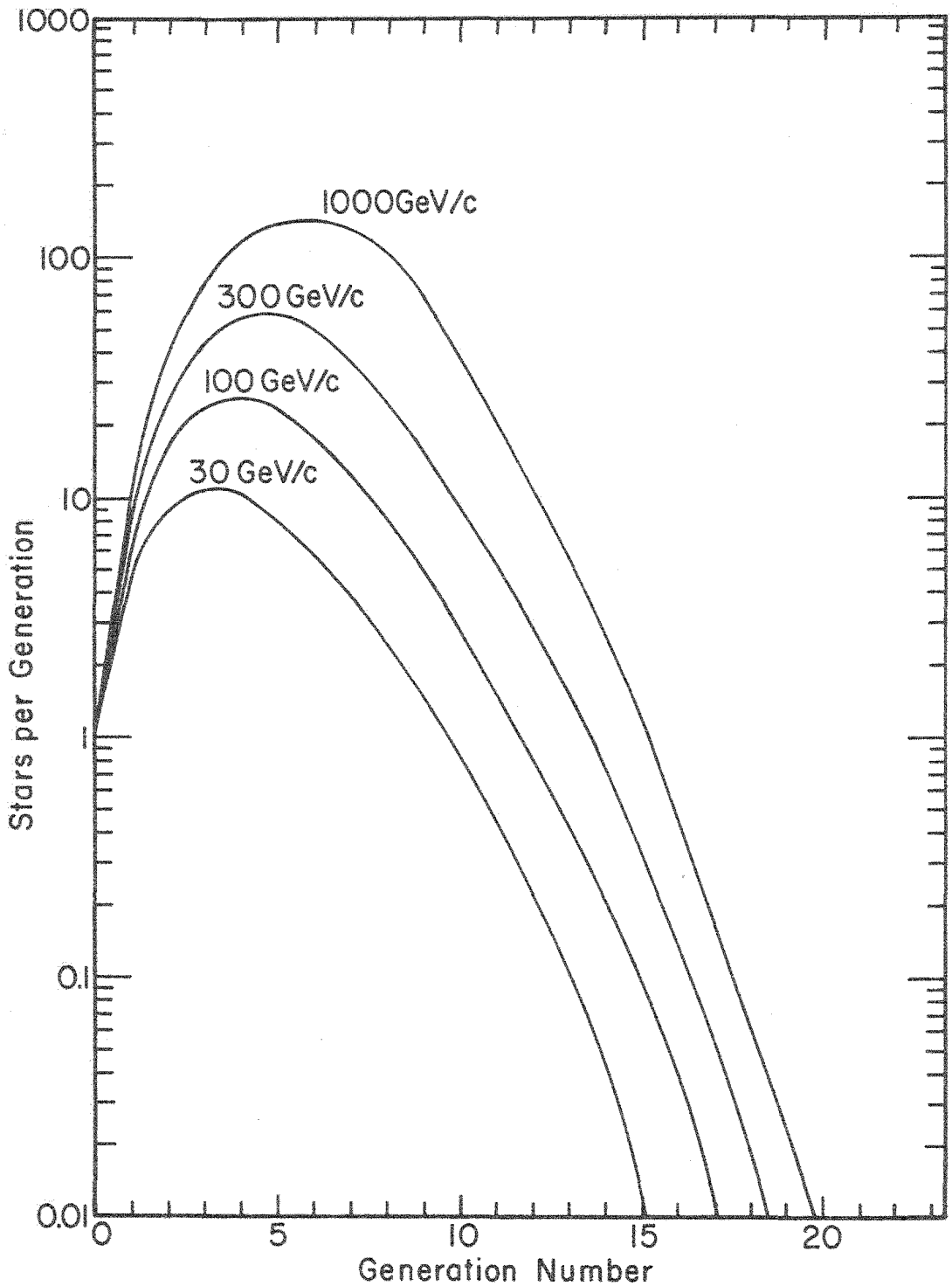

Fig. III.4. Average number of stars in each generation for 30 to 1000 GeV/c protons incident on a large solid iron cylinder.

Energy Deposition Density Calculations

IV. ENERGY DEPOSITION DENSITY CALCULATIONS

This section and the next are devoted to a description of presently implemented capabilities of CASIM.

The calculation of energy deposition is important, e.g., for estimating heating effects in beam dumps and accelerator components. By nature of its approach, CASIM computes the average energy deposition of the cascade but does not deal with the fluctuations on a particle by particle basis. Consequently it is not well suited in its present form to study ionization calorimeter responses. Nonetheless, the average behavior is also of interest in these problems (see below). Perhaps with certain basic modifications to CASIM the goal of calculating calorimeter responses with a realistic production model could be reached.

In the present calculation four components contribute to the energy deposition viz.:

(i) electromagnetic showers initiated by π^0 decay;

(ii) energy loss of charged particles by ionization (and at very high energy losses by pair production and bremsstrahlung);

(iii) de-excitation and recoil of the compound nucleus created by an inelastic collision;

(iv) the contribution by particles below the calculational threshold.

The calculation attempts to predict what an idealized general experiment would measure as deposited energy. The energy involved in the removal of a nucleon from the nucleus or in producing long-lived radioactivity is generally not detected. This is also true in practical applications such as target heating.

A. Electromagnetic Showers

The CASIM approach appears well suited to study the average behavior of electromagnetic (e.m.) showers in terms of underlying fundamental processes. No doubt

great savings in computer time could be gained using the CASIM approach instead of that used in e.m. calculations which follow individual particles. However, this concept has not yet been implemented.

Presently, a strictly empirical prescription is used to describe the average depth and radial dependence of the e.m. shower. This prescription has been tested against experimental data and other calculations for elements in the Z = 4 to 82 range and for incident electron and photon energies up to 45 GeV. Some accuracy is sacrificed for simplicity.

1. Longitudinal Behavior

The Z dependence is described by the parameter λ_c as given by Bathow et al.[20] For the present purposes λ_c is sufficiently closely given by

$$\lambda_c = 325\ (\ln Z)^{-1.73} \qquad \text{in } g\cdot cm^{-2} \qquad (7)$$

The energy dependence is known to be roughly logarithmic. These two statements can be combined into a new unit

$$\lambda_\ell = 325\ (\ln Z)^{-1.73}\ (\ln E^e_{inc}) \qquad \text{in } g\cdot cm^{-2} \qquad (8)$$

where E^e_{inc} is the incident electron energy expressed in MeV. When depths are expressed in units of λ_ℓ, all "transition curves" merge approximately into a "universal curve".

Included are some plots showing comparisons of data and of MC results with this universal curve. These comparisons are not exhaustive. Those presented here cover most of the Z-range and incident momentum range encountered in the present calculations. Other comparisons not shown here yield similar fits. Fig. IV.1 shows the 6 GeV incident electron data of Bathow, et al.[20], upon which the present universal curve is based. The low energy results of Cranell[21] (Fig. IV.2) show marked deviations

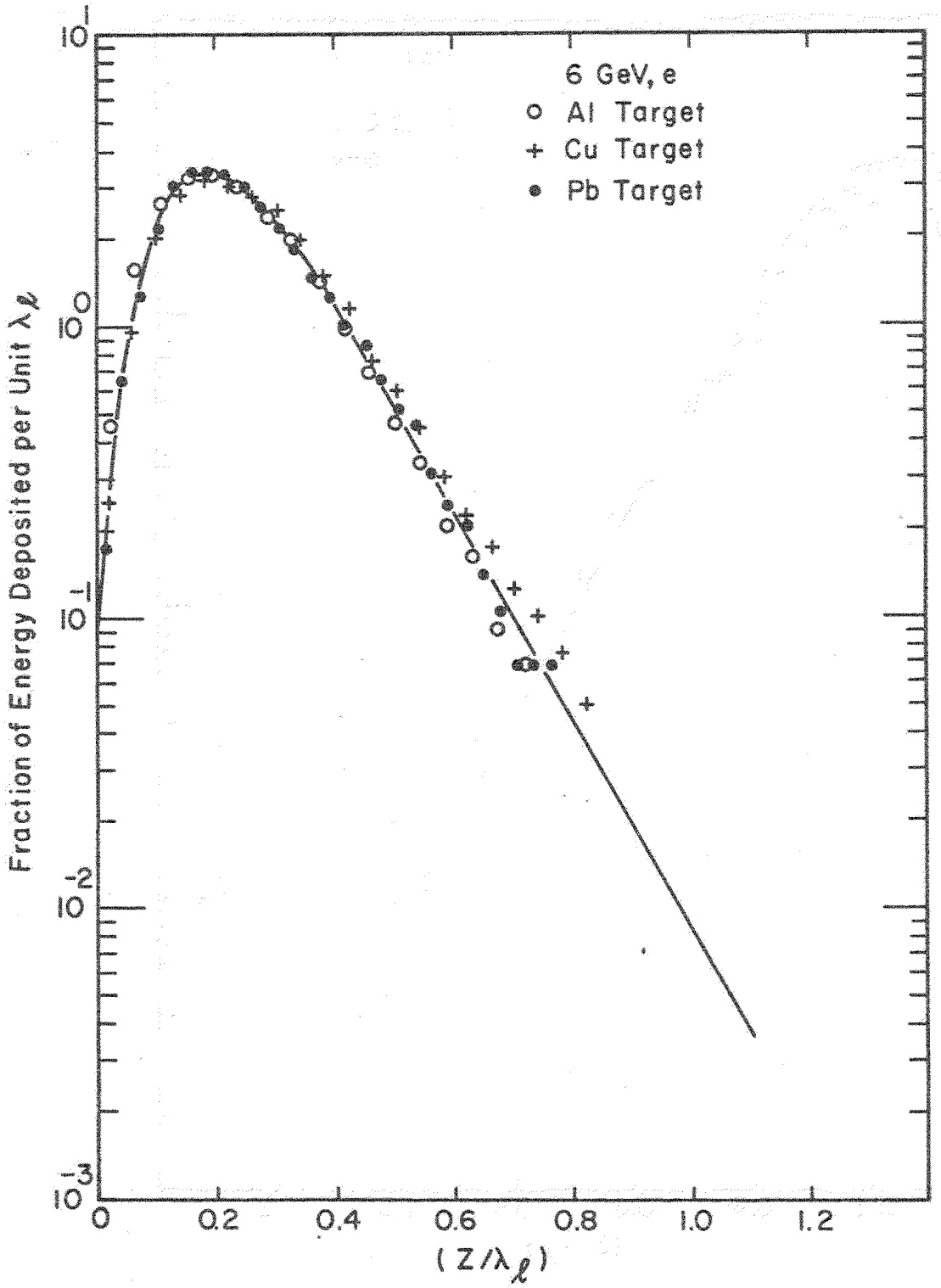

Fig. IV.1. Fraction of total energy deposited per unit λ_ℓ versus depth (in units λ_ℓ) for the data of Bathow et al.[20] Solid line is the universal curve assumed in this work (see text).

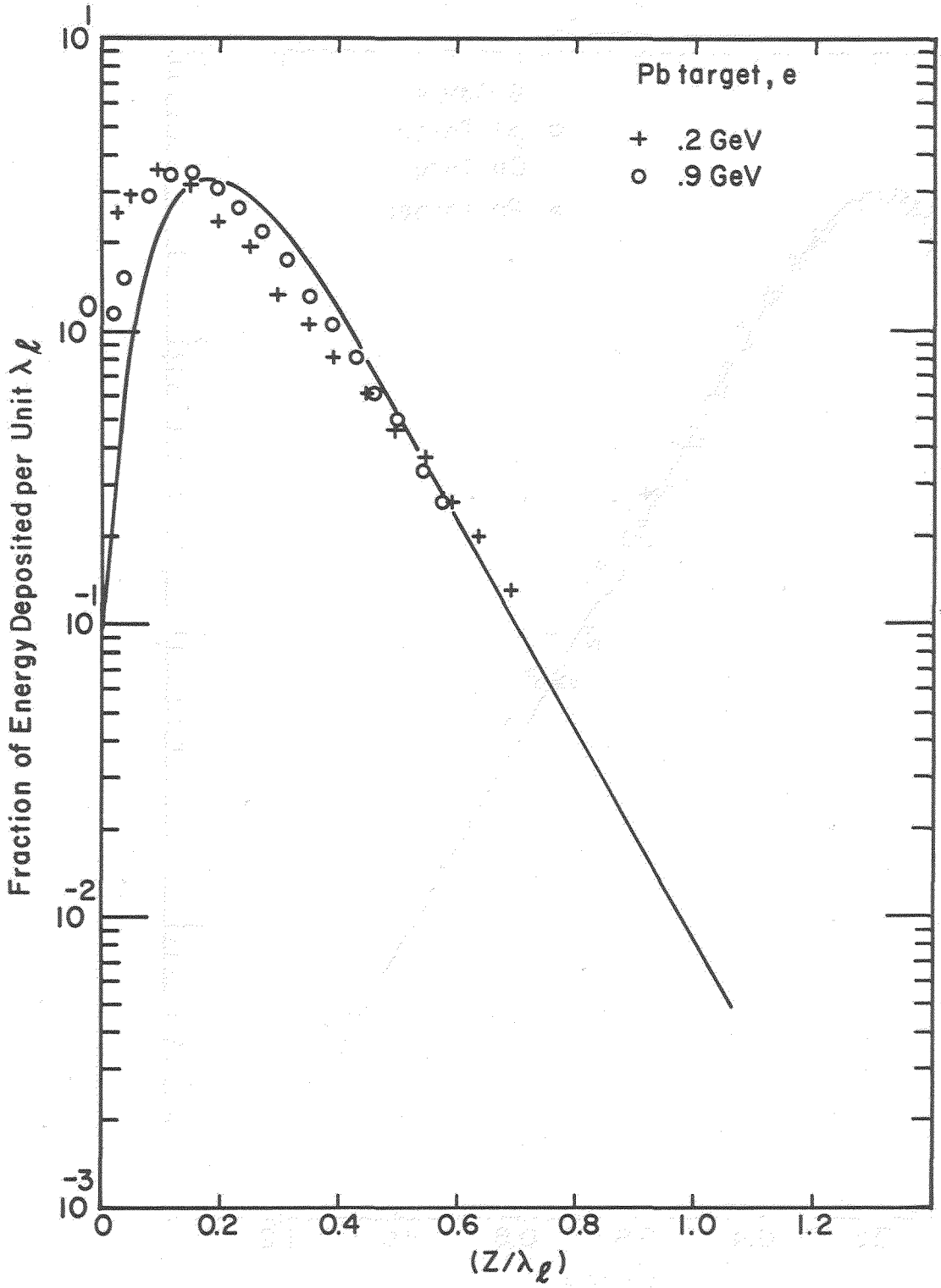

Fig. IV.2. Fraction of total energy deposited per unit λ_ℓ versus depth (in units λ_ℓ) for the data of Crannell.[21] Solid line is the universal curve assumed in this work (see text).

from the curve, especially at low depth. The fit could be improved by a change in the definition of λ_ℓ, but this would likely result in a more cumbersome expression. Considering that (a) errors in the energy deposition of of low energy electrons involve smaller absolute errors; (b) λ_ℓ is smaller (though only logarithmically) at low energy, deviations arising from use of the simple expression can be tolerated. For example, the error in the longitudinal location of the cascade maximum for a 500 MeV electron in copper is about 0.05 λ_ℓ (or about 1.4 cm). This is about one tenth of a hadron interaction length and fluctuations in the hadronic cascade will mask the error in the electromagnetic energy deposition. The data of Muller[22] (Fig. IV.3) on Pb over an incident electron range of 2-15 GeV show impressive scaling and agree moderately well with the curve. The MC results of Alsmiller and Moran[23] and of Alsmiller[24] obtained for 45 GeV photons incident on Be, Cu and Ta are shown in Fig. IV.4. To compare with electron data the abcissa was displaced 9/7 radiation lengths (the average distance for pair production), and one half the incident energy was used in the derivation of λ_ℓ. The agreement for Be is very good, apart from the expected deviations at low depths. The agreement is less satisfactory for Cu and Ta, but these results suffer from large statistical uncertainties.

2. Radial Behavior

The material dependence of the radial spread can be removed by expressing radial distances in Molière units (X_M),

$$X_M \equiv \frac{X_o \, E_s}{E_{crit}} \tag{9}$$

where X_o is the radiation length, E_s is taken to be 21 MeV and E_{crit} is the critical energy of the material, in MeV.[25] Further, Völkel[26] has shown that if depths are expressed in units of the depth at which the maximum electron or photon

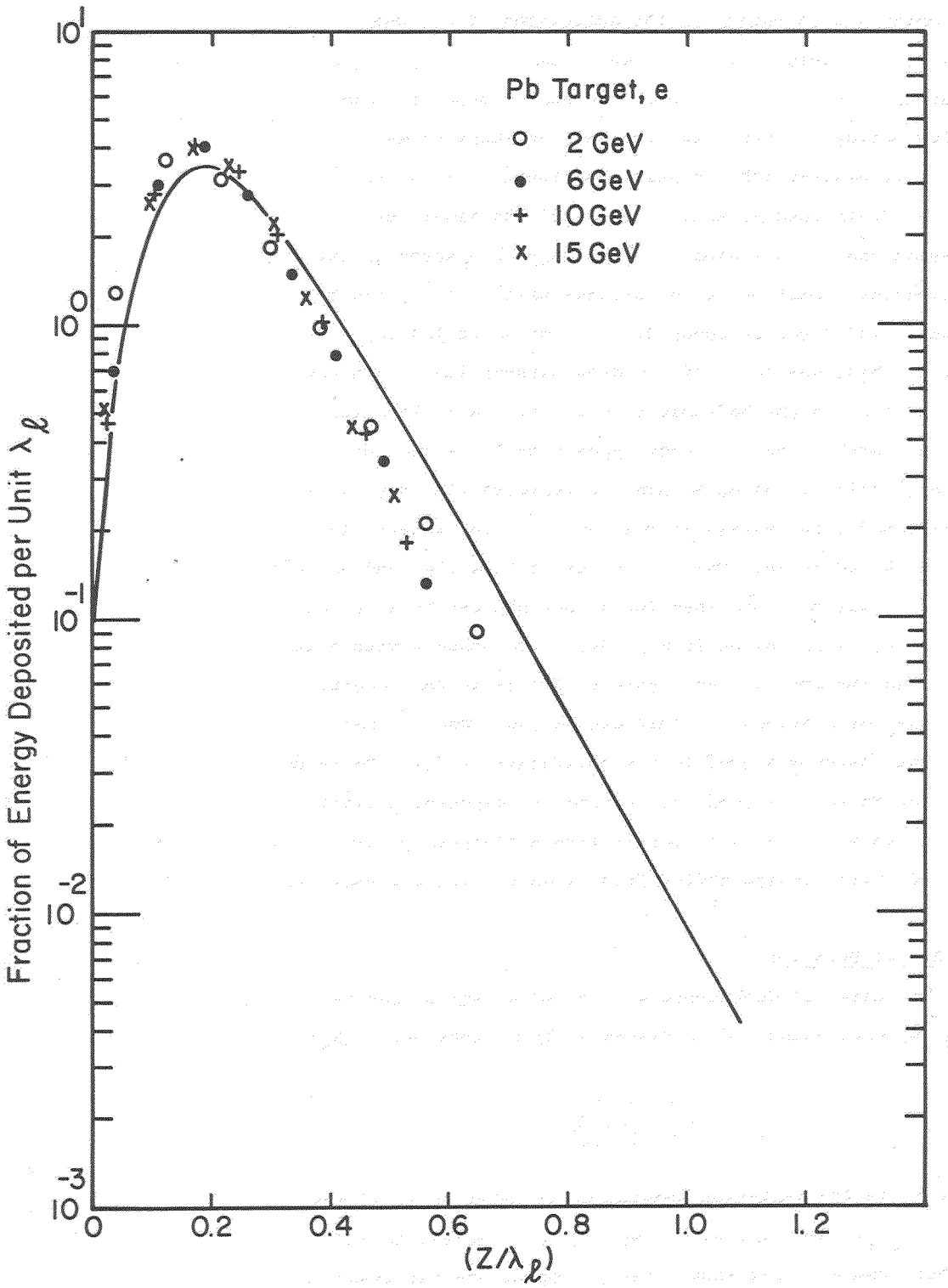

Fig. IV.3. Fraction of total energy deposited per unit λ_ℓ versus depth (in units λ_ℓ) for the data of Muller.[22] Solid line is the universal curve assumed in this work (see text).

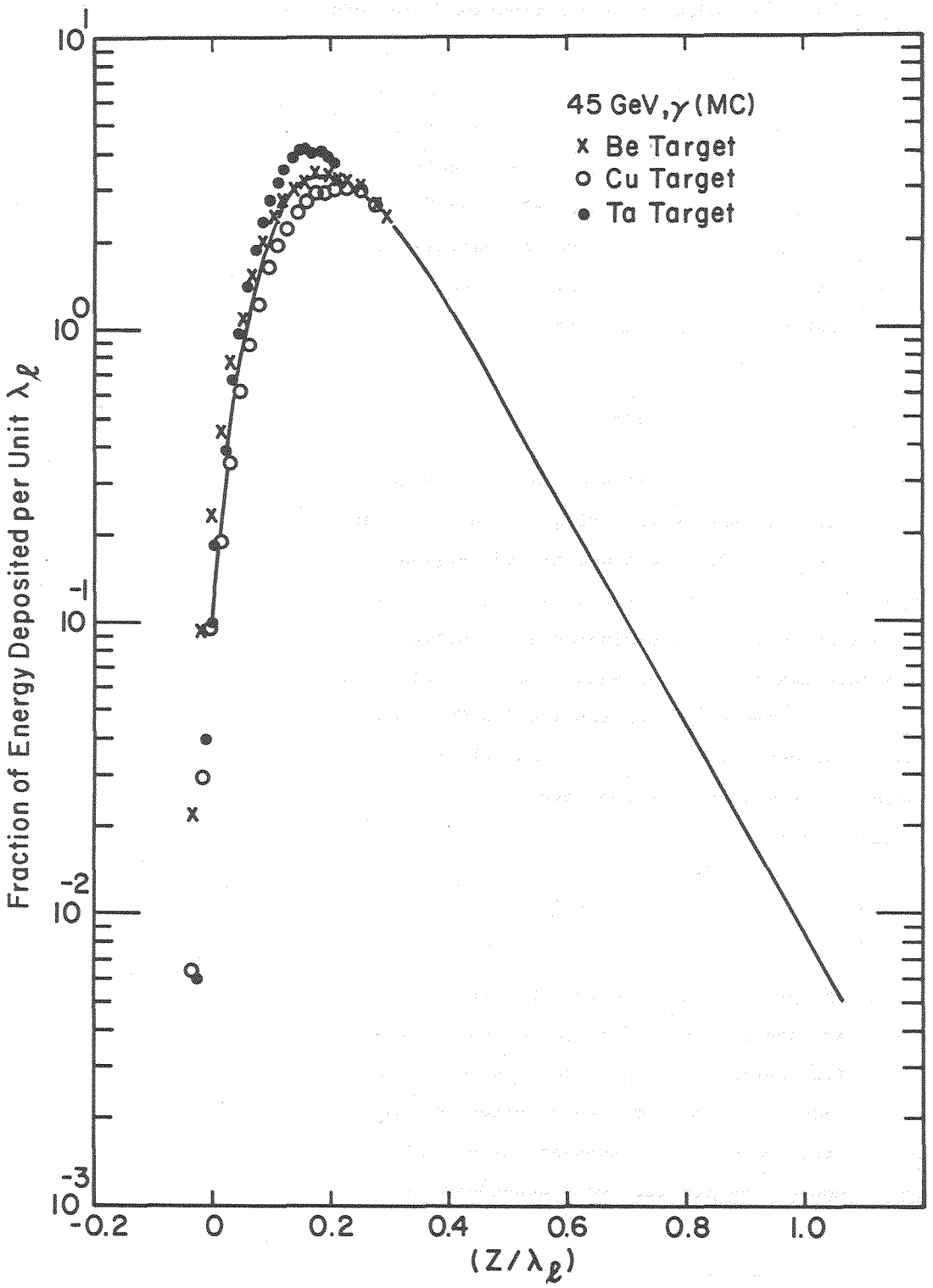

Fig. IV.4. Fraction of total energy deposited per unit λ_ℓ versus depth (in units λ_ℓ) for the data of Alsmiller and Moran,[23] and of Alsmiller.[24] Solid line is the universal curve assumed in this work (see text).

flux occurs, then the radial flux distributions are independent of incident electron (photon) energy. In these units the energy deposition distributions should also be approximately independent of incident energy. Thus, for depths expressed in units of λ_ℓ and radii in units of X_M the radial behavior is independent of E^e_{inc} and Z.

For ease of implementation in the MC calculations it is attractive to further simplify this (at the expense of accuracy) by introducing the variable

$$\theta = \frac{(r/X_M)}{(z/\lambda_\ell)} \tag{10}$$

Figs. IV.5-7 show plots of the radial distributions (i.e., the energy deposited in a ring of constant width) as a function of θ at different depths and derived from References 21, 23, 24. (Muller's study[22] does not include radial distributions). The ordinates are unnormalized. As can be seen the depth dependence enters significantly only at large θ. The Alsmiller results for Cu and Ta also show large deviations at small θ but their statistical uncertainty may account for this.

A rough fit of the form

$$F(\theta) \propto e^{-.46\theta} \tag{11}$$

is shown on the plots. Numerically, the errors in the scale of distance are again in the cm range and for most applications the fluctuations in radial development of the hadronic cascade will dominate. An alternative scheme could have a two (or multi-) component universal curve with each component having its own θ dependence.

3. Monte Carlo Application

The above method of describing energy deposition was implemented in a simple MC scheme to compute the average

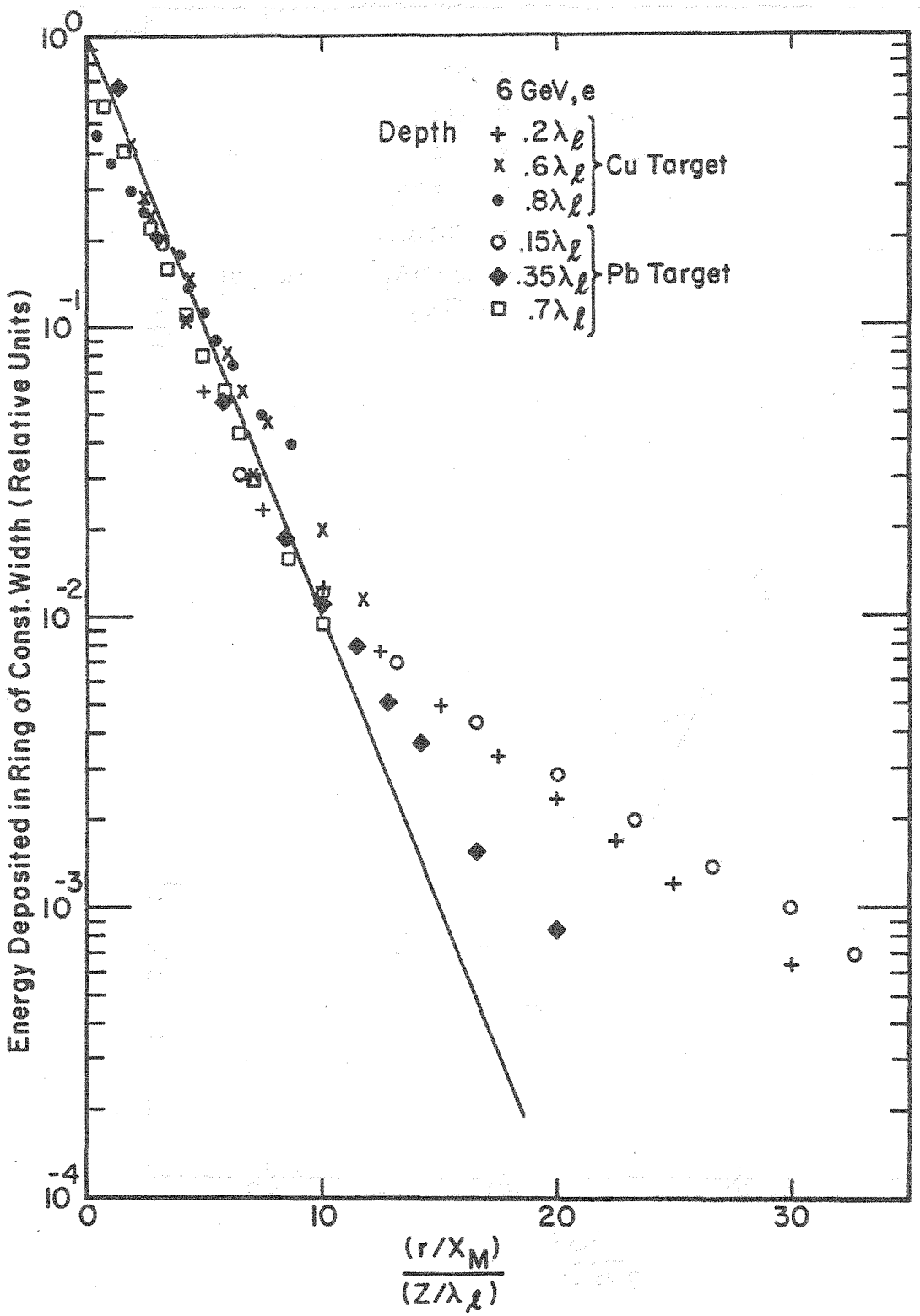

Fig. IV.5. Radial distribution of energy deposited as a function of $\theta = (r/X_m)/(Z/\lambda_\ell)$ in arbitrary units for the data of Bathow et al.[20] The variables are defined in the text.

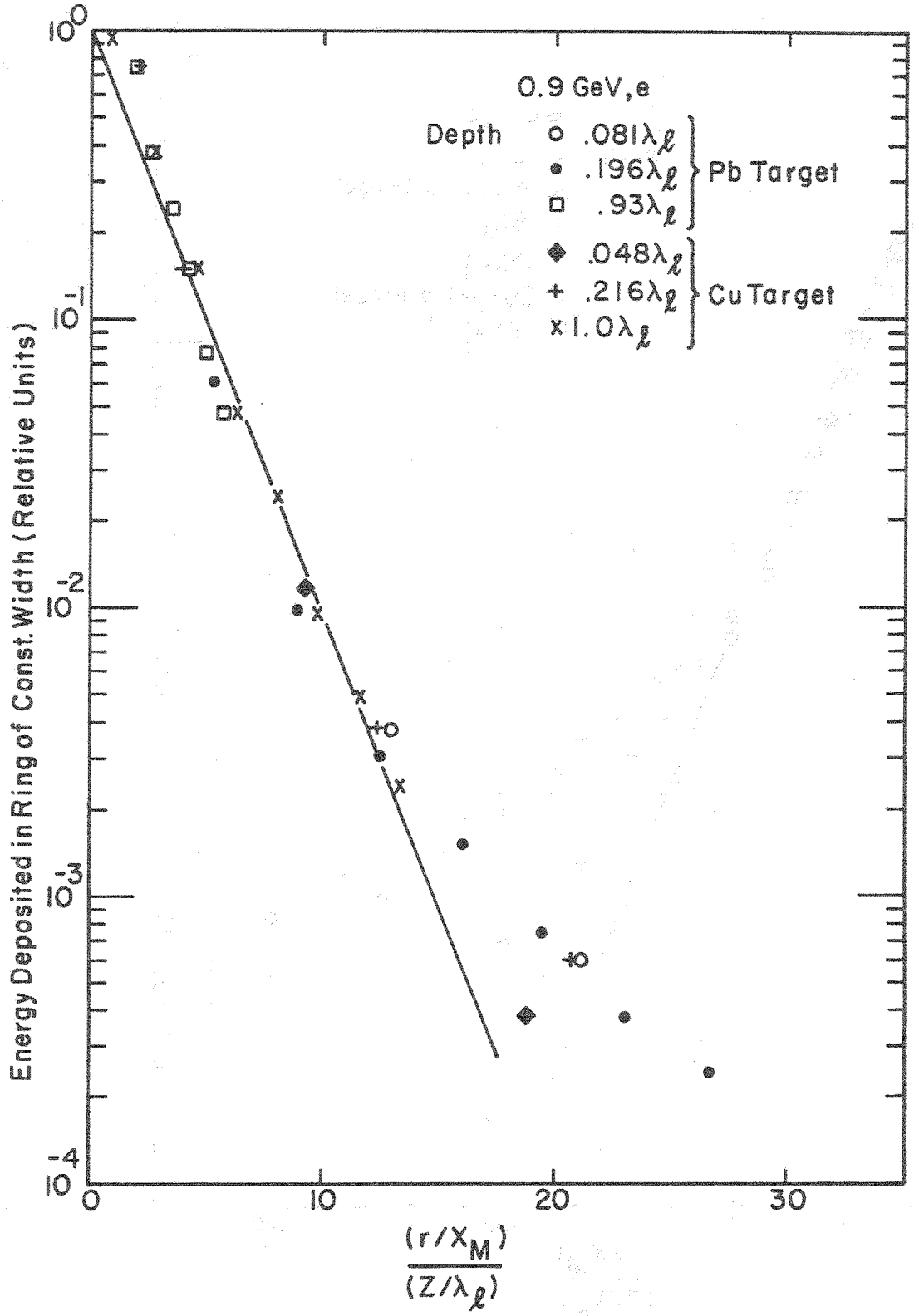

Fig. IV.6. Radial distribution of energy deposited as a function of $\theta = (r/X_m)/(Z/\lambda_\ell)$ in arbitrary units for the data of Crannell.[21] The variables are defined in the text.

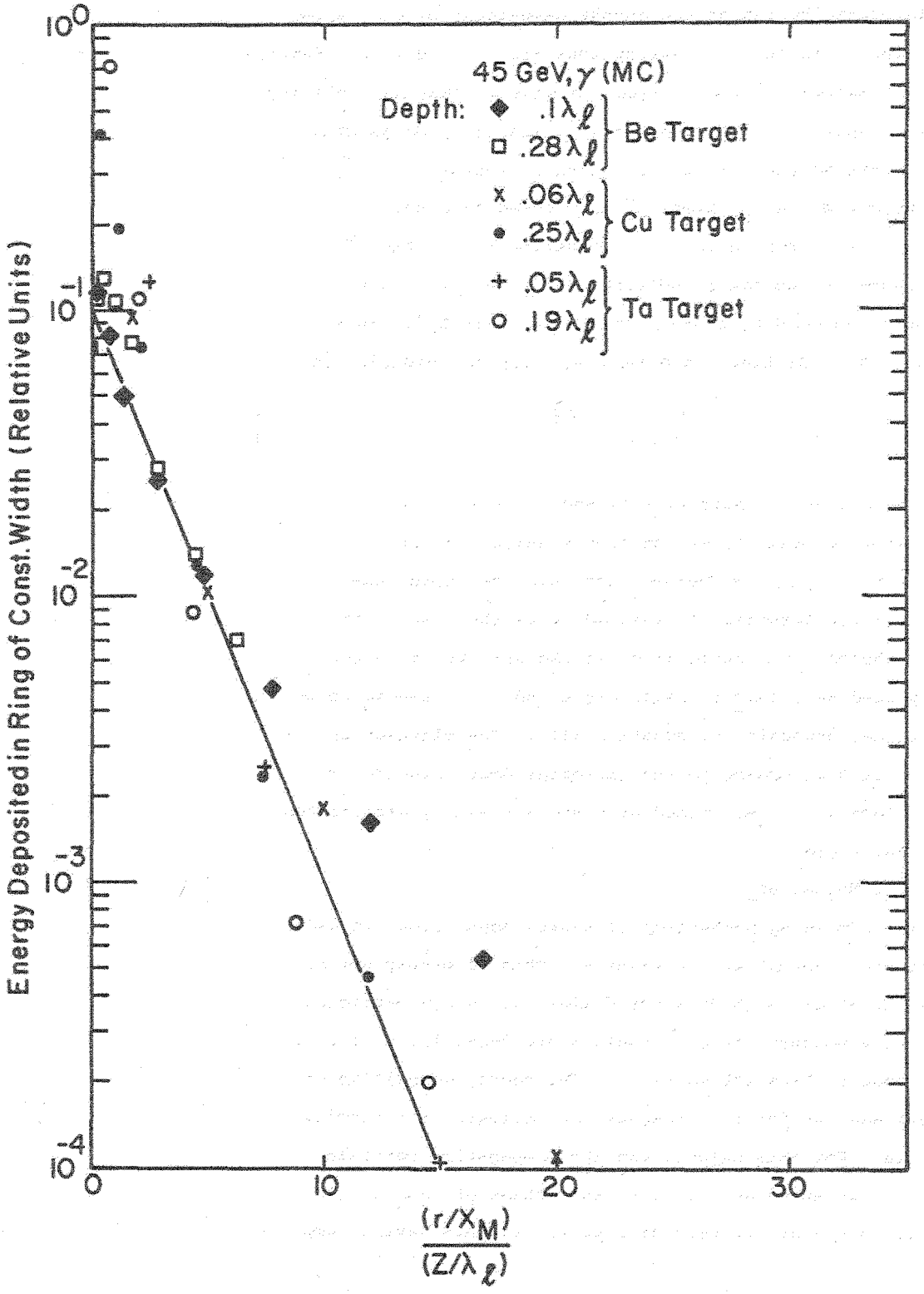

Fig. IV.7. Radial distribution of energy deposited as a function of $\theta = (r/X_m)/(Z/\lambda_\ell)$ in arbitrary units for the data of Alsmiller and Moran[23] and Alsmiller.[24] The variables are defined in the text.

spatial distribution of the energy deposition by e.m. showers. The π^o inclusive distributions are assumed to be identical to (non-leading) π^+ and π^- with the same average multiplicity for each species. Then every time a charged pion is created in the MC run, it is also taken to represent a π^o, with weight W = 0.5. Every π^o is assumed to decay into two photons. From an isotropic distribution in the π^o rest-frame one photon is selected (W' = 2W = 1). Every photon is assumed to produce an $e^+ - e^-$ pair a distance x away. This distance is determined from the distribution[27]

$$F(x) \propto e^{-\frac{7x}{9X_o}} \tag{12}$$

One electron of the pair is followed (W" = 2W' = 2). Its energy is randomly chosen from a uniform distribution over the interval between zero and the photon energy, and its direction is assumed to be the same as that of the photon. The ratio (r/z) in the variable θ is now interpreted as a (small) polar angle and θ is assumed to be distributed according to equation (11). The electron energy is deposited according to the universal depth dependence curve along a ray determined by θ and a randomly distributed azimuthal angle.

B. Other Mechanisms

The remaining mechanisms of energy deposition are calculated in somewhat cruder fashion. This is partly out of necessity since CASIM does not follow low energy particles, and partly because these mechanisms are generally of lesser importance at Fermilab energies. The energy deposition of the cascade particles is computed by following a recording particle. For this calculation the propagating particle (which is selected according to the scheme of Section II.C) may also serve as the recording particle, thus saving computer time.

1. Ionization

Ionization losses, including losses from bremsstrahlung and direct pair production are derived from a table (dE/dx) values taken from existing compilations.[18,19] This energy is calculated and deposited stepwise along the trajectory of the recording particle in the same way as in a star density calculation.

2. De-excitation of Struck Nuclei

The excitation energy as a function of incident energy is assumed to follow equation (6) and evaporation of low energy particles is considered to be the dominant mode of de-excitation. From Dostrofsky et al.[28], the average number of nucleons emitted is

$$\langle \Delta A \rangle = \frac{E^*}{8.9 + .97\ \tau_o} \tag{13}$$

with E* (excitation energy) and τ_o (nuclear temperature) in MeV and $\tau_o = (10E^*/A)^{\frac{1}{2}}$. An average binding energy of 8 MeV per nucleon is excluded from the energy to be deposited. The remainder,

$$E^{*\prime} = \frac{0.9 + .97\ \tau_o}{8.9 + .97\ \tau_o} E^* \tag{14}$$

is assumed to be equally distributed between charged particle and neutron evaporation. The charged particle fraction of the excitation energy is deposited locally at each recording event. The evaporation neutrons can be expected to propagate in a complicated fashion until they eventually are absorbed or escape. Their history is rather drastically simplified by assuming that one half of this fraction of E*' is deposited one interaction length away (isotropically distrubuted) from the pseudo event.[5] For ease of computation E*' is stored in tables as a function of energy (for neutrons) or range (for charged particles).

3. Particles Below Threshold

The energy of particles emitted below threshold, E_{BT}, is stored in tabular form and treated like E*', i.e., 015 E_{BT} is deposited locally at each pseudo event and 0.25 E_{BT} is deposited one interaction length away. When a charged particle will fall below threshold during the next recording step, all its kinetic energy is deposited at a distance of one half the range at threshold momentum along its direction of motion. For pions, in addition one half of the rest mass energy is deposited, at a distance equal to the full range at threshold along its direction of motion. This crudely reflects the facts that (a) π^+ generally decay ($\mu^+\nu$) and the μ^+ decays subsequently ($e^+\nu\bar{\nu}$), and only the μ^+ and e^+ ionization is observed; (b) while π^- generally interact with a nucleus, the histories of the particles emitted are not followed, and binding energy corrections etc., cause less than the full rest mass energy to be observed.

Special Calculations

V. SPECIAL CALCULATIONS

For a number of applications the star density calculations described in Section II.C and Section III require some modifications to obtain statistically significant results in a reasonable amount of computer time. A brief description of a few such applications and the techniques required follows.

A. Biased Calculations

The particle selection schemes of Section II.C are aimed at giving general answers. For calculations for which the primary interest pertains to a particular region of space or range of particle momenta the above techniques are not very efficient. Where geometry or dimensions pose no special problems these schemes may still be sufficient. However, for a large class of problems special handling is necessary. This class can be further divided according to whether biasing is introduced in the cascade propagating stage, in the recording stage, or both. An illustrative example of each is included in this section. Biasing of the distance to collision has already been mentioned in Section II. What follows is only a brief description of the techniques actually used. More general considerations can be found in textbooks on MC methods.[29] Since the results of these special calculations are only of limited interest they have not been included.

1. Neutral Beam into Liquid D_2 Cryostat

The configuration as idealized by P. Gollon[30] from an actual experimental design is depicted in Fig. V.1 in the form of a cross section through the upper half of the (assumed) cylindrically symmetric cryostat and sweeping magnets. A magnet following the Be target deflects the charged particles, sweeping them off the center line and into a beamdump.

Only the very forward neutrons emerging from the Be target will contribute significantly to the dose rates at

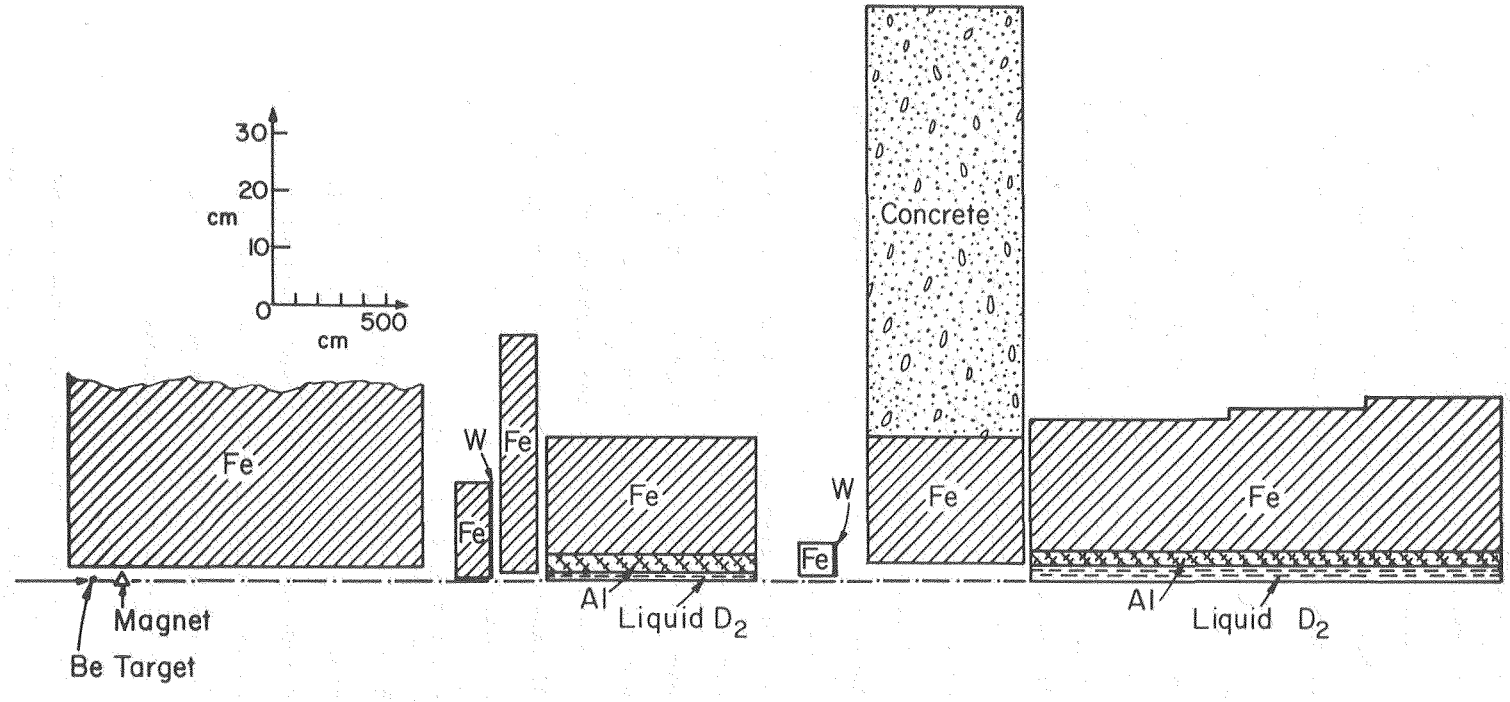

Fig. V.1. Idealized shielding configuration for the Fermilab Proton Area Neutral Beam. Note the difference in scale for lateral and radial dimension.

large depths and radii. For this reason a different selection scheme is employed. The polar angle of the propagating particles in the Be target is chosen from a distribution $\exp(-\theta/\langle\theta\rangle)$ with $\langle\theta\rangle = .001$ rad. Their momenta are selected from the function $S(p) \propto p$ for nucleons and $S(p) = \text{const.}$ for pions. Since the sweeping magnet deflects all charged particles off axis, the particle emerging from the last interaction in the Be is always assumed to be a neutron.

With this procedure a crude estimate of the relevant dose rates is obtained. While further biasing might enhance the statistics this benefit could not justify additional programming efforts and computer time.

2. Dose Rate to General Population

There is a directive at Fermilab to limit annual accelerator produced doses at the site boundary to ten millirem. The question of what is adequate shielding for a distant region cannot be readily deduced from the study of star densities in the shield itself.

An example is the study performed for the Fermilab Neutrino Section consisting of a 180 cm steel beamstop followed by two kilometers of air to a heavily travelled highway (Ill. 38) which is situated near the site boundary. Since the dose rate at ground level or at small elevation is of prime interest some forward biasing is needed. Six "target regions" are established at 0, 3, 10, 30 and 100m off the axis, all at 2 km from the beamstop. Every time a particle undergoes a collision in the steel or in the air, one or more recording particles are aimed at the target regions. The number of recording particles at each collision is determined from the weight of the parent particle and the distance to the target region. The particle momenta are chosen from a set of crude approximations to the thermodynamical spectra and to the knock-out nuclear spectra, then they are weighted according to equation (1). In this manner relatively smooth

momentum spectra are derived for each of the different particle types at each of the six target regions. Dose rates can then be estimated. This technique also has applications for the design of targets and collimators. It has already been used for studying background problems in particle detectors at selected locations of an experimental layout for Fermilab Experiment No. 177.

B. Other Outputs

A number of other quantities are readily derived from the star densities and momentum spectra described in Section III. Examples are radiological dose and dose equivalent, light output of a scintillator including the nonlinear effects as well as production of radionuclides. This last one is important to estimate radioactivation of accelerator components, radioactivity produced in the environment outside a shielding configuration and also to calculate accurately the response of activation detectors.

A natural application is the prediction of "ionization calorimeter" outputs for incident hadrons of various energies. This is described below.

C. Ionization Calorimeters

The design of ionization calorimeters may be divided into two parts, (a) the choice of materials and overall dimensions so that a certain fraction of the incident energy is deposited in the calorimeter, (b) the choice of number of energy deposited sensors, type, mass, etc. After these choices are made, questions may be asked about the response of the calorimeter, to various particles with different incident energies.

In this volume, curves are given to help selecting outside dimensions for steel calorimeters. The energy deposited in steel has been integrated as a function of radius for various lengths, Figures VIII.74 through VIII.77, and as a function of length for various radii, Figures VIII.78 through VIII.81. This is shown for the four standard energies in each form of presentation. Figures VIII.82 through VIII.85 are equal energy density contours

which may be useful for designing non-uniform calorimeter structures.

Work useful in estimating energy resolution of calorimeters is now in progress.

Radiation Protection

VI. RADIATION PROTECTION

The star density graphs of Section VIII can be readily converted into quantities of radiological interest. This is less accurate than calculating them directly in the MC program but it keeps the volume of output more manageable. The necessary conversion factors are given below, along with the assumptions made for their derivation.

A. Fluxes and Dose Rates

It must be recalled that the star densities pertain to particles exceeding a certain threshold momentum, specifically 0.3 GeV/c for the results presented in this manual. The value of the cut-off is important in determining the conversion factors for stars to dose and to dose equivalent. What follows pertains specifically to the 0.3 GeV/c value. As mentioned before, this threshold is introduced mainly for convenience of computation. At low energies the Hagedorn-Ranft production model (Section II.B) is not valid. Furthermore the cross sections vary rapidly with energy in this region. To include such effects in sufficient detail calls for a large store of additional information and for rather different techniques. Alsmiller's group at ORNL has performed such calculations.

It is well known from ORNL's and similar calculations and also from observation that for a sufficiently well developed cascade, the shape of the spectrum for the low energy particles is rather independent of location within the shield, incident energy or even shielding material (as long as the hydrogen content is essentially the same). This is also borne out by the CASIM spectra even with their relatively high cut-off momentum.

To include low energy particle effects in the derivation of fluxes and dose rates it is then sufficient to assume a representative shape for the lower end of the energy spectrum. Fig. VI.1 shows the assumed spectrum of low energy particles as calculated by Gabriel and Santoro[31] of ORNL for the (soil)

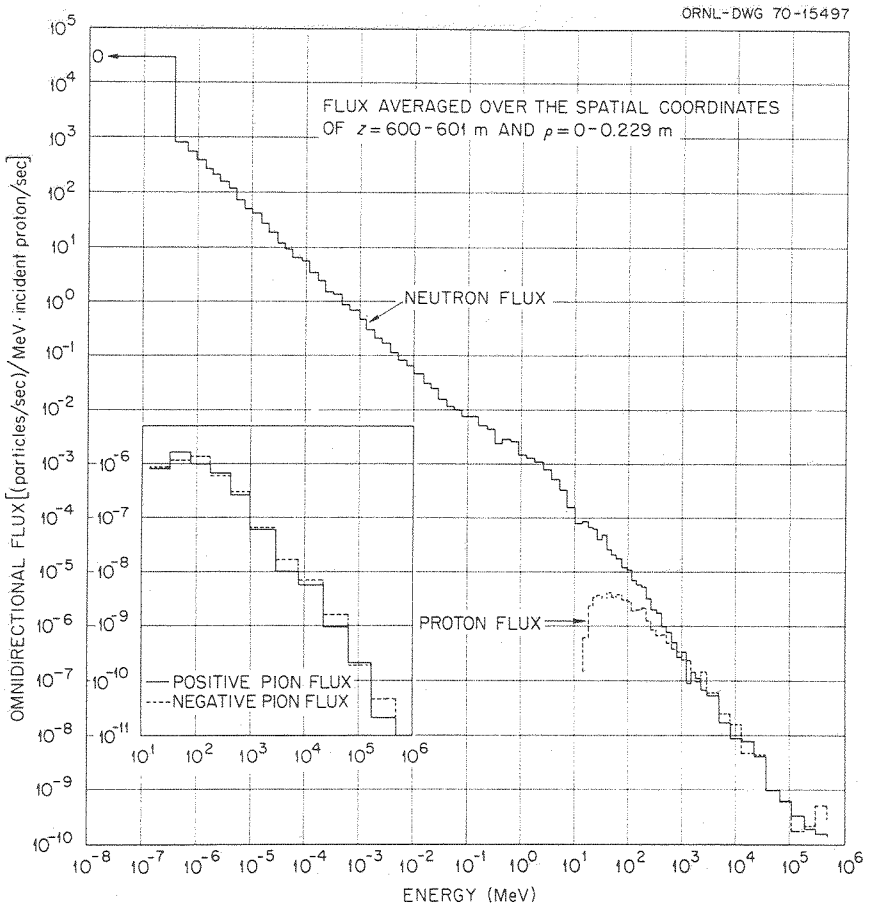

Fig. VI.1. Kinetic energy spectrum of hadrons as calculated by T. Gabriel and R. Santoro[31] for the backwall of a target-tunnel configuration. This spectrum is assumed to be representative of an equilibrium spectrum and is used to calculate the effects of low energy particles not followed in CASIM.

back wall of a target-tunnel configuration. This spectrum is then separately normalized to the CASIM results in the 0.3-0.8 GeV/c momentum range for protons, neutrons and pions. The higher energy part of the spectrum of Fig. VI.1 does not enter into these calculations.

The spectrum of Gabriel and Santoro[31] is used in this manner even for regions in the shield where the assumption of cascade equilibrium is not valid, i.e., close to where the beam enters. Even if sufficient information were available, it would be quite cumbersome to evaluate the proper conversion factors in these regions because the shape of the low energy

spectrum is expected to vary rapidly with location. The results obtained using the equilibrium spectrum are overestimates for these cases. On the other hand since the assumed spectrum of Gabriel and Santoro[31] is calculated for a material containing 1.2% by weight of hydrogen, its use in hydrogen free materials may underestimate the flux and related quantities.

In all cases the conversion factors (and quantities derived from them) carry a somewhat larger uncertainty than the direct MC results (star densities) since the normalization of the low energy end of the spectrum hinges on the results for a small momentum region. However, this is a small effect because the number of particles contained in this momentum region is always a significant fraction of the total and in fact in regions of poor statistics the spectrum is dominated by these particles. Results are presented below for conversion factors relating star density to hadron flux, entrance absorbed dose and maximum dose equivalent.

1. Total Hadron Flux

The omnidirectional hadron flux above threshold (hadrons/cm^2 inc. proton) is obtained by multiplying the star density (stars/cm^3) by the interaction length (in cm). The total omnidirectional flux (including effects of low energy particles) per star as a function of location in a large irom beamstop is shown in Fig. VI.2 both for 30 GeV/c and 1000 GeV/c incident protons. This conversion factor is roughly the same in all regions where the cascade is well developed. Fig. VI.3 shows similar results for a concrete beamstop.

2. Entrance Absorbed Dose

The entrance absorbed dose is the energy absorbed per gram of tissue (in rad) at or near the surface of a slab of tissue bombarded with the particles at that location.

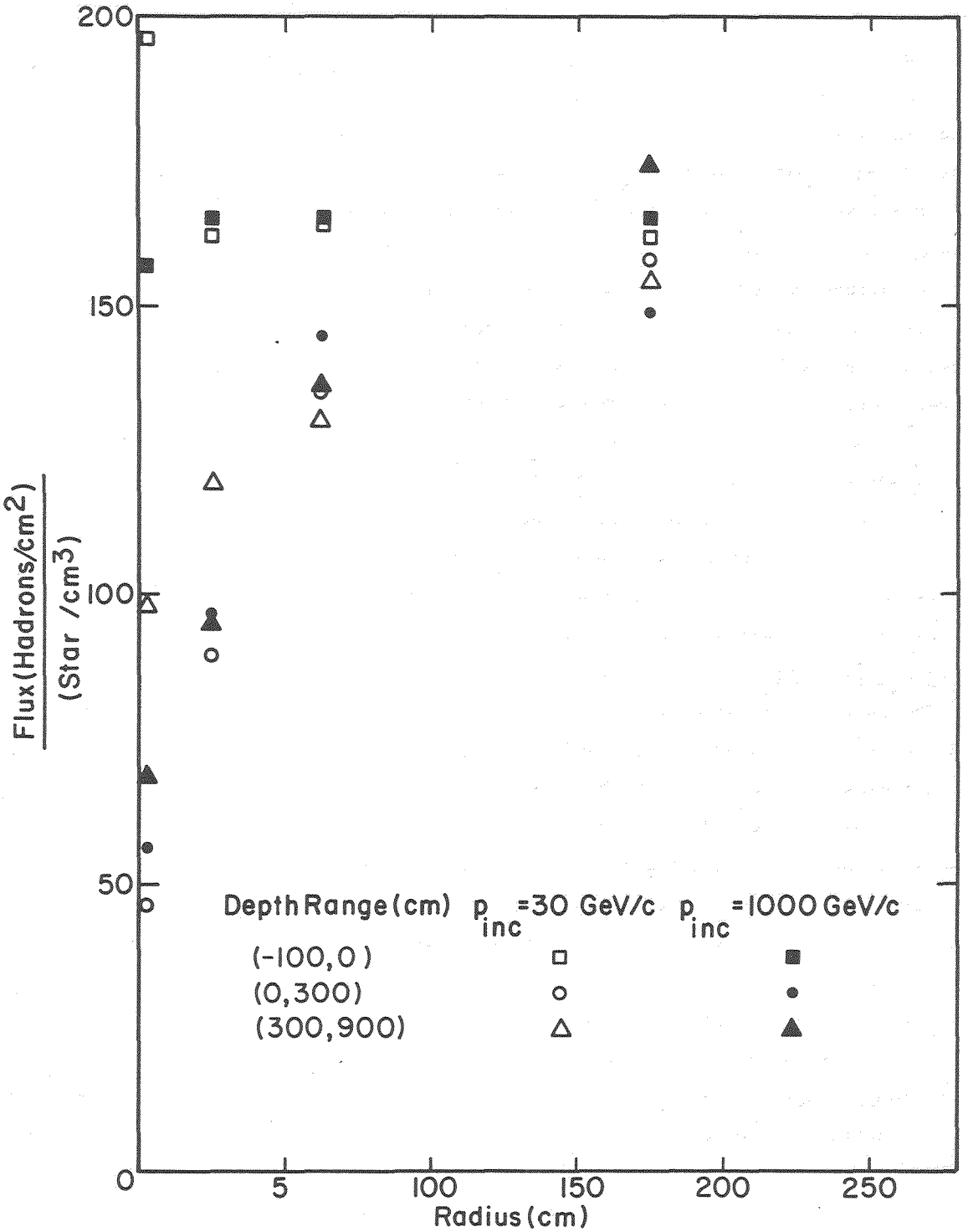

Fig. VI.2. Conversion factor of star density (stars/cm^3) to omnidirectional flux (hadrons/cm^2) as a function of radius for a solid iron cylinder at various depths for incident proton momenta of 30 and 1000 GeV/c.

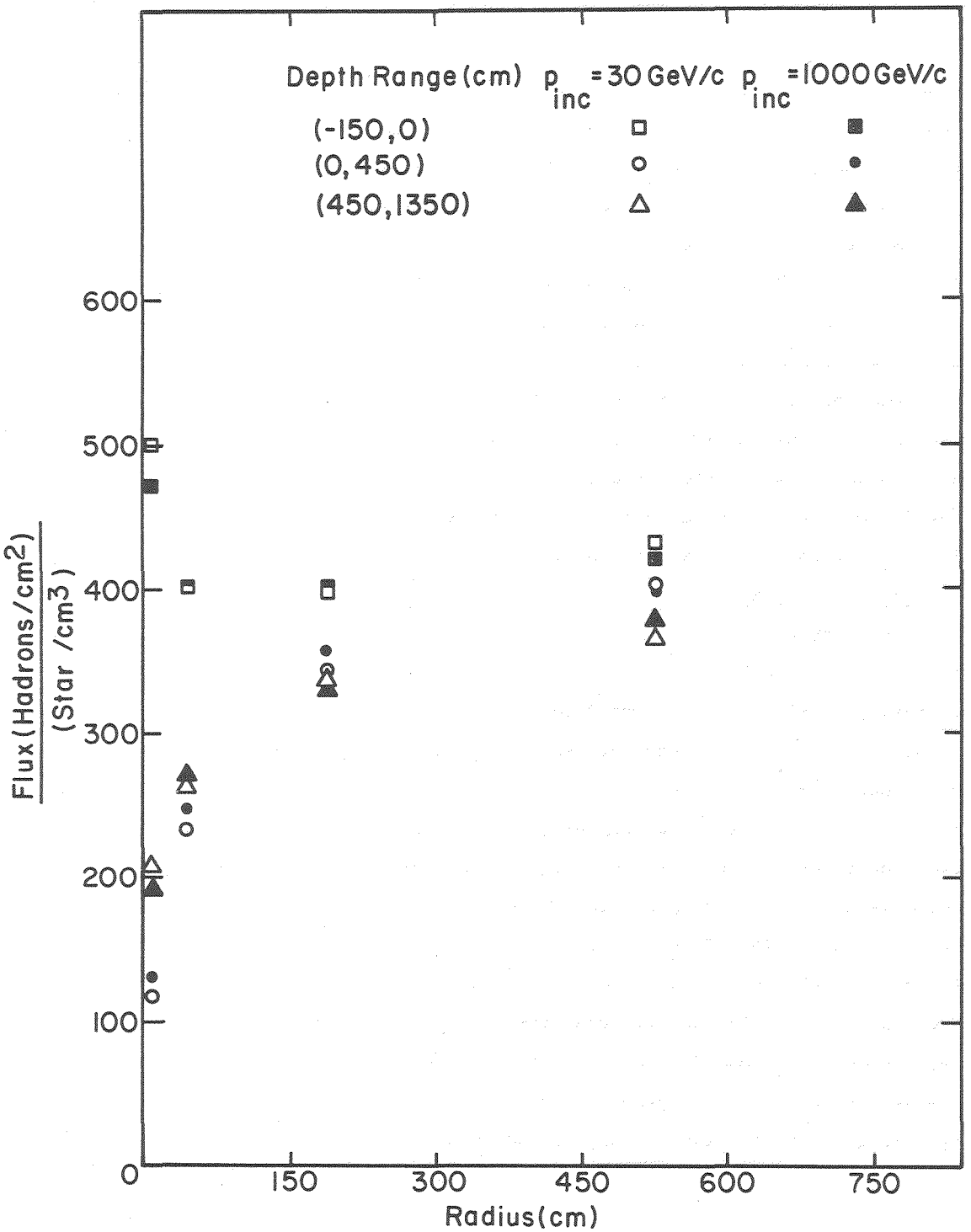

Fig. VI.3. Conversion factor of star density (stars/cm^3) to omnidirectional flux (hadrons/cm^2) as a function of radius for a solid concrete cylinder at various depths for incident proton momenta of 30 and 1000 GeV/c.

It is expected to be roughly proportional to what is measured with a detector such as a tissue equivalent ionization chamber. The results presented herein include the effects of low energy particles and of e.m. showers initiated by π^o. The entrance absorbed dose and maximum dose equivalent (see below) per particle as a function of energy for hadrons in the range of 10^{-8} MeV to 10^6 MeV is based on various sources.[32] The effect of π^o decay is roughly included by converting the charged pion star density to energy density. Each charged pion star is assumed to contribute one half the total energy of the pion. Fig. VI.4 shows the entrance absorbed dose per star (rad/star cm^{-3}) as a function of location in a large iron beamdump for 30 GeV/c and 1000 GeV/c incident protons. Fig. VI.5 is the corresponding graph for a concrete beamdump.

3. Maximum Dose Equivalent

In calculating the dose equivalent, a "quality factor" varying with particle type and with energy is assumed to modify the absorbed dose to yield a rough measure of biological effectiveness. This quality may vary considerably with depth in the human body. The International Commission on Radiological Protection[33] recommends that any evaluation of radiation hazards shall assume that every particle in the spectrum contributes the maximum dose equivalent as calculated for a 30 cm slab of tissue. This is of course an upper bound since particles of different energy generally will deposit their maximum dose equivalent at different depths. However, this is generally not a severe overestimate since the largest contribution is usually due to neutrons in the 1-50 MeV energy range, and for these particles the maximum dose equivalent occurs very near the entrance surface. A more realistic estimate would be obtained by calculating the dose equivalent integral over the spectrum at each

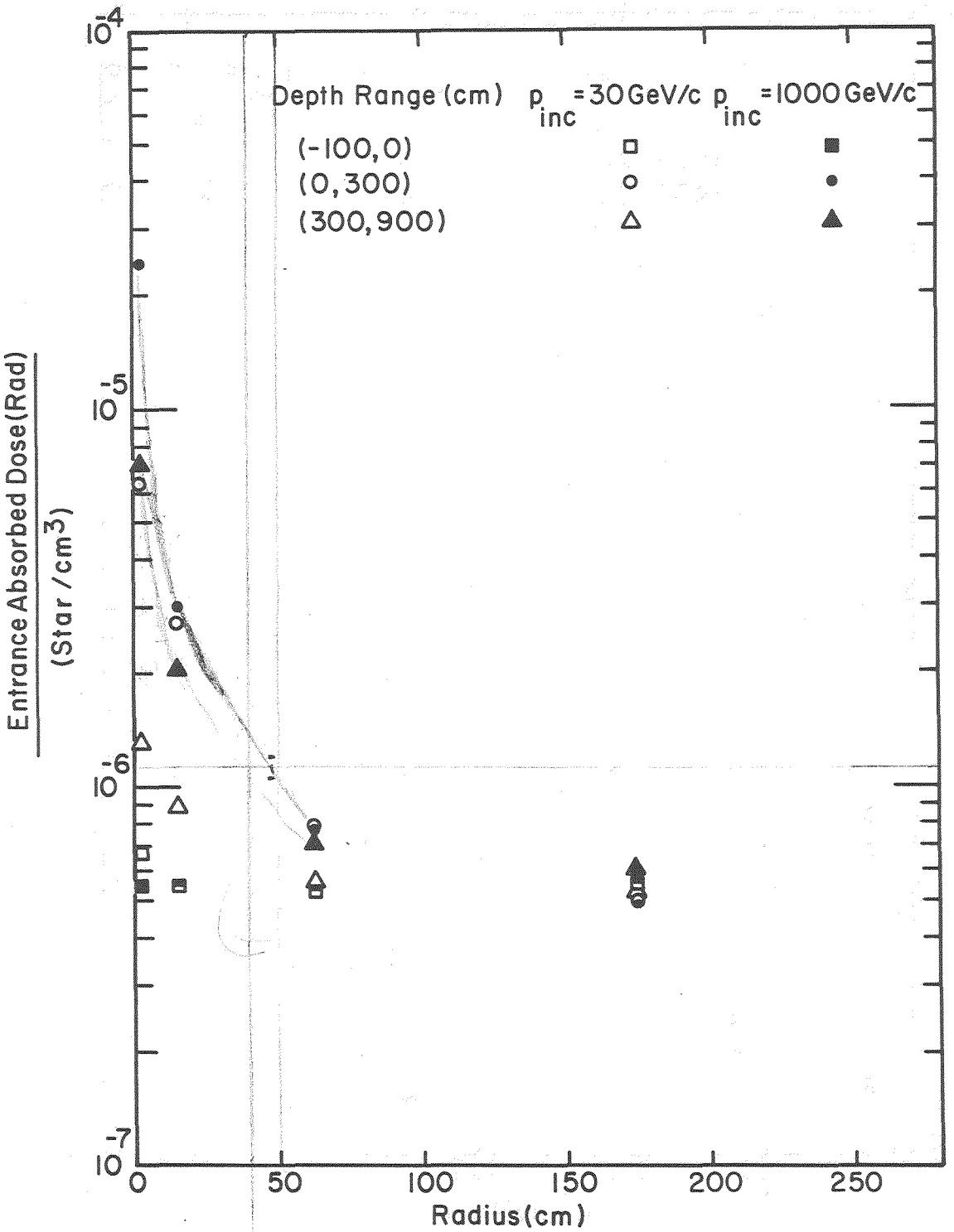

Fig. VI.4. Conversion factor of star density (stars/cm^3) to entrance absorbed dose (rad) as a function of radius for a solid iron cylinder at various depths for incident proton momenta of 30 and 1000 GeV/c.

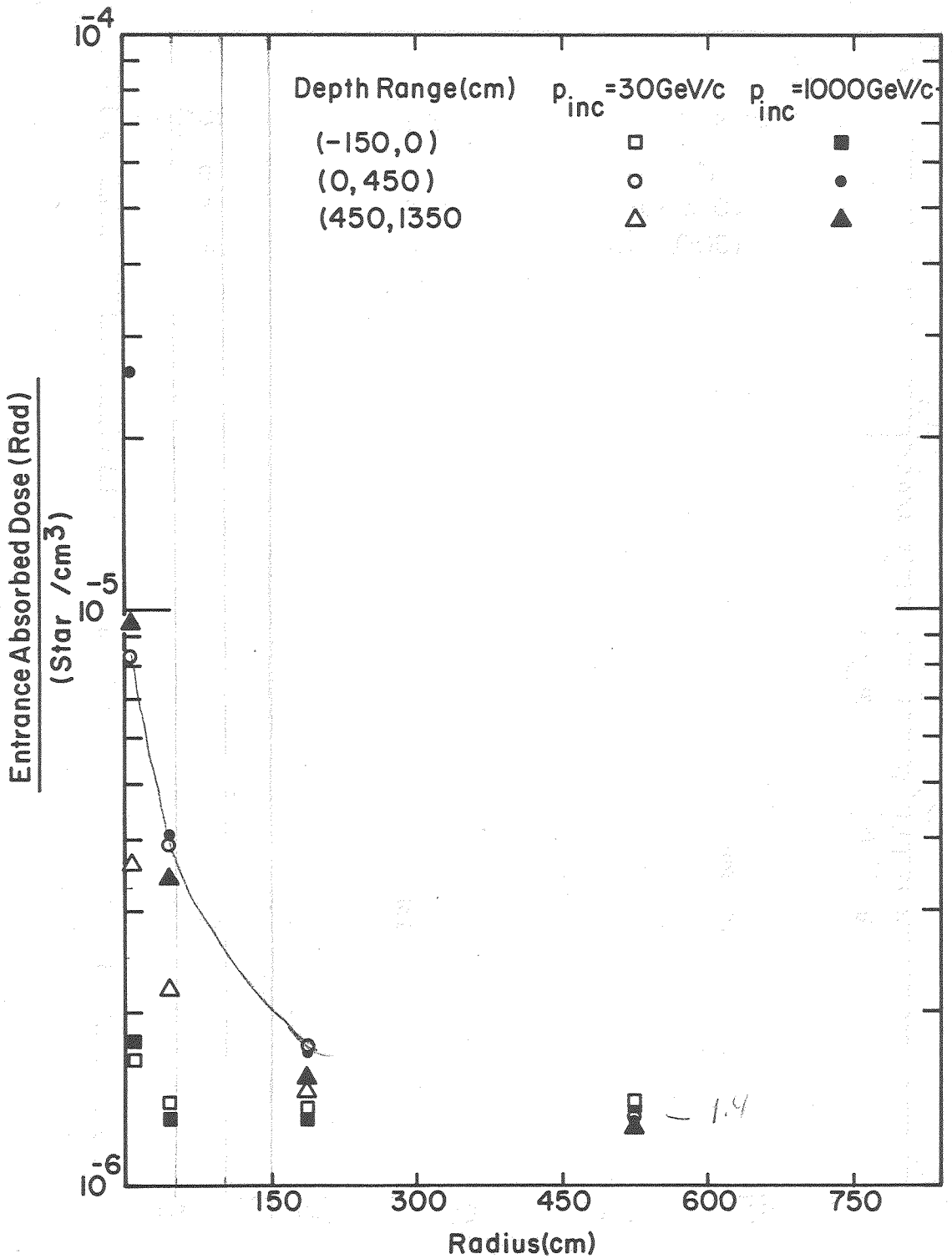

Fig. VI.5. Conversion factor of star density (stars/cm^3) to entrance absorbed dose (rad) as a function of radius for a solid ~~iron~~ cylinder at various depths for incident proton momenta of 30 and 1000 GeV/c.

concrete

depth in a slab of tissue, and then finding its maximum value. This has been discussed by Shaw et al.[34] For exposures over long periods of time, changes in position and orientation of the body will generally reduce the maximum dose equivalent even more.[35] However, such questions have been avoided because of the rather arbitrary assumptions which must necessarily enter any a priori estimate of this effect. In the present work, the π^0 contribution to the maximum dose equivalent was added with a quality factor of unity. Plots of the spatial dependence of the maximum dose equivalent per star (rem/star cm^{-3}) are shown in Figs. VI.6 and 7, again for 30 GeV/c and 1000 GeV/c protons incident on iron and on concrete. It can be seen again that in all regions where the cascade is well developed, the conversion factors are approximately equal.

4. Use of Conversion Factors

The variation of the conversion factors with location in the semi-infinite shield may be interpreted as the variation of the same factors in a finite shield of those dimensions. This is a consequence of the fact that the development of the cascade is almost uniformly forward and radially outward, so truncation of the shield has little effect on the star density inside the shield.

As can be expected the conversion factors are proportional to the interaction length (expressed in cm). The material dependence of the conversion factors can be removed by expressing them as rem(rad)/($cm^2 \cdot$ particle). For iron and concrete the conversion factors at sufficiently large depths and radii are summarized in Table VI.1.

5. Relative Contributions to Flux and Dose Rates as a Function of Energy

Most dosimeters and detectors are sensitive only to a limited range of incident hadron energies. To ascertain

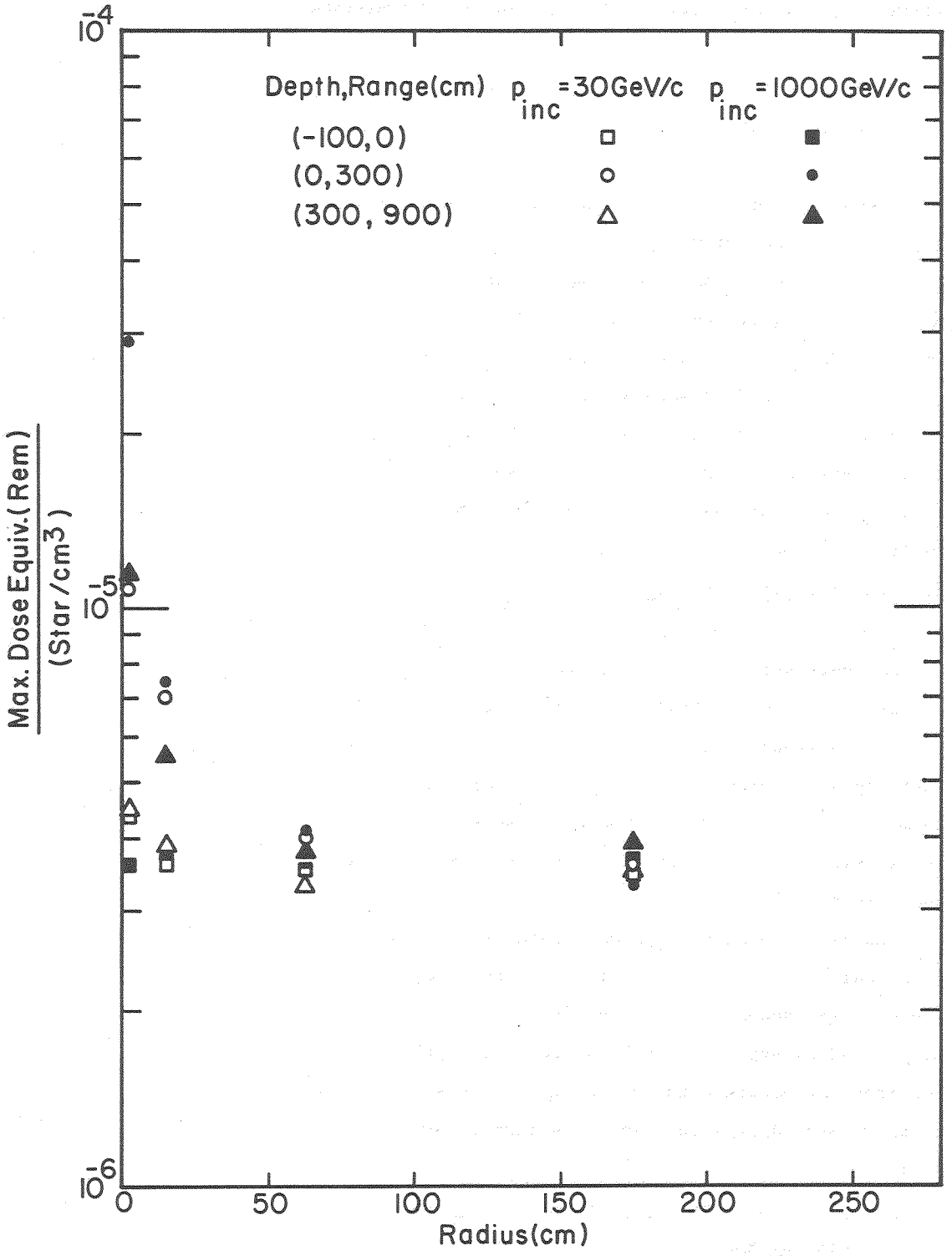

Fig. VI.6. Conversion factor of star density (stars/cm^3) to maximum dose equivalent (rem) as a function of radius for a solid iron cylinder at various depths for incident proton momenta of 30 and 1000 GeV/c.

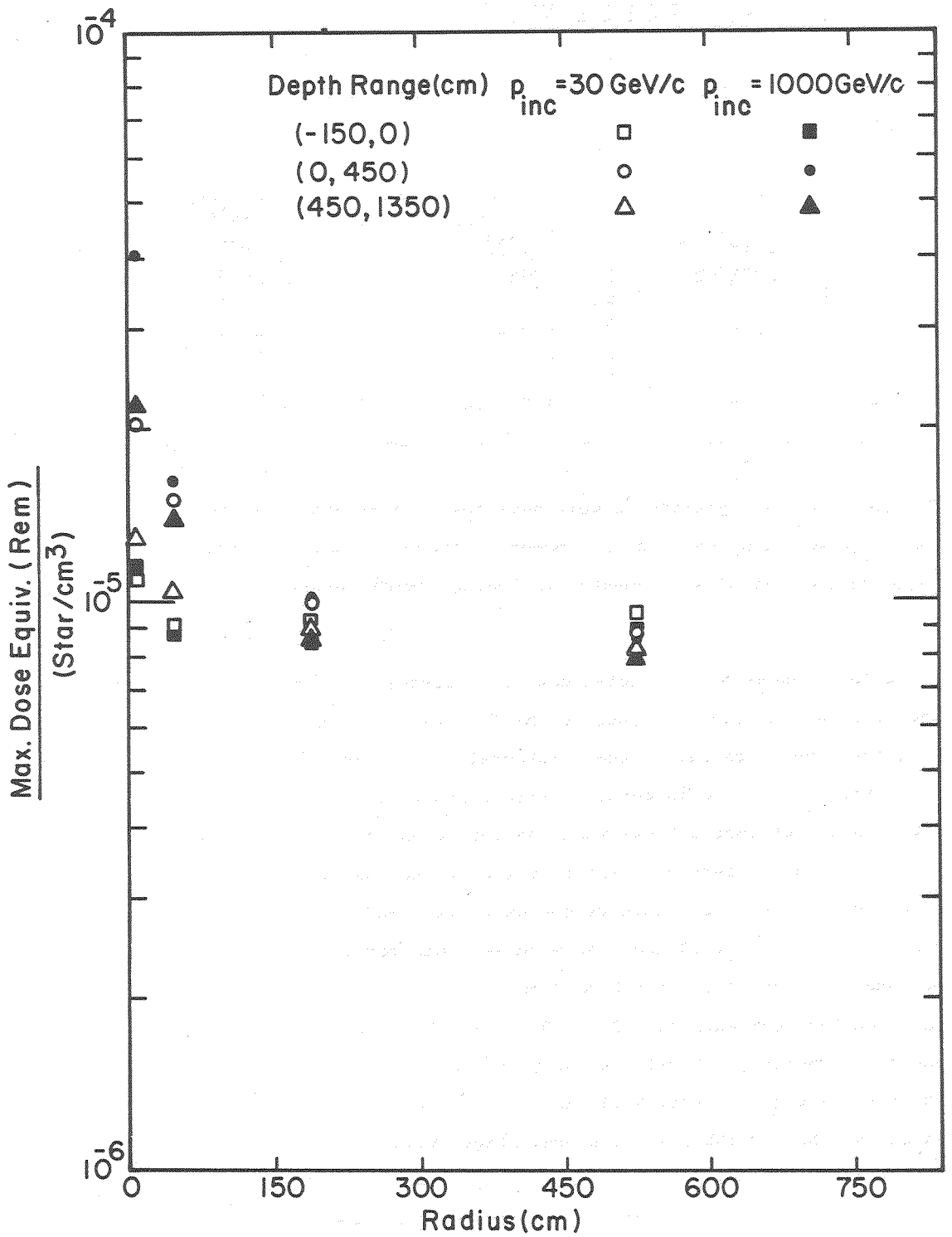

Fig. VI.7. Conversion factor of star density (stars/cm^3) to maximum dose equivalent (rem) as a function of radius for a solid concrete cylinder at various depths for incident proton momenta of 30 and 1000 GeV/c.

TABLE VI.I
CONVERSION FACTORS FOR STAR DENSITIES IN IRON AND CONCRETE*

Material	Flux $\frac{\text{Hadrons/cm}^2}{\text{Stars/cm}^3}$	Entrance Absorbed Dose $\frac{\text{Rad}}{\text{Stars/cm}^3}$	Maximum Dose Equivalent $\frac{\text{Rem}}{\text{Stars/cm}^3}$
Iron	130	6.0×10^{-7}	3.5×10^{-6}
Concrete	350	1.5×10^{-6}	9.0×10^{-6}

*In regions where cascade is well developed. Star densities refer to stars produced by hadrons with momentum above 0.3 GeV/c. Fluxes are for hadrons of all momenta, including thermal neutrons.

the effectiveness of such detectors it is useful to plot the differential contributions to the fluence and dose as a function of energy or their integrals as a function of energy. Here, the integral contributions to flux, entrance absorbed dose and maximum dose equivalent are included for easy reference. The fraction of the dose to which the detector is sensitive can be easily read off the graphs. Figs. VI.8 and 9 show these plots for 30 GeV/c protons incident on an iron beam dump for a region centered on the beam axis ($0 \leq Z \leq 300$ cm, $0 \leq R \leq 5$ cm), and for a region relatively far away ($0 \leq Z \leq 300$ cm, $100 \leq R \leq 250$ cm). Figs. VI.10 and 11 show the equivalent graphs for 100 GeV/c protons. Figs. VI.12 and 13 are similar plots for a region at large radii ($0 \leq Z \leq 450$ cm, $300 \leq R \leq 750$ cm) in a concrete beam dump irradiated by 30 GeV/c and 1000 GeV/c respectively.

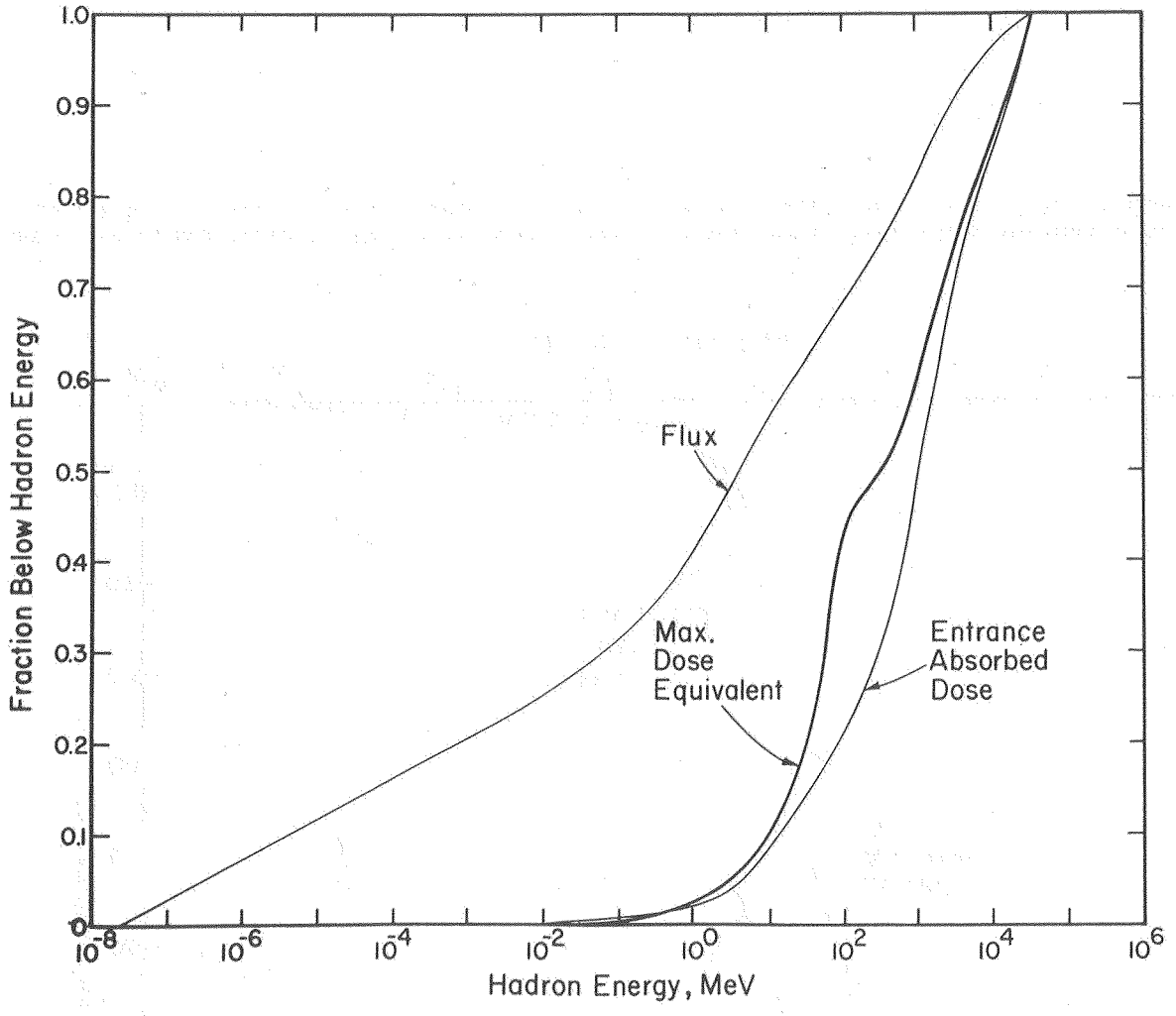

Fig. VI.8. 30 GeV/c protons incident on a solid iron cylinder. Fraction of the omnidirectional flux, entrance absorbed dose and maximum dose equivalent below hadron kinetic energy on abcissa (in MeV) for the region between zero and 300 cm depth and between zero and 5 cm radius.

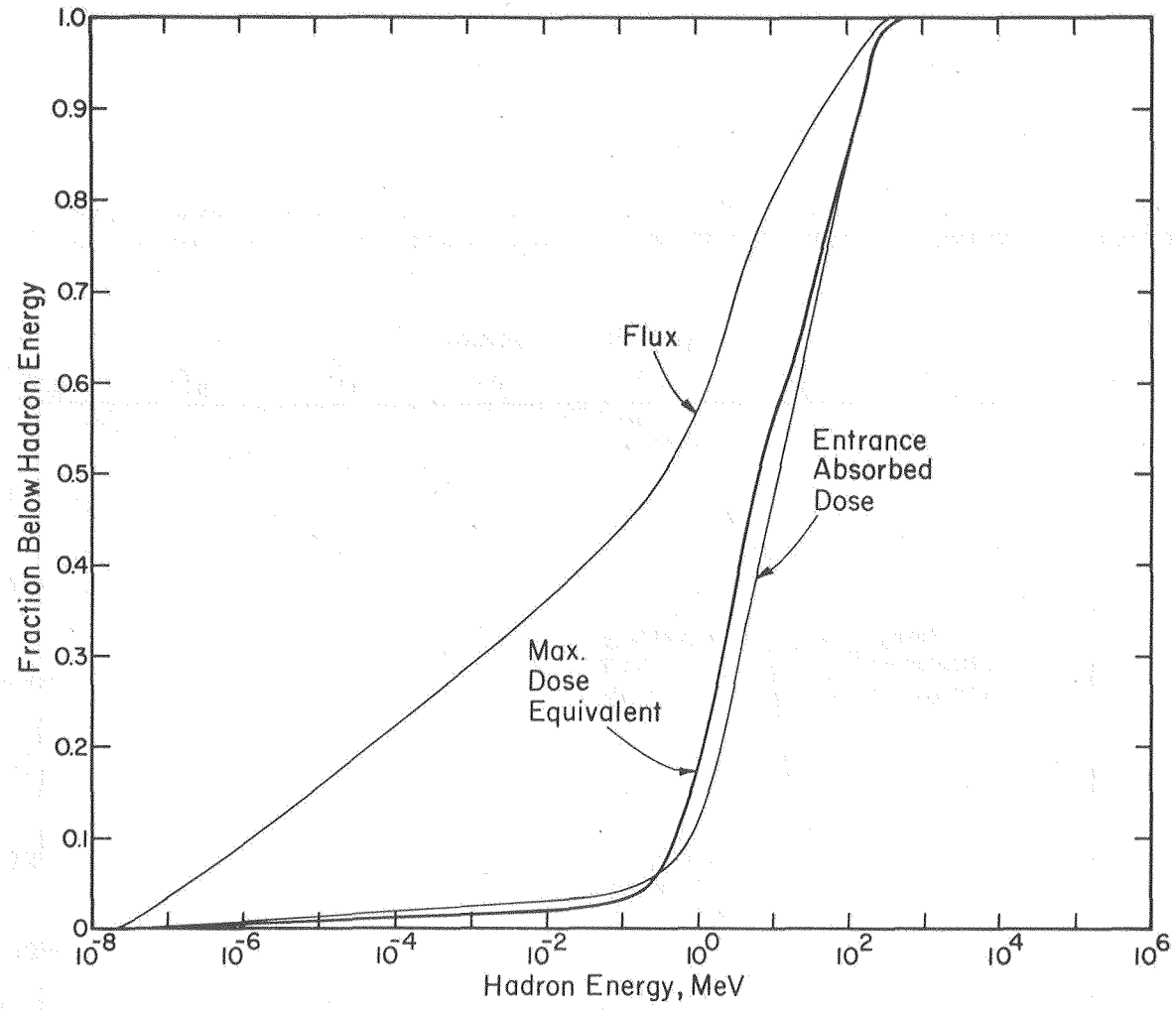

Fig. VI.9. 30 GeV/c protons incident on a solid iron cylinder. Fraction of the omnidirectional flux, entrance absorbed dose and maximum dose equivalent below hadron kinetic energy on abcissa (in MeV) for the region between zero and 300 cm depth and between 100 cm and 250 cm radius.

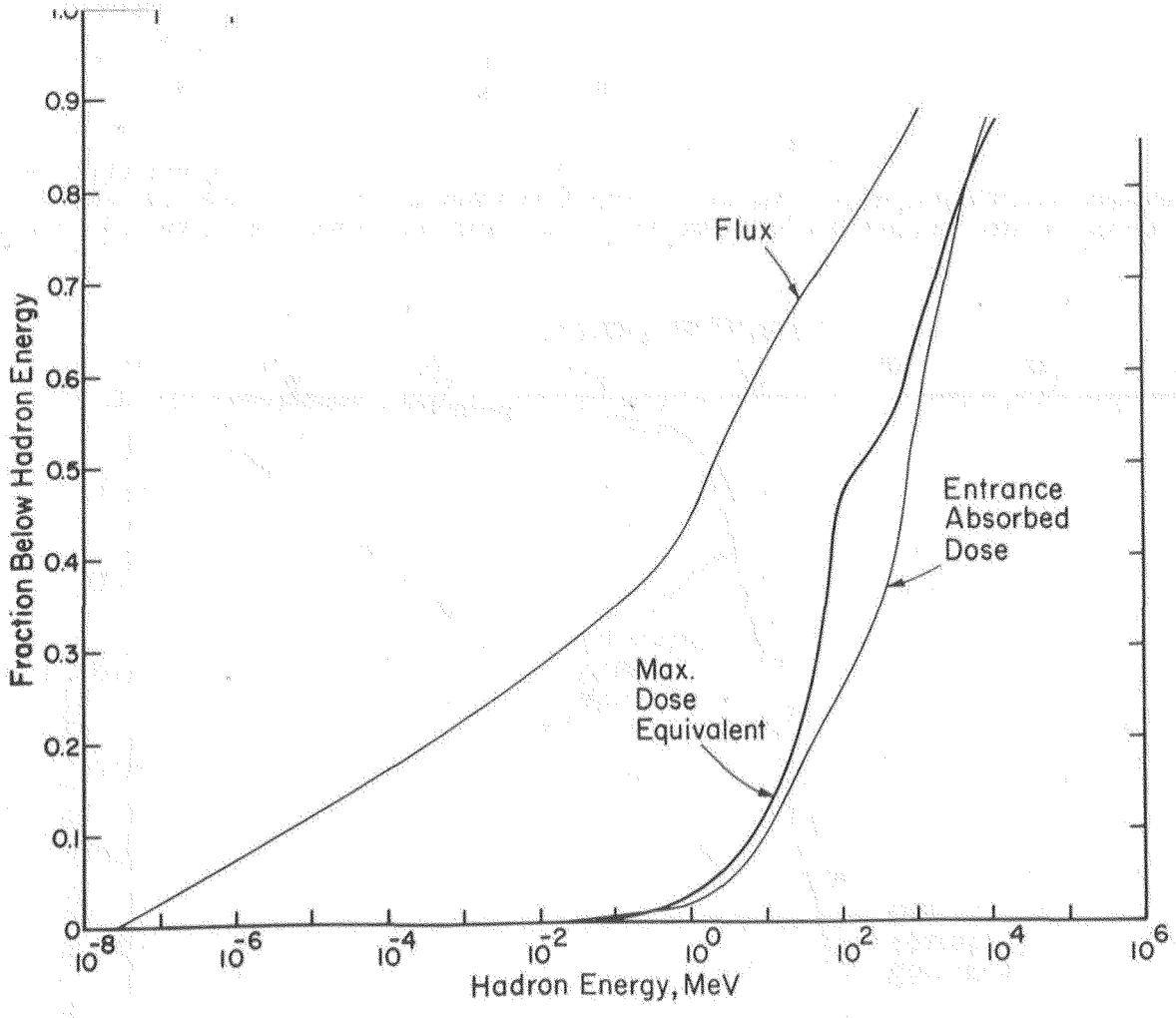

Fig. VI.10. 1000 GeV/c protons incident on a solid iron cylinder. Fraction of the omnidirectional flux, entrance absorbed dose and maximum dose equivalent below hadron kinetic energy on abcissa (in MeV) for the region between zero and 300 cm depth and between 100 cm and 250 cm radius.

error in caption ?

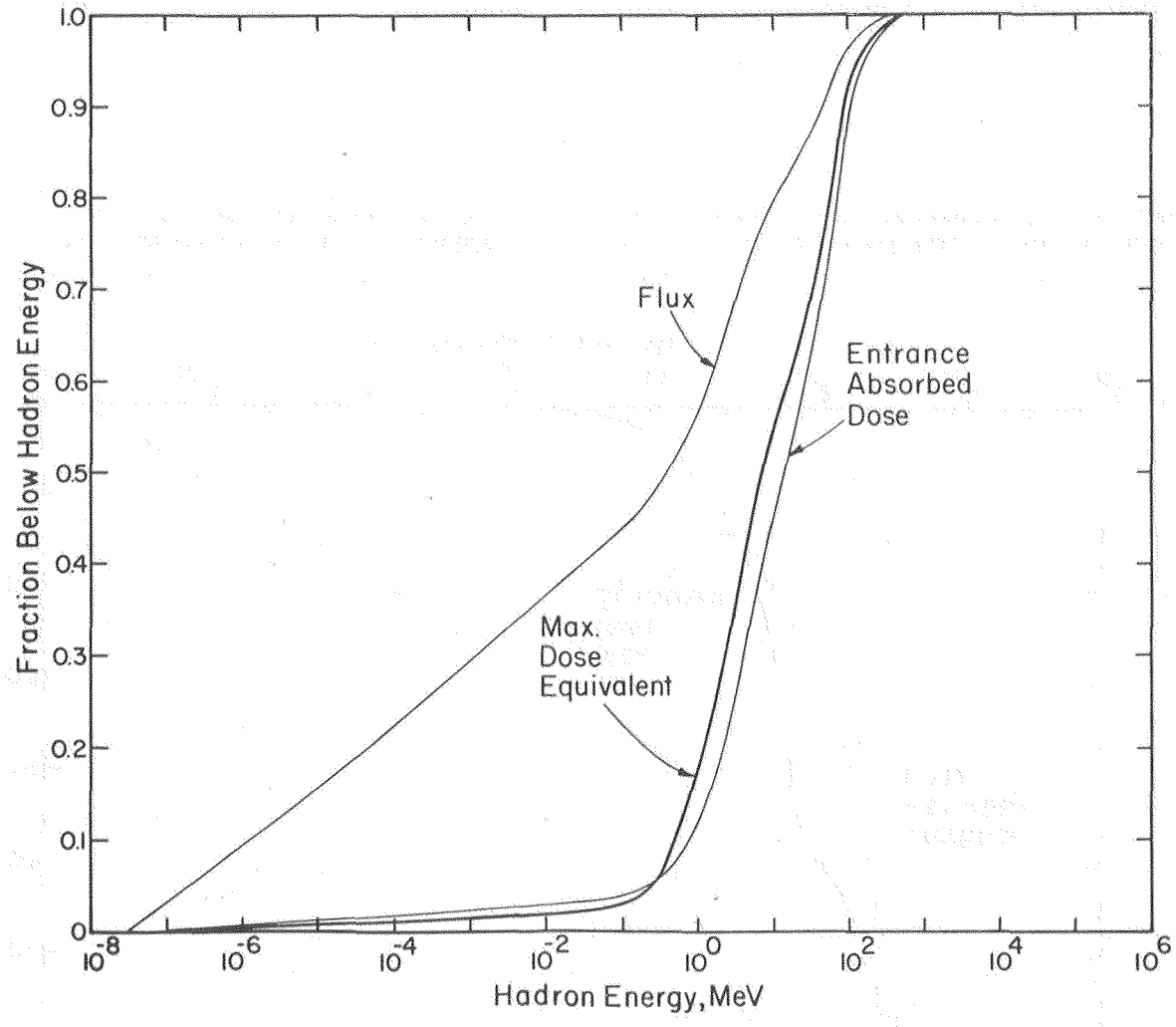

Fig. VI.11. 1000 GeV/c protons incident on a solid cylinder. Fraction of the omnidirectional flux, entrance absorbed dose and maximum dose and maximum dose equivalent below hadron kinetic energy on abcissa (in MeV) for the region between zero and 300 cm depth and between 100 cm and 250 cm radius.

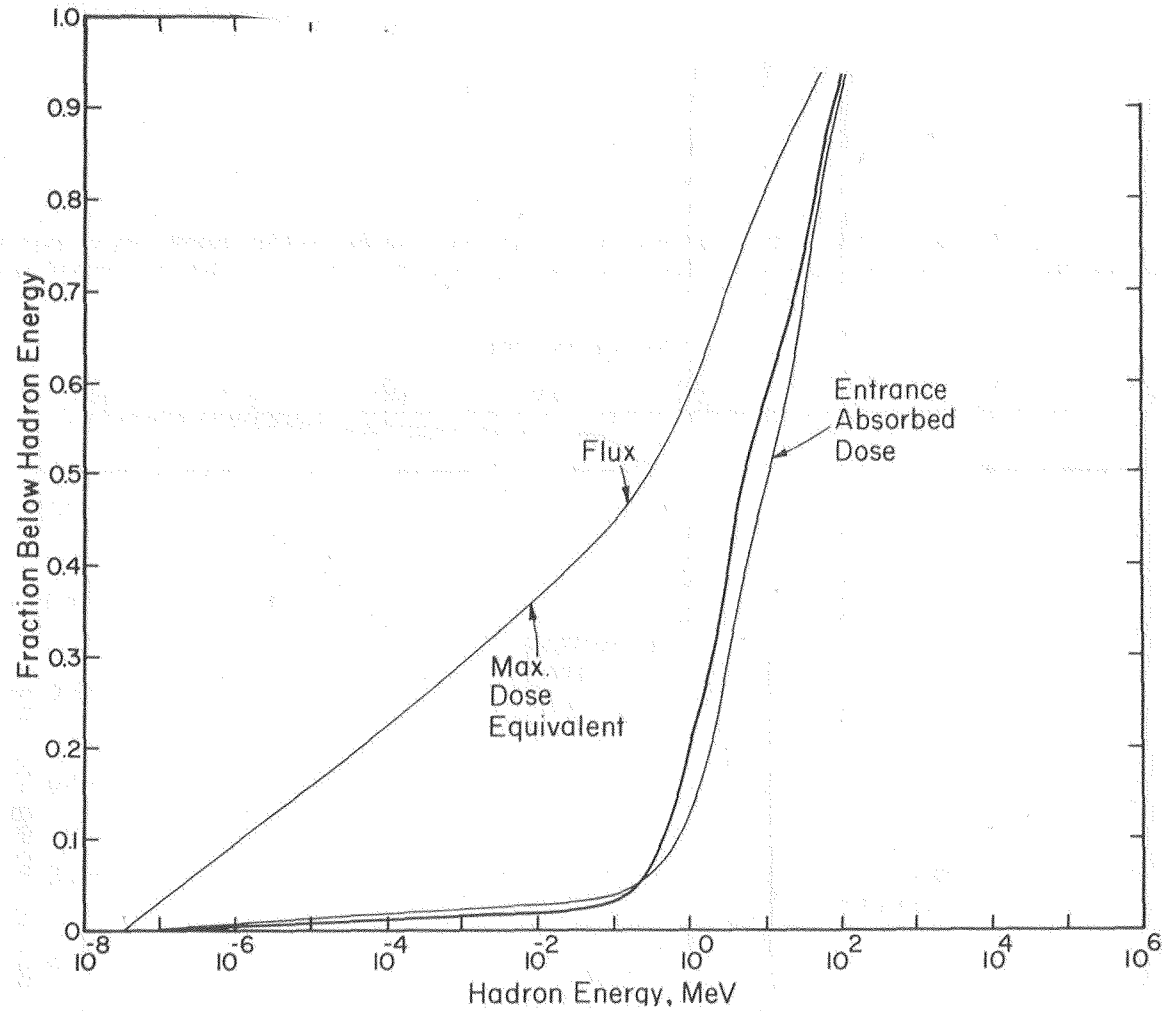

Fig. VI.12. 30 GeV/c protons incident on a solid concrete cylinder. Fraction of the omnidirectional flux, entrance absorbed dose and maximum dose equivalent below hadron kinetic energy on abcissa (in MeV) for the region between zero and 450 cm depth and between 300 cm and 750 cm radius.

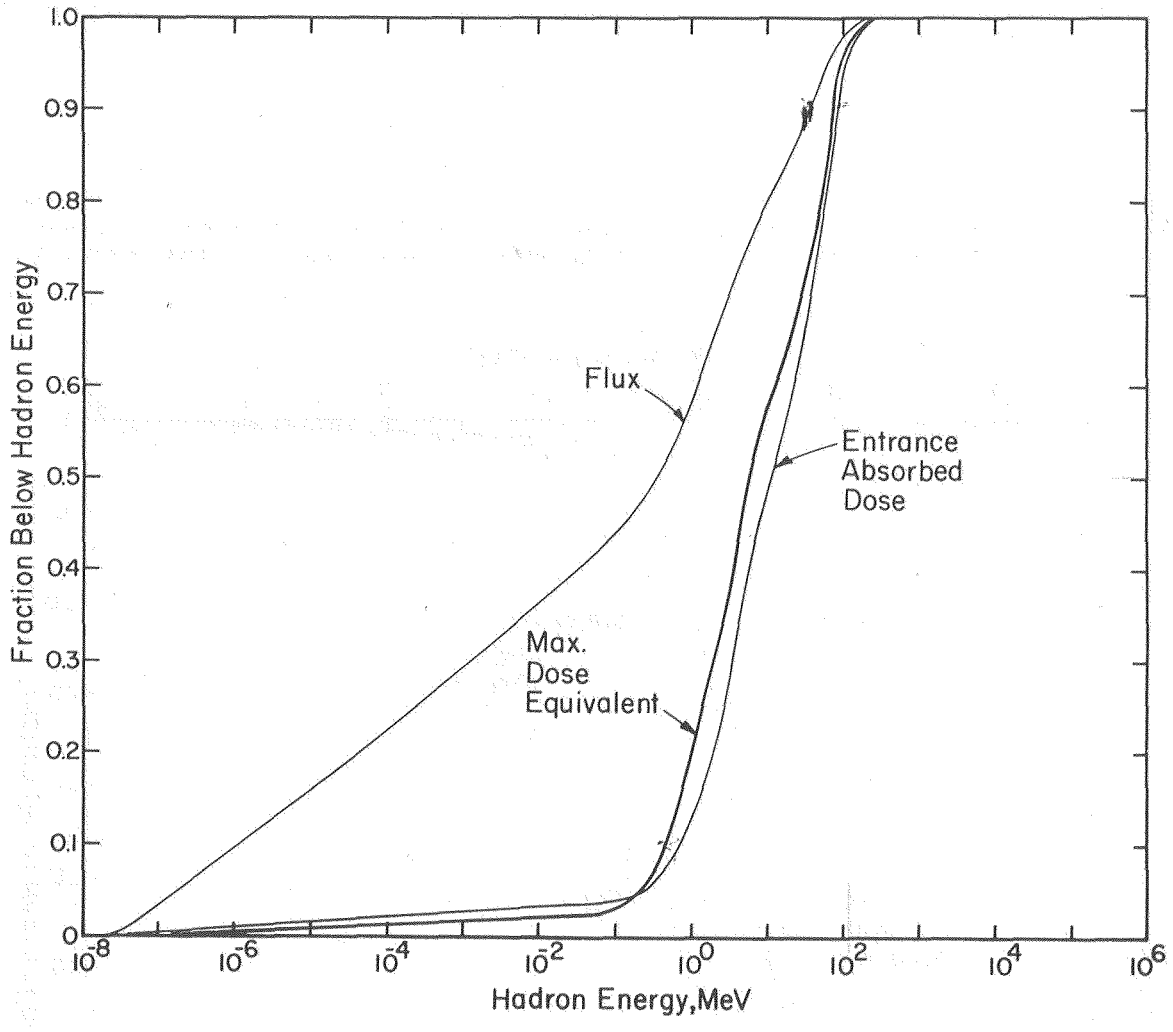

Fig. VI.13. 1000 GeV/c protons incident on a solid concrete cylinder. Fraction of the omnidirectional flux, extrance absorbed dose and maximum dose equivalent below hadron kinetic energy on abcissa (in MeV) for the region between zero and 450 cm depth and between 300 cm and 750 cm radius.

B. Exposure Rate from Induced Radioactivity

Another application of the star density curves is their relation to the dose rate resulting from induced radioactivity in targets and shields. Where the cascade is sufficiently dose to equilibrium the conversion factor is expected to be constant. Comparison of the detailed radioactivation calculations of Armstrong and Alsmiller[36] for 200 GeV protons uniformly lost along the axis of an iron cylinder, with the star density predictions of CASIM, yields the required conversion factor. For the case of infinite irradiation time and zero cooling time, the conversion factor so derived is 9.0×10^{-6} (rad/hr^{-1})/(stars cm^{3} sec^{-1}). This is in good agreement with the value of 7.5×10^{-6} quoted by Goebel et al.[37] based on a similar comparison of the Armstrong and Alsmiller result with Ranft's calculations. Since, this is a calculation of absorbed dose in soft tissue, rads are used instead of Roentgens. These values refer to the dose rate on contact. A more useful value perhaps is the dose rate at a distance of about 30 cm. However, this will depend on the dimensions and geometry of the radioactive object. The decay of the radioactivity in the iron (after an infinite irradiation time) is very gradual, reaching half its initial value only after a lapse of about one month.[36]

The above values pertain specifically to iron, they will generally be different for other materials. It must also be borne in mind that the above calculations assume that the cascade is at or near equilibrium.

C. Environmental Protection

The production of radionuclides in the soil surrounding the accelerator complex can also be estimated with the help of CASIM. This can either be performed by direct calculation using an excitation function for the prominently produced long-lived radionuclides in the soil, or by estimating their production from the star density. Since one is ultimately

concerned with the off-site transport of these radionuclides, their leachability and transit times must be taken into account. Extremely conservative arguments and calculations of radionuclide production, leachability and transport to the boundaries of the Fermilab site,[38] lead to a shielding criterion which permits not more than 0.015 stars/incident proton to be formed in uncontrolled soil around the Fermilab accelerators, beam lines and beam dumps.

References

VII. REFERENCES

[1] A. Van Ginneken, "Weighted Monte Carlo Calculations of Hadronic Cascades in Thick Targets", NAL-FN-250 (1972).

[2] R. Hagedorn, Suppl. Nuovo Cim. 3, 147 (1965); R. Hagedorn and J. Ranft, Suppl. Nuovo Cim. 6, 169 (1968); H. Grote, R. Hagedorn and J. Ranft, "Atlas of Particle Spectra", CERN, Geneva (1970).

[3] K. Goebel, Ed., "Radiation Problems Encountered in the Design of Multi-GeV Research Facilities", CERN-II-71-21 (1971).

[4] H. W. Patterson and R. H. Thomas, Particle Accelerators 2, 77 (1971).

[5] J. Ranft, Particle Accelerators 3, 77 (1971).

[6] T. W. Armstrong et al., Nucl. Sci. Eng., 49, 82 (1972).

[7] W. V. Jones, Phys. Rev. 187, 1869 (1969).

[8] G. H. Trilling, "Pion and Proton Fluxes from High Energy Proton Collisions", UCID-10148, LRL (1966).

[9] J. Ranft and T. Borak, "Improved Nucleon-Meson Cascade Calculations", NAL-FN-193 (1969).

[10] J. E. Butt and D. T. King in Experiments on High Energy Particle Collisions - 1973 (Vanderbilt Univ.), R. Panvini, Ed., A.I.P., N.Y. (1973), p. 121; J. R. Florian et al., ibid, p. 126; J. Hebert et al., ibid, p. 131; P. L. Jain, ibid, p. 141.

[11] J. Ranft and J. T. Routti, "Hadron Cascade Calculations of Angular Distribution of Secondary Particle Fluxes from External Targets and Description of Program FLUKU", CERN-II-RA/72-8 (1972).

[12] H. W. Bertini, Phys. Rev. 188, 1711 (1969).

[13] J. Ranft, "Secondary Particle Spectra According to the Thermodynamical Model. A Fit to Data Measured in p-Nucleus Collisions", TUL36, Karl Marx Univ., DDR (1970).

[14] J. V. Allaby, et al., "High Energy Particle Spectra from Proton Interactions at 19.2 GeV/c", CERN-70-12 (1970).

[15] P. M. Fishbane, J. L. Newmeyer and J. S. Trefil, Phys. Rev. Lett. 29, 685 (1972); A. Dar and J. Vary, Phys. Rev. D6, 2412 (1972); A. S. Goldhaber, Phys. Rev. D7, 765 (1973).

[16] D. Shaw, "Atomic and Nuclear Properties of Materials", in W. Galbraith and W. S. C. Williams, High Energy and Nuclear Physics Data Handbook, RHEL, 1964.

[17] N. Metropolis, et al., Phys. Rev. 110, 185 (1958); ibid, 110, 204 (1958).

[18] W. H. Barkas and M. J. Berger, "Tables of Energy Losses and Ranges of Heavy Charged Particles", in Studies in Penetration of Charged Particles in Matter, NSS-39 NAD-NRC Pub. 1133, p. 103 (1964).

[19] D. Theriot, "Muon dE/dx and Range Tables: Preliminary Results for Shielding Materials", NAL-TM-229 (1970).

[20] G. Bathow, et al., Nucl. Phys. B20, 592 (1970).

[21] C. J. Cranell, Phys. Rev. 161, 310 (1967).

[22] D. Müller, Phys. Rev. D5, 2677 (1972).

[23] R. G. Alsmiller, Jr. and H. S. Moran, Nucl. Sci. Eng., 40. 483 (1970).

[24] R. G. Alsmiller, Jr., private communication.

[25] K. Greisen, Prog. Cosmic Ray Physics, III, 3 (1956).

[26] U. Völkel, DESY preprint 65-6 (1965).

[27] B. Rossi, High Energy Particles, p. 81, Prentice Hall, Englewood Cliffs, N. J., (1952).

[28] I. Dostrofsky, et al., Phys. Rev. 111, 1959 (1958).

[29] J. Spanier and E. M. Gelbard, Monte Carlo Principles and Neutron Transport Problems, Addison-Wesley, Reading, Mass. (1969); E. D. Cashwell and C. J. Everett, Monte Carlo Method for Random Walk Problems, Pergamon Press, New York (1959); J. M. Hammersley and D. C. Handscomb, Monte Carlo Methods, Methuen, London (1964).

[30] P. J. Gollon, private communication.

[31] T. A. Gabriel and R. T. Santoro, "Calculation of the Long-Lived Activity in Soil Produced by 500 GeV Protons", ORNL-TM-3262.

[32] C. D. Zerby and W. E. Kinney, ORNL-TM-1038 (May 1965); D. C. Irving, R. G. Alsmiller and H. S. Moran, ORNL-TM-1522 (Dec. 7, 1966); R. G. Alsmiller and H. S. Moran, ORNL-TM-2026 (Oct. 20, 1967); R. G. Alsmiller, T. W. Armstrong and W. A. Coleman, ORNL-TM-2924, Rev. (July 15, 1970); R. G. Alsmiller, T. W. Armstrong and B. L. Bishop, ORNL-TM-3105 (August 24, 1970); T. W. Armstrong and K. C. Chandler, ORNL-TM-3758 (May 1972).

[33] ICRP Pub. 21, Data for Protection Against Ionizing Radiation from External Sources, Suppl. to ICRP Pub. 15, p. 9 (1973).

[34] K. B. Shaw, G. R. Stevenson and R. H. Thomas, Health Phys. 17, 459 (1969).

[35] G. R. Stevenson et al., "Proposal for Standardizing the Fluence to Dose Equivalent Conversion Factors for Whole Body Neutron Exposures", IAEA Symposium on Neutron Monitoring for Radiation Protection Purposes, Vienna, SM-167/21 (1972).

[36] T. W. Armstrong and R. G. Alsmiller, Jr. "Calculations of the Residual Photon Dose Rate Around High-Energy Proton Accelerators", ORNL-TM-2498 (1969).

[37] K. Goebel, J. Ranft and G. R. Stevenson, "Remanent Radioactivity in the Accelerator Structure", Chap. VIII. Sec. A. in Ref. 3.

[38] M. Awschalom, Calculation of Radionuclide Production in Surroundings of NAL Neutrino Laboratory", NAL-TM-292 (1971).

Graphs

VIII. GRAPHS

This section contains the main results in the form of graphs from a sample of CASIM outputs.

The various cases discussed here are presented in Table VIII.1. More detailed information is provided in the figure captions and in Section III.B. Distances are expressed in cm throughout; in a few cases they are also indicated in "metric feet" (30 cm).

TABLE VIII.I

FIGURE NUMBER

Hagedorn-Ranft production model used except where otherwise noted.

Incident Proton Momentum, (GeV/c)	30	100	300	1000
SOLID IRON CYLINDER				
Equal Star Density Contours	1	2	3	4
Depth Dependence	5	6	7	8
Radial Dependence	9	10	11	12
Momentum Spectra	13	14	15	16
Equal Star Density Contours (Trilling)			17	
SOLID CONCRETE CYLINDER				
Equal Star Density Contours	18	19	20	21
Depth Dependence	22	23	24	25
Radial Dependence	26	27	28	29
Momentum Spectra	30	31	32	33
IRON CAVE, TARGET ON AXIS				
Equal Star Density Contours			34	35
Momentum Spectra			36, 37	38, 39

TABLE VIII.I

FIGURE REFERENCE

Incident Proton Momentum, GeV/c	30	100	300	1000
CONCRETE CAVE, TARGET ON AXIS				
Equal Star Density Contours			40	41
Momentum Spectra			42, 43	44, 45
IRON PIPE (10 cm inner radius), BEAM LOST ON WALL				
Equal Star Density Contours	46,47,48	49,50,51	52,53,54	55,56,57
Momentum Spectra	58,59,60	61,62,63	64,65,66	67,68,69
IRON PIPE (1 cm inner radius), BEAM LOST ON WALL				
Equal Star Density Contours			70	
IRON PIPE (10 cm inner radius), TARGET ON AXIS				
Equal Star Density Contours			71	
Momentum Spectra			72,73	
ENERGY DEPOSITION				
Integrals at Various Depths, Radial Dependence	74	75	76	77
Integrals at Various Radii, Depth Dependence	78	79	80	81
Equal Energy Deposition Density Contours	82	83	84	85

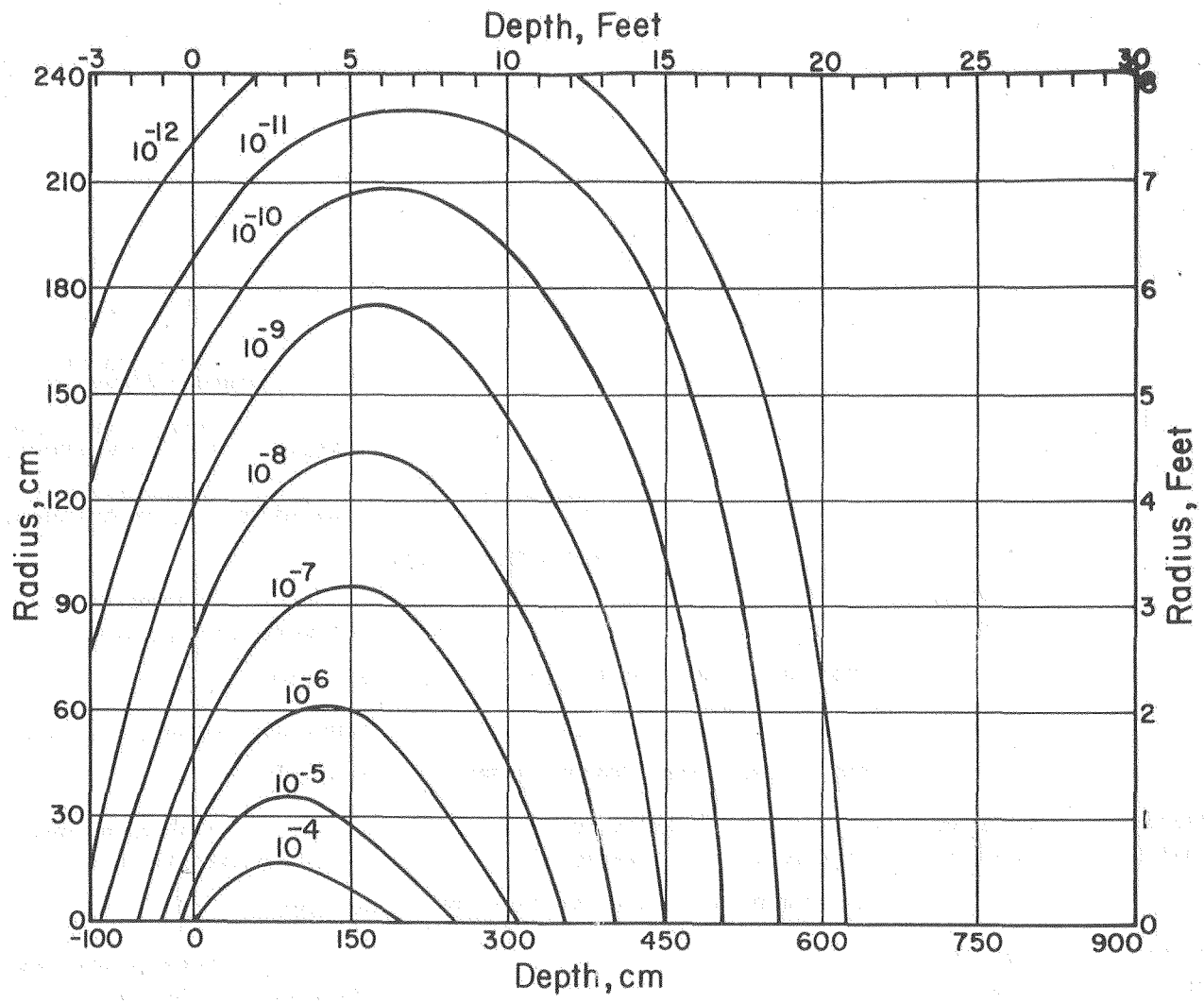

Fig. VIII.1. 30 GeV/c protons incident on a solid iron cylinder. Contours of equal star density (stars/cm^3 · inc. proton). The beam of 0.3 × 0.3 cm cross section is centered on the cylinder axis and starts to interact at zero depth. The star density includes only those due to hadrons above 0.3 GeV/c momentum. Contours of higher star density are not shown for clarity of the plot, those of lower star density are not included due to statistical uncertainty.

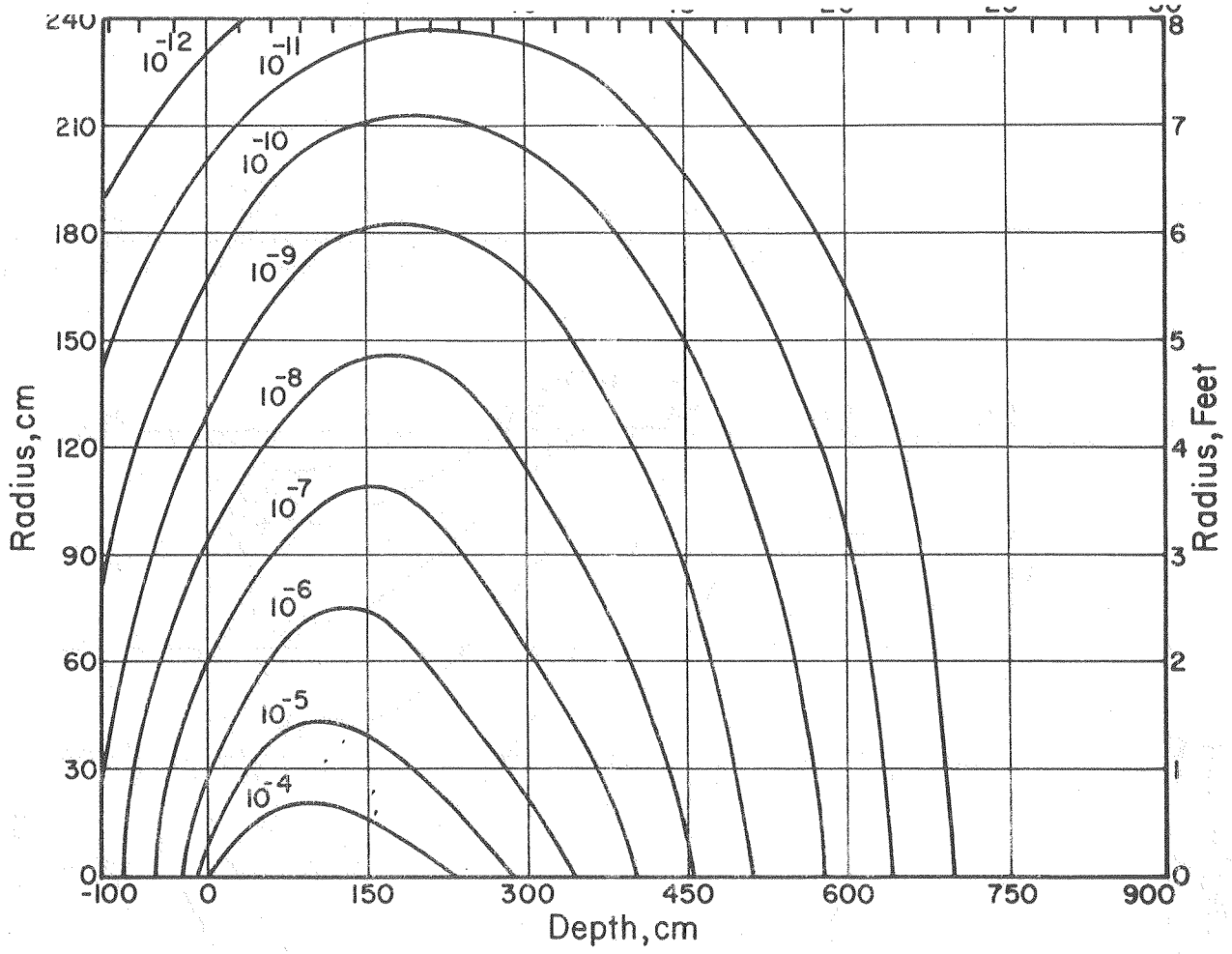

Fig. VIII.2. 100 GeV/c protons incident on a solid iron cylinder. Contours of equal star density (stars/cm^3 · inc. proton). The beam of 0.3 × 0.3 cm cross section is centered on the cylinder axis and starts to interact at zero depth. The star density includes only those due to hadrons above 0.3 GeV/c momentum. Contours of higher star density are not shown for clarity of the plot, those of lower star density are not included due to statistical uncertainty.

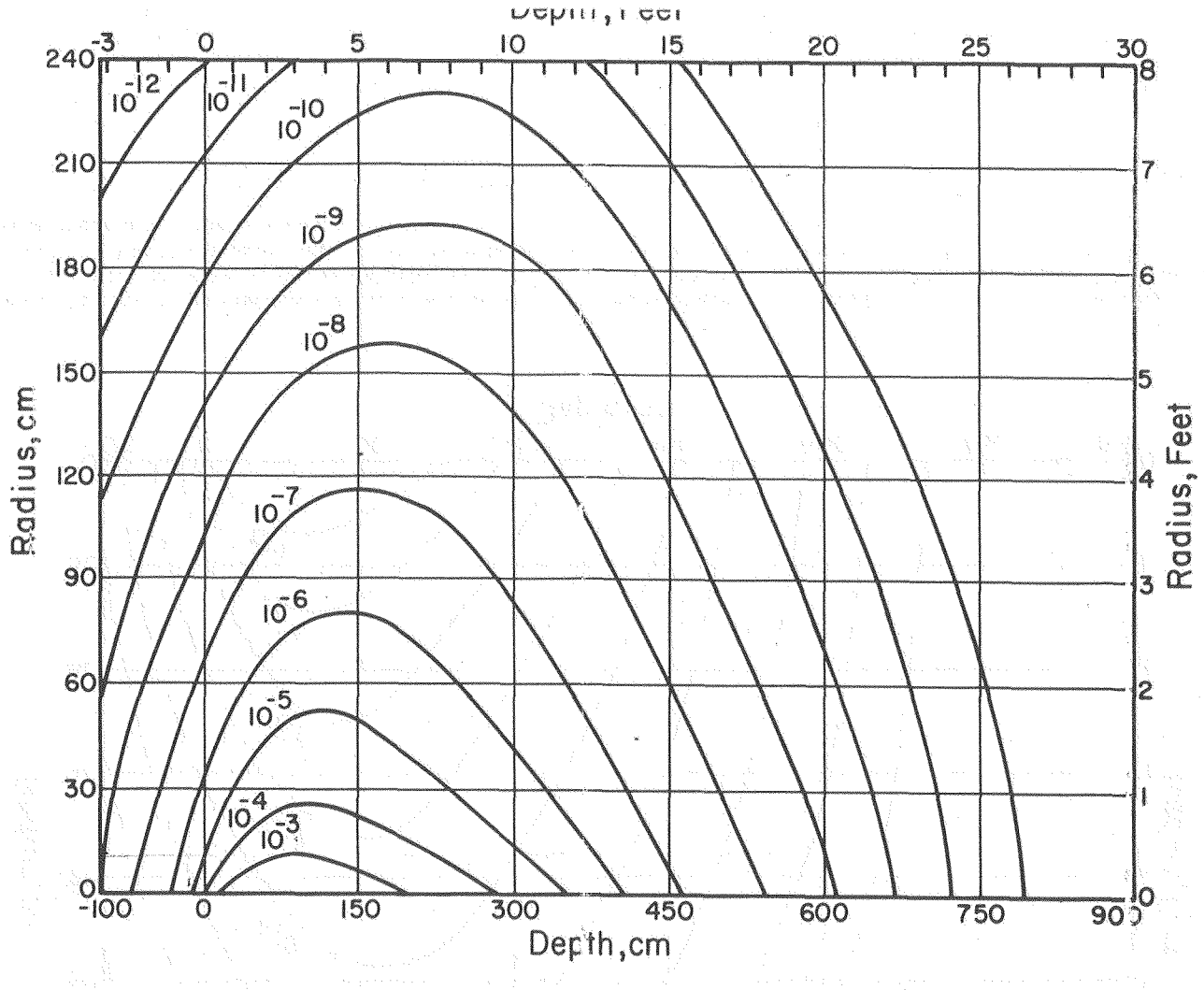

Fig. VIII.3. 300 GeV/c protons incident on a solid iron cylinder. Contours of equal star density (stars/cm^3 · inc. proton). The beam of 0.3×0.3 cm cross section is centered on the cylinder axis and starts to interact at zero depth. The star density includes only those due to hadrons above 0.3 GeV/c momentum. Contours of higher star density are not shown for clarity of the plot, those of lower star density are not included due to statistical uncertainty.

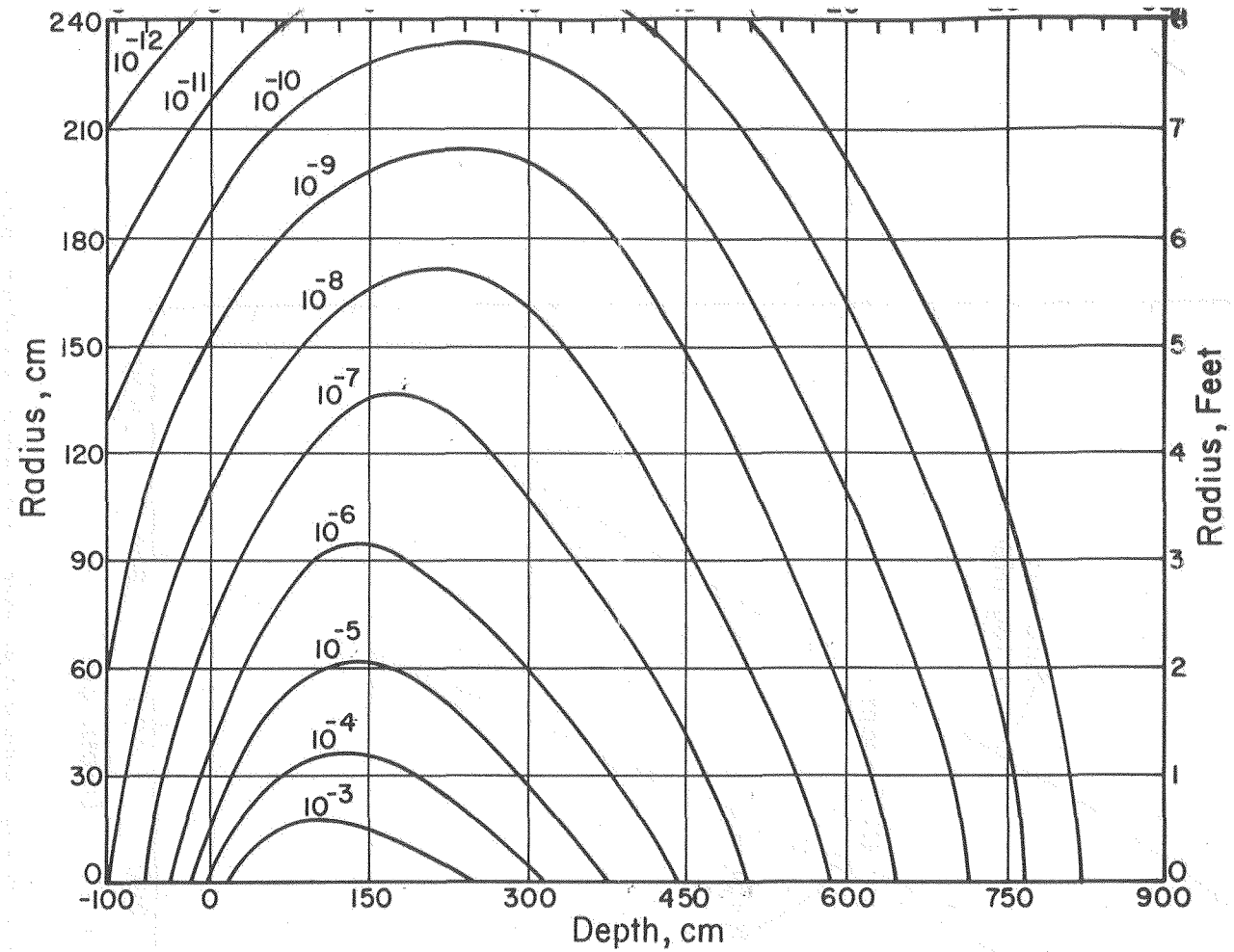

Fig. VIII.4. 1000 GeV/c protons incident on a solid iron cylinder. Contours of equal star density (stars/cm^3 · inc. proton). The beam of 0.3 × 0.3 cm cross section is centered on the cylinder axis and starts to interact at zero depth. The star density includes only those due to hadrons above 0.3 GeV/c momentum. Contours of higher star density are not shown for clarity of the plot, those of lower star density are not included due to statistical uncertainty.

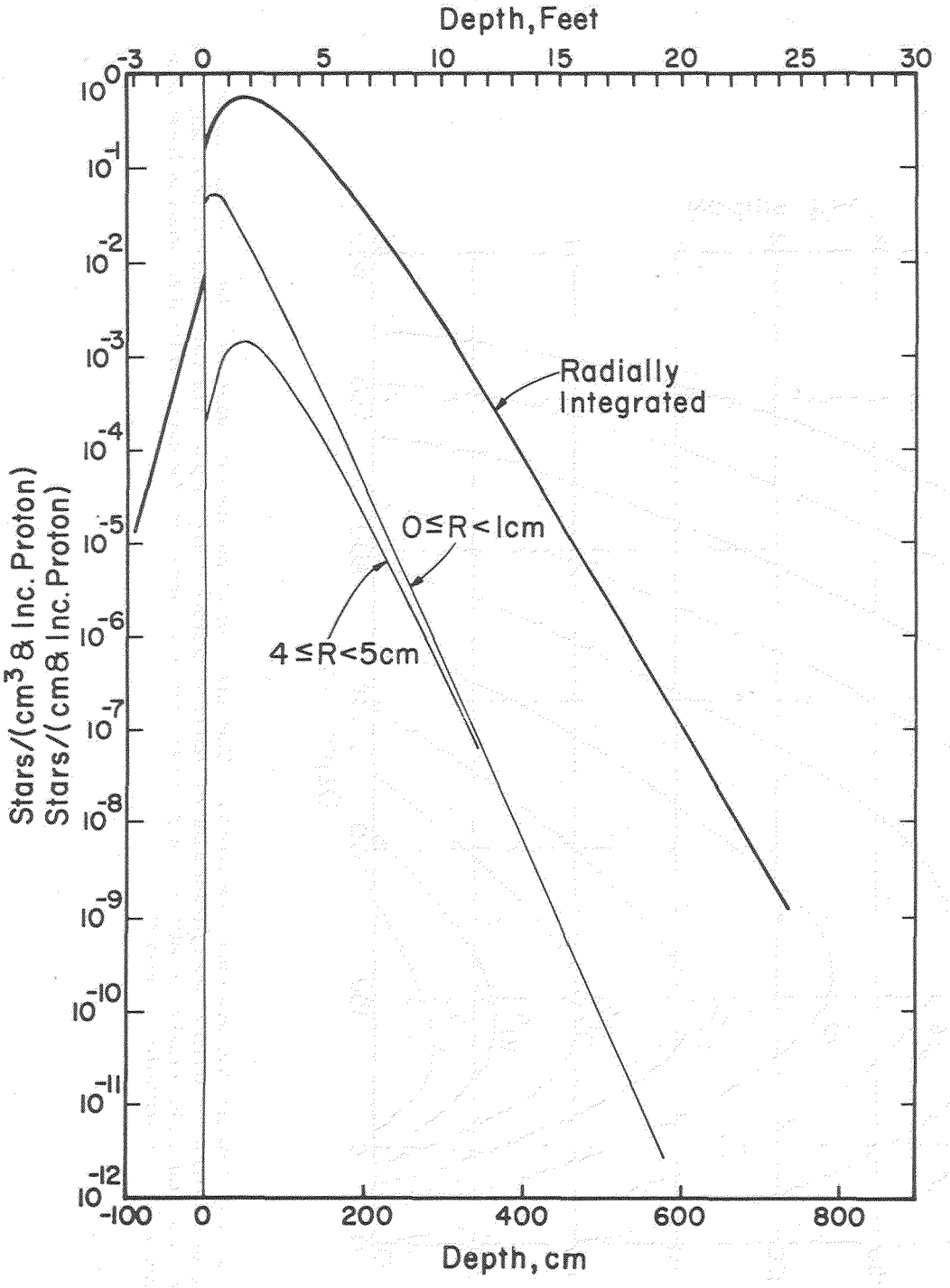

Fig. VIII.5. 30 GeV/c protons incident on a solid iron cylinder. Depth dependence of the radially integrated star density (stars/cm · inc. proton) and the star density at small radii (stars/cm^3 · inc. proton). The beam of 0.3 × 0.3 cm cross section is centered on the cylinder axis and starts to interact at zero depth. The star density includes only those due to hadrons above 0.3 GeV/c momentum. The star densities at small radii are not shown in the backward region due to statistical uncertainty.

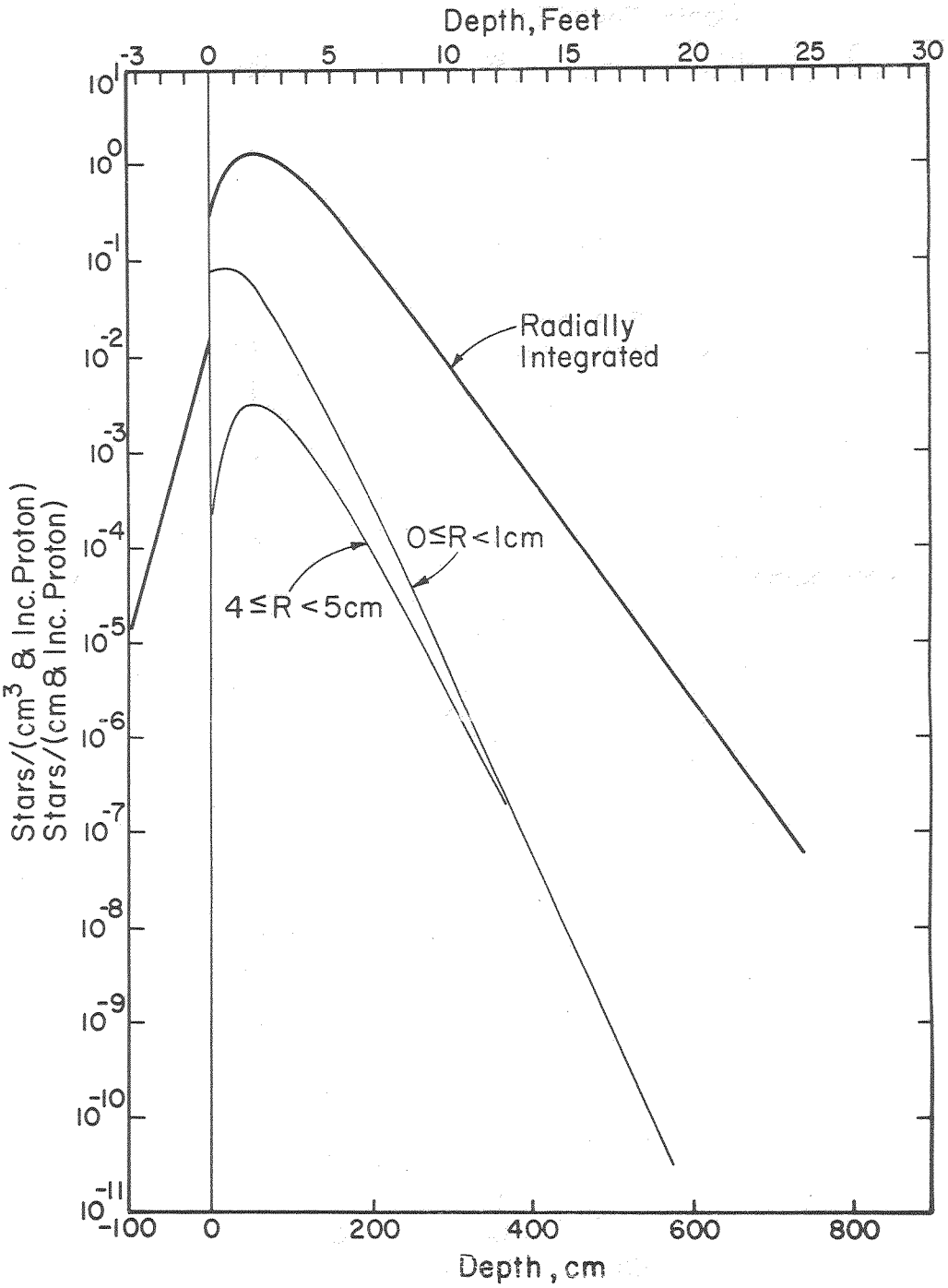

Fig. VIII.6. 100 GeV/c protons incident on a solid iron cylinder. Depth dependence of the radially integrated star density (stars/cm · inc. proton) and the star density at small radii (stars/cm^3 · inc. proton). The beam of 0.3 × 0.3 cm cross section is centered on the cylinder axis and starts to interact at zero depth. The star density includes only those due to hadrons above 0.3 GeV/c momentum. The star densities at small radii are not shown in the backward region due to statistical uncertainty.

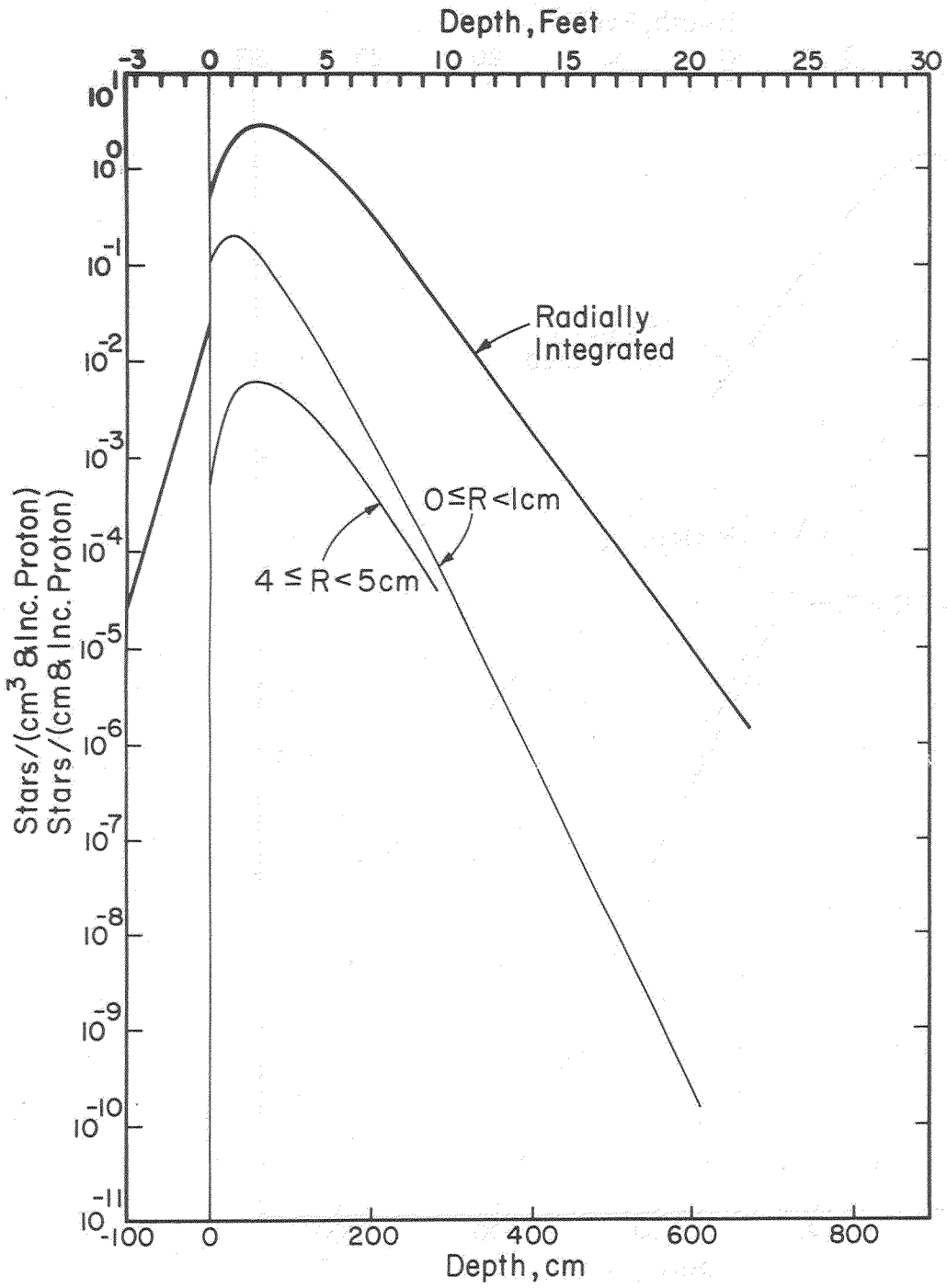

Fig. VIII.7. 300 GeV/c protons incident on a solid iron cylinder. Depth dependence of the radially integrated star density (stars/cm · inc. proton) and the star density at small radii (stars/cm^3 · inc. proton). The beam of 0.3 × 0.3 cm cross section is centered on the cylinder axis and starts to interact at zero depth. The star density includes only those due to hadrons above 0.3 GeV/c momentum. The star densities at small radii are not shown in the backward region due to statistical uncertainty.

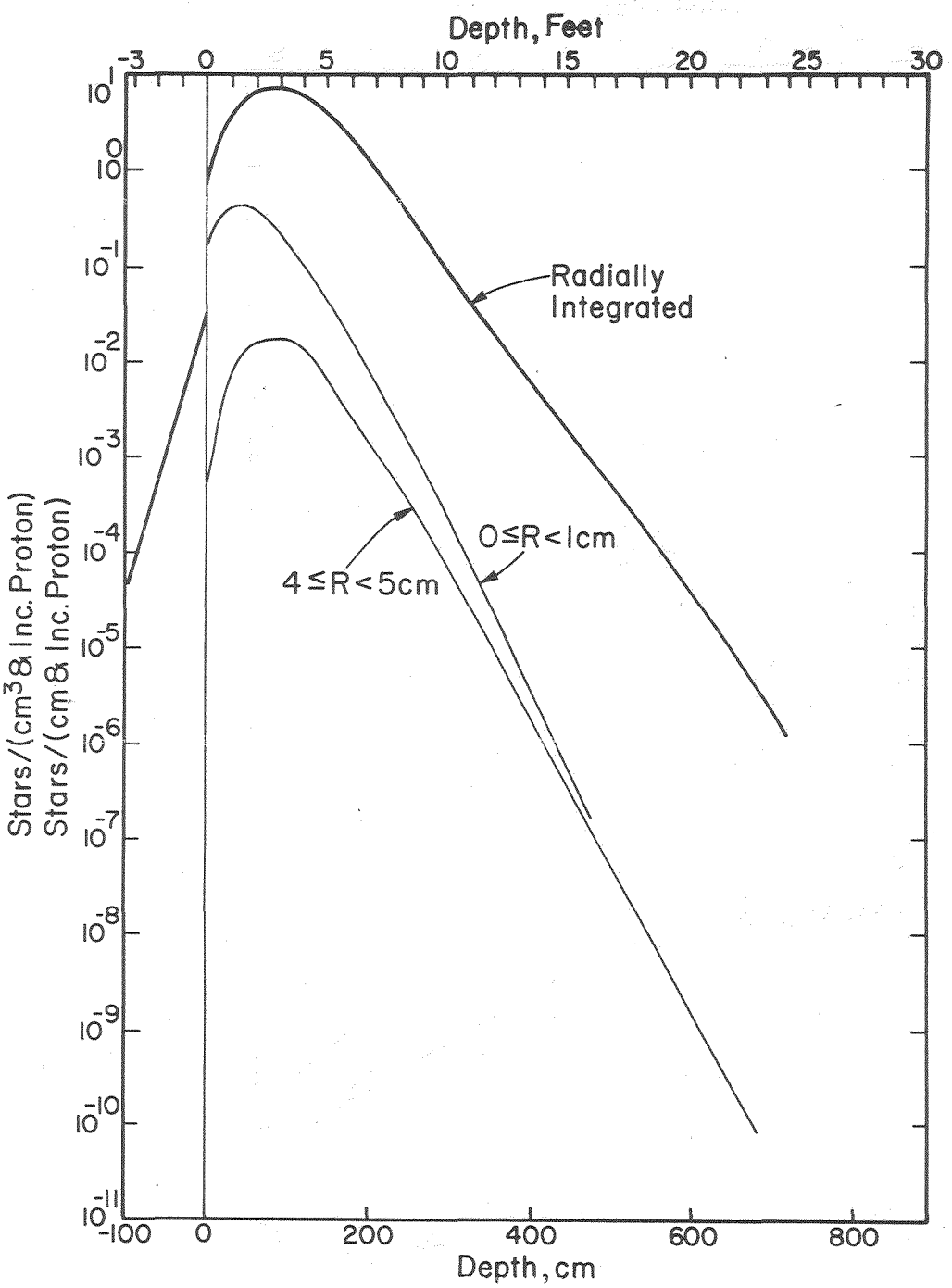

Fig. VIII.8. 1000 GeV/c protons incident on a solid iron cylinder. Depth dependence of the radially integrated star density (star/cm · inc. proton) and the star density at small radii (stars/cm^3 · inc. proton). The beam of 0.3 × 0.3 cm cross section is centered on the cylinder axis and starts to interact at zero depth. The star density includes only those due to hadrons above 0.3 GeV/c momentum. The star densities at small radii are not shown in the backward region due to statistical uncertainty.

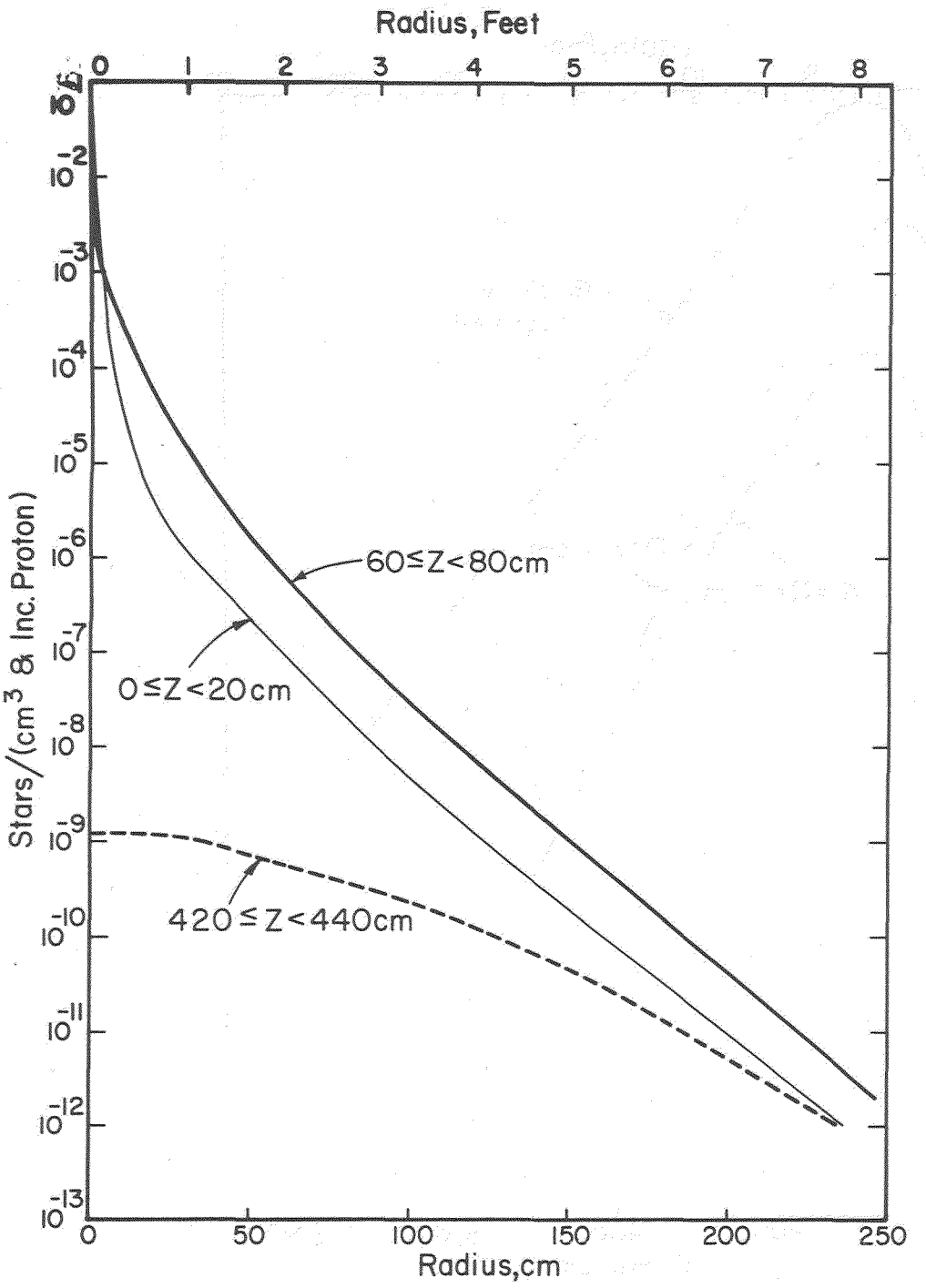

Fig. VIII.9. 30 GeV/c protons incident on a solid iron cylinder. Radial dependence of the star density (stars/cm^3 · inc. proton) at selected depths. The beam of 0.3 × 0.3 cm cross section is centered on the cylinder axis. The star density includes only those due to hadrons above 0.3 GeV/c momentum.

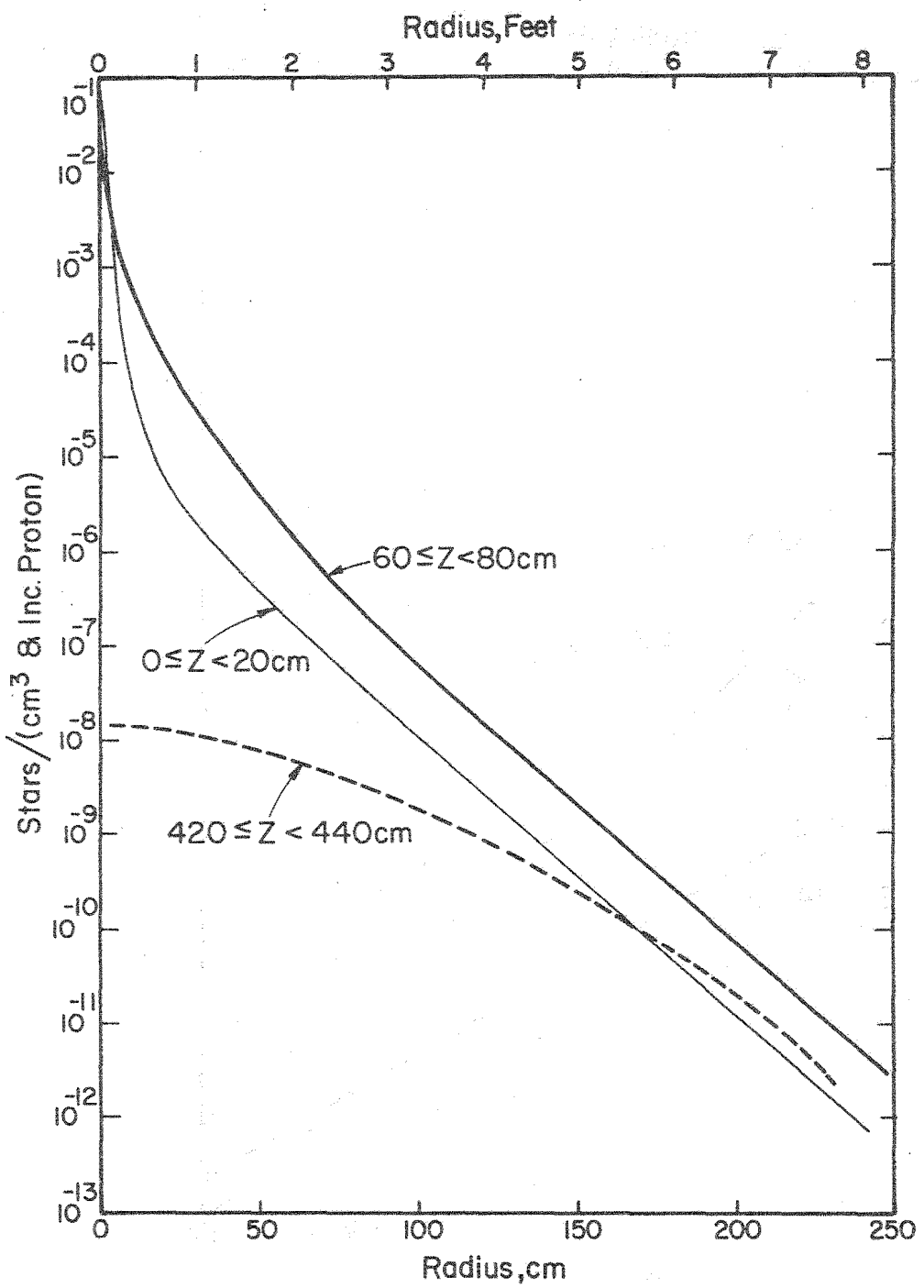

Fig. VIII.10. 100 GeV/c protons incident on a solid iron cylinder. Radial dependence of the star density (stars/cm^3 · inc. proton) at selected depths. The beam of 0.3 × 0.3 cm cross section is centered on the cylinder axis. The star density includes only those due to hadrons above 0.3 GeV/c momentum.

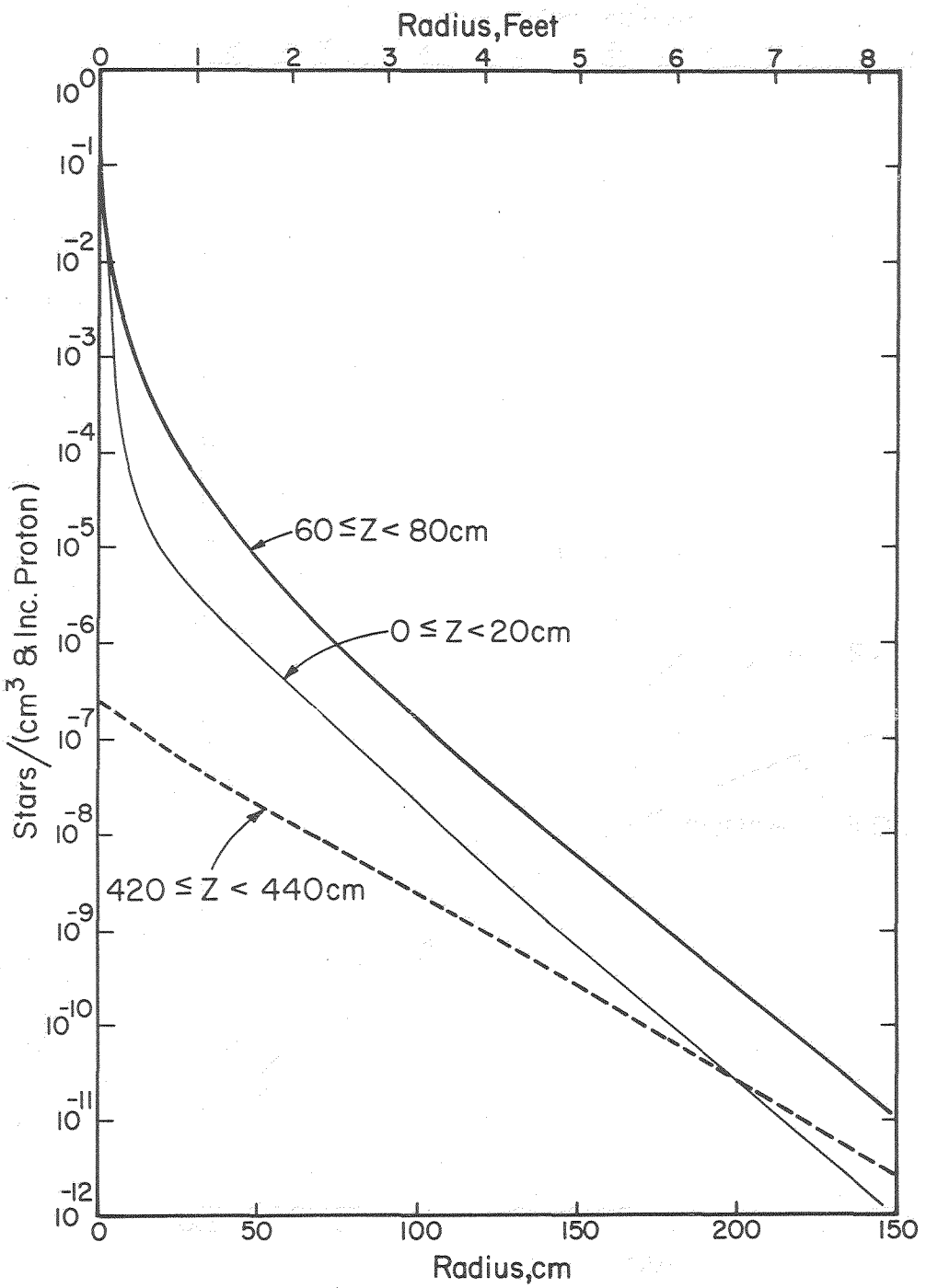

Fig. VIII.11. 300 GeV/c protons incident on a solid iron cylinder. Radial dependence of the star density (stars/cm^3 · inc. proton) at selected depths. The beam of 0.3 × 0.3 cm cross section is centered on the cylinder axis. The star density includes only those due to hadrons above 0.3 GeV/c momentum.

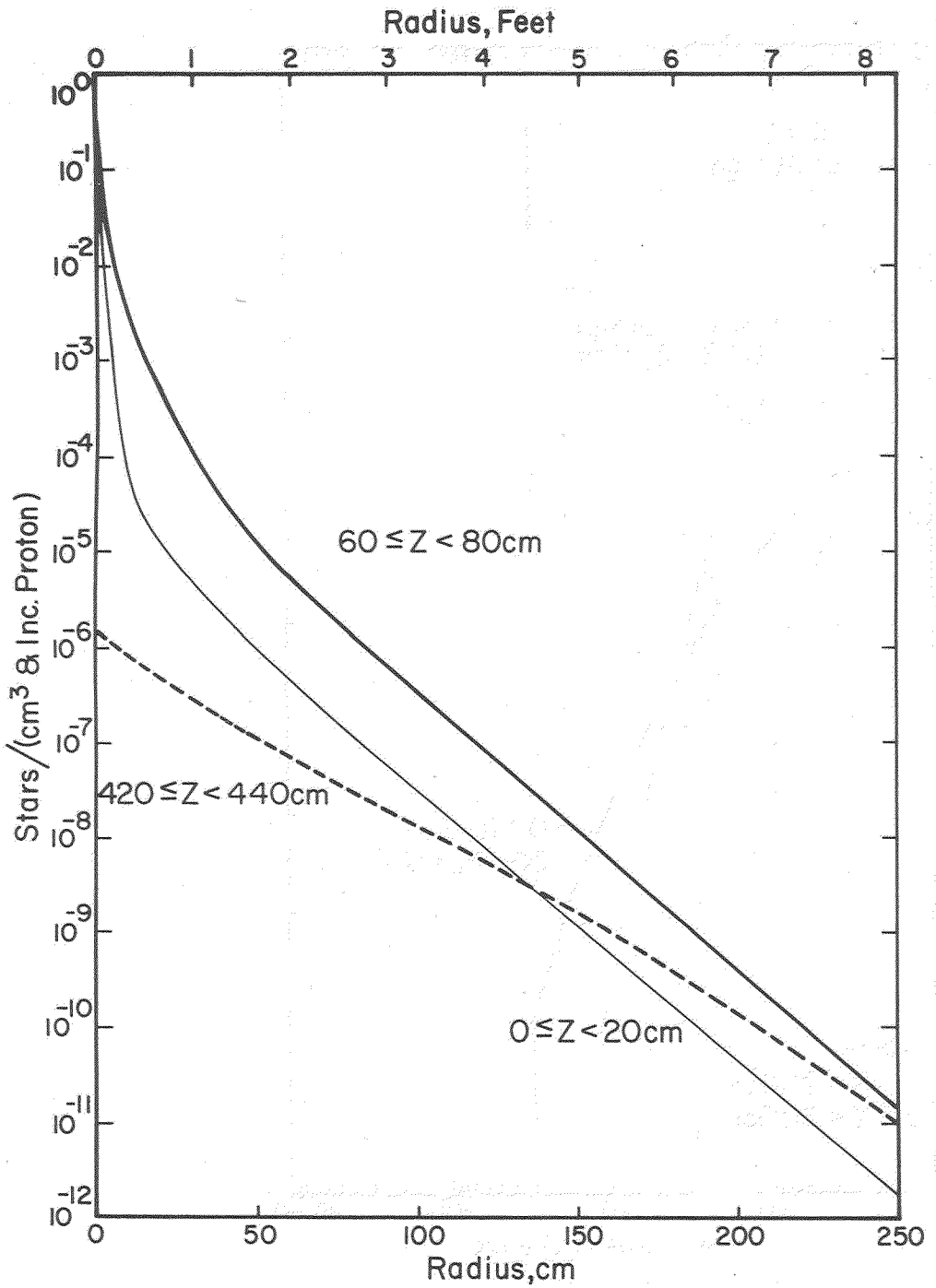

Fig. VIII.12. 1000 GeV/c protons incident on a solid iron cylinder. Radial dependence of the star density (stars/cm^3 · inc. proton) at selected depths. The beam of 0.3 × 0.3 cm cross section is centered on the cylinder axis. The star density includes only those due to hadrons above 0.3 GeV/c momentum.

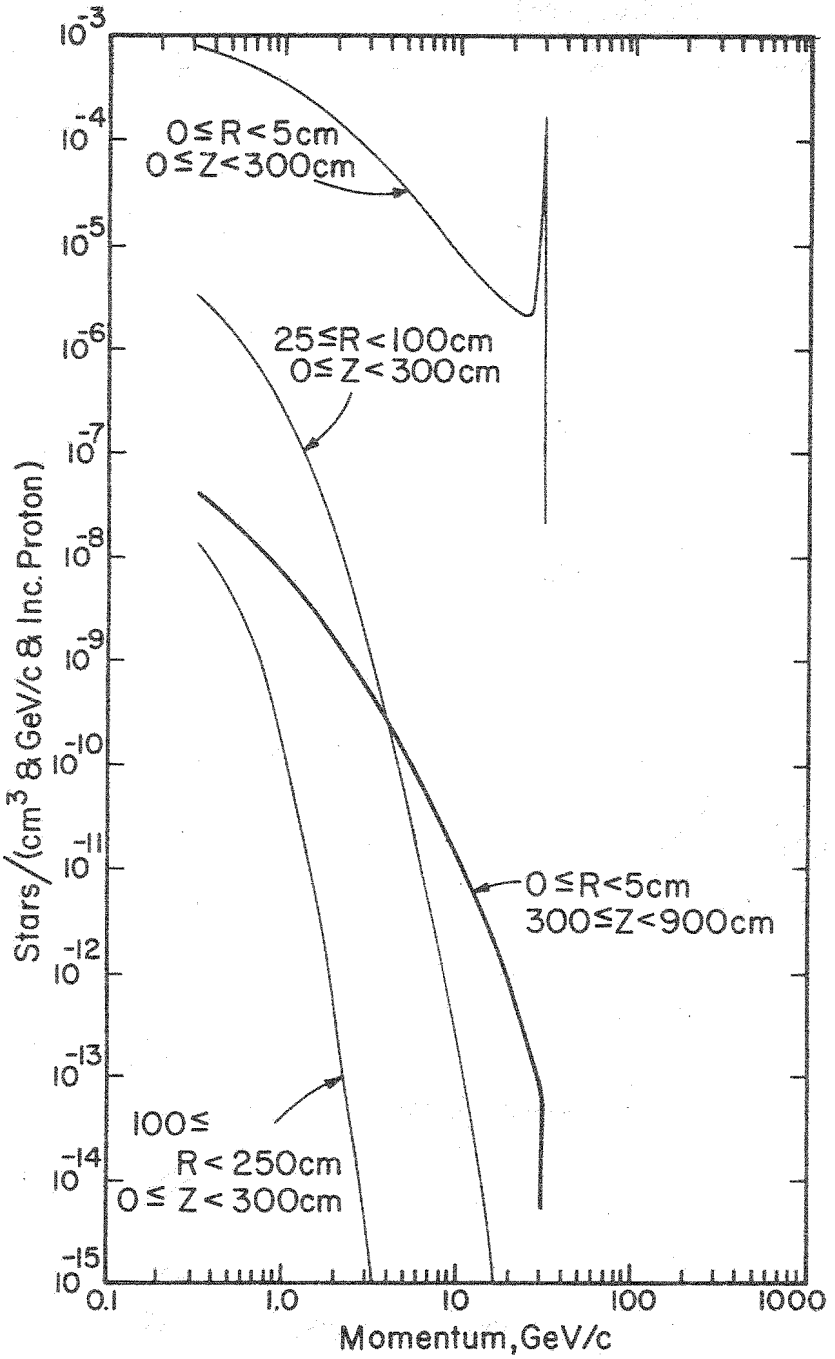

Fig. VIII.13. 30 GeV/c protons incident on a solid iron cylinder. Momentum spectra of interacting hadrons (stars/cm^3 · GeV/c · inc. proton) for selected regions. The beam of 0.3 × 0.3 cm cross section is centered on the cylinder axis. The spectra are not calculated below 0.3 GeV/c momentum.

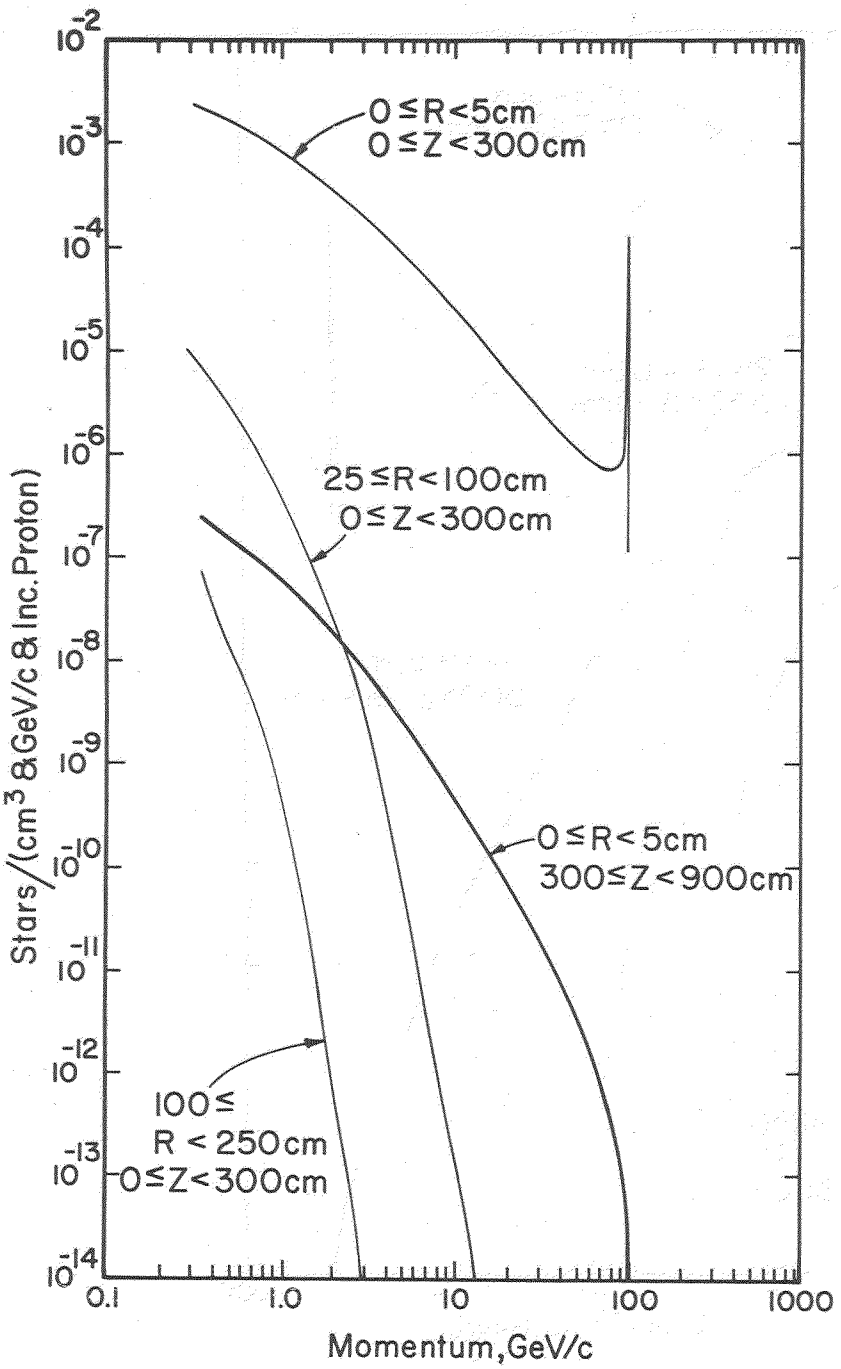

Fig. VIII.14. 100 GeV/c protons incident on a solid iron cylinder. Momentum spectra of interacting hadrons (stars/cm^3 · GeV/c · inc. proton) for selected regions. The beam of 0.3 × 0.3 cm cross section is centered on the cylinder axis. The spectra are not calculated below 0.3 GeV/c momentum.

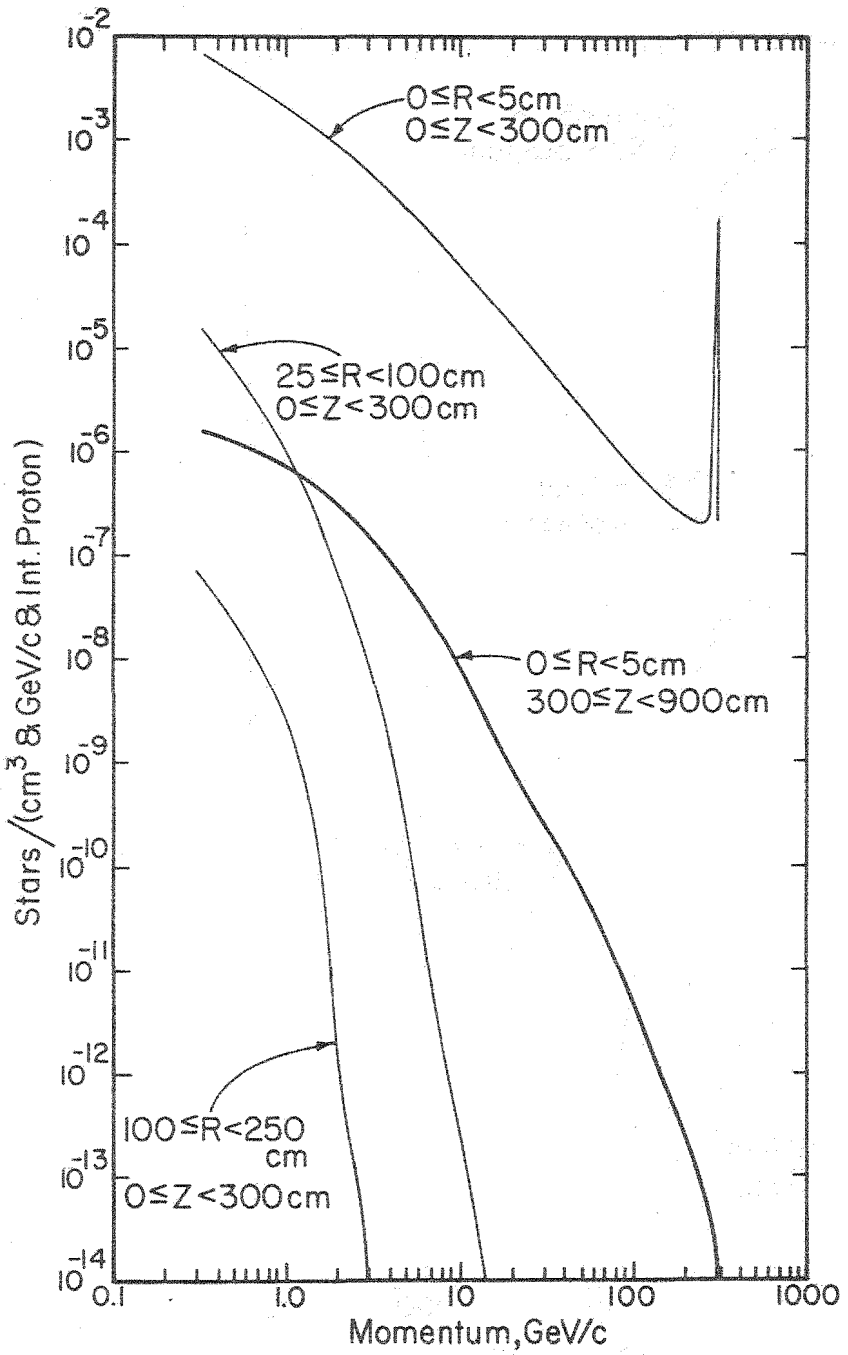

Fig. VIII.15. 300 GeV/c protons incident on a solid iron cylinder. Momentum spectra of interacting hadrons (stars/cm^3 · GeV/c · inc. proton) for selected regions. The beam of 0.3 × 0.3 cm cross section is centered on the cylinder axis. The spectra are not calculated below 0.3 GeV/c momentum.

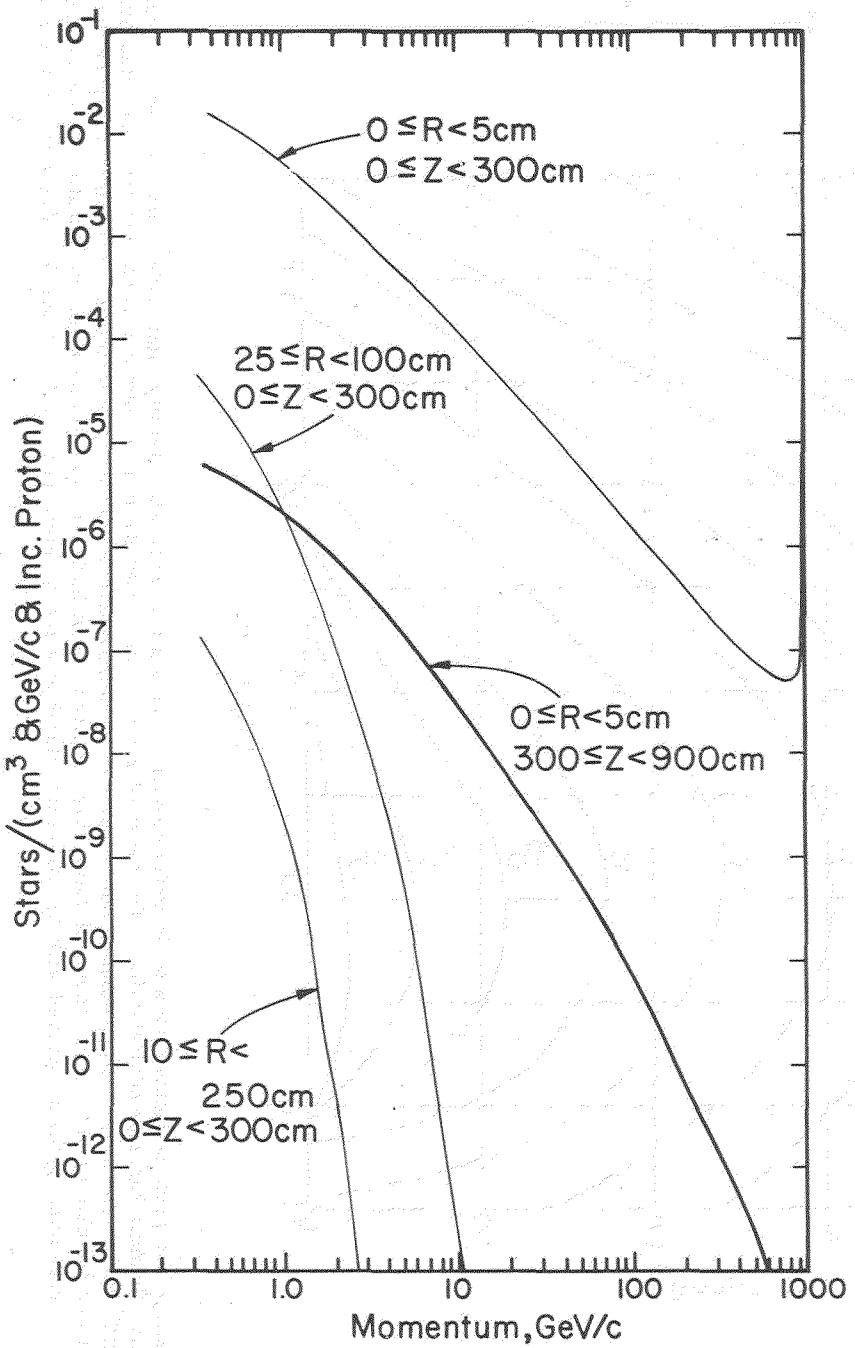

Fig. VIII.16. 1000 GeV/c protons incident on a solid iron cylinder. Momentum spectra of interacting hadrons (stars/cm^3 · GeV/c · inc. proton) for selected regions. The beam of 0.3 × 0.3 cm cross section is centered on the cylinder axis. The spectra are not calculated below 0.3 GeV/c momentum.

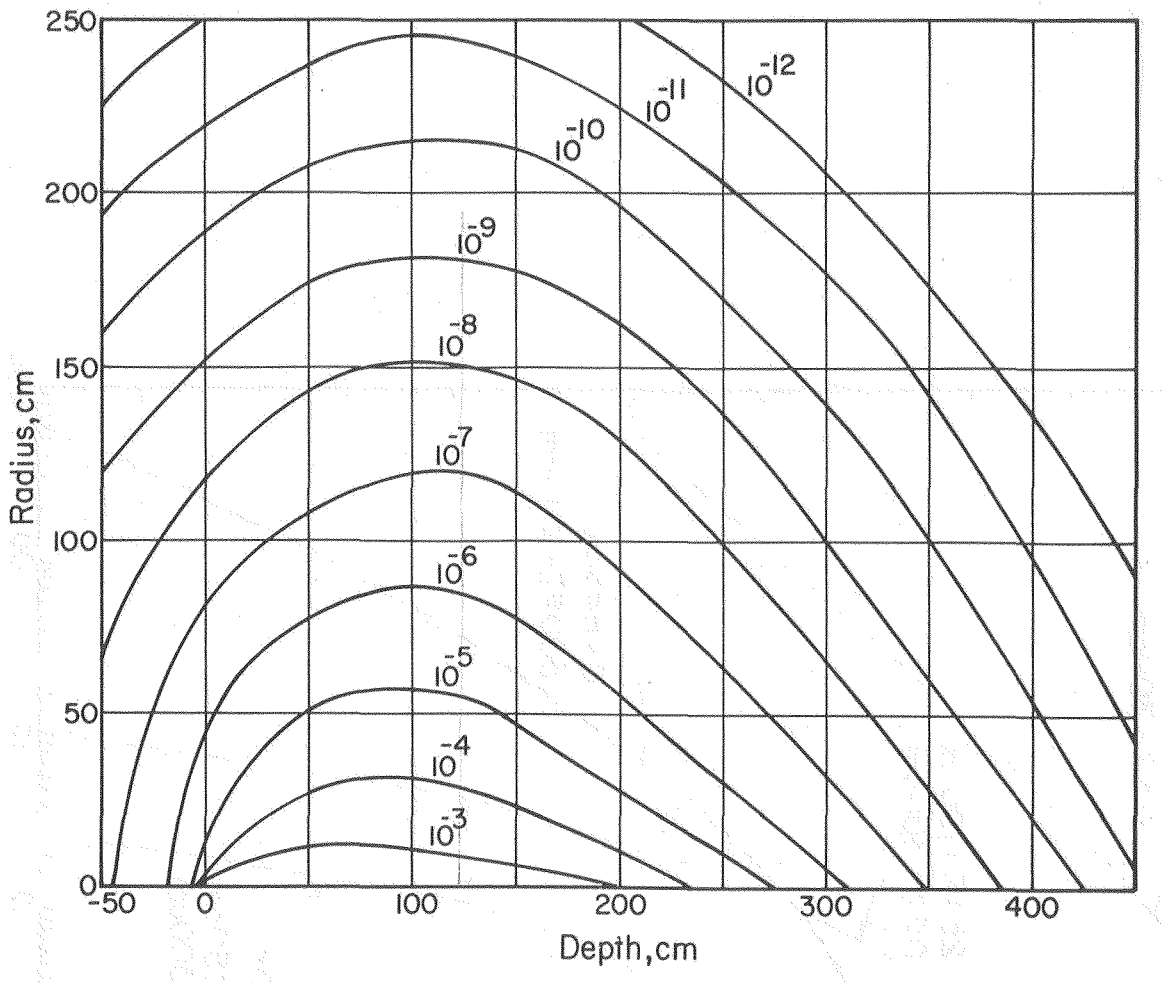

Fig. VIII.17. 300 GeV/c protons incident on a solid iron cylinder. Contours of equal star density (stars/cm^3 · inc. proton) calculated with the Trilling formula for hadron production. The beam of 0.3 × 0.3 cm cross section is centered on the cylinder axis and starts to interact at zero depth. The star density includes only those due to hadrons above 0.3 GeV/c momentum. Contours of higher star density are not shown for clarity of the plot, those of lower star density are not included due to statistical uncertainty. In comparing this graph with the corresponding result derived with the Hagedorn-Ranft production model (Fig. VIII.3) note the difference in scales.

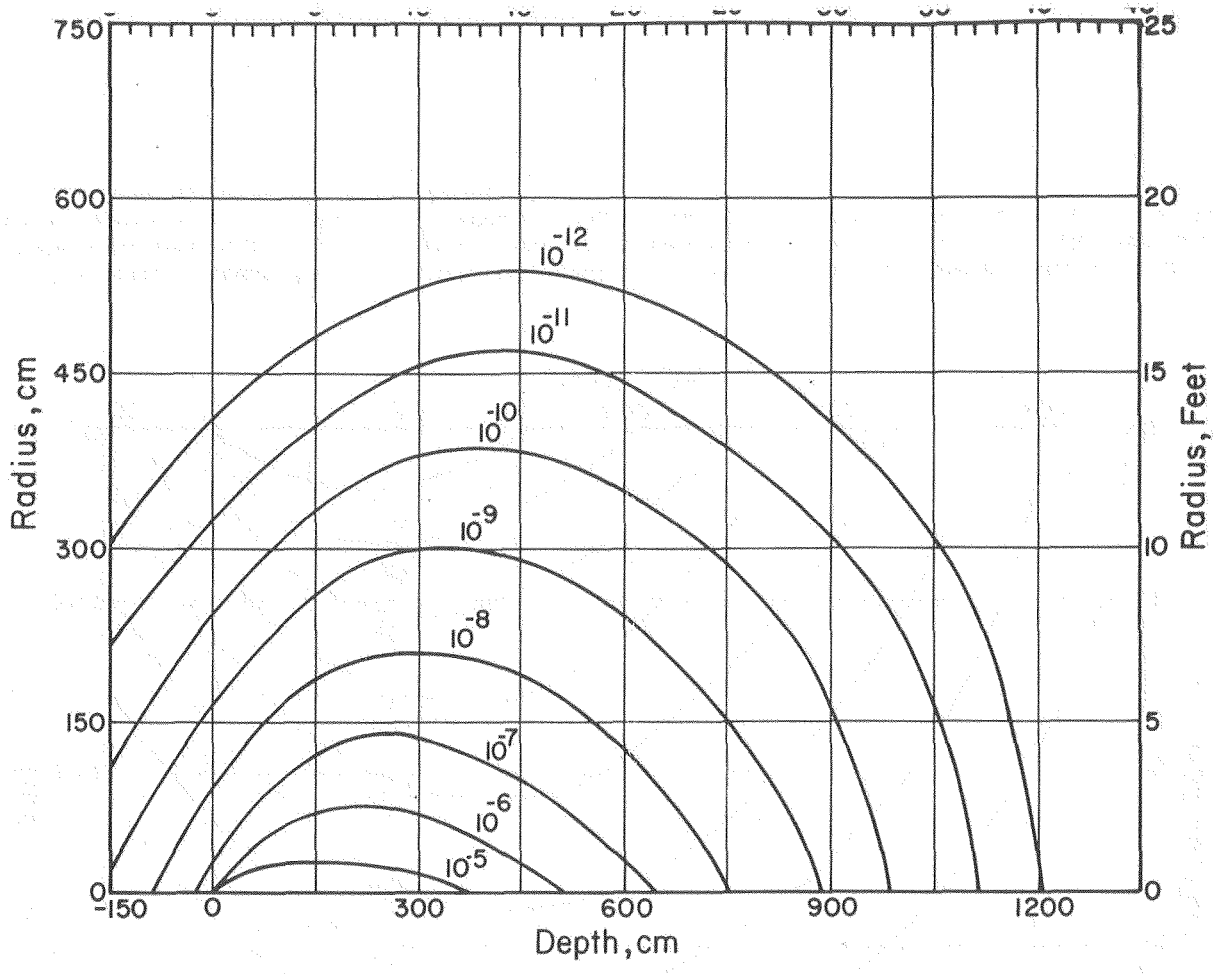

Fig. VIII.18. 30 GeV/c protons incident on a solid concrete cylinder. Contours of equal star density (stars/cm^3 · inc. proton). The beam of 0.3×0.3 cm cross section is centered on the cylinder axis and starts to interact at zero depth. The star density includes only those due to hadrons above 0.3 GeV/c momentum. Contours of higher star density are not shown for clarity of the plot, those of lower star density are not included due to statistical uncertainty.

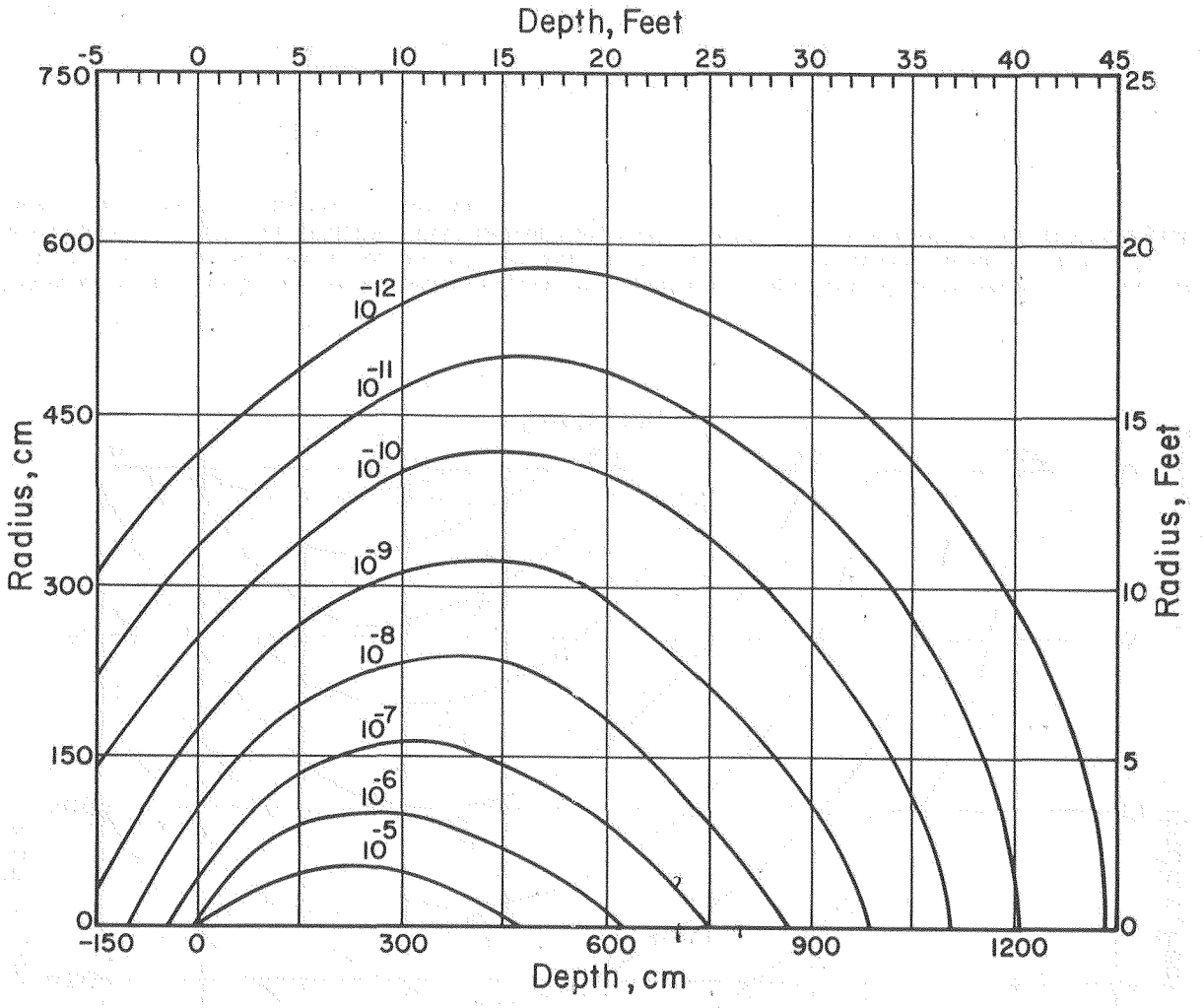

Fig. VIII.19. 100 GeV/c protons incident on a solid concrete cylinder. Contours of equal star density (stars/cm^3 · inc. proton). The beam of 0.3×0.3 cm cross section is centered on the cylinder axis and starts to interact at zero depth. The star density includes only those due to hadrons above 0.3 GeV/c momentum. Contours of higher star density are not shown for clarity of the plot, those of lower star density are not included due to statistical uncertainty.

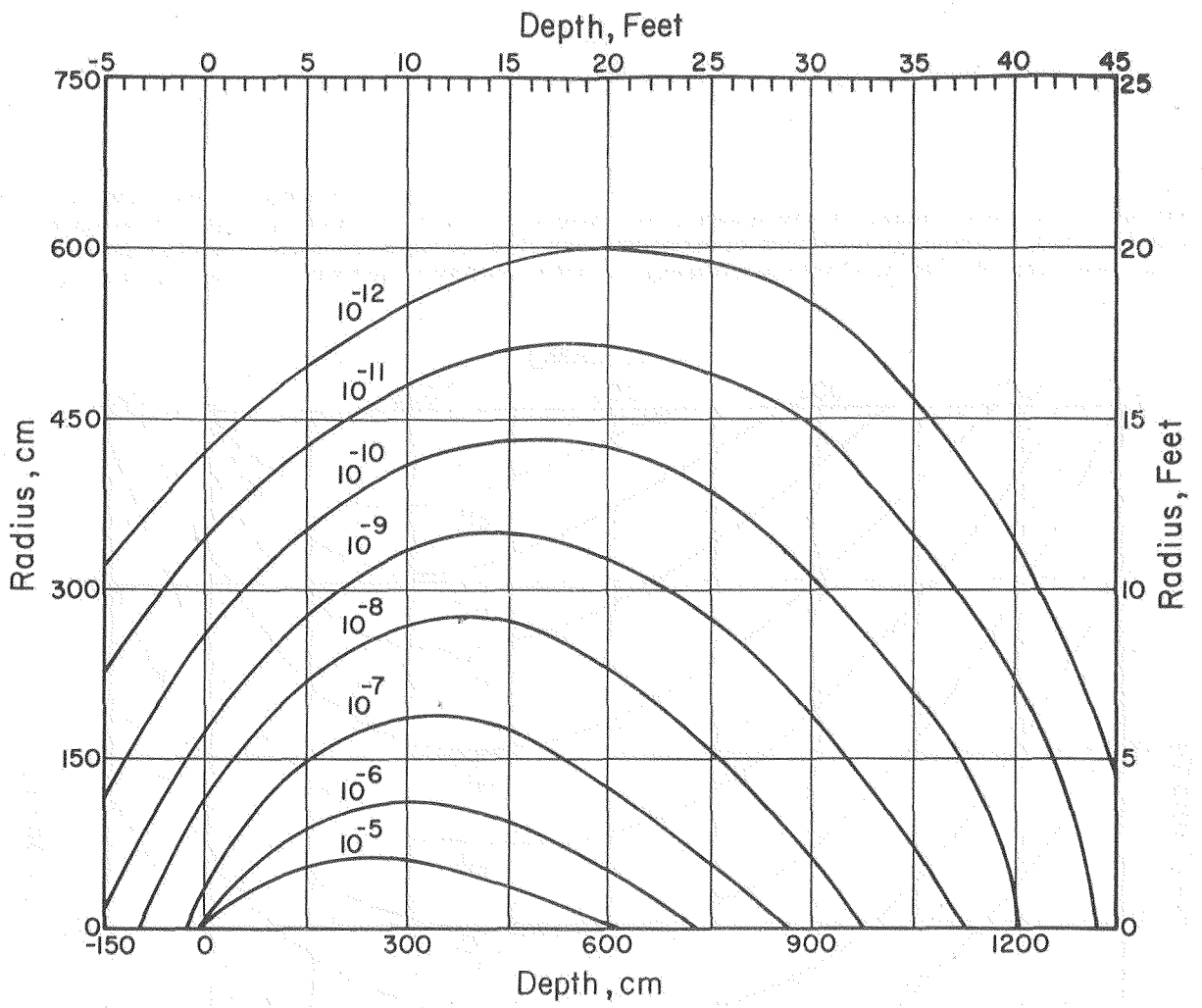

Fig. VIII.20. 300 GeV/c protons incident on a solid concrete cylinder. Contours of equal star density (stars/cm^3 · inc. proton). The beam of 0.3 × 0.3 cm cross section is centered on the cylinder axis and starts to interact at zero depth. The star density includes only those due to hadrons above 0.3 GeV/c momentum. Contours of higher star density are not shown for clarity of the plot, those of lower star density are not included due to statistical uncertainty.

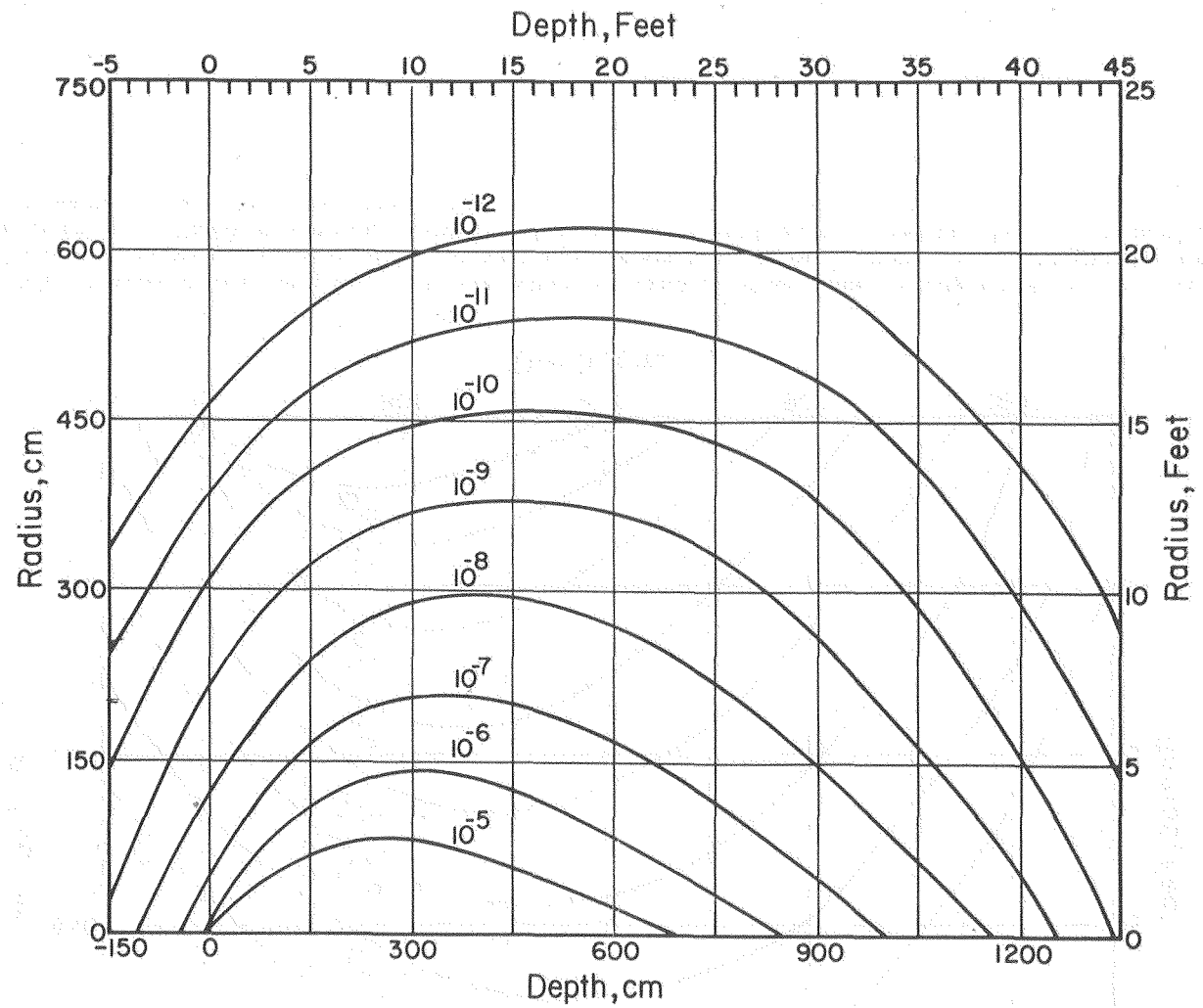

Fig. VIII.21. 1000 GeV/c protons incident on a solid concrete cylinder. Contours of equal star density (stars/cm^3 · inc. proton). The beam of 0.3 × 0.3 cm cross section is centered on the cylinder axis and starts to interact at zero depth. The star density includes only those due to hadrons above 0.3 GeV/c momentum. Contours of higher star density are not shown for clarity of the plot, those of lower star density are not included due to statistical uncertainty.

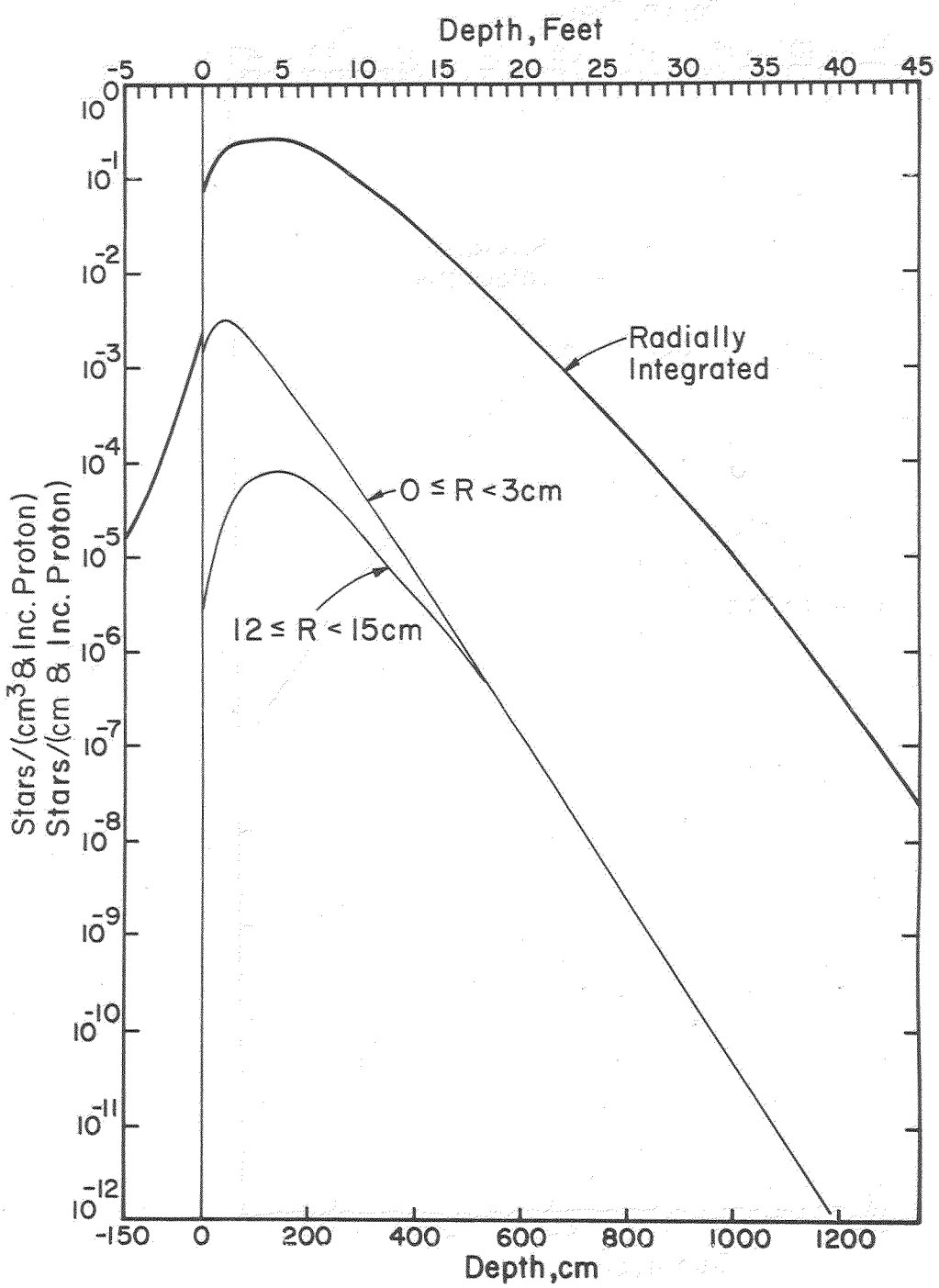

Fig. VIII.22. 30 GeV/c protons incident on a solid concrete cylinder. Depth dependence of the radially integrated star density (stars/cm · inc. proton) and the star density at small radii (stars/cm^3 · inc. proton). The beam of 0.3 × 0.3 cm cross section is centered on the cylinder axis and starts to interact at zero depth. The star density includes only those due to hadrons above 0.3 GeV/c momentum. The star densities at small radii are not shown in the backward region due to statistical uncertainty.

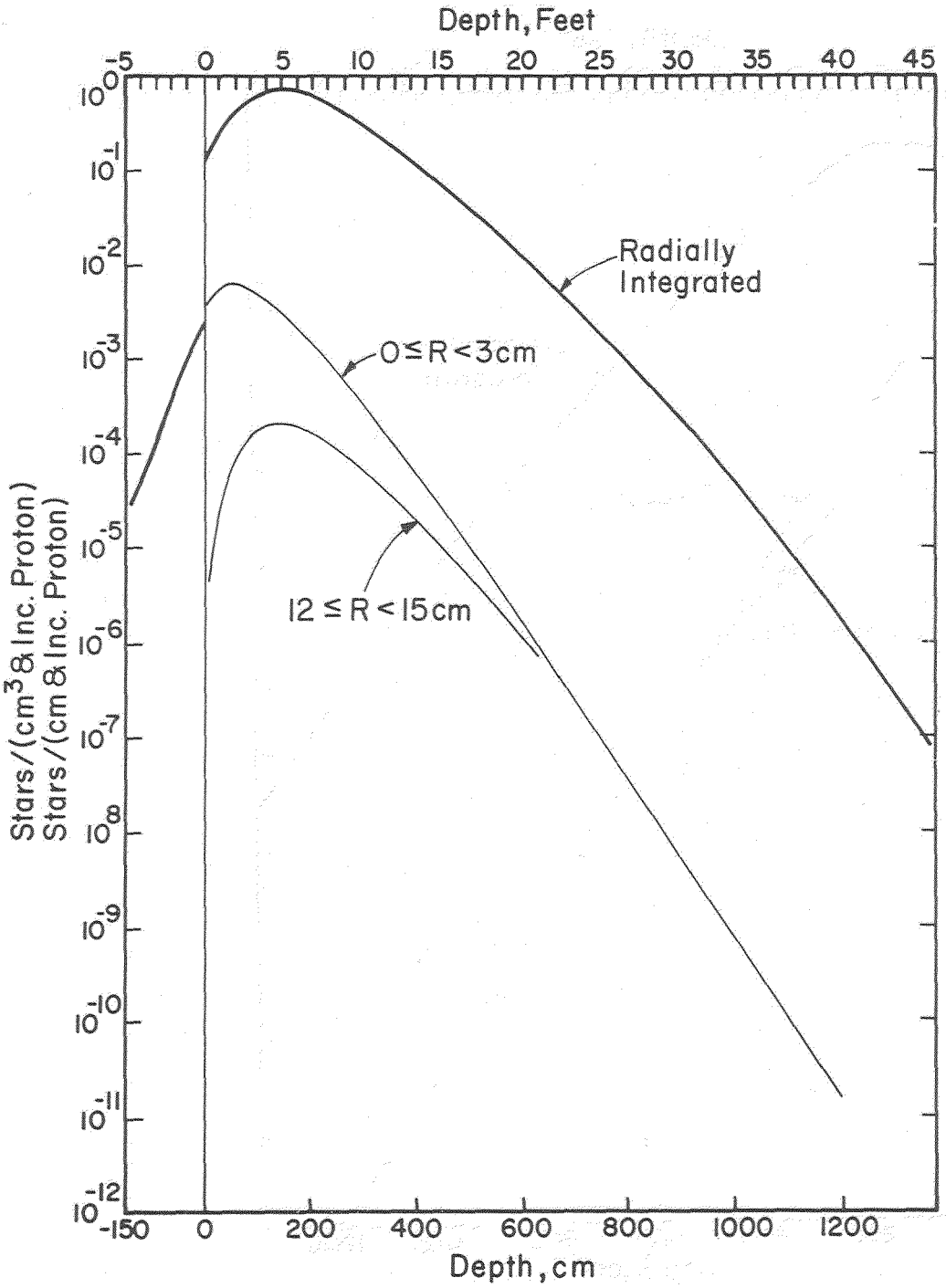

Fig. VIII.23. 100 GeV/c protons incident on a solid concrete cylinder. Depth dependence of the radially integrated star density (stars/cm · inc. proton) and the star density at small radii (stars/cm^3 · inc. proton). The beam of 0.3 × 0.3 cm cross section is centered on the cylinder axis and starts to interact at zero depth. The star density includes only those due to hadrons above 0.3 GeV/c momentum. The star densities at small radii are not shown in the backward region due to statistical uncertainty.

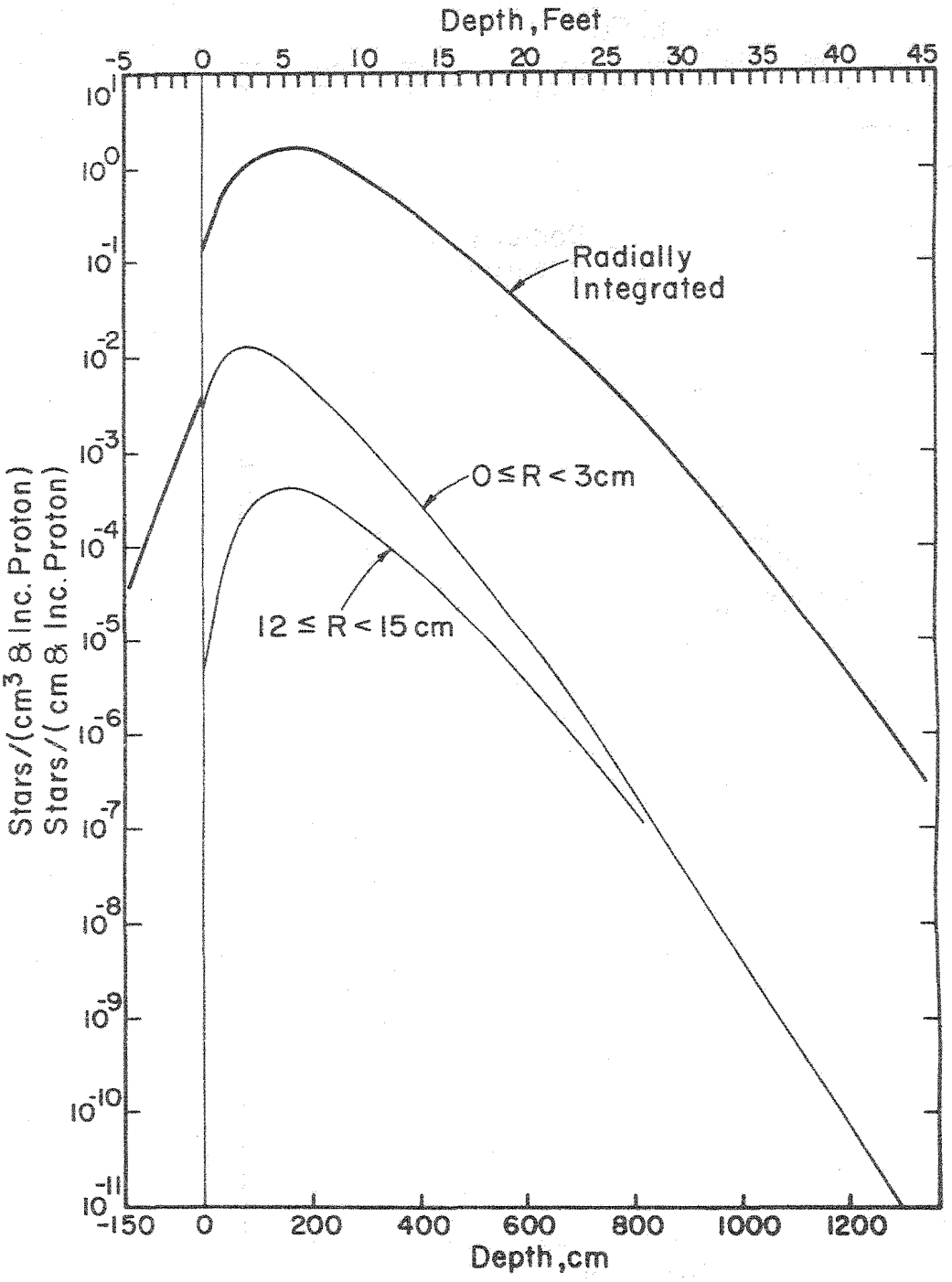

Fig. VIII.24. 300 GeV/c protons incident on a solid concrete cylinder. Depth dependence of the radially integrated star density (stars/cm · inc. proton) and the star density at small radii (stars/cm^3 · inc. proton). The beam of 0.3 × 0.3 cm cross section is centered on the cylinder axis and starts to interact at zero depth. The star density includes only those due to hadrons above 0.3 GeV/c momentum. The star densities at small radii are not shown in the backward region due to statistical uncertainty.

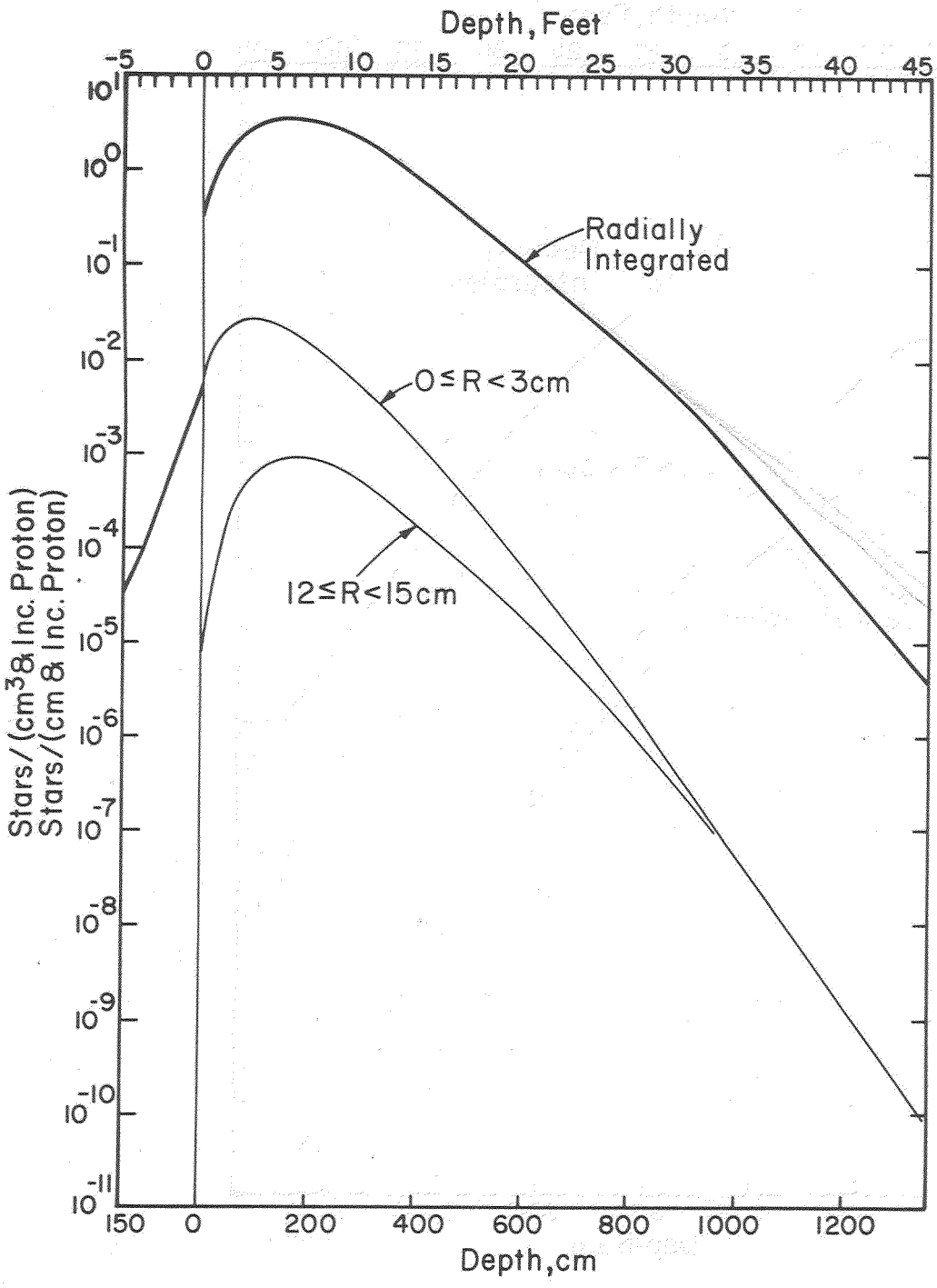

Fig. VIII.25. 1000 GeV/c protons incident on a solid concrete cylinder. Depth dependence of the radially integrated star density (stars/cm · inc. proton) and the star density at small radii (stars/cm^3 · inc. proton). The beam of 0.3 × 0.3 cm cross section is centered on the cylinder axis and starts to interact at zero depth. The star density includes only those due to hadrons above 0.3 GeV/c momentum. The star densities at small radii are not shown in the backward region due to statistical uncertainty.

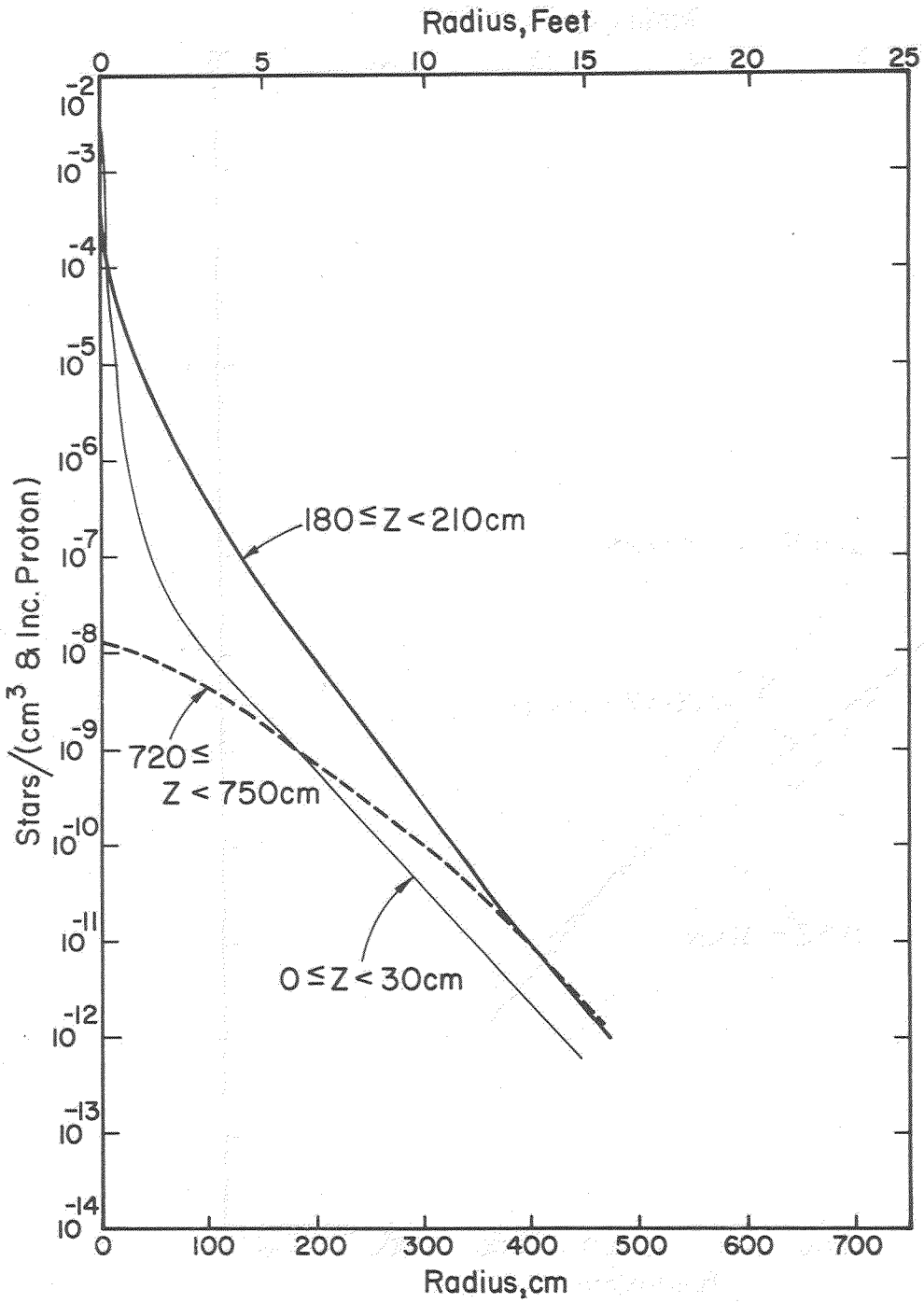

Fig. VIII.26. 30 GeV/c protons incident on a solid concrete cylinder. Radial dependence of the star density (stars/cm^3 · inc. proton) at selected depths. The beam of 0.3 × 0.3 cm cross section is centered on the cylinder axis. The star density includes only those due to hadrons above 0.3 GeV/c momentum.

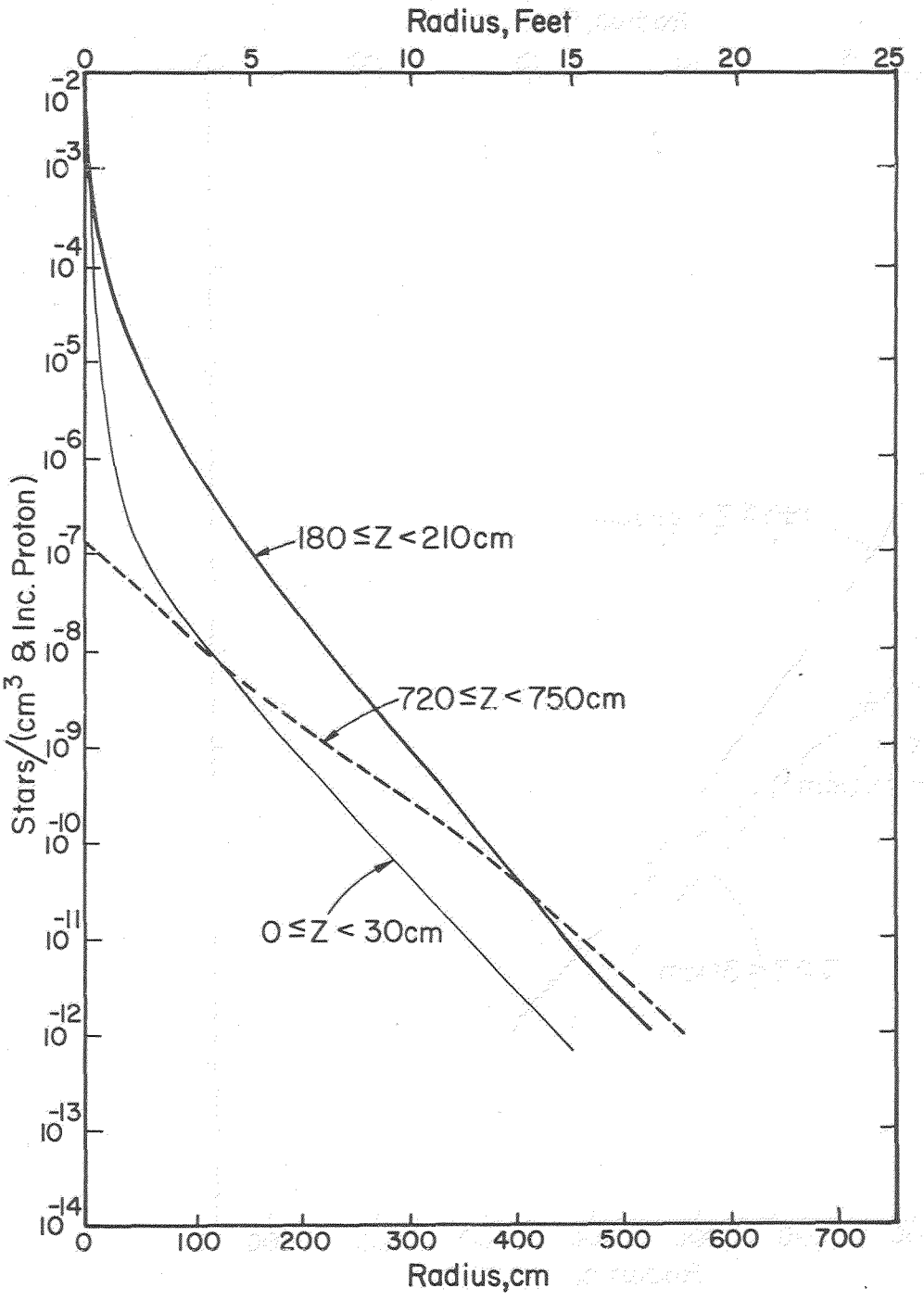

Fig. VIII.27. 100 GeV/c protons incident on a solid concrete cylinder. Radial dependence of the star density (stars/cm^3 · inc. proton) at selected depths. The beam of 0.3 × 0.3 cm cross section is centered on the cylinder axis. The star density includes only those due to hadrons above 0.3 GeV/c momentum.

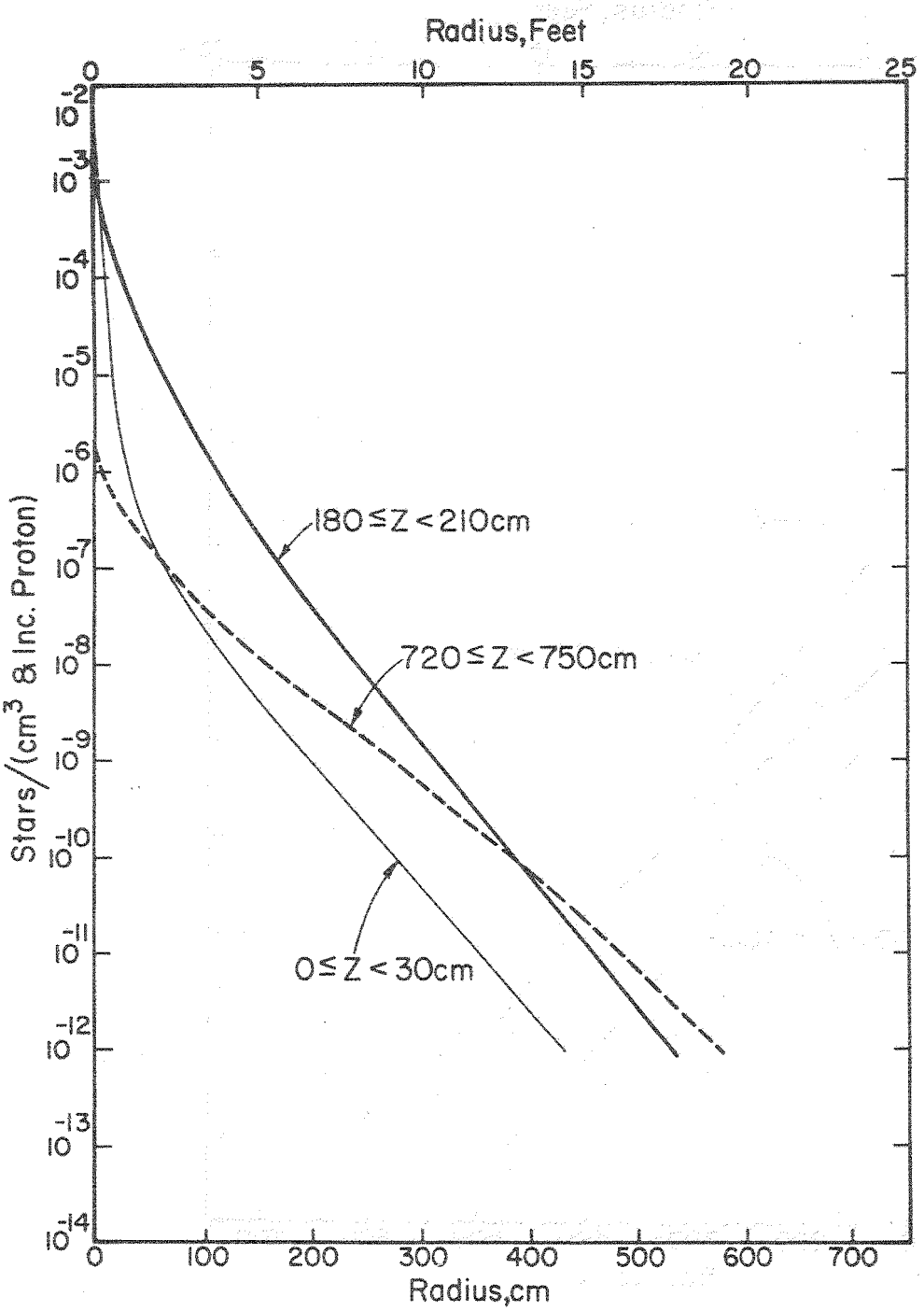

Fig. VIII.28. 300 GeV/c protons incident on a solid concrete cylinder. Radial dependence of the star density (stars/cm^3 · inc. proton) at selected depths. The beam of 0.3 × 0.3 cm cross section is centered on the cylinder axis. The star density includes only those due to hadrons above 0.3 GeV/c momentum.

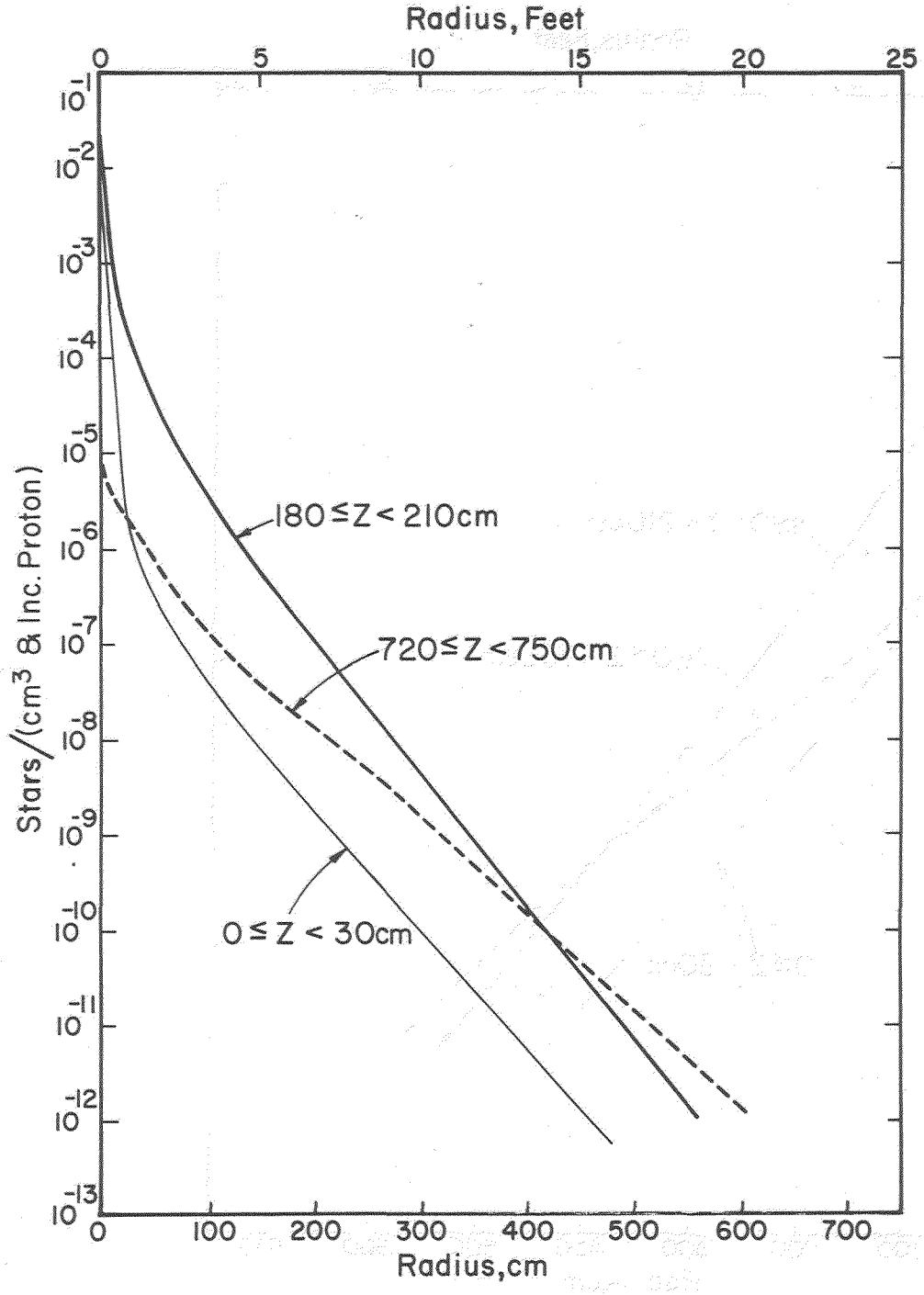

Fig. VIII.29. 1000 GeV/c protons incident on a solid concrete cylinder. Radial dependence of the star density (stars/cm^3 · inc. proton) at selected depths. The beam of 0.3×0.3 cm cross section is centered on the cylinder axis. The star density includes only those due to hadrons above 0.3 GeV/c momentum.

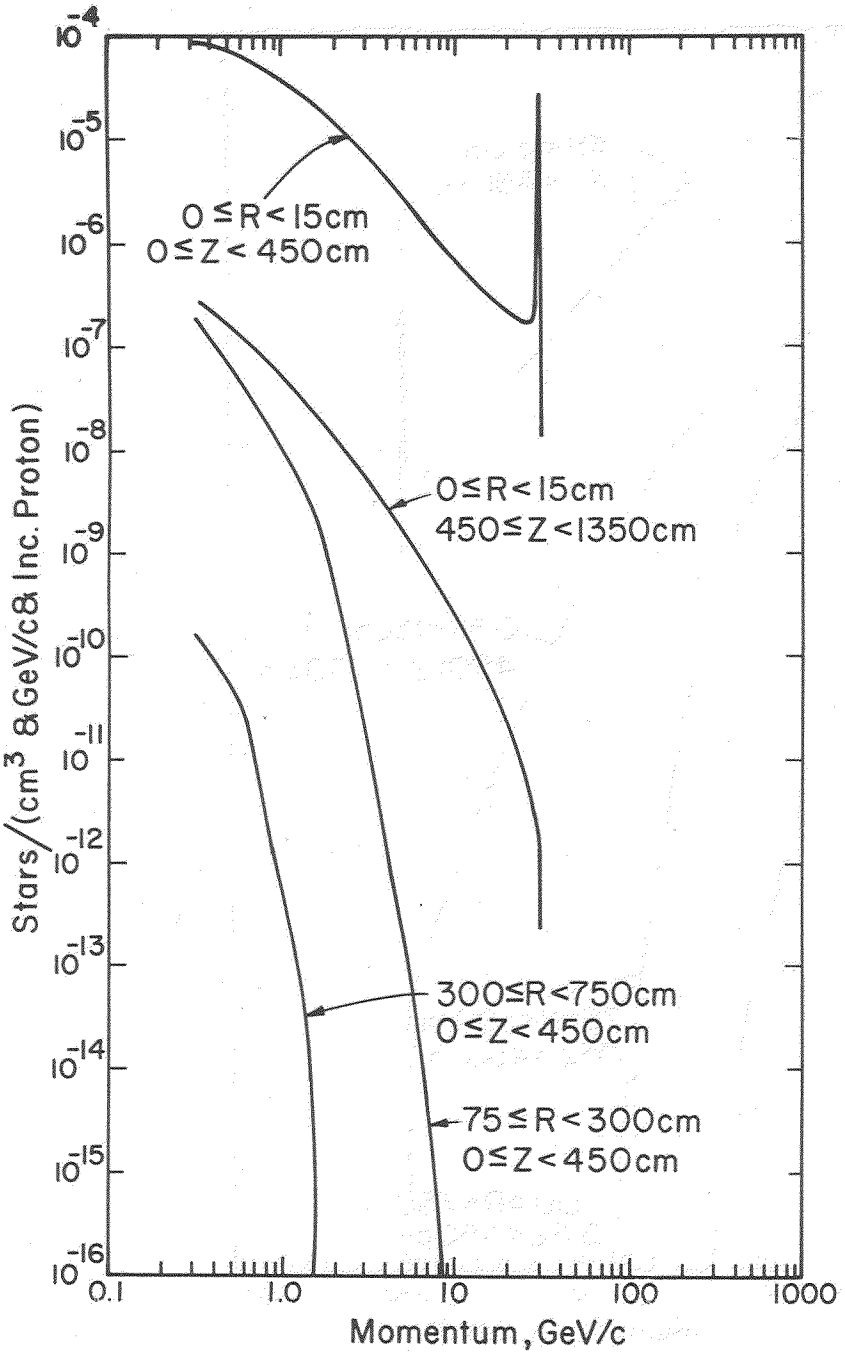

Fig. VIII.30. 30 GeV/c protons incident on a solid concrete cylinder. Momentum spectra of interacting hadrons (stars/cm^3 · GeV/c · inc. proton) for selected regions. The beam of 0.3 × 0.3 cm cross section is centered on the cylinder axis. The spectra are not calculated below 0.3 GeV/c momentum.

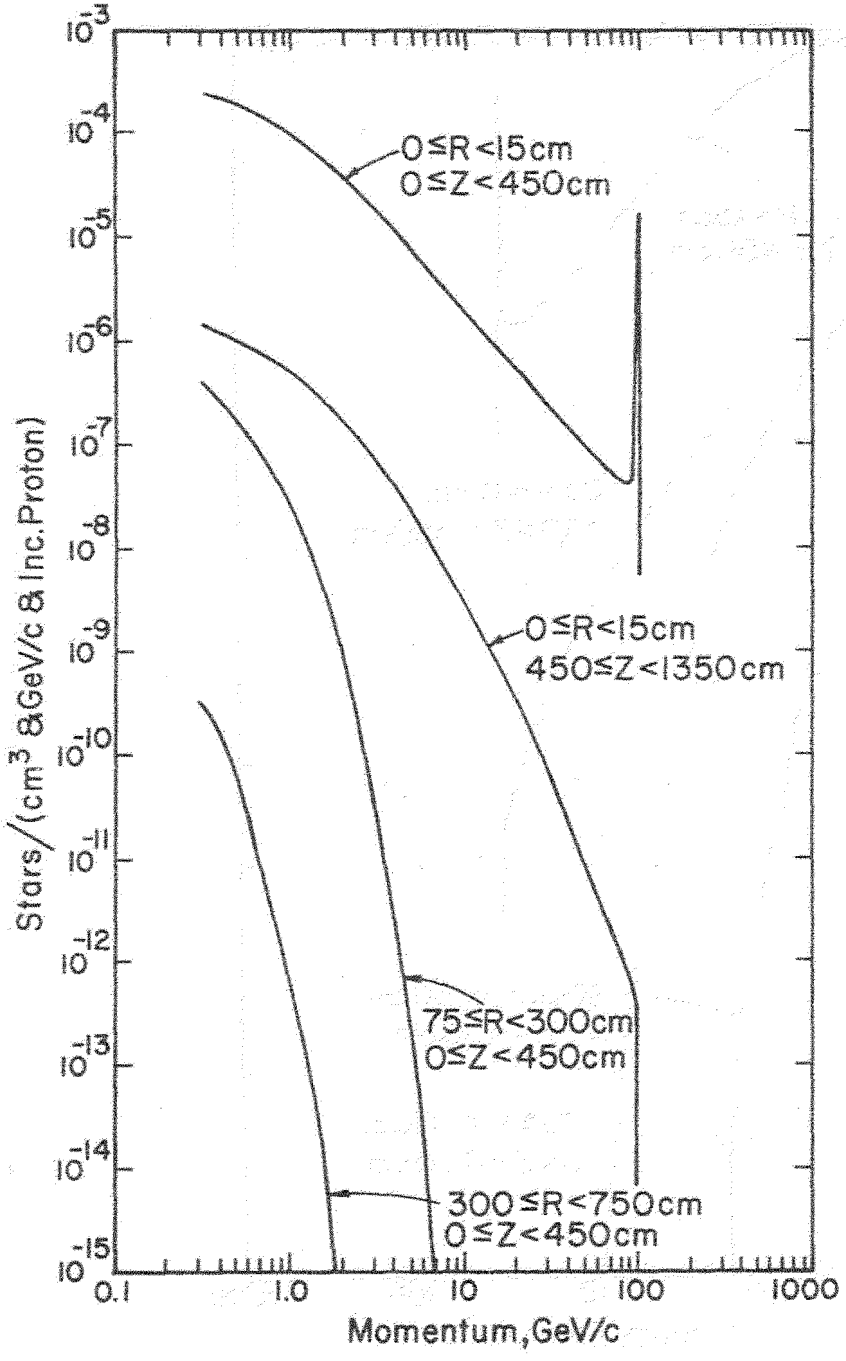

ig. VIII.31. 100 GeV/c protons incident on a solid concrete cylinder. Momentum spectra of interacting hadrons (stars/cm^3 · GeV/c · inc. proton) for selected regions. The beam of 0.3 × 0.3 cm cross section is centered on the cylinder axis. The spectra are not calculated below 0.3 GeV/c momentum.

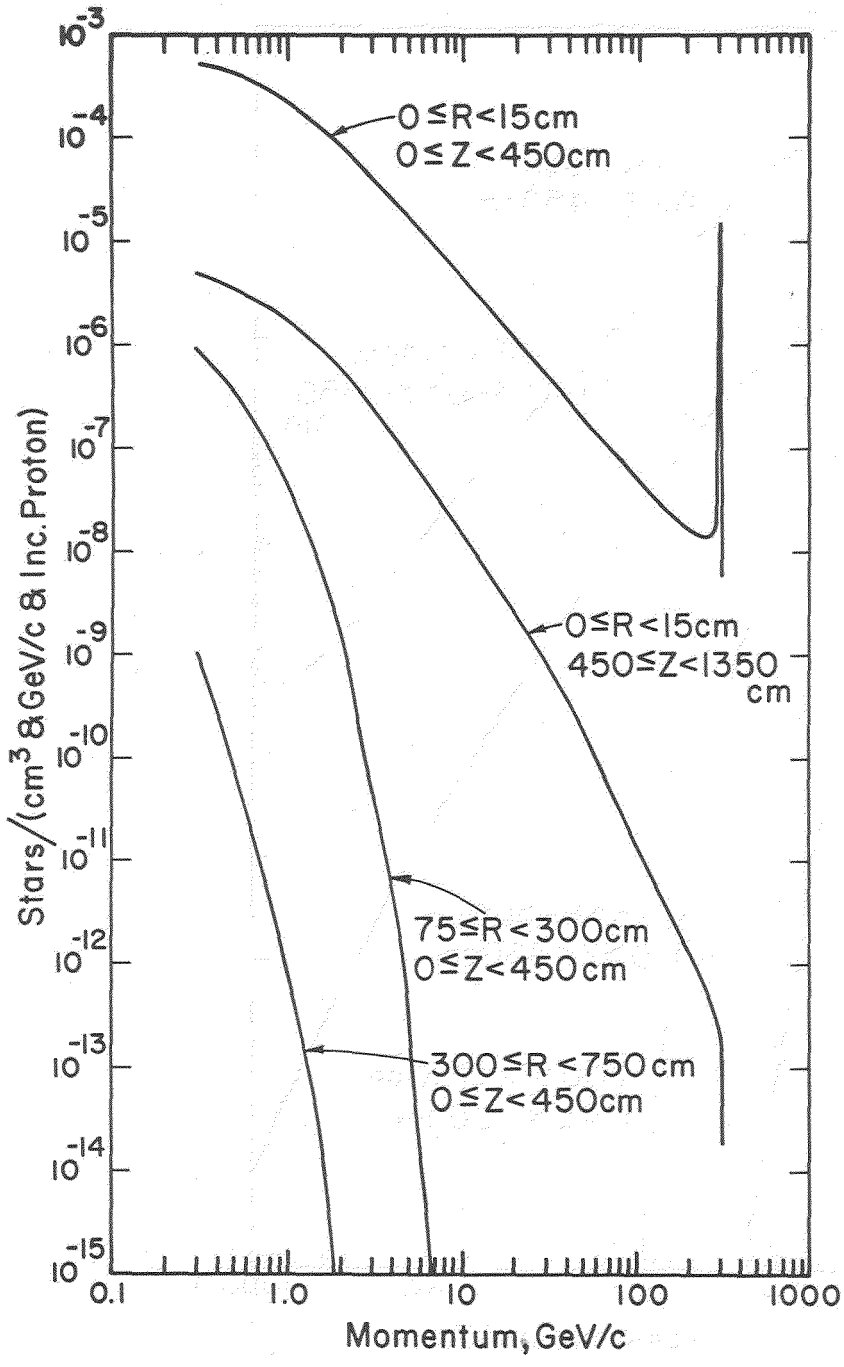

Fig. VIII.32. 300 GeV/c protons incident on a solid concrete cylinder. Momentum spectra of interacting hadrons (stars/cm^3 · GeV/c · inc. proton) for selected regions. The beam of 0.3 × 0.3 cm cross section is centered on the cylinder axis. The spectra are not calculated below 0.3 GeV/c momentum.

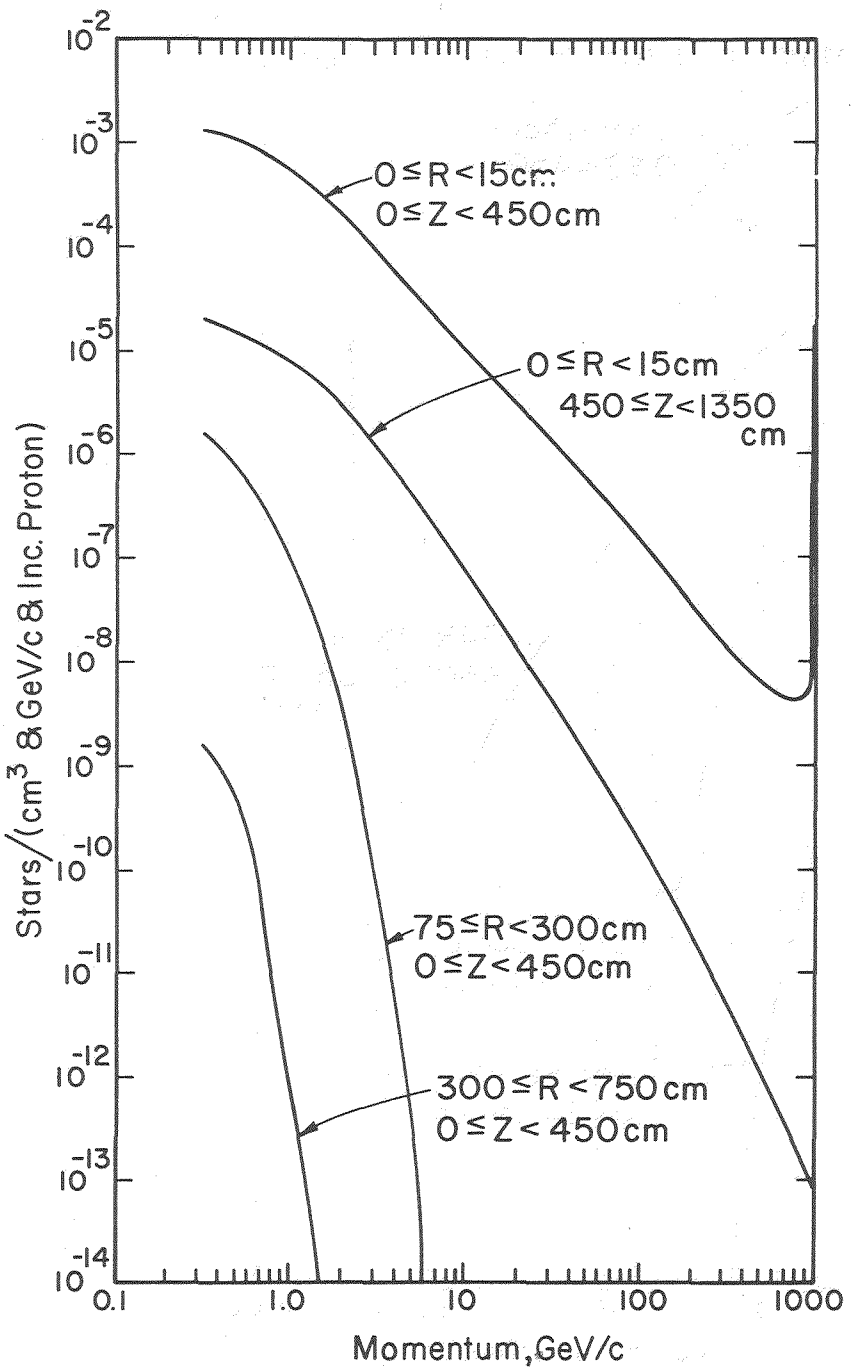

Fig. VIII.33. 1000 GeV/c protons incident on a solid concrete cylinder. Momentum spectra of interacting hadrons (stars/cm^3 · GeV/c · inc. proton) for selected regions. The beam of 0.3 × 0.3 cm cross section is centered on the cylinder axis. The spectra are not calculated below 0.3 GeV/c momentum.

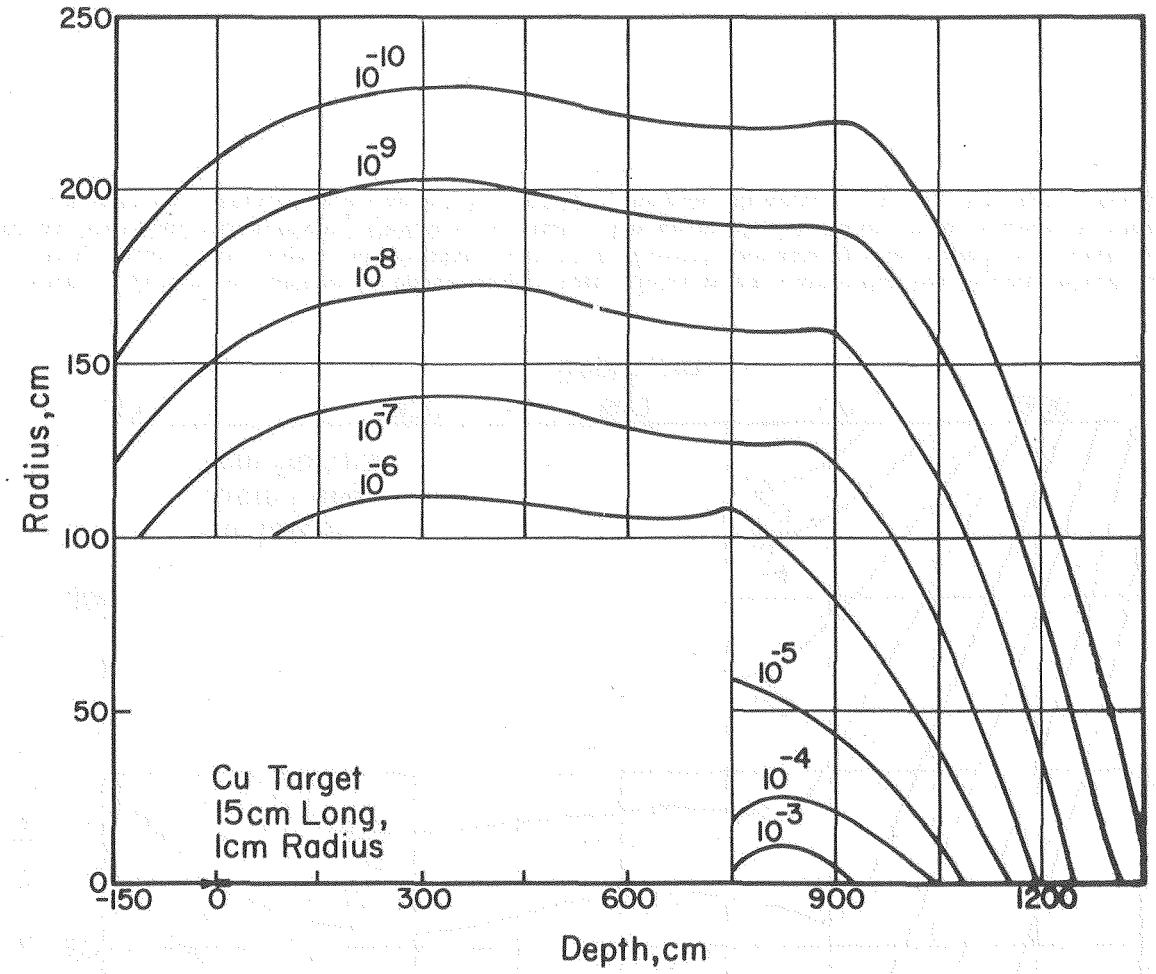

Fig. VIII.34. 300 GeV/c protons incident on a copper target, approximately one interaction length long, placed in an iron cave represented by a cylindrical tunnel in a large solid cylinder. Contours of equal star density (stars/cm^3 · inc. proton). The star density includes only those due to hadrons above 0.3 GeV/c momentum. The beam of 0.3 × 0.3 cm cross section is centered on the cylinder axis. Contours of higher star density are not shown for clarity of the plot, those of lower star density are not included due to statistical uncertainty.

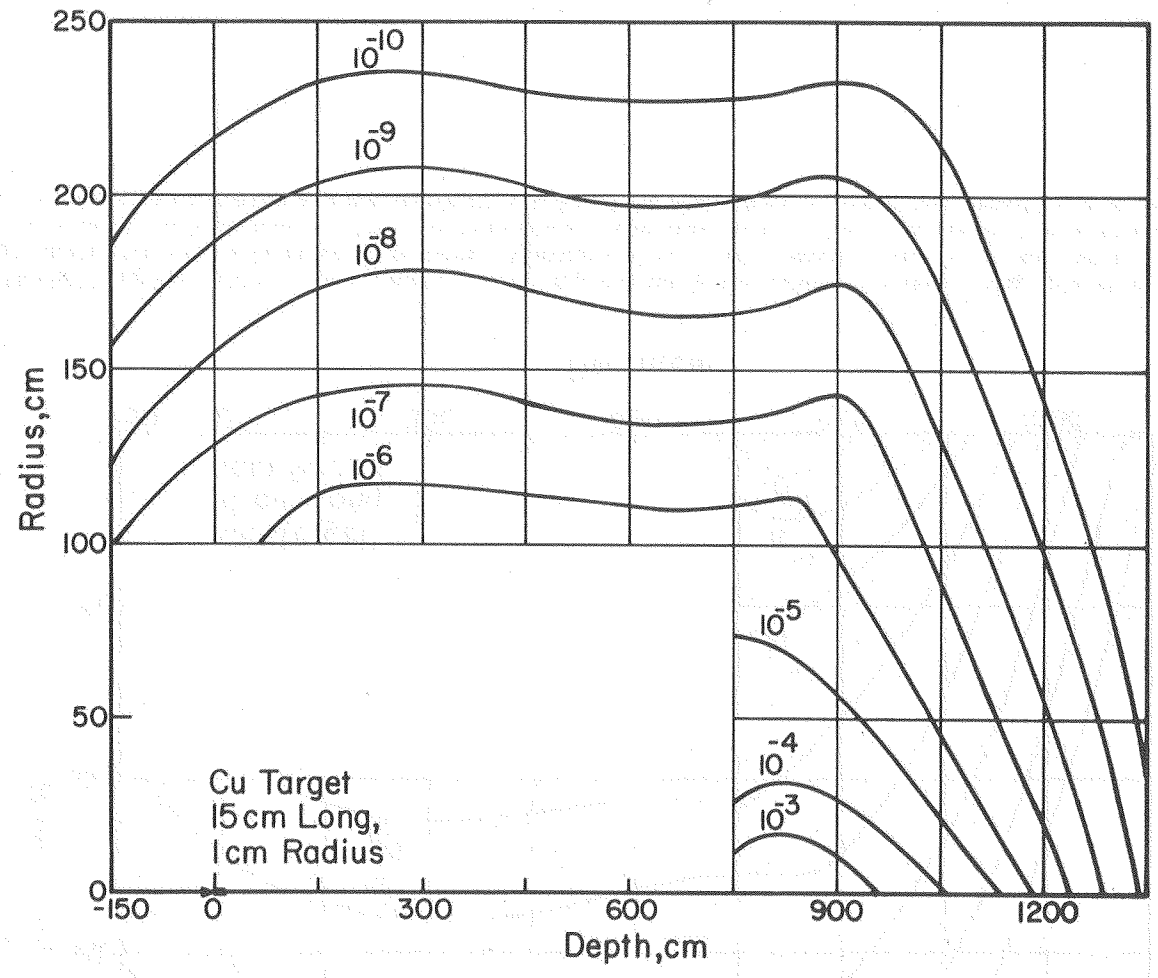

Fig. VIII.35. 1000 GeV/c protons incident on a copper target, approximately one interaction length long, placed in an iron cave represented by a cylindrical tunnel in a large solid cylinder. Contours of equal star density (stars/cm^3 · inc. proton). The star density includes only those due to hadrons above 0.3 GeV/c momentum. The beam of 0.3 × 0.3 cm cross section is centered on the cylinder axis. Contours of higher star density are not shown for clarity of the plot, those of lower star density are not included due to statistical uncertainty.

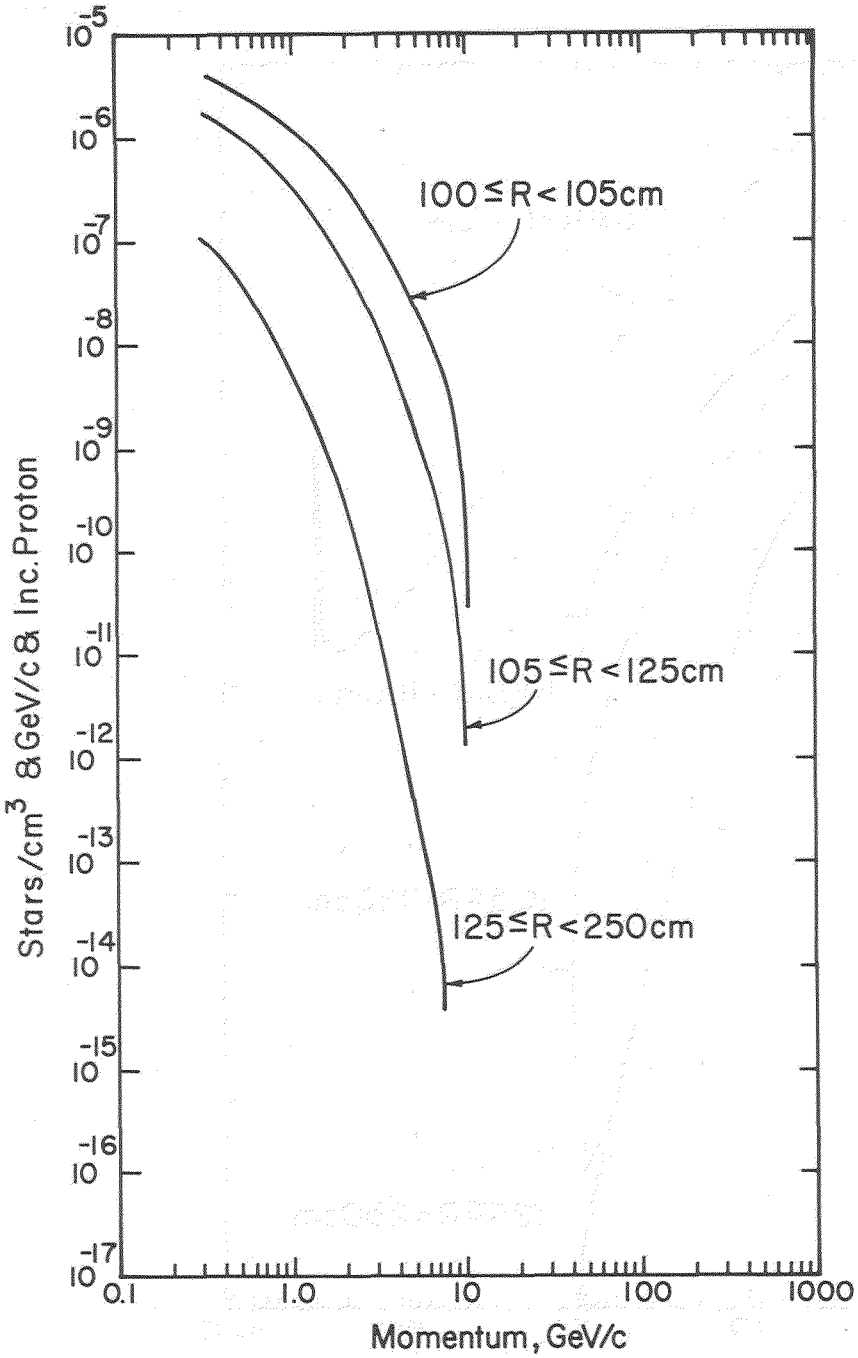

Fig. VIII.36. 300 GeV/c protons incident on a copper target, approximately one interaction length long, placed in an iron cave represented by a cylindrical tunnel in a large solid cylinder. Momentum spectra of interacting hadrons (stars/cm^3 · GeV/c · inc. proton) between zero and 750 cm depth (tunnel region) in three radial regions. The beam of 0.3 × 0.3 cm cross section is centered on the cylinder axis. The spectra are not calculated below 0.3 GeV/c momentum.

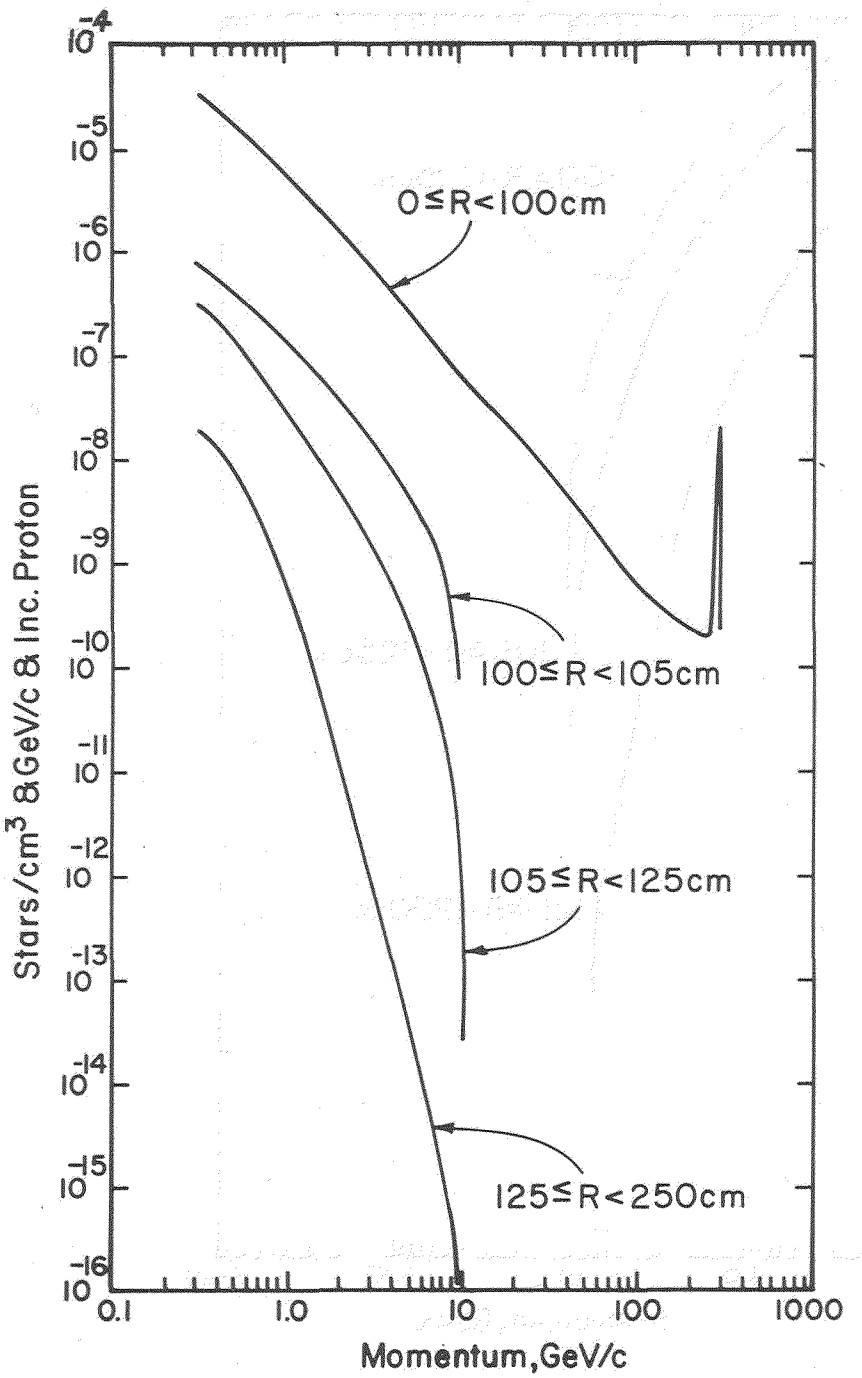

Fig. VIII.37. 300 GeV/c protons incident on a copper target, approximately one interaction length long, placed in an iron cave represented by a cylindrical tunnel in a large solid cylinder. Momentum spectra of interacting hadrons (stars/cm^3 · GeV/c · inc. proton) between 750 cm and 1350 cm depth (backwall) in four radial regions. The beam of 0.3 × 0.3 cm cross section is centered on the cylinder axis. The spectra are not calculated below 0.3 GeV/c momentum.

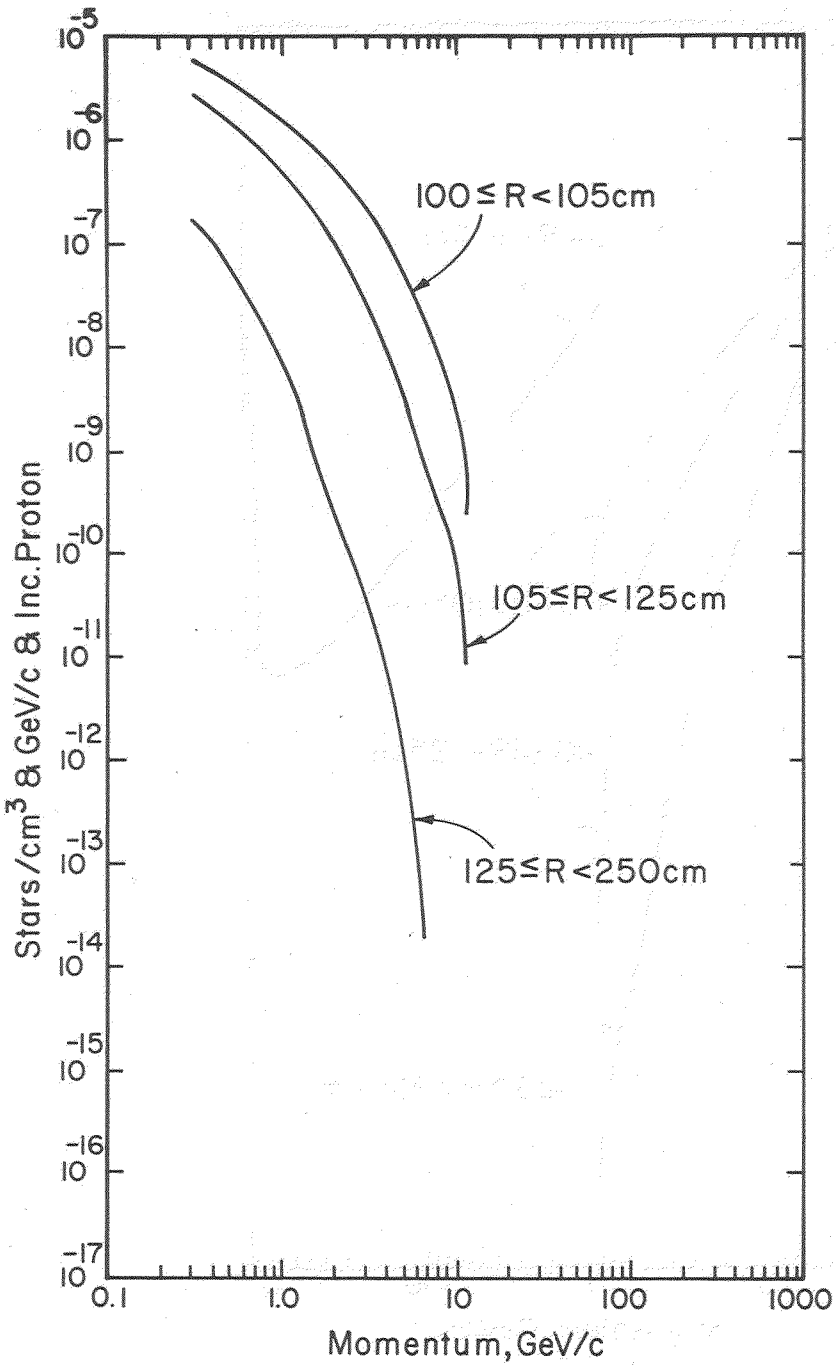

Fig. VIII.38. 1000 GeV/c protons incident on a copper target, approximately one interaction length long, placed in an iron cave represented by a cylindrical tunnel in a large solid cylinder. Momentum spectra of interacting hadrons (stars/cm^3 · GeV/c · inc. proton) between zero and 750 cm depth (tunnel region) in three radial regions. The beam of 0.3 × 0.3 cm cross section is centered on the cylinder axis. The spectra are not calculated below 0.3 GeV/c momentum.

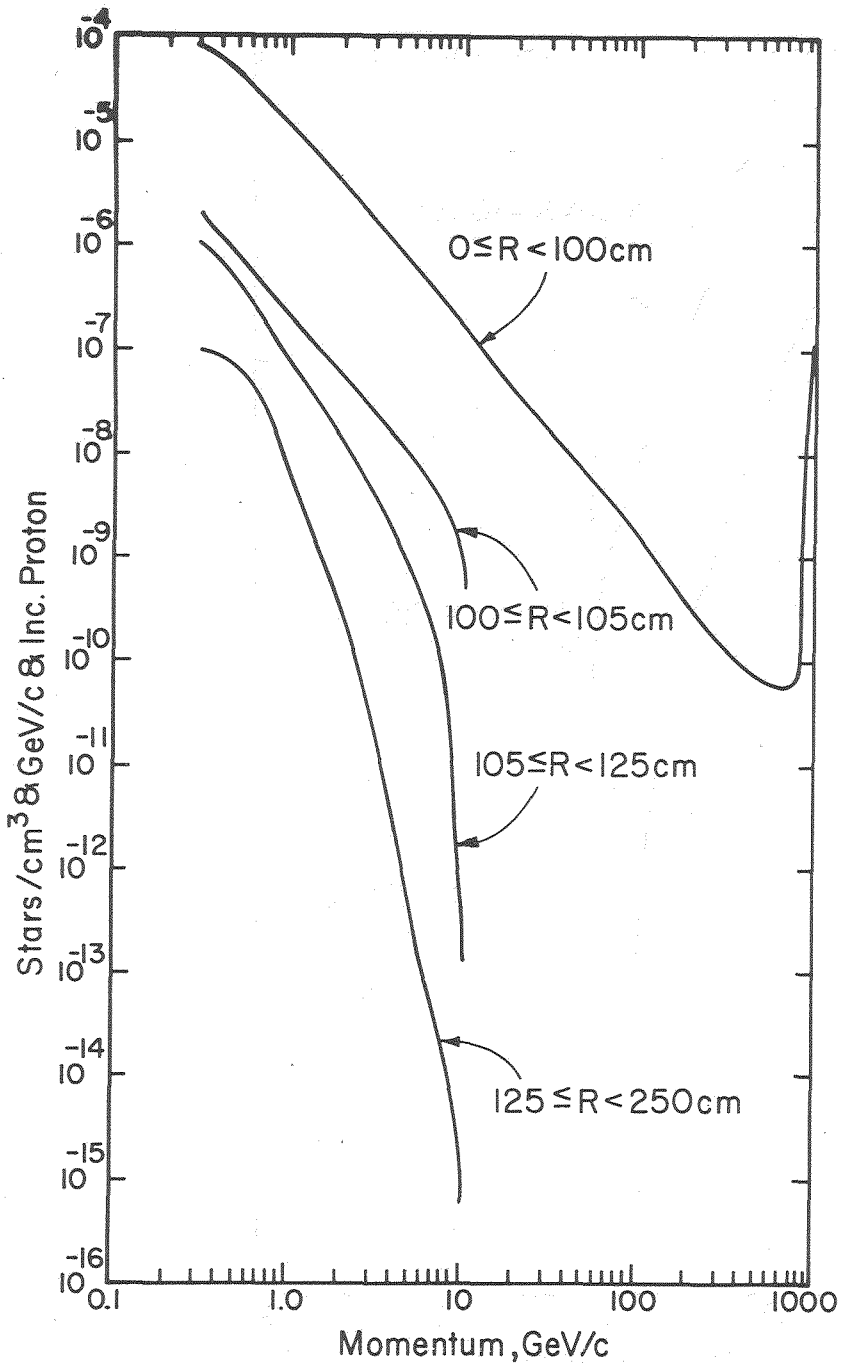

Fig. VIII.39. 1000 GeV/c protons incident on a copper target, approximately one interaction length long, placed in an iron cave represented by a cylindrical tunnel in a large solid cylinder. Momentum spectra of interacting hadrons (stars/cm^3 · GeV/c · inc. proton) between 750 cm and 1350 cm depth (backwall) in four radial regions. The beam of 0.3 × 0.3 cm cross section is centered on the cylinder axis. The spectra are not calculated below 0.3 GeV/c momentum.

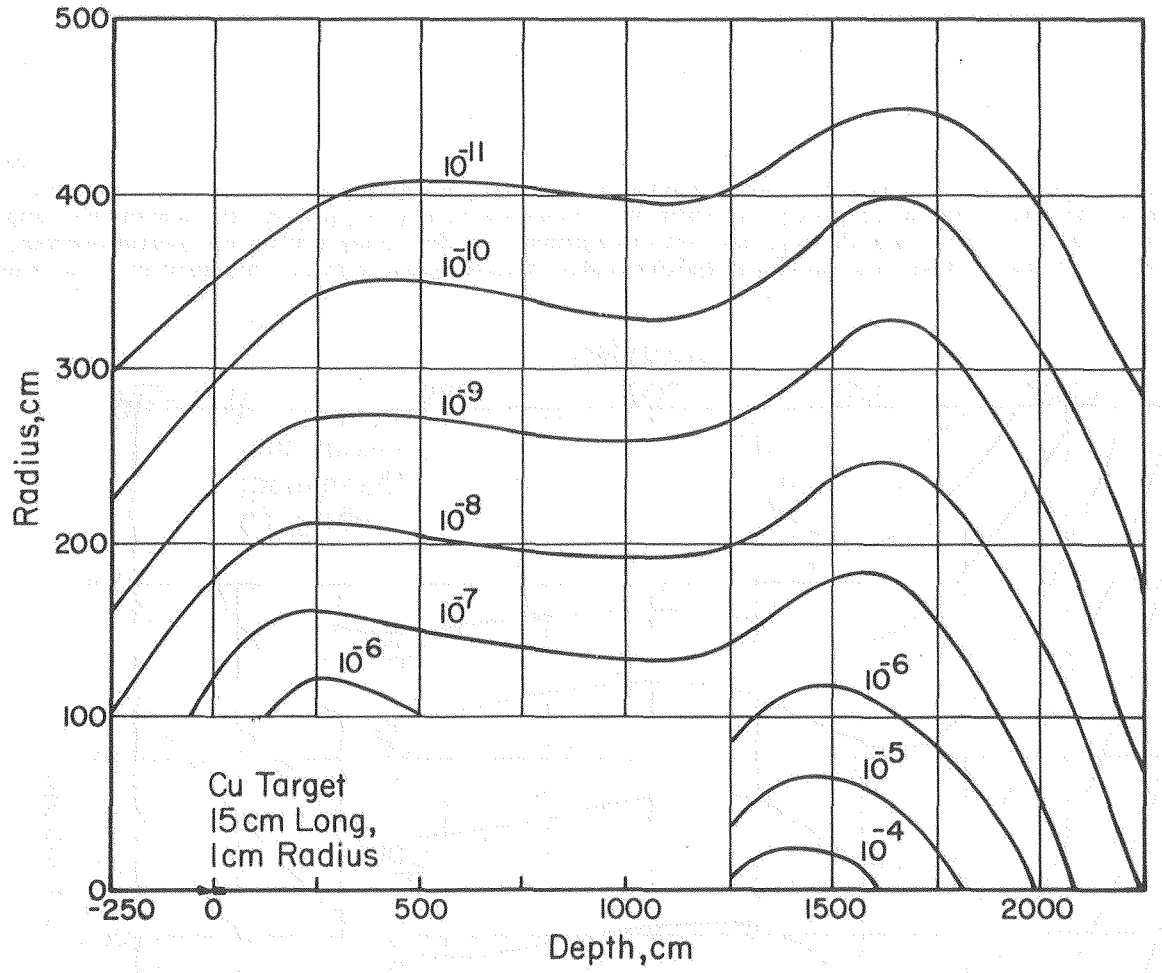

Fig. VIII.40. 300 GeV/c protons incident on a copper target, approximately one interaction length long, placed in a concrete cave represented by a cylindrical tunnel in a large solid cylinder. Contours of equal star density (stars/cm^3 · inc. proton). The star density includes only those due to hadrons above 0.3 GeV/c momentum. The beam of 0.3 × 0.3 cm cross section is centered on the cylinder axis. Contours of higher star density are not shown for clarity of the plot, those of lower star density are not included due to statistical uncertainty.

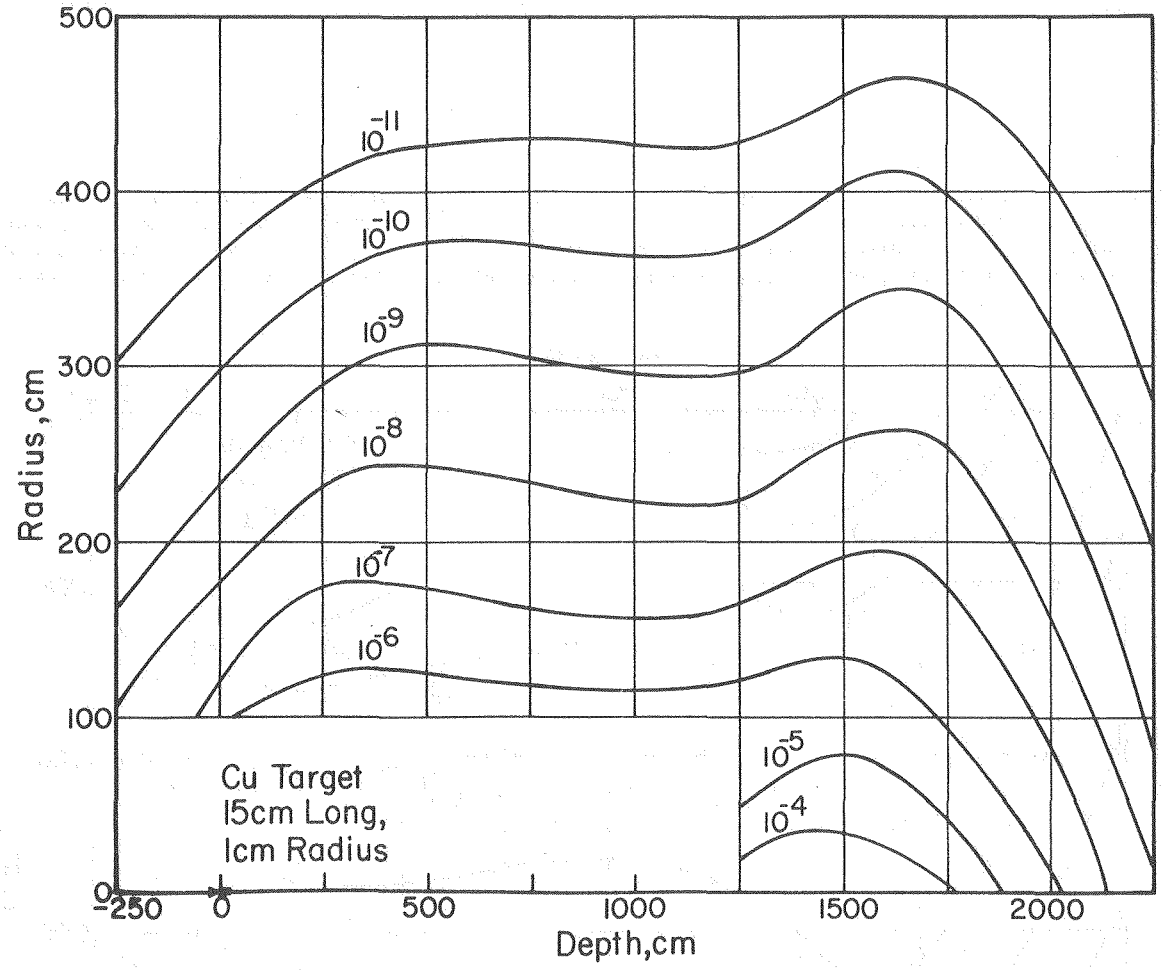

Fig. VIII.41. 1000 GeV/c protons incident on a copper target, approximately one interaction length long, placed in a concrete cave represented by a cylindrical tunnel in a large solid cylinder. Contours of equal star density (stars/cm^3 · inc. proton). The star density includes only those due to hadrons above 0.3 GeV/c momentum. The beam of 0.3 × 0.3 cm cross section is centered on the cylinder axis. Contours of higher star density are not shown for clarity of the plot, those of lower star density are not included due to statistical uncertainty.

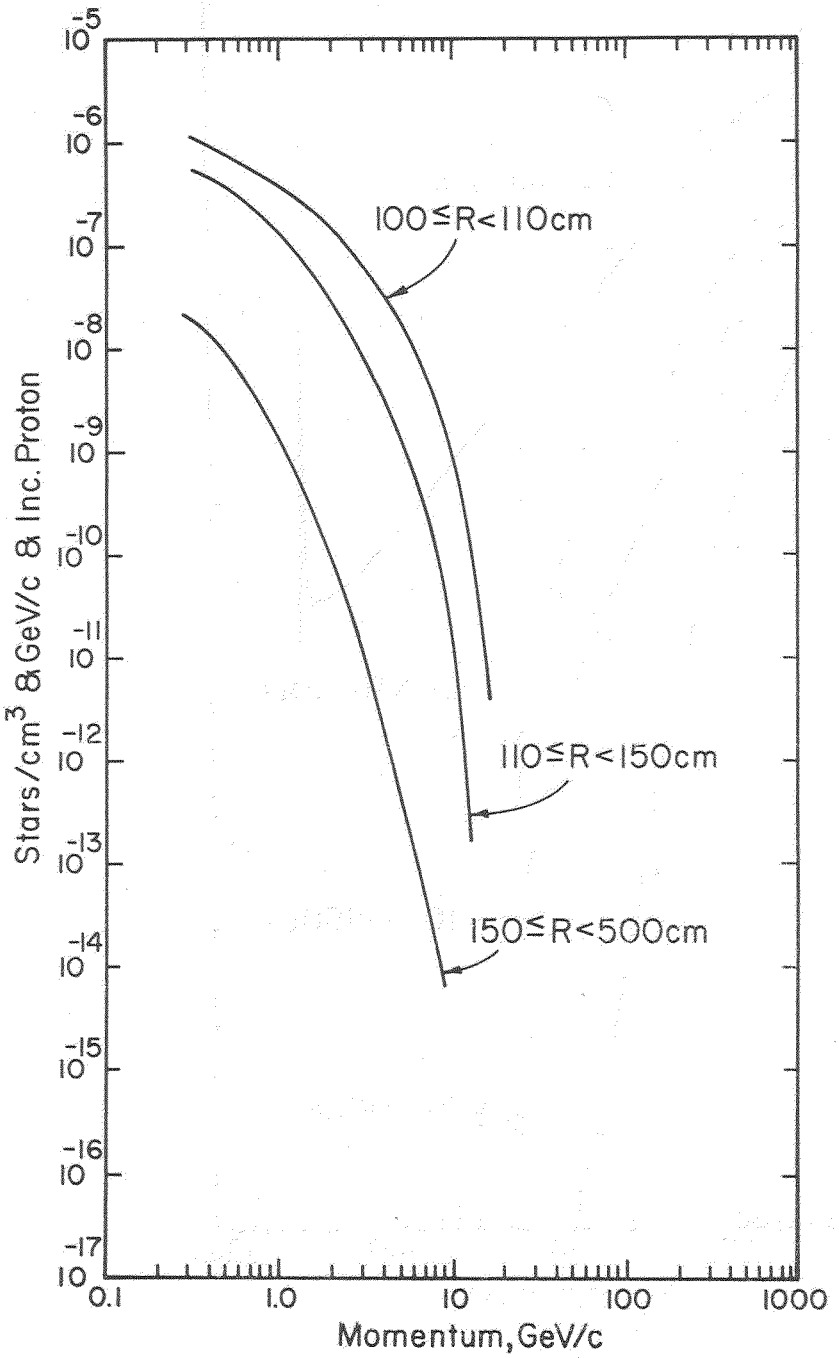

Fig. VIII.42. 300 GeV/c protons incident on a copper target, approximately one interaction length long, placed in a concrete cave represented by a cylindrical tunnel in a large solid cylinder. Momentum spectra of interacting hadrons (stars/cm^3 · GeV/c · inc. proton) between zero and 1250 cm depth (tunnel region) in three radial regions. The beam of 0.3 × 0.3 cm cross section is centered on the cylinder axis. The spectra are not calculated below 0.3 GeV/c momentum.

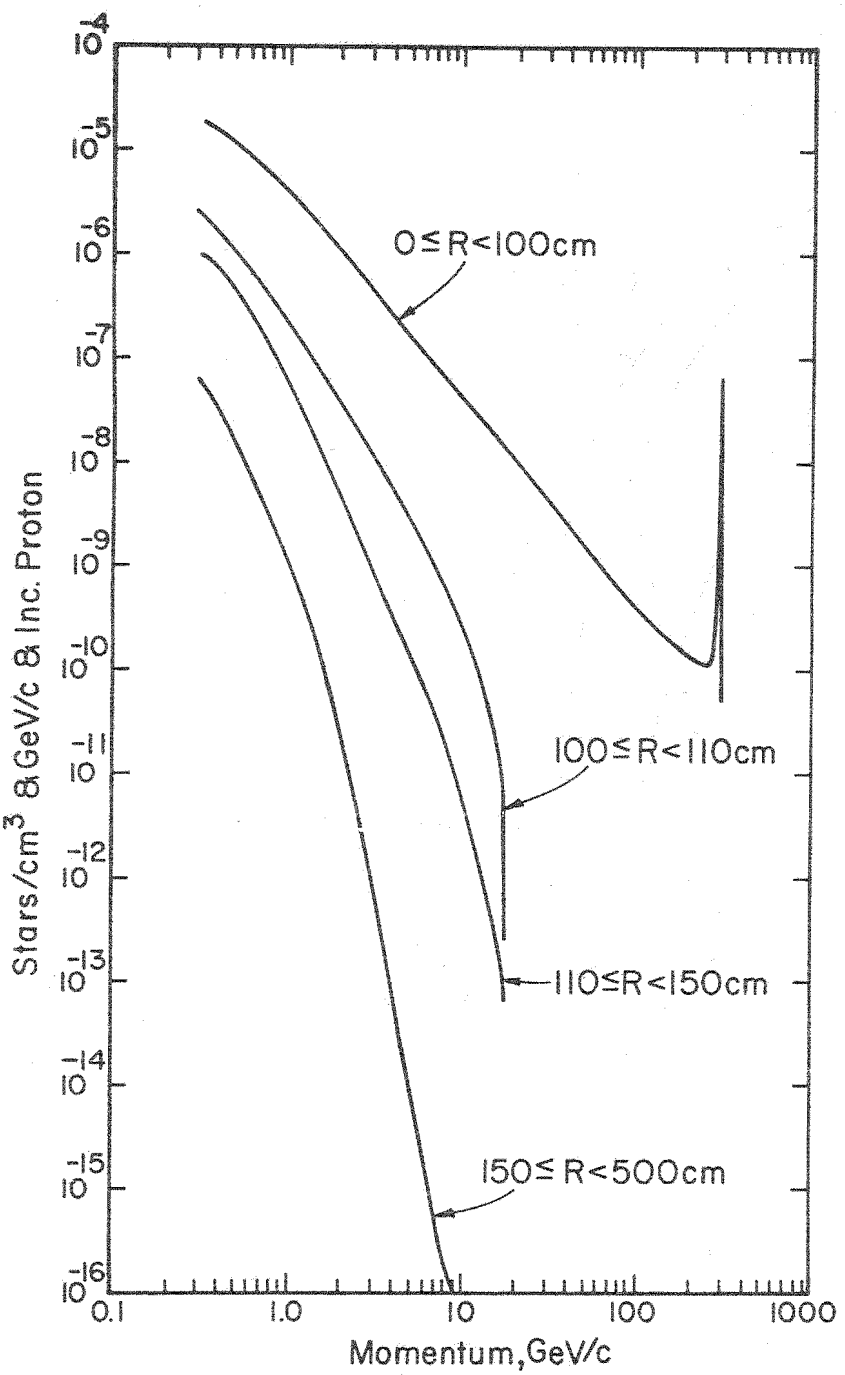

Fig. VIII.43. 300 GeV/c protons incident on a copper target, approximately one interaction length long, placed in a concrete cave represented by a cylindrical tunnel in a large solid cylinder. Momentum spectra of interacting hadrons (stars/cm^3 · GeV/c · inc. proton) between 1250 cm and 2250 cm depth (backwall) in four radial regions. The beam of 0.3 × 0.3 cm cross section is centered on the cylinder axis. The spectra are not calculated below 0.3 GeV/c momentum.

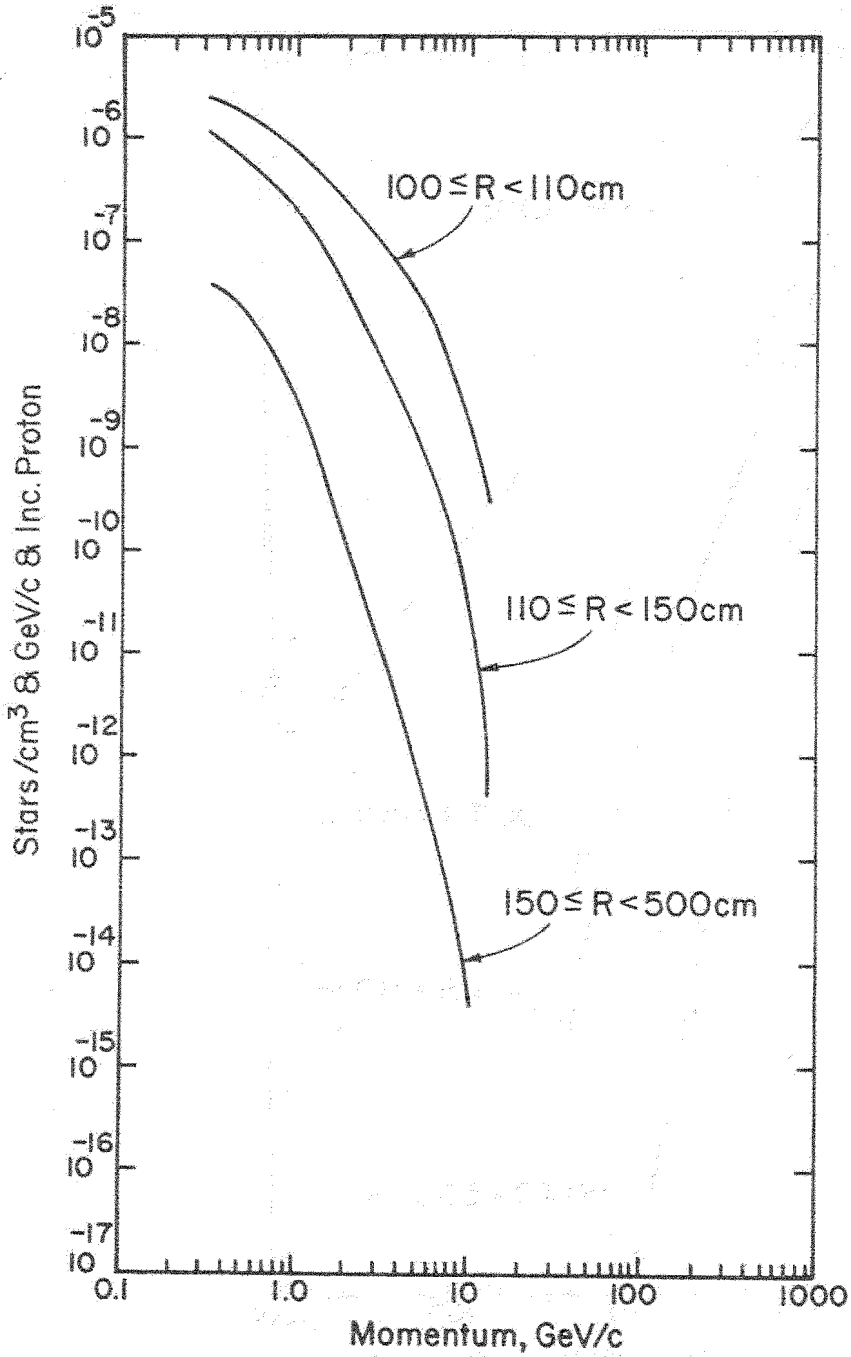

Fig. VIII.44. 1000 GeV/c protons incident on a copper target, approximately one interaction length long, placed in a concrete cave represented by a cylindrical tunnel in a large solid cylinder. Momentum spectra of interacting hadrons (stars/cm^3 · GeV/c · inc. proton) between zero and 1250 cm depth (tunnel region) in three radial regions. The beam of 0.3 × 0.3 cm cross section is centered on the cylinder axis. The spectra are not calculated below 0.3 GeV/c momentum.

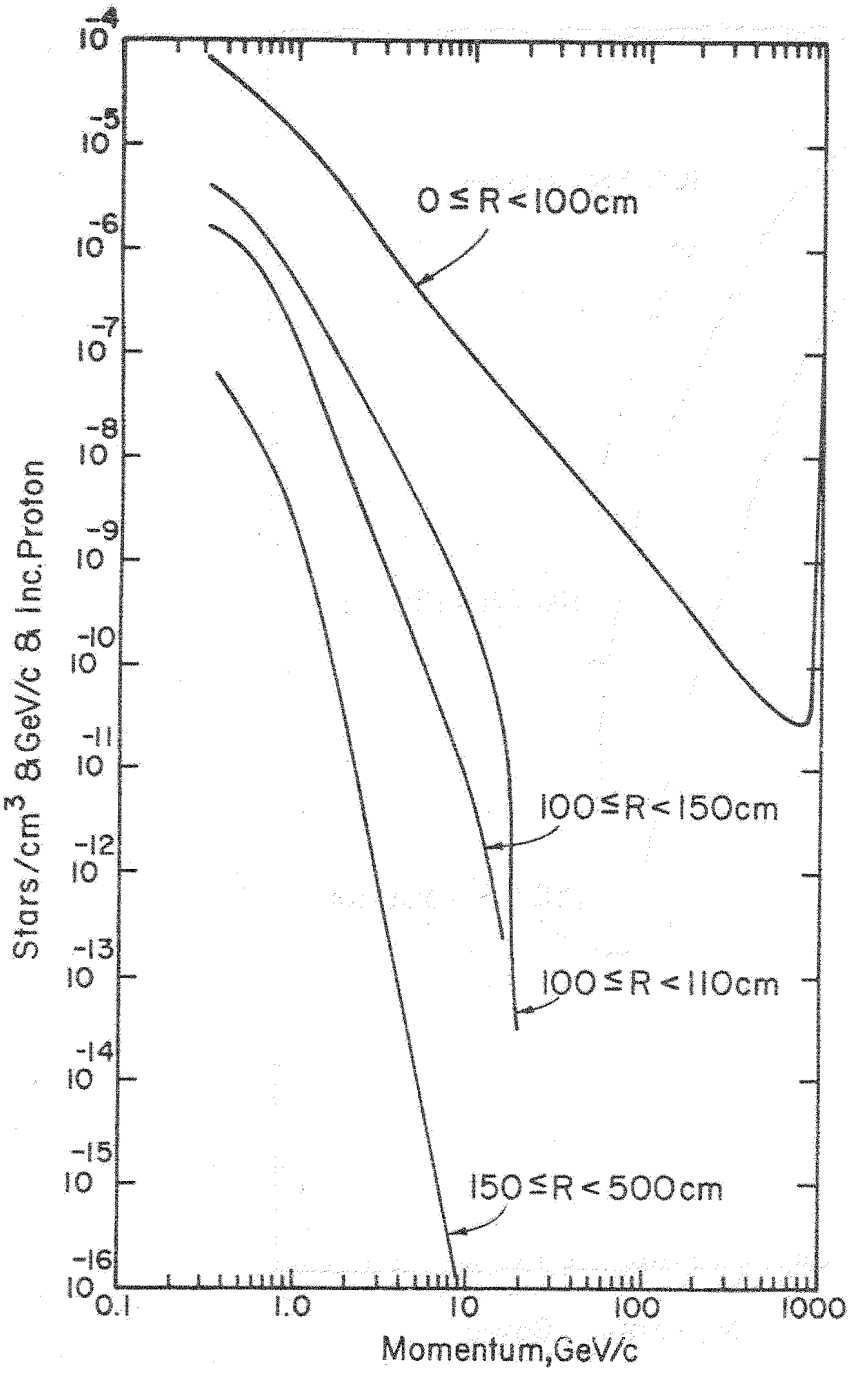

Fig. VIII.45. 1000 GeV/c protons incident on a copper target, approximately one interaction length long, placed in a concrete cave represented by a cylindrical tunnel in a large solid cylinder. Momentum spectra of interacting hadrons (stars/cm^3 · GeV/c · inc. proton) between 1250 cm and 2250 cm depth (backwall) in four radial regions. The beam of 0.3 × 0.3 cm cross section is centered on the cylinder axis. The spectra are not calculated below 0.3 GeV/c momentum.

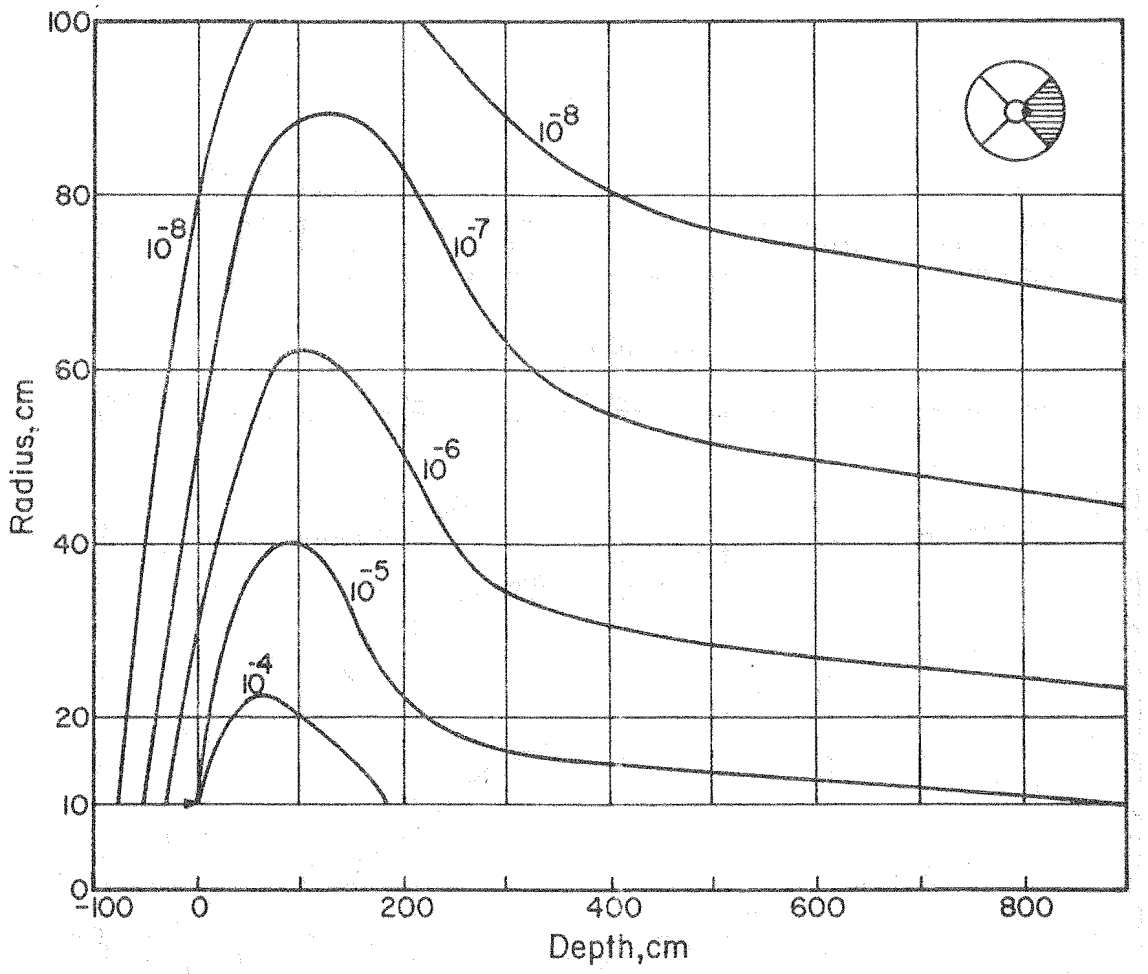

Fig. VIII.46. 30 GeV/c protons incident on the inner wall of an iron pipe (10 cm inner radius). The beam of infinitesimal cross section travels parallel to the pipe axis at an infinitesimal distance into the inner wall and starts to interact at zero depth. Contours of equal star density (stars/cm^3 · inc. proton) for quadrant struck by the beam (see inset). The star density includes only those due to hadrons above 0.3 GeV/cm momentum. Contours of higher star density are not shown for clarity of the plot, those of lower star density are not included due to statistical uncertainty.

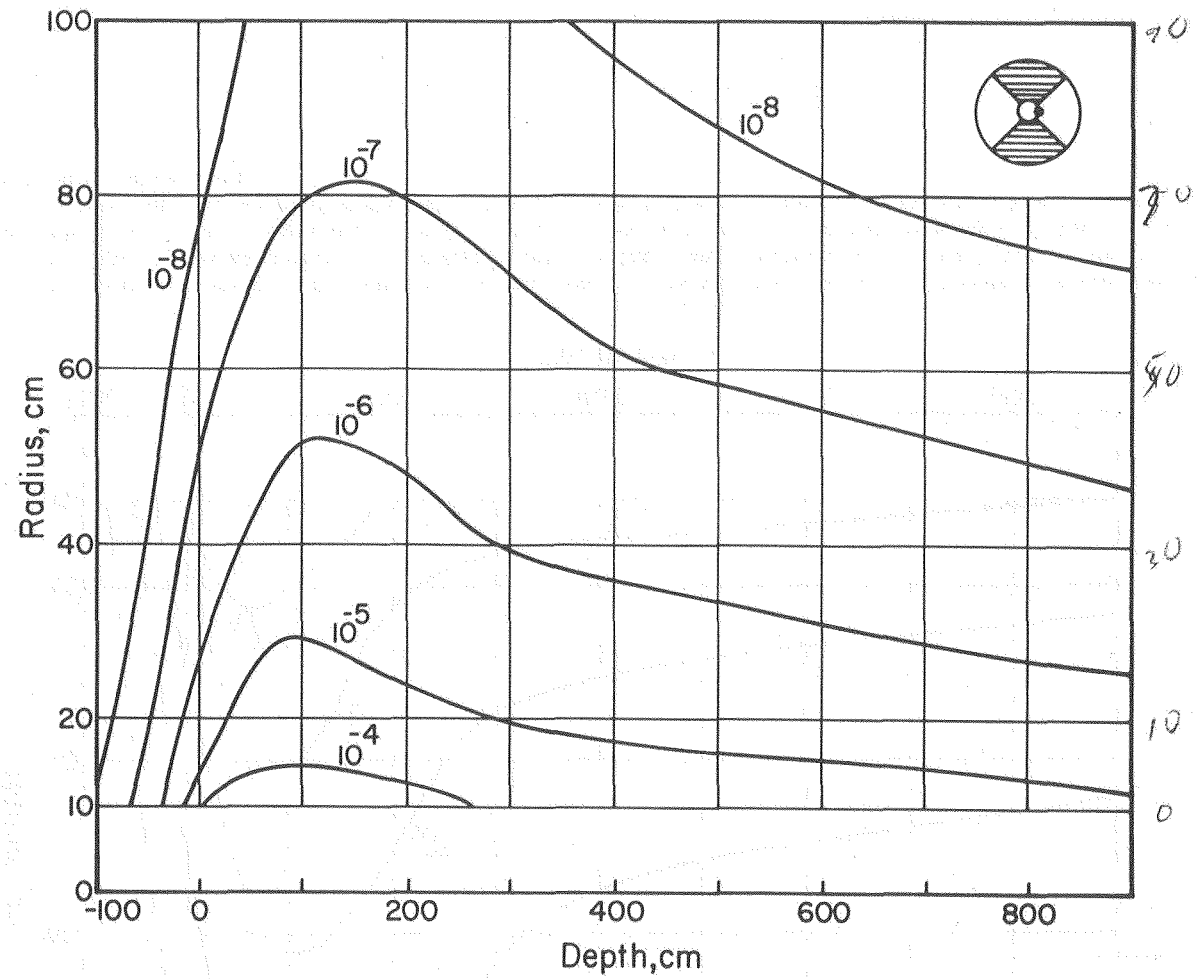

Fig. VIII.47. 30 GeV/c protons incident on the inner wall of an iron pipe (10 cm inner radius). The beam of infinitesimal cross section travels parallel to the pipe axis at an infinitesimal distance into the inner wall and starts to interact at zero depth. Contours of equal star density (stars/cm^3 · inc. proton) for quadrant centered at right angles to the beam (see inset). The star density includes only those due to hadrons above 0.3 GeV/cm momentum. Contours of higher star density are not shown for clarity of the plot, those of lower star density are not included due to statistical uncertainty.

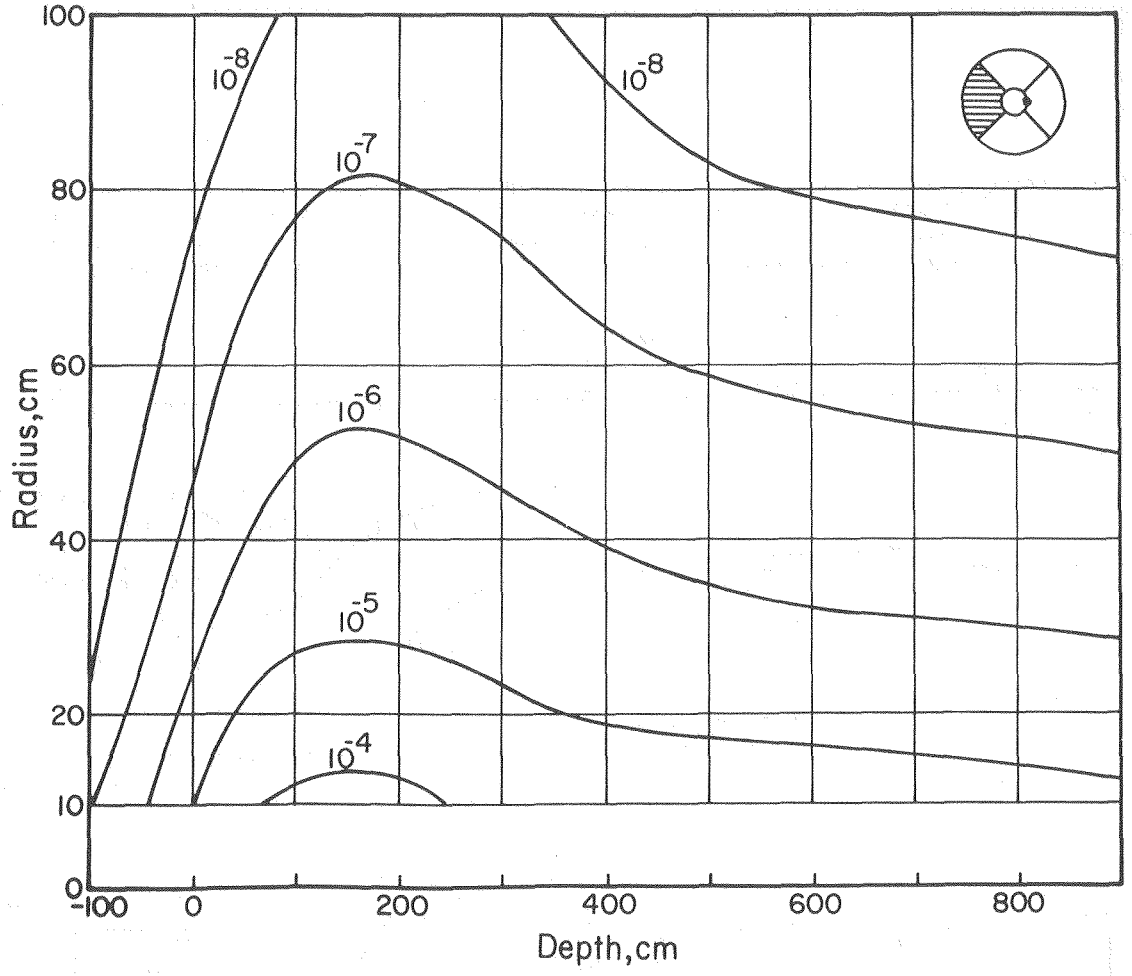

Fig. VIII.48. 30 GeV/c protons incident on the inner wall of an iron pipe (10 cm inner radius). The beam of infinitesimal cross section travels parallel to the pipe axis at an infinitesimal distance into the inner wall and starts to interact at zero depth. Contours of equal star density (stars/cm^3 · inc. proton) for quadrant opposite the beam (see inset). The star density includes only those due to hadrons above 0.3 GeV/cm momentum. Contours of higher star density are not shown for clarity of the plot, those of lower star density are not included due to statistical uncertainty.

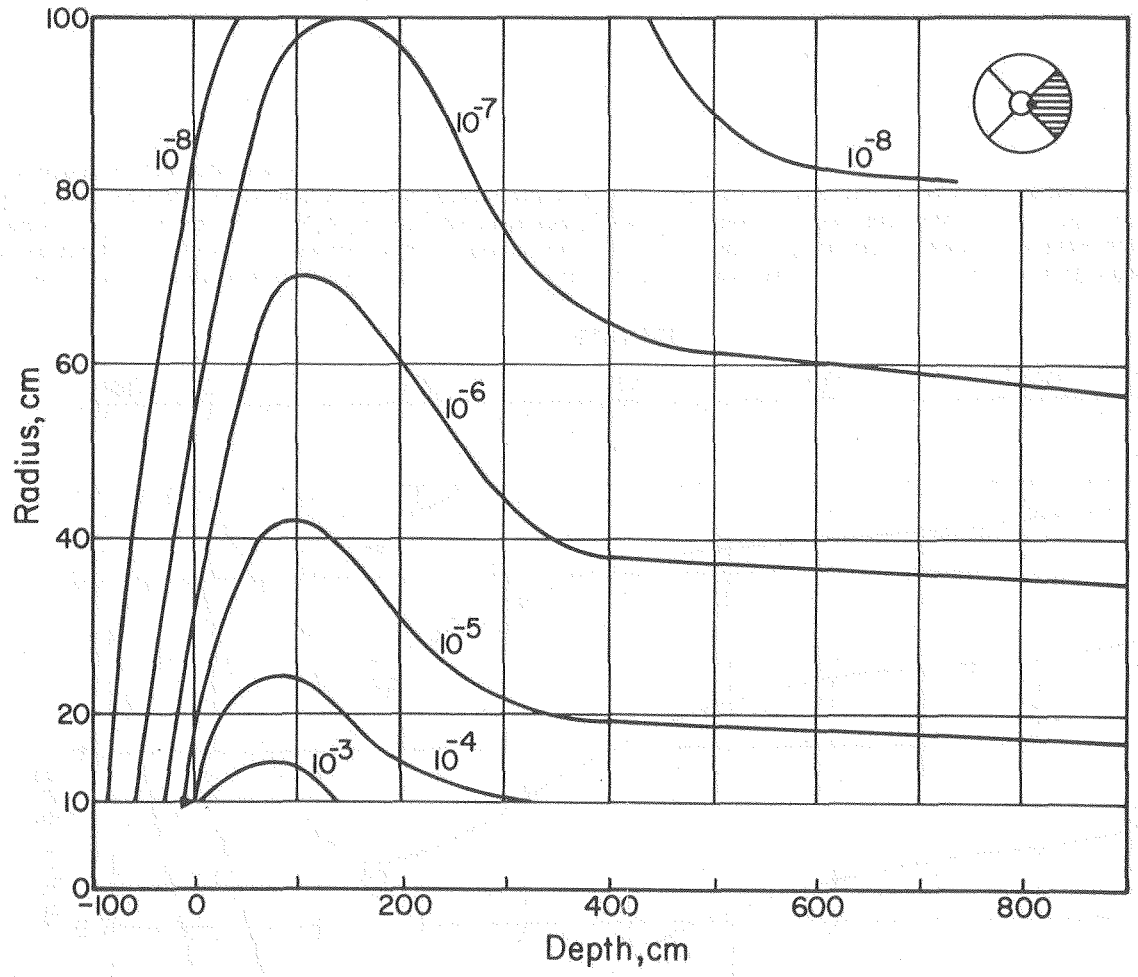

Fig. VIII.49. 100 GeV/c protons incident on the inner wall of an iron pipe (10 cm inner radius). The beam of infinitesimal cross section travels parallel to the pipe axis at an infinitesimal distance into the inner wall and starts to interact at zero depth. Contours of equal star density (stars/cm^3 · inc. proton) for quadrant struck by the beam (see inset). The star density includes only those due to hadrons above 0.3 GeV/cm momentum. Contours of higher star density are not shown for clarity of the plot, those of lower star density are not included due to statistical uncertainty.

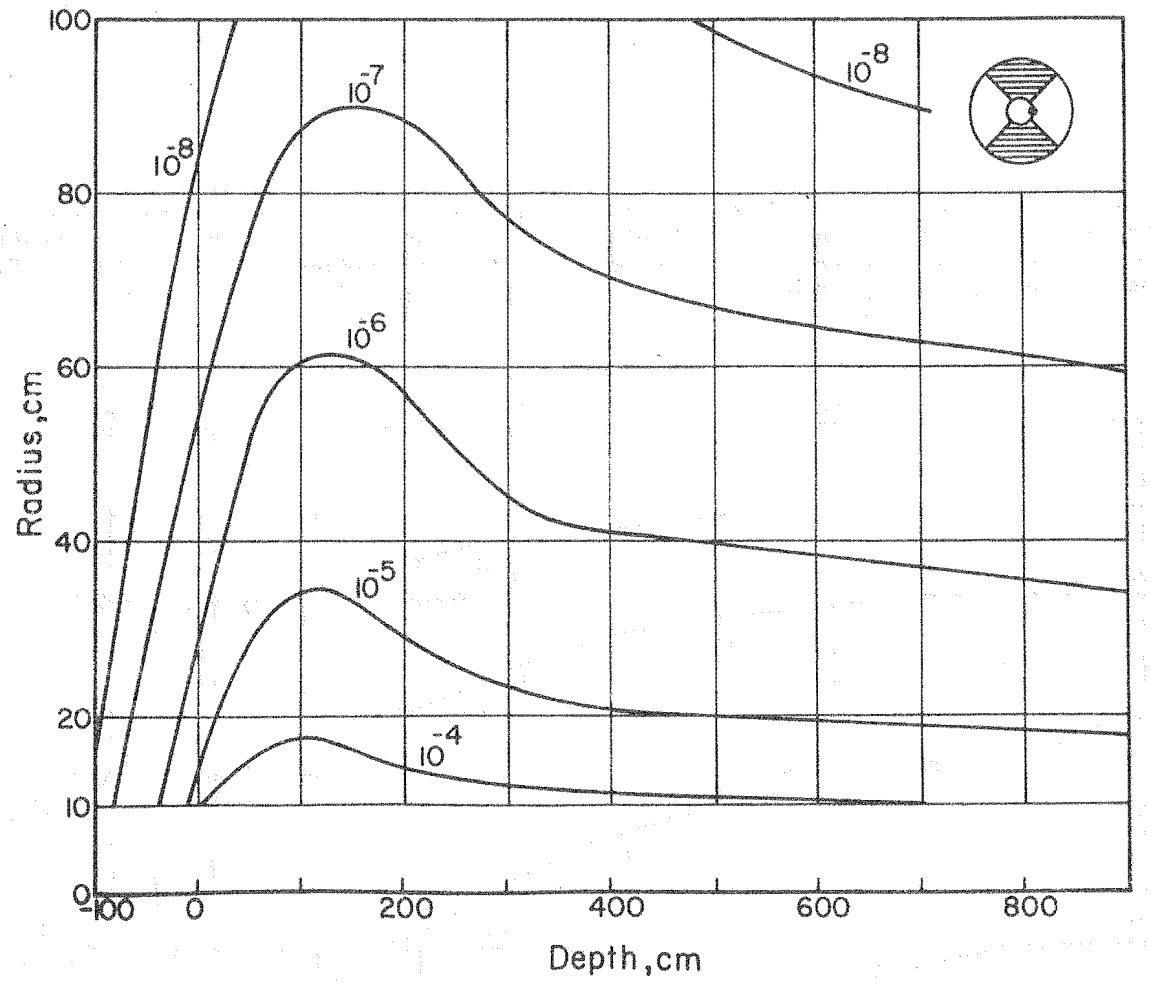

Fig. VIII.50. 100 GeV/c protons incident on the inner wall of an iron pipe (10 cm inner radius). The beam of infinitesimal cross section travels parallel to the pipe axis at an infinitesimal distance into the inner wall and starts to interact at zero depth. Contours of equal star density (stars/cm^3 · inc. proton) for quadrant centered at right angles to the beam (see inset). The star density includes only those due to hadrons above 0.3 GeV/cm momentum. Contours of higher star density are not shown for clarity of the plot, those of lower star density are not included due to statistical uncertainty.

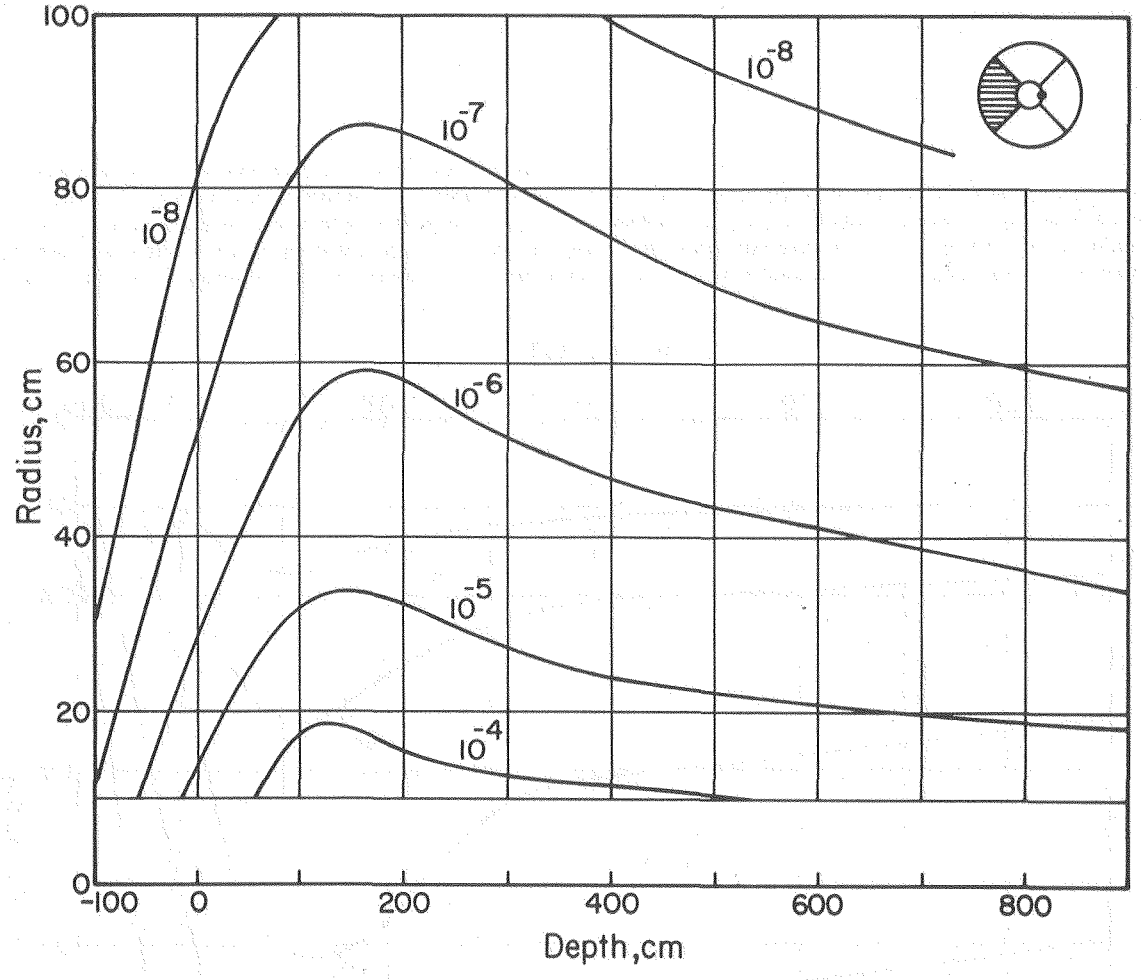

Fig. VIII.51. 100 GeV/c protons incident on the inner wall of an iron pipe (10 cm inner radius). The beam of infinitesimal cross section travels parallel to the pipe axis at an infinitesimal distance into the inner wall and starts to interact at zero depth. Contours of equal star density (stars/cm^3 · inc. proton) for quadrant opposite the beam (see inset). The star density includes only those due to hadrons above 0.3 GeV/cm momentum. Contours of higher star density are not shown for clarity of the plot, those of lower star density are not included due to statistical uncertainty.

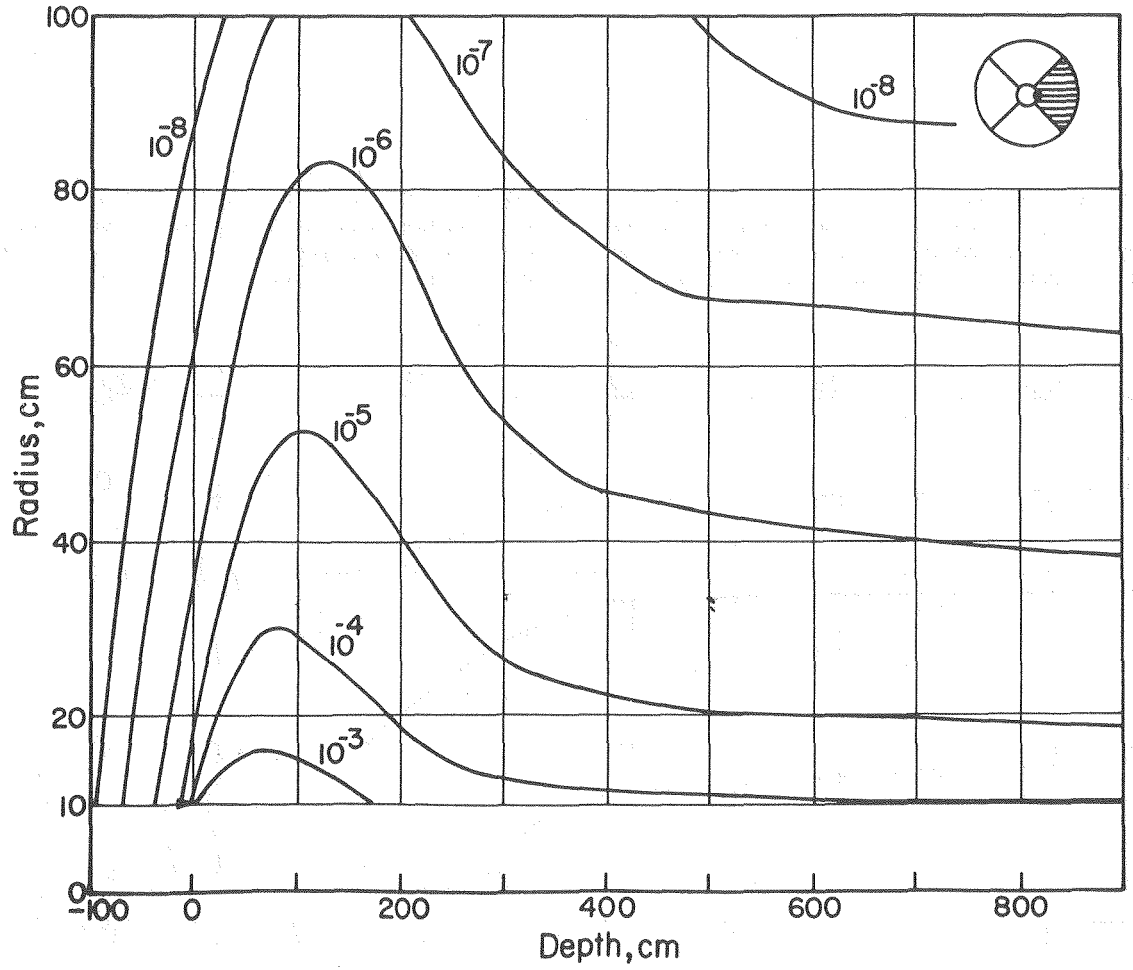

Fig. VIII.52. 300 GeV/c protons incident on the inner wall of an iron pipe (10 cm inner radius). The beam of infinitesimal cross section travels parallel to the pipe axis at an infinitesimal distance into the inner wall and starts to interact at zero depth. Contours of equal star density (stars/cm^3 · inc. proton) for quadrant struck by the beam (see inset). The star density includes only those due to hadrons above 0.3 GeV/cm momentum. Contours of higher star density are not shown for clarity of the plot, those of lower star density are not included due to statistical uncertainty.

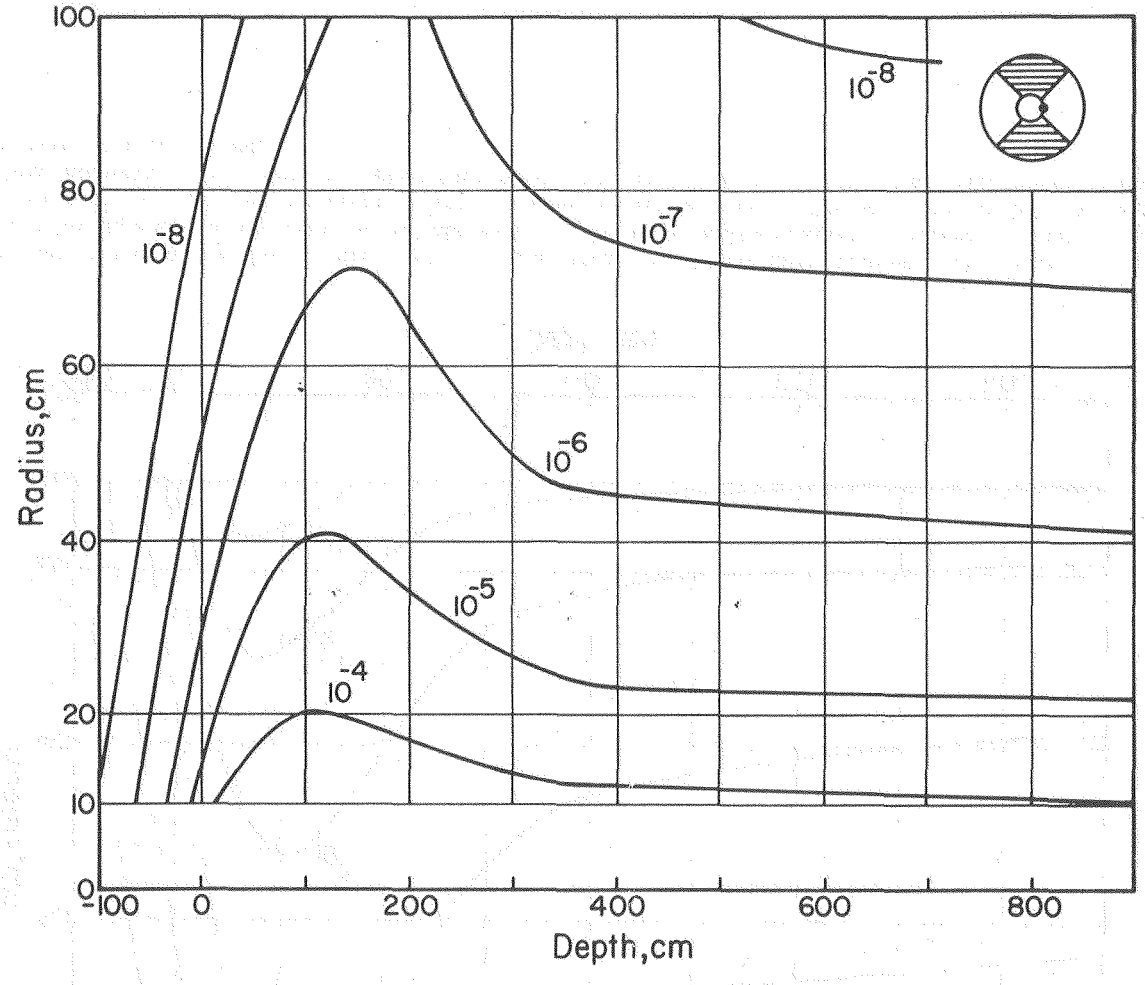

Fig. VIII.53. 300 GeV/c protons incident on the inner wall of an iron pipe (10 cm inner radius). The beam of infinitesimal cross section travels parallel to the pipe axis at an infinitesimal distance into the inner wall and starts to interact at zero depth. Contours of equal star density (stars/cm^3 · inc. proton) for quadrant centered at right angles to the beam (see inset). The star density includes only those due to hadrons above 0.3 GeV/cm momentum. Contours of higher star density are not shown for clarity of the plot, those of lower star density are not included due to statistical uncertainty.

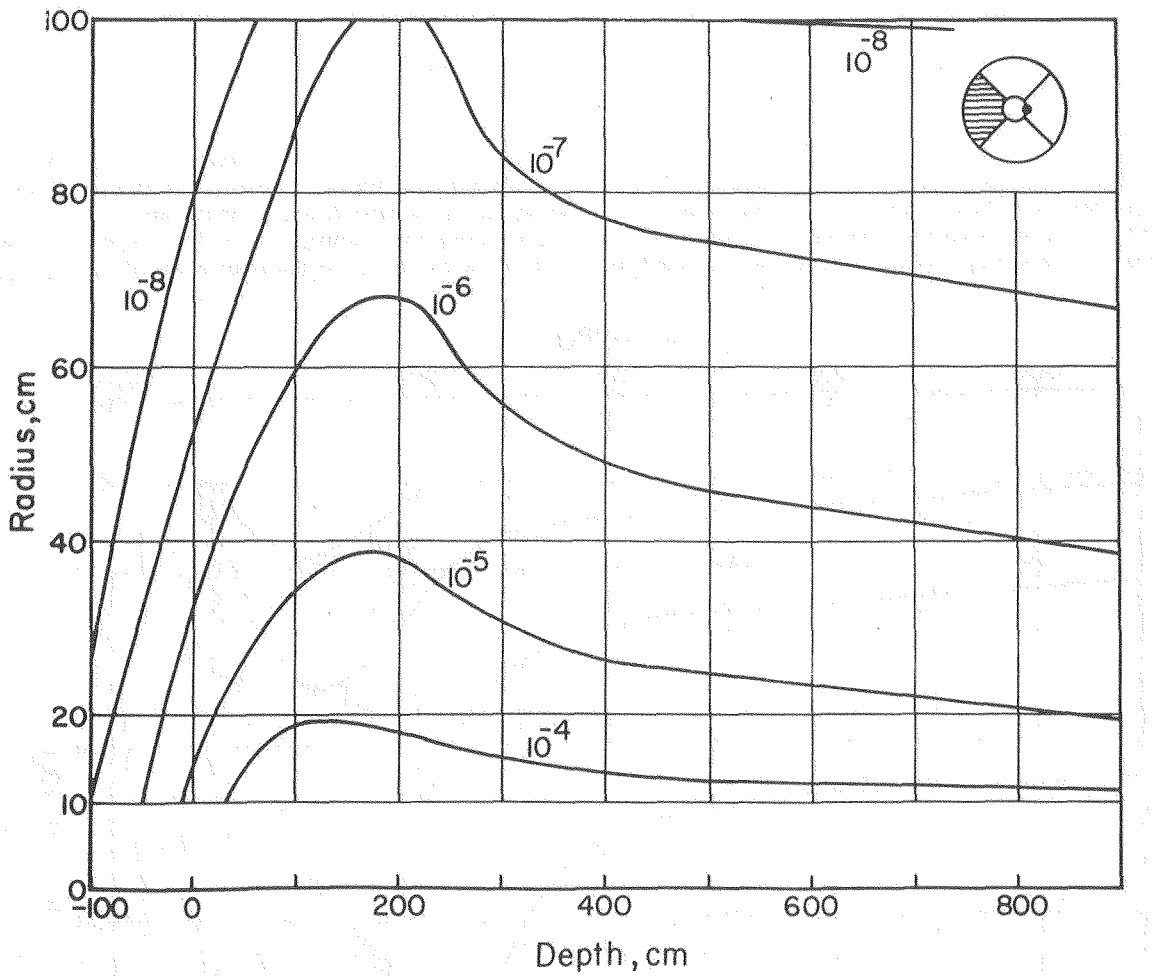

Fig. VIII.54. 300 GeV/c protons incident on the inner wall of an iron pipe (10 cm inner radius). The beam of infinitesimal cross section travels parallel to the pipe axis at an infinitesimal distance into the inner wall and starts to interact at zero depth. Contours of equal star density (stars/cm^3 · inc. proton) for quadrant opposite the beam (see inset). The star density includes only those due to hadrons above 0.3 GeV/cm momentum. Contours of higher star density are not shown for clarity of the plot, those of lower star density are not included due to statistical uncertainty.

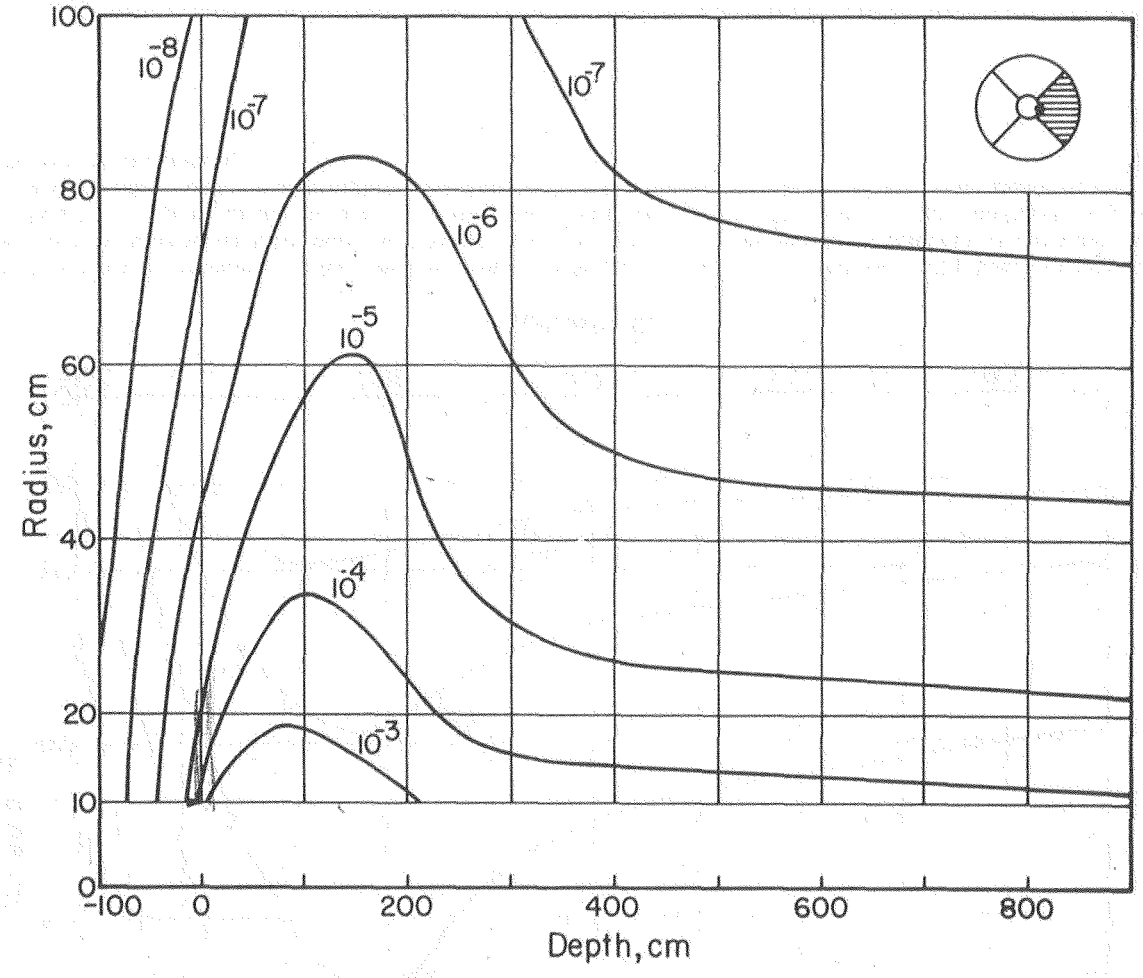

Fig. VIII.55. 1000 GeV/c protons incident on the inner wall of an iron pipe (10 cm inner radius). The beam of infinitesimal cross section travels parallel to the pipe axis at an infinitesimal distance into the inner wall and starts to interact at zero depth. Contours of equal star density (stars/cm^3 · inc. proton) for quadrant struck by the beam (see inset). The star density includes only those due to hadrons above 0.3 GeV/cm momentum. Contours of higher star density are not shown for clarity of the plot, those of lower star density are not included due to statistical uncertainty.

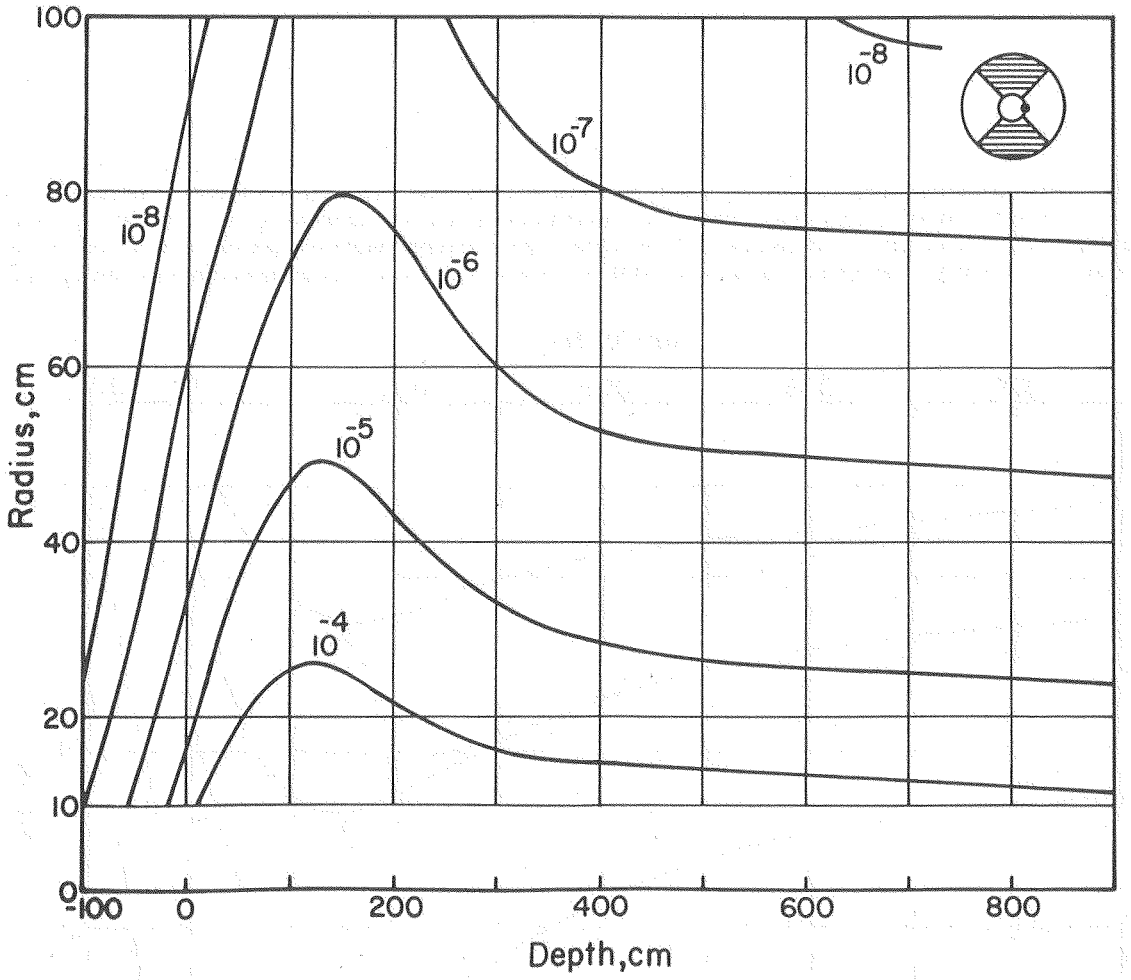

Fig. VIII.56. 1000 GeV/c protons incident on the inner wall of an iron pipe (10 cm inner radius). The beam of infinitesimal cross section travels parallel to the pipe axis at an infinitesimal distance into the inner wall and starts to interact at zero depth. Contours of equal star density (stars/cm^3 · inc. proton) for quadrant centered at right angles to the beam (see inset). The star density includes only those due to hadrons above 0.3 GeV/cm momentum. Contours of higher star density are not shown for clarity of the plot, those of lower star density are not included due to statistical uncertainty.

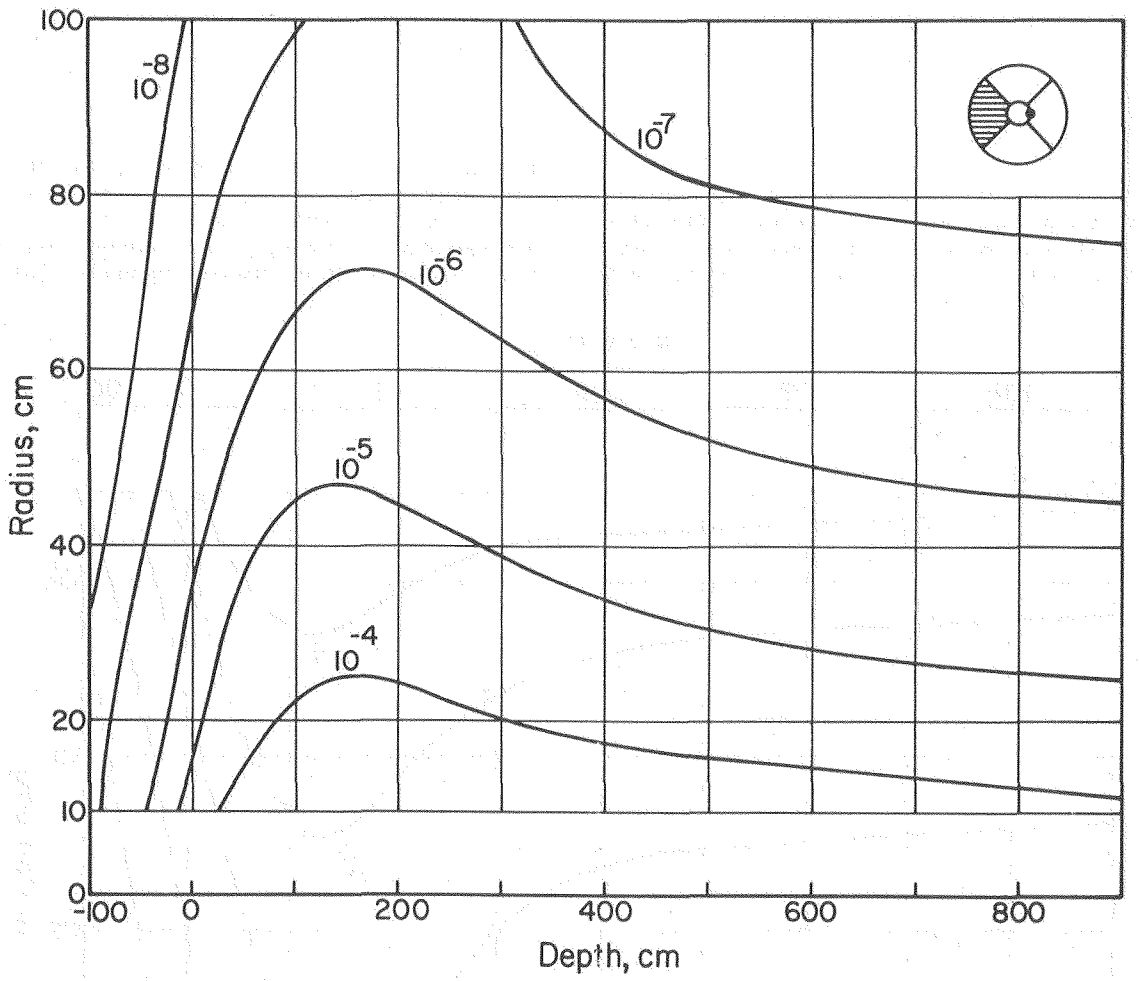

Fig. VIII.57. 1000 GeV/c protons incident on the inner wall of an iron pipe (10 cm inner radius). The beam of infinitesimal cross section travels parallel to the pipe axis at an infinitesimal distance into the inner wall and starts to interact at zero depth. Contours of equal star density (stars/cm^3 · inc. proton) for quadrant opposite the beam (see inset). The star density includes only those due to hadrons above 0.3 GeV/cm momentum. Contours of higher star density are not shown for clarity of the plot, those of lower star density are not included due to statistical uncertainty.

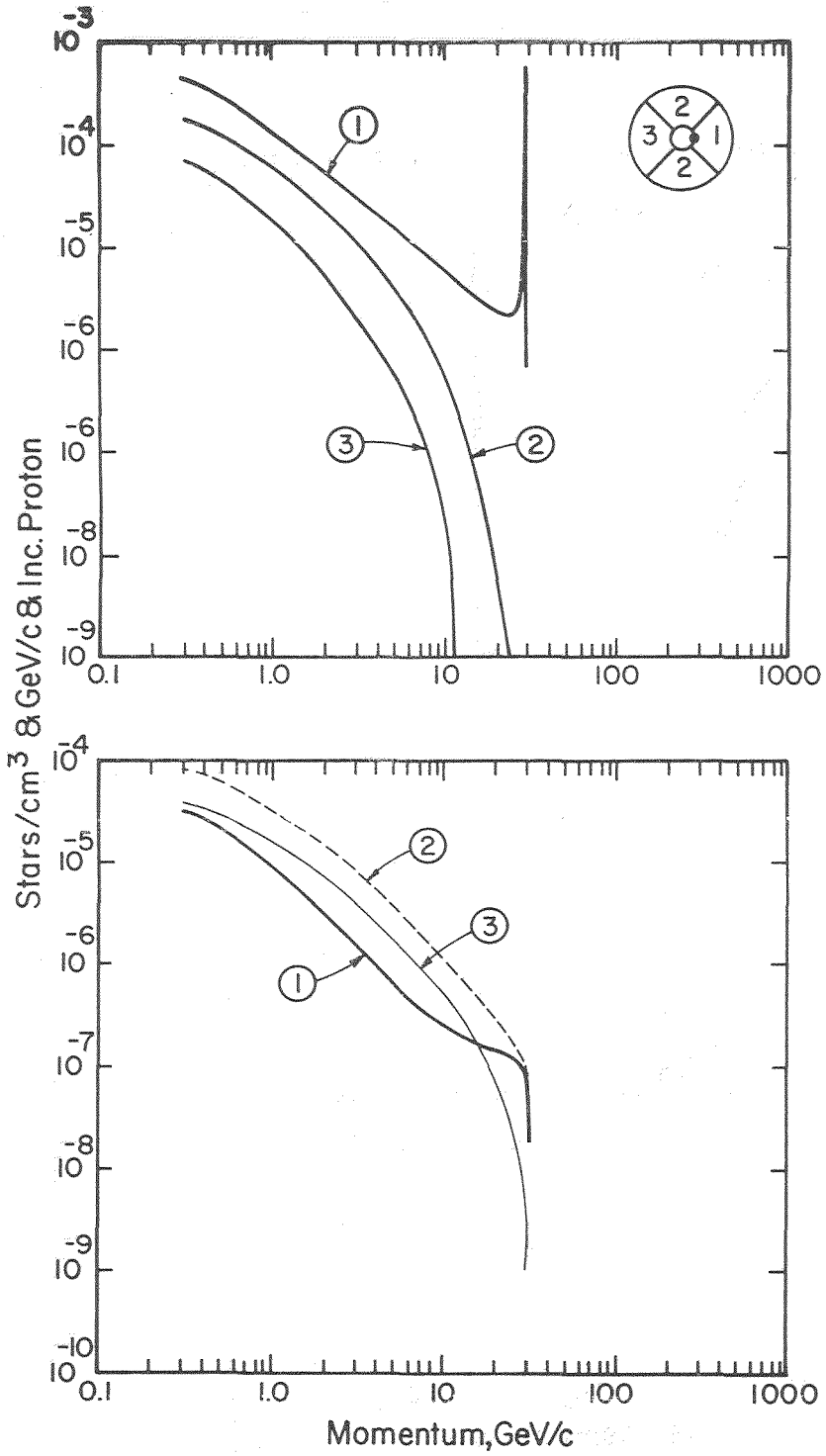

Fig. VIII.58. 30 GeV/c protons incident on the inner wall of an iron pipe (10 cm inner radius). The beam of infinitesimal cross section travels parallel to the pipe axis at an infinitesimal distance into the inner wall. Momentum spectra of interacting hadrons (stars/cm^3 · GeV/c · inc. proton) for the radial region between 10 cm and 12 cm from the axis (zero and 2 cm from the inner wall) for each quadrant (see inset) and for depths between zero and 200 cm (above) and between 200 cm and 900 cm (below). The spectra are not calculated below 0.3 GeV/c momentum.

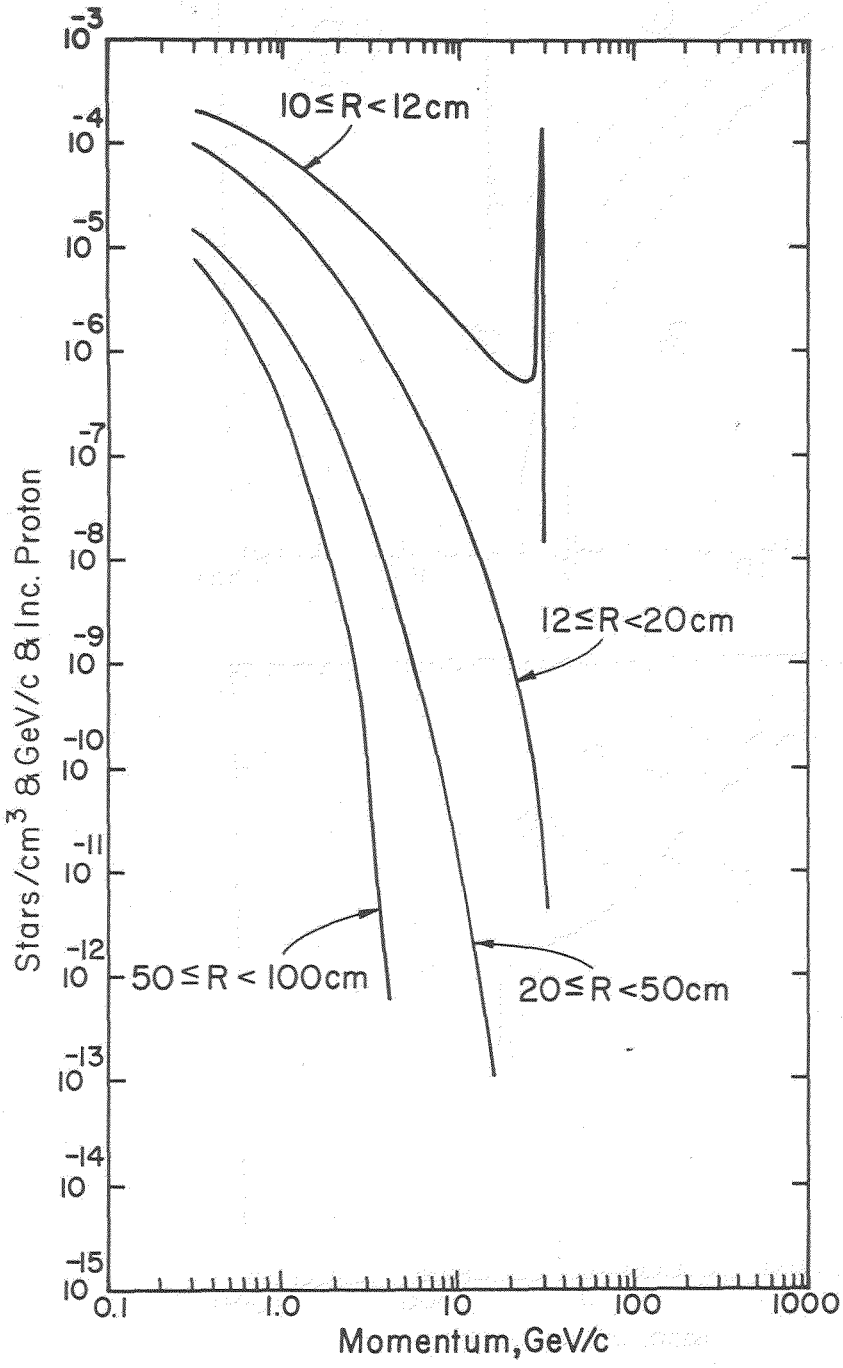

Fig. VIII.59. 30 GeV/c protons incident on inner wall of an iron pipe (10 cm inner radius). The beam of infinitesimal cross section travels parallel to the pipe axis at an infinitesimal distance into the inner wall. Momentum spectra of interacting hadrons (stars/cm^3 · GeV/c · inc. proton) for four radial regions averaged over azimuth and for depths between zero and 200 cm. The spectra are not calculated below 0.3 GeV/c momentum.

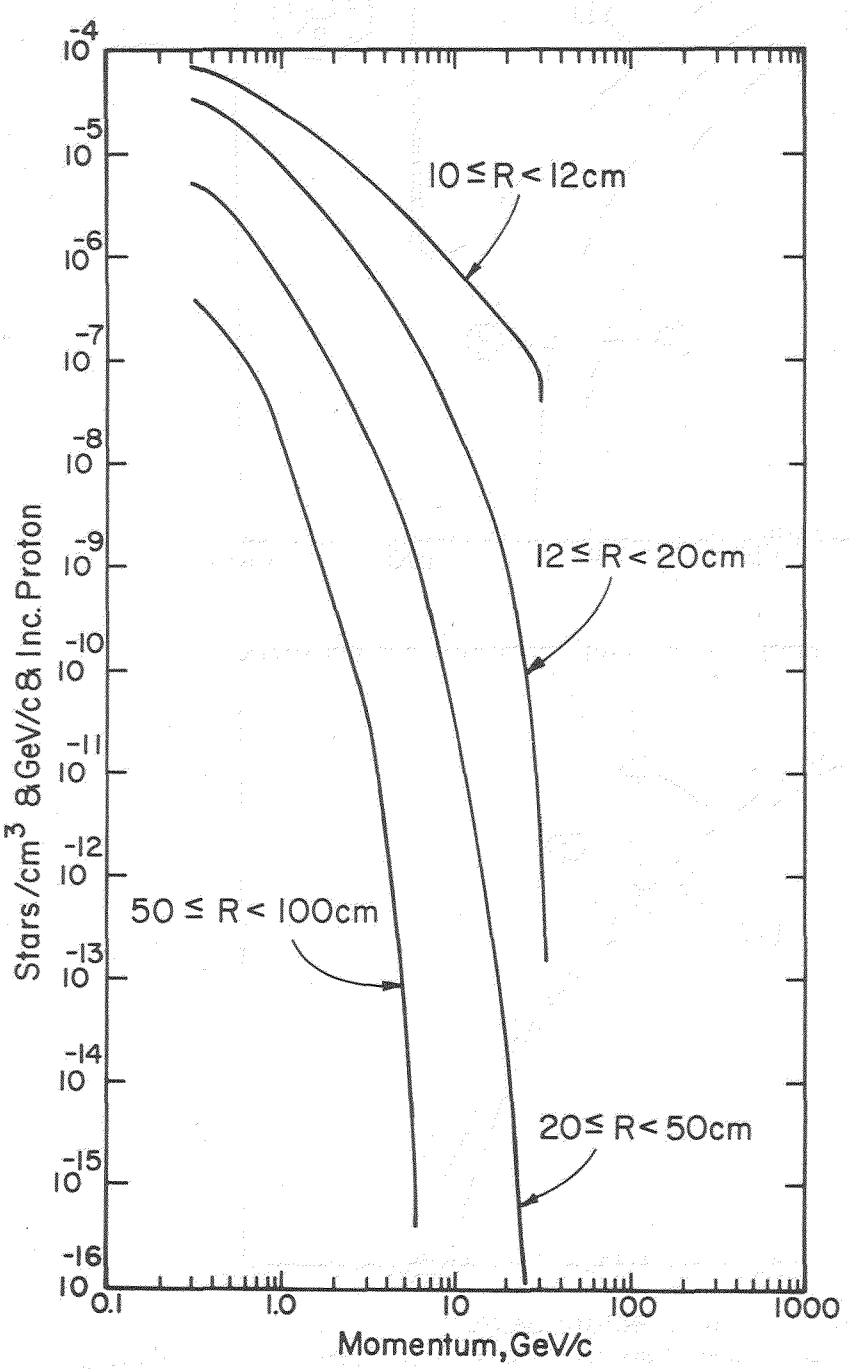

Fig. VIII.60. 30 GeV/c protons incident on inner wall of an iron pipe (10 cm inner radius). The beam of infinitesimal cross section travels parallel to the pipe axis at an infinitesimal distance into the inner wall. Momentum spectra of interacting hadrons (stars/cm^3 · GeV/c · inc. proton) for four radial regions averaged over azimuth and for depths between 200 cm and 900 cm. The spectra are not calculated below 0.3 GeV/c momentum.

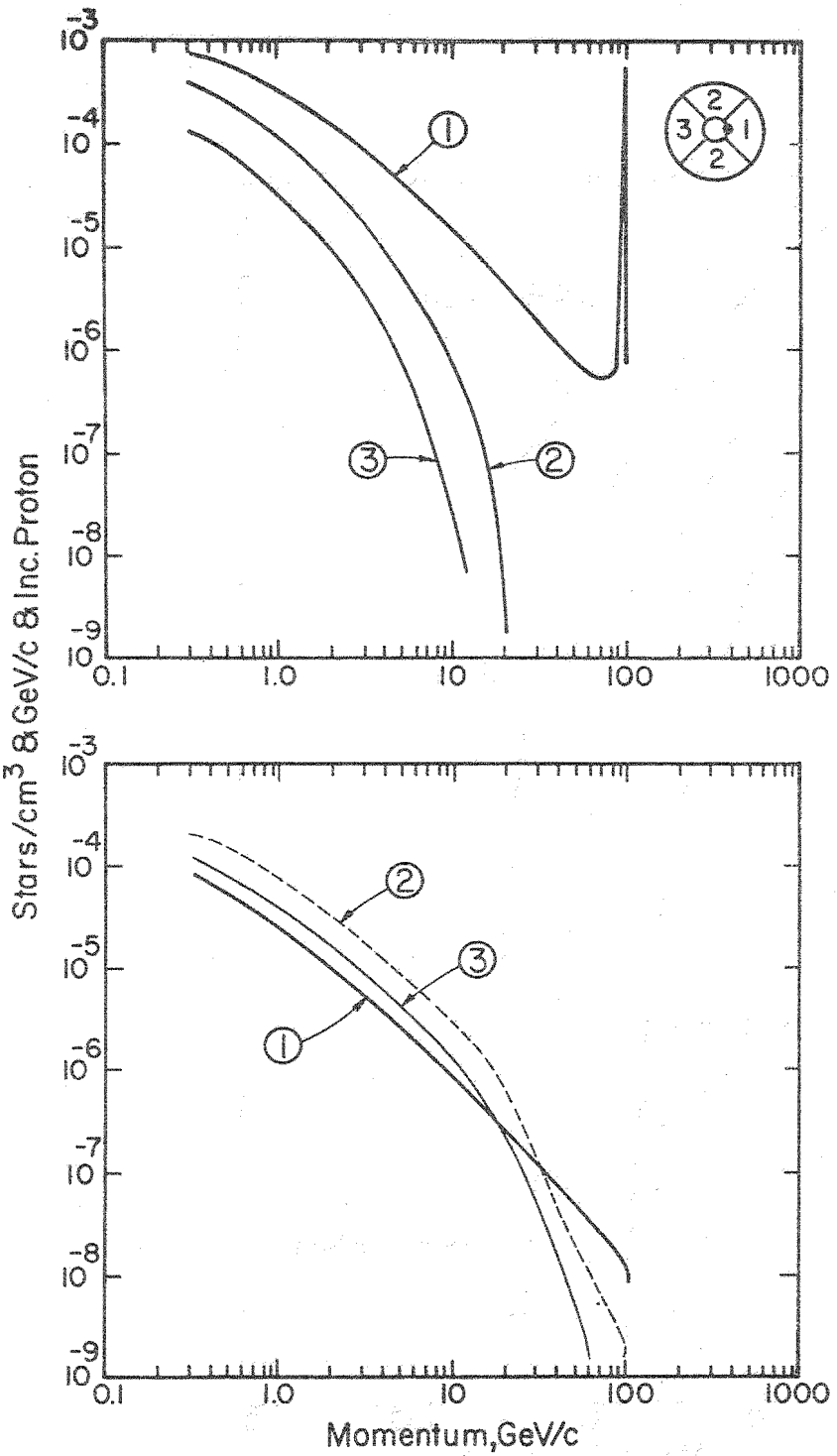

Fig. VIII.61. 100 GeV/c protons incident on the inner wall of an iron pipe (10 cm inner radius). The beam of infinitesimal cross section travels parallel to the pipe axis at an infinitesimal distance into the inner wall. Momentum spectra of interacting hadrons (stars/cm^3 · GeV/c · inc. proton) for the radial region between 10 cm and 12 cm from the axis (zero and 2 cm from the inner wall) for each quadrant (see inset) and for depths between zero and 200 cm (above) and between 200 cm and 900 cm (below). The spectra are not calculated below 0.3 GeV/c momentum.

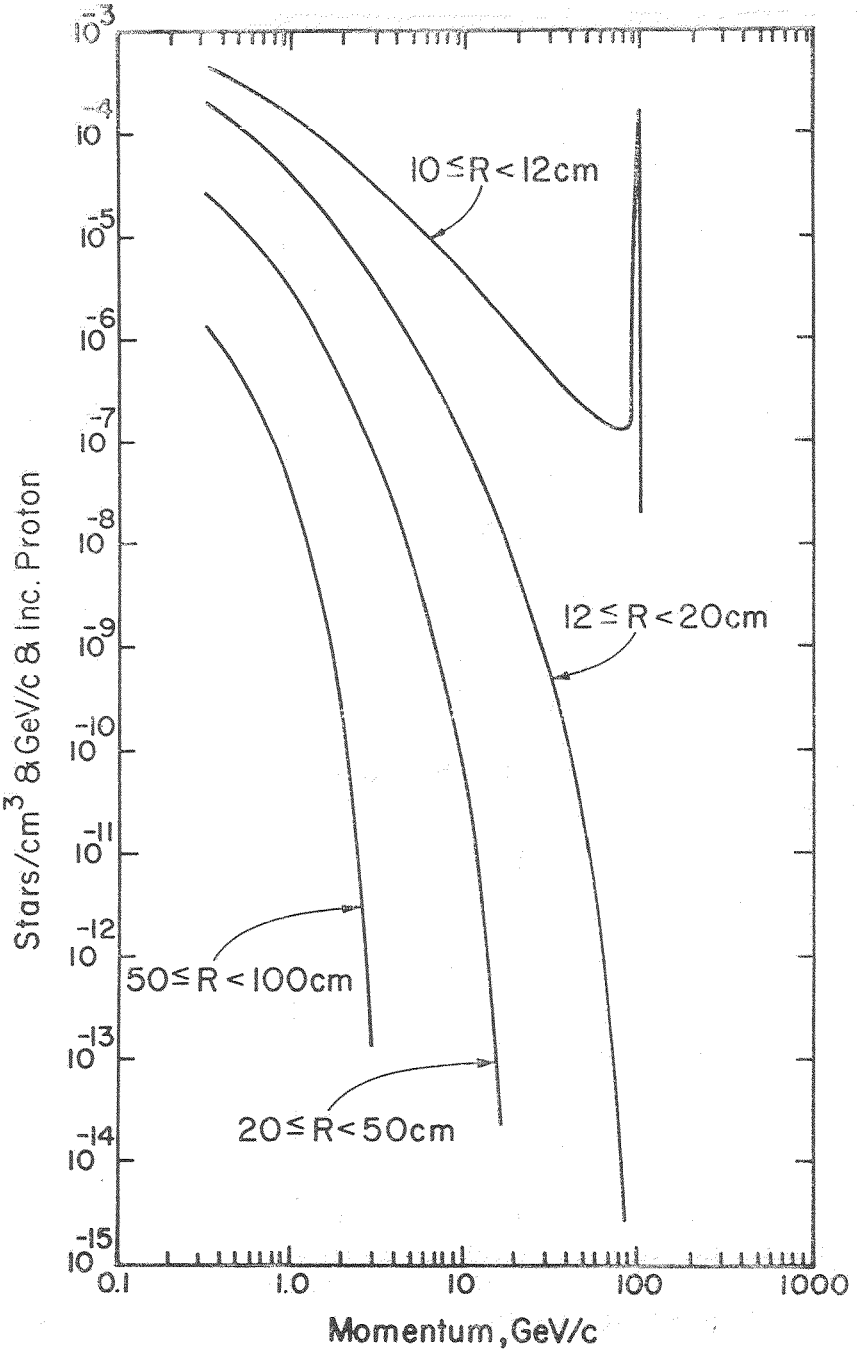

Fig. VIII.62. 100 GeV/c protons incident on inner wall of an iron pipe (10 cm inner radius). The beam of infinitesimal cross section travels parallel to the pipe axis at an infinitesimal distance into the inner wall. Momentum spectra of interacting hadrons (stars/cm^3 · GeV/c · inc. proton) for four radial regions averaged over azimuth for depths between zero and 200 cm. The spectra are not calculated below 0.3 GeV/c momentum.

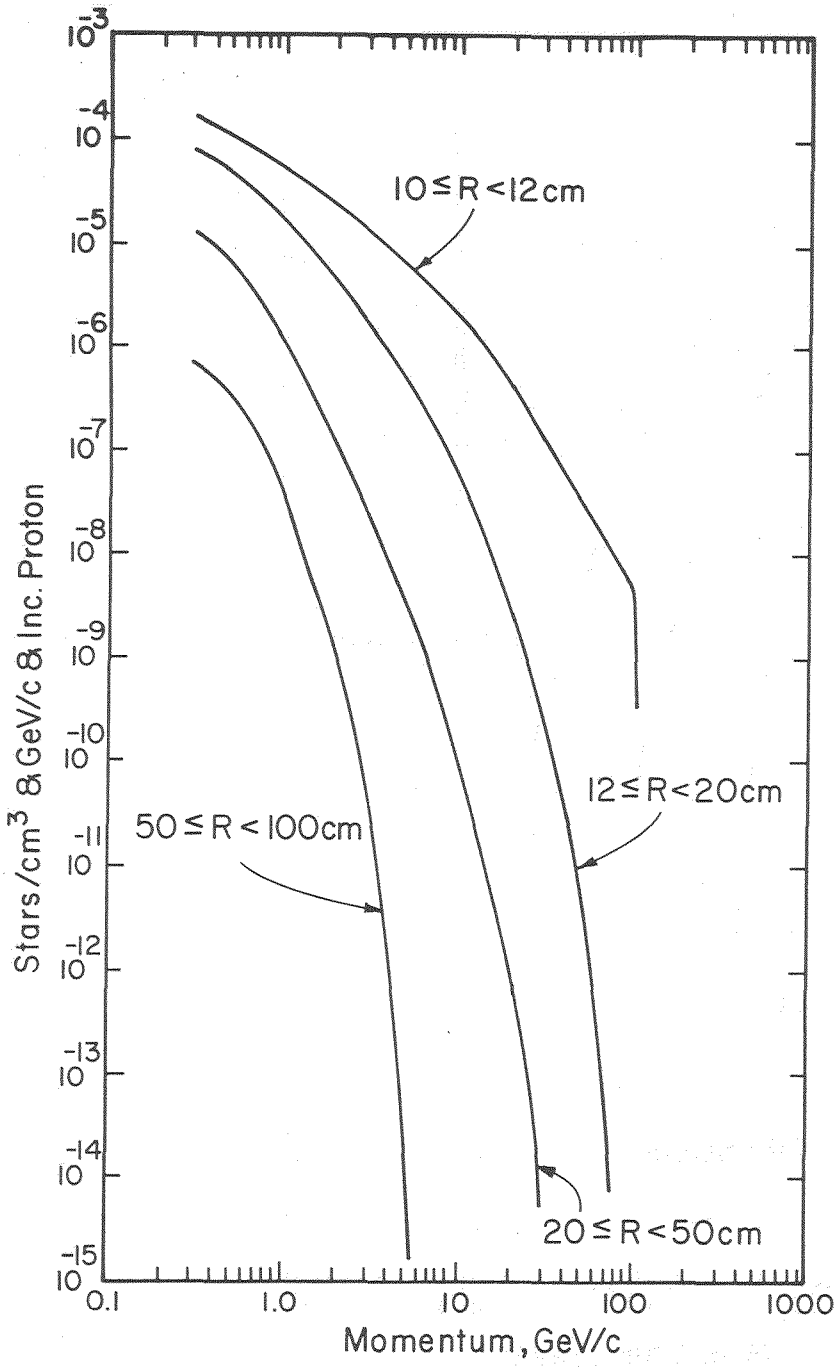

Fig. VIII.63. 100 GeV/c protons incident on inner wall of an iron pipe (10 cm inner radius). The beam of infinitesimal cross section travels parallel to the pipe axis at an infinitesimal distance into the inner wall. Momentum spectra of interacting hadrons (stars/cm^3 · GeV/c · inc. proton) for four radial regions averaged over azimuth and for depths between 200 cm and 900 cm. The spectra are not calculated below 0.3 GeV/c momentum.

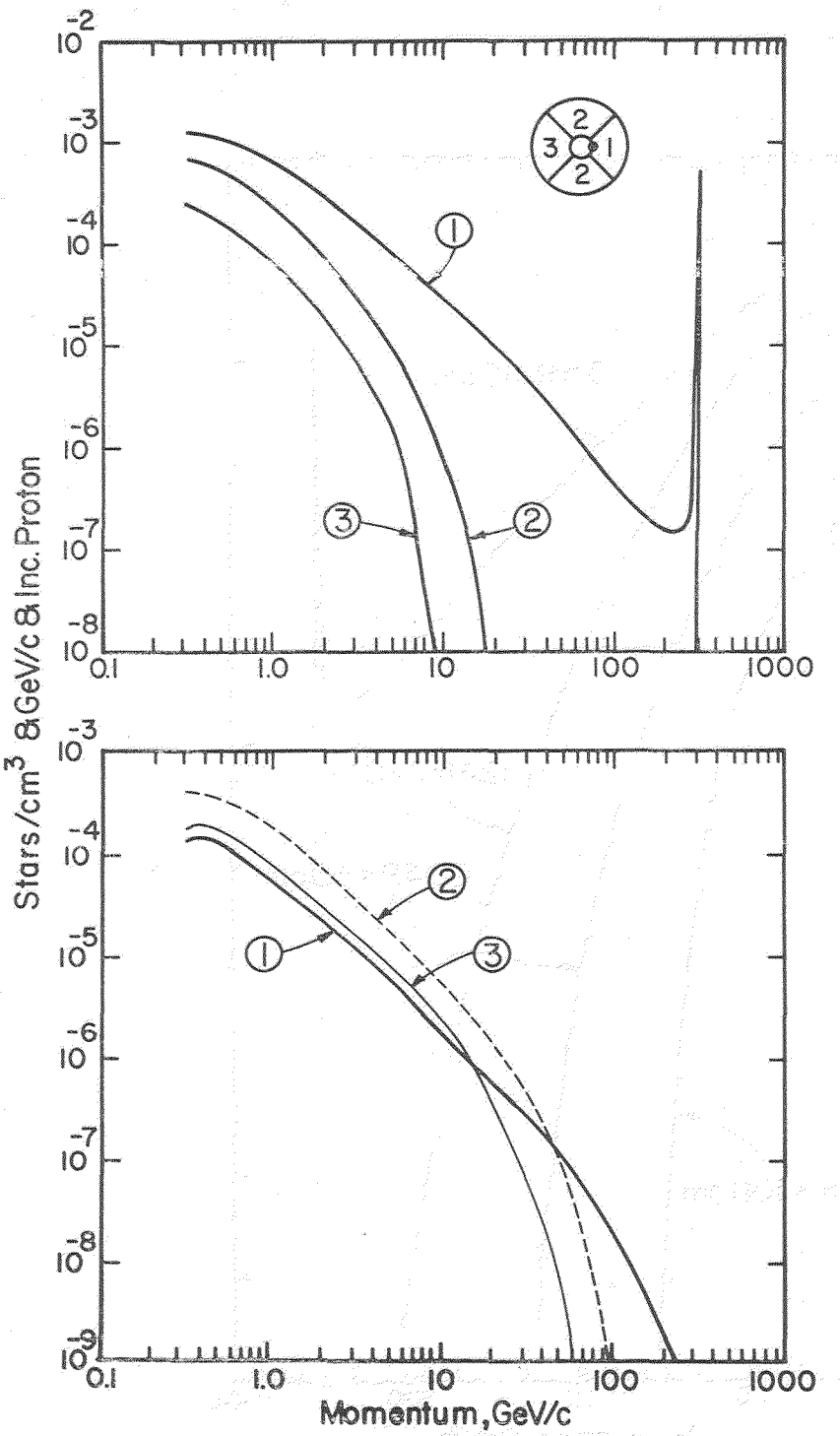

Fig. VIII.64. 300 GeV/c protons incident on the inner wall of an iron pipe (10 cm inner radius). The beam of infinitesimal cross section travels parallel to the pipe axis at an infinitesimal distance into the inner wall. Momentum spectra of interacting hadrons (stars/cm^3 · GeV/c · inc. proton) for the radial regions between 10 cm and 12 cm from the axis (zero and 2 cm from the inner wall for each quadrant (see inset) and for depths between zero and 200 cm (above) and between 200 cm and 900 cm (below). The spectra are not calculated below 0.3 GeV/c momentum.

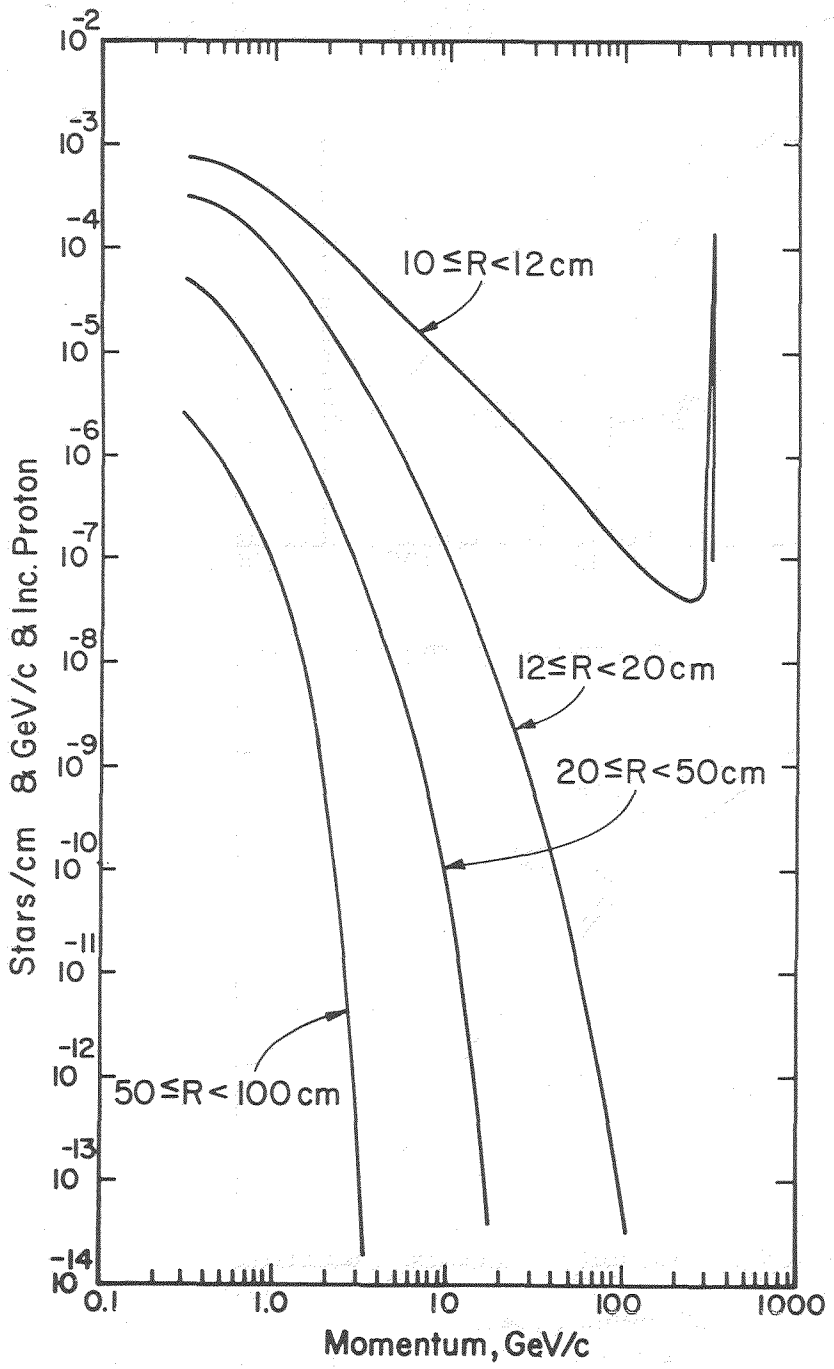

Fig. VIII.65. 300 GeV/c protons incident on inner wall of an iron pipe (10 cm inner radius). The beam of infinitesimal cross section travels parallel to the pipe axis at an infinitesimal distance into the inner wall. Momentum spectra of interacting hadrons (stars/cm^3 · GeV/c · inc. proton) for four radial regions averaged over azimuth and for depths between zero and 200 cm. The spectra are not calculated below 0.3 GeV/c momentum.

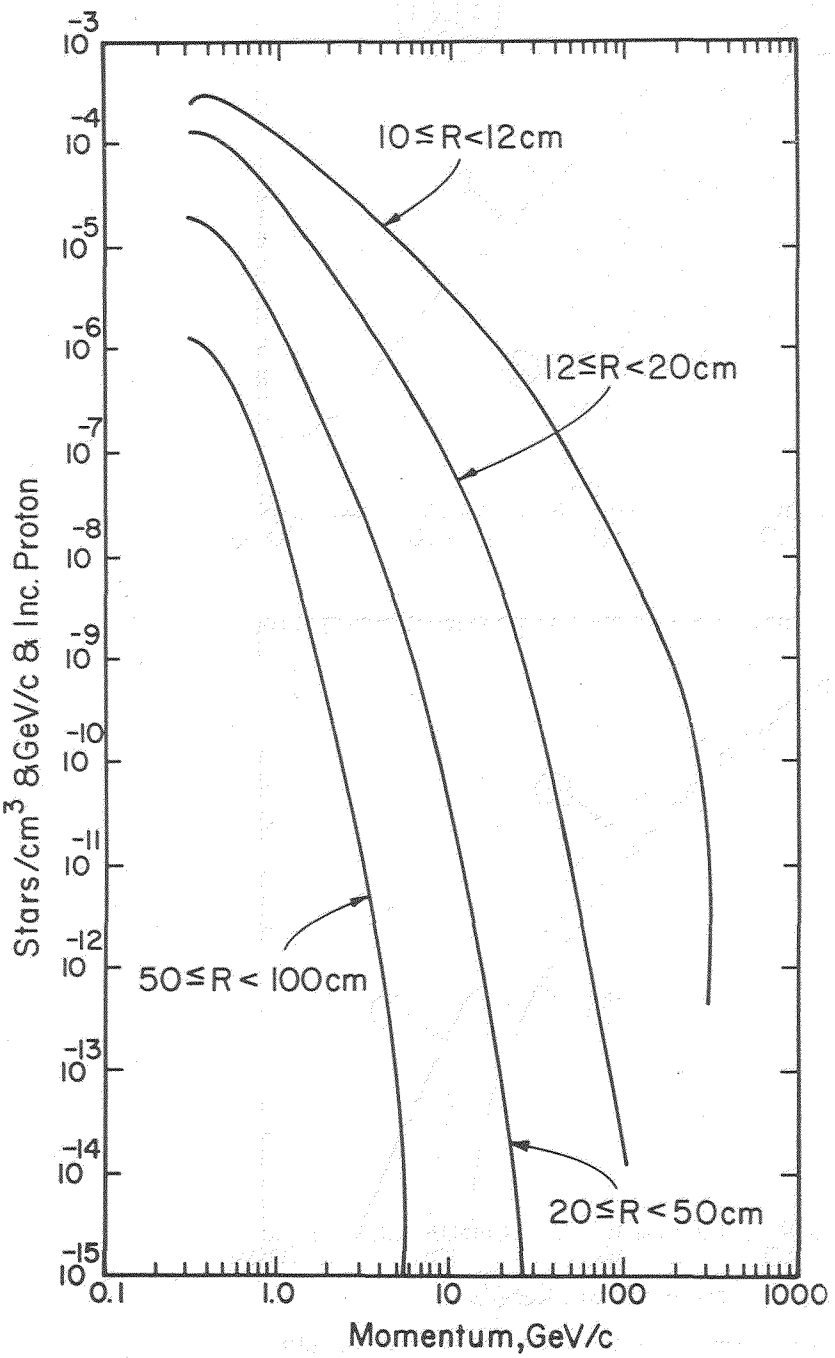

Fig. VIII.66. 300 GeV/c protons incident on inner wall of an iron pipe (10 cm inner radius). The beam of infinitesimal cross section travels parallel to the pipe axis at an infinitesimal distance into the inner wall. Momentum spectra of interacting hadrons (stars/cm^3 · GeV/c · inc. proton) for four radial regions averaged over azimuth and for depths between 200 cm and 900 cm. The spectra are not calculated below 0.3 GeV/c momentum.

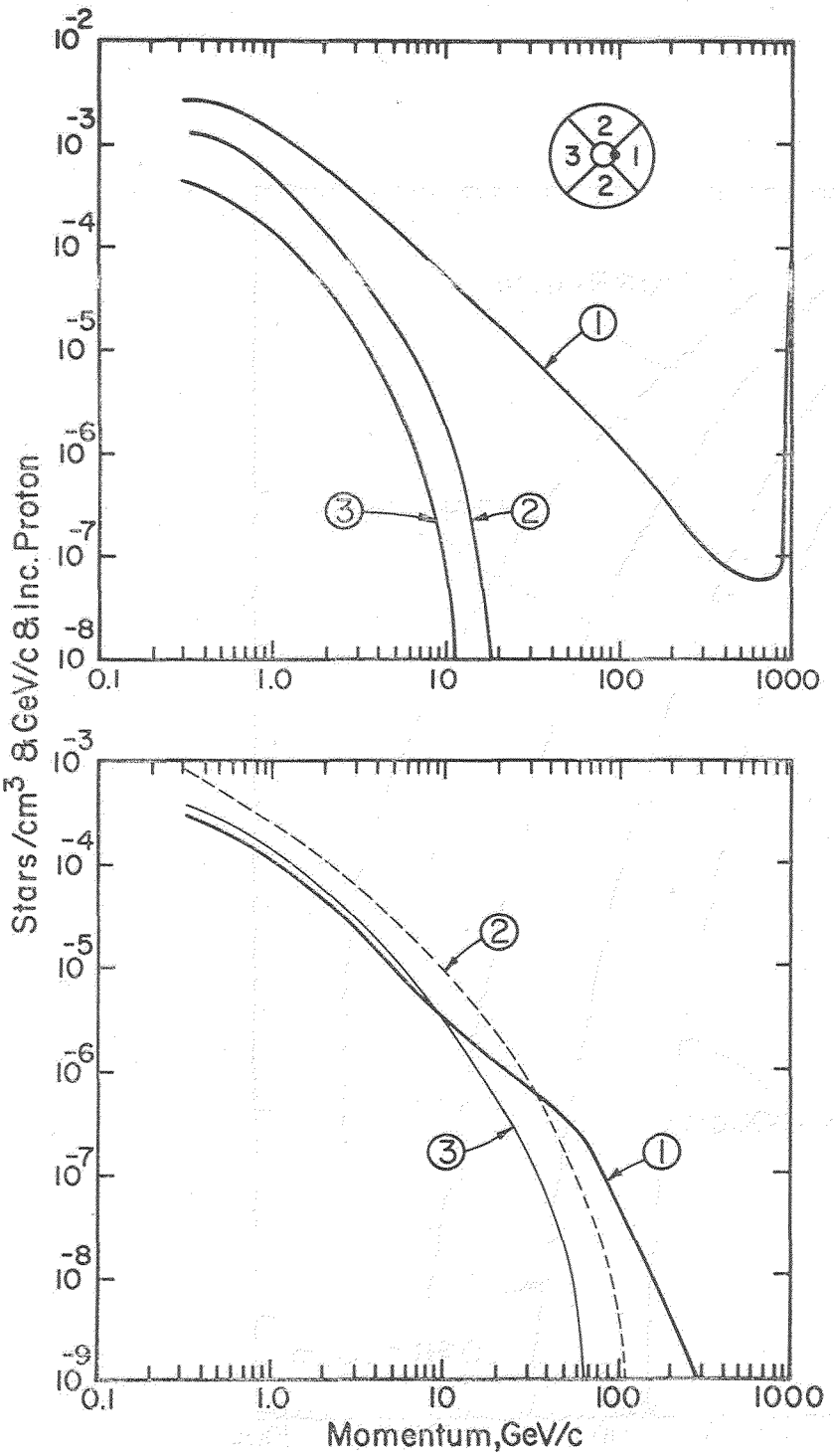

Fig. VIII.67. 100 GeV/c protons incident on the inner wall of an iron pipe (10 cm inner radius). The beam of infinitesimal cross section travels parallel to the pipe axis at an infinitesimal distance into the inner wall. Momentum spectra of interacting hadrons (stars/cm^3 · GeV/c · inc. proton) for the radial region between 10 cm and 12 cm from the axis (zero and 2 cm from the inner wall) for each quadrant (see inset) and for depths between zero and 200 cm (above) and between 200 cm and 900 cm (below). The spectra are not calculated below 0.3 GeV/c momentum.

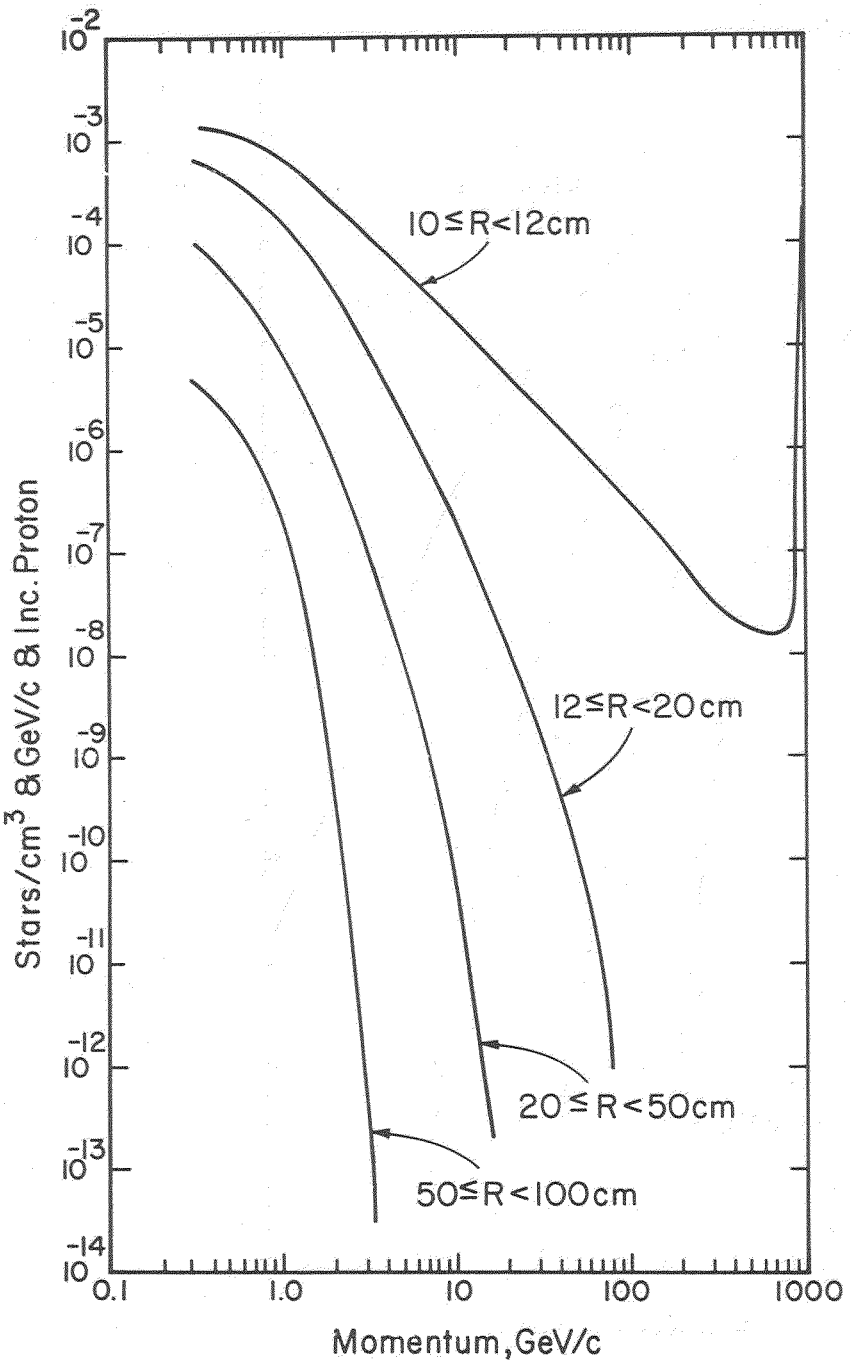

Fig. VIII.68. 1000 GeV/c protons incident on inner wall of an iron pipe (10 cm inner radius). The beam of infinitesimal cross section travels parallel to the pipe axis at an infinitesimal distance into the inner wall. Momentum spectra of interacting hadrons (stars/cm^3 · GeV/c · inc. proton) for four radial regions averaged over azimuth and for depths between zero and 200 cm. The spectra are not calculated below 0.3 GeV/c momentum.

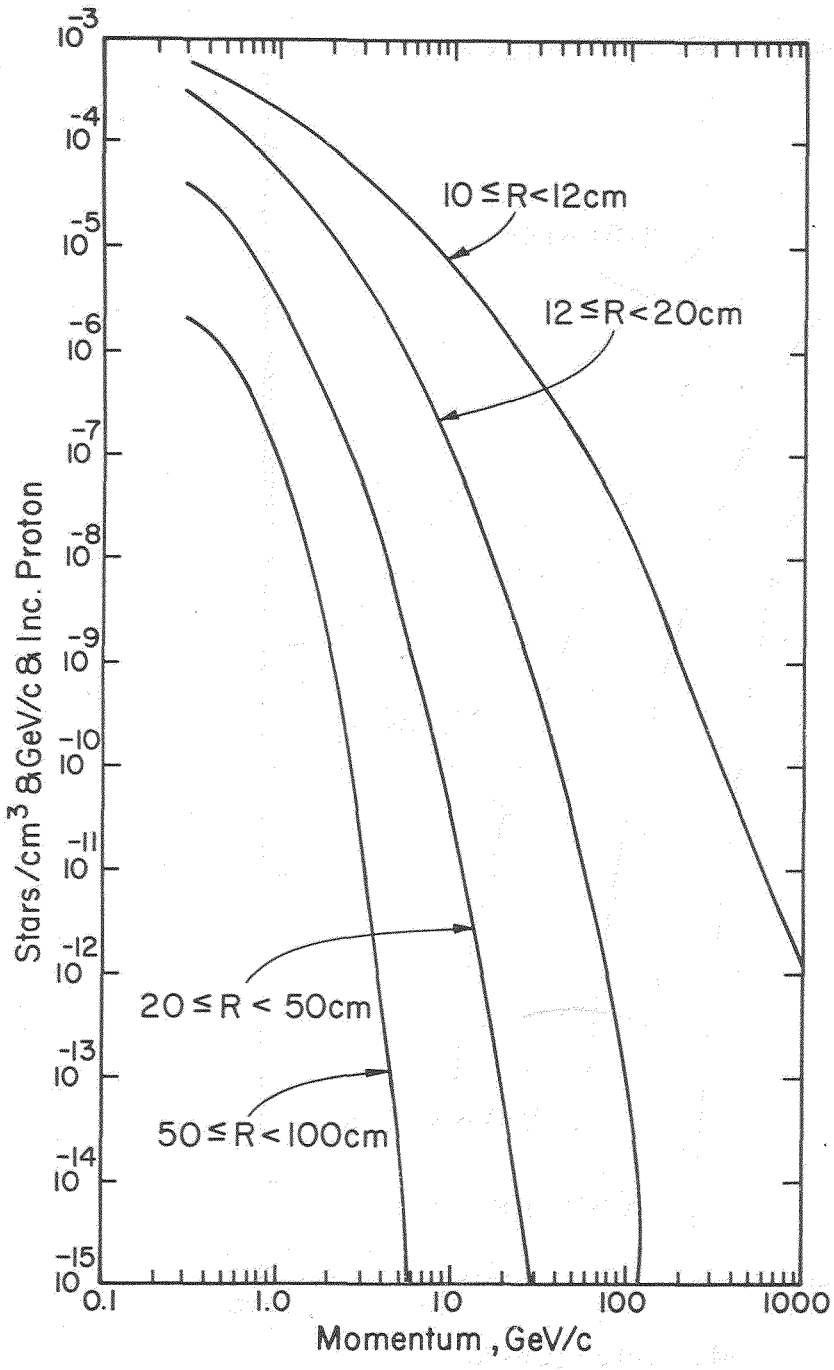

Fig. VIII.69. 1000 GeV/c protons incident on inner wall of an iron pipe (10 cm inner radius). The beam of infinitesimal cross section travels parallel to the pipe axis at an infinitesimal distance into the inner wall. Momentum spectra of interacting hadrons (stars/cm^3 · GeV/c · inc. proton) for four radial regions averaged over azimuth and for depths between 200 cm and 900 cm. The spectra are not calculated below 0.3 GeV/c momentum.

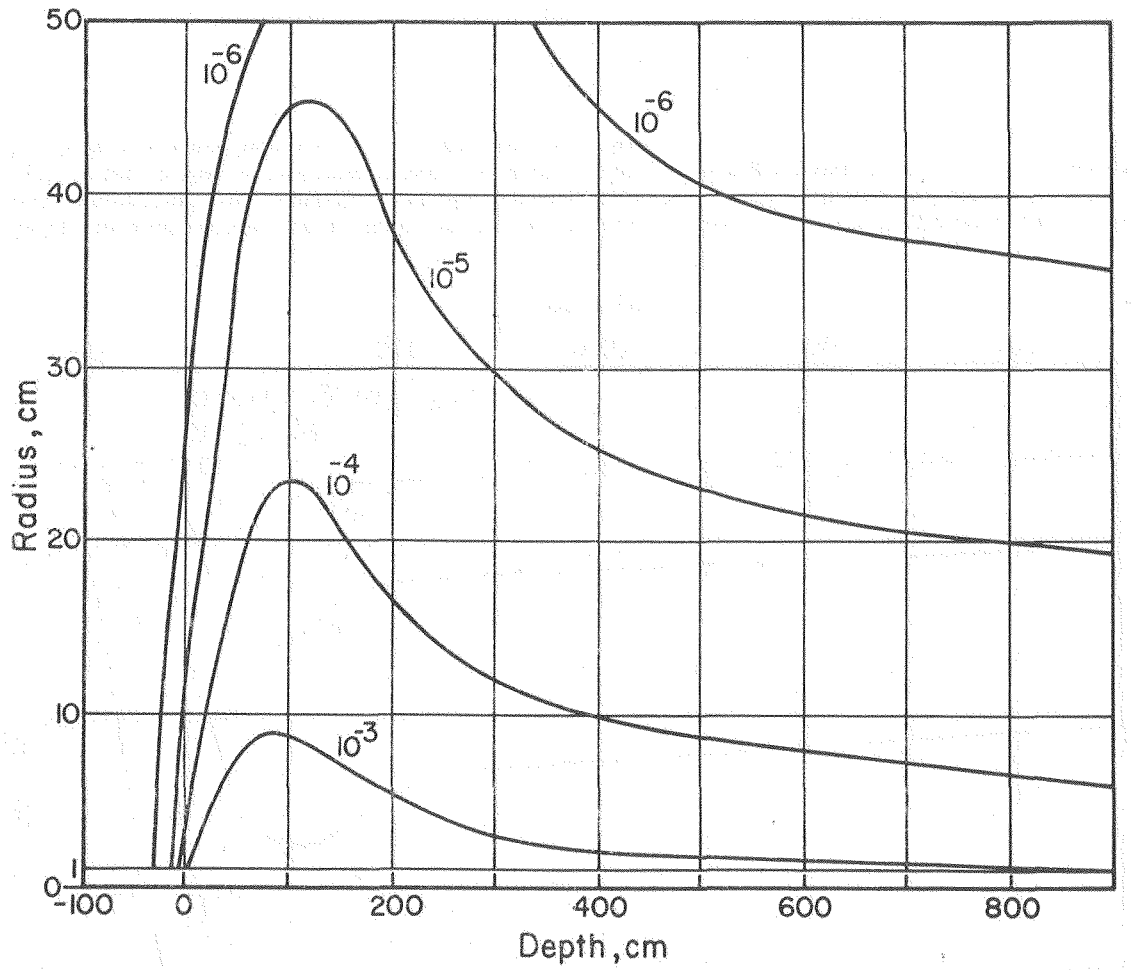

Fig. VIII.70. 300 GeV/c protons incident on the inner wall of an iron pipe (1 cm inner radius). The beam of infinitesimal cross section travels parallel to the pipe axis at an infinitesimal distance into the inner wall and starts to interact at zero depth. Contours of equal star density (stars/cm^3 · inc. proton) averaged over azimuth. The star density includes only those due to hadrons above 0.3 GeV/c momentum. Contours of higher star density are not shown for clarity of the plot, those of lower star density are not included due to statistical uncertainty. The star density, as analyzed by CASIM for the different quadrants, depends only weakly on azimuth.

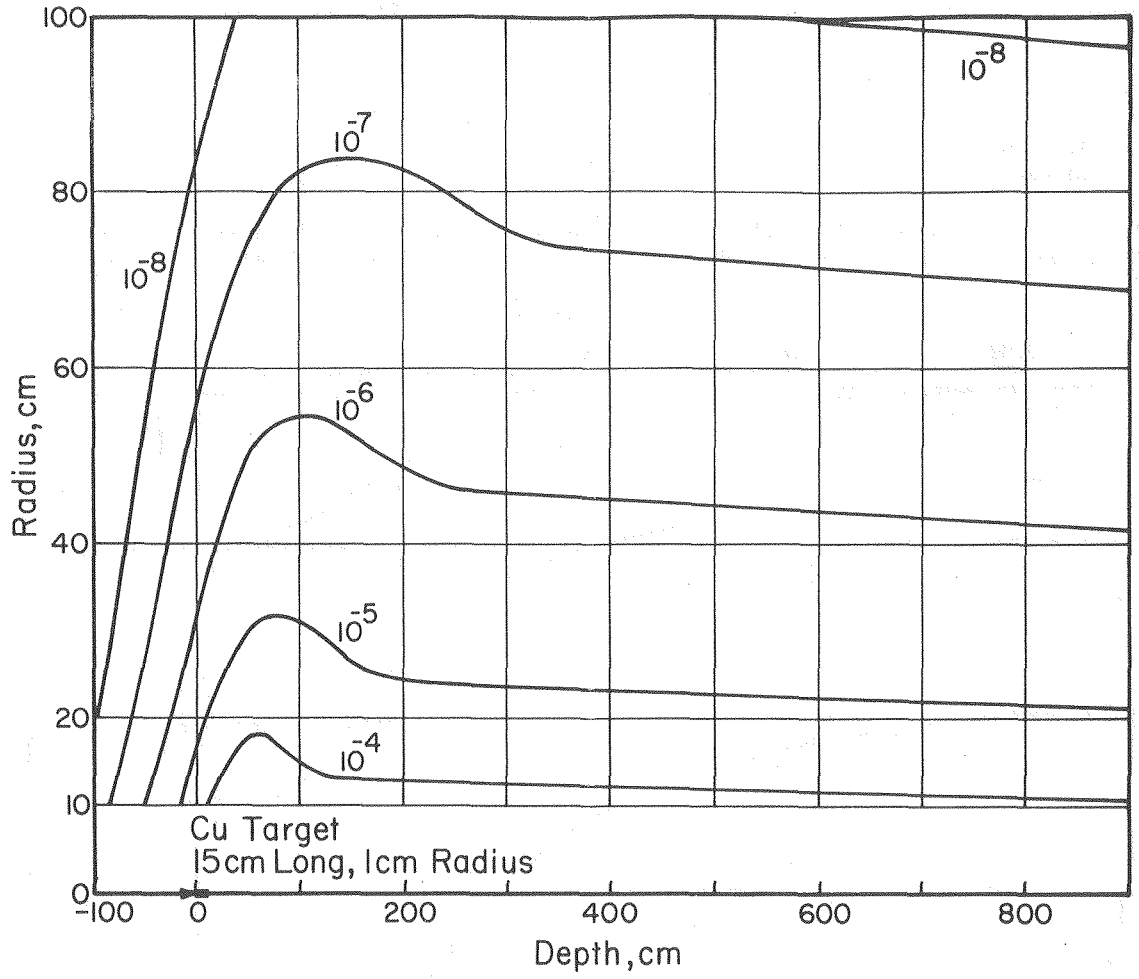

Fig. VIII.71. 300 GeV/c protons incident on a copper target, approximately one interaction length long, placed in an iron pipe. Contours of equal star density (stars/cm^3 · inc. proton). The star density includes only those due to hadrons above 0.3 GeV/c momentum. The beam of 0.3 × 0.3 cm cross section is centered on the pipe axis. Contours of higher star density are not shown for clarity of the plot, those of lower star density are not included due to statistical uncertainty.

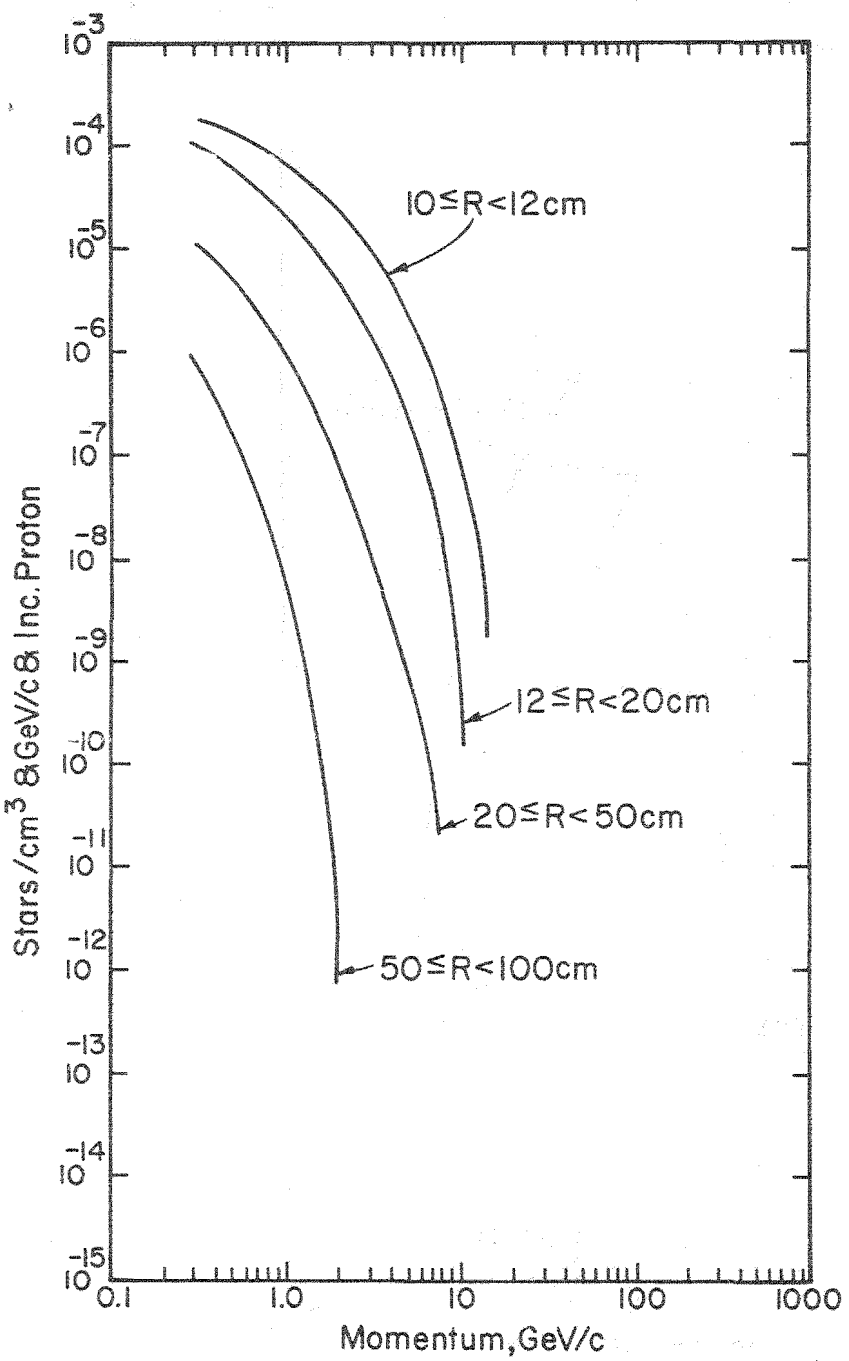

Fig. VIII.72. 300 GeV/c protons incident on a copper target, approximately one interaction length long, placed in an iron pipe. Momentum spectra of interacting hadrons (stars/cm^3 · GeV/c · inc. proton) for four radial regions and for depths between zero and 200 cm. The spectra are not calculated below 0.3 GeV/c momentum.

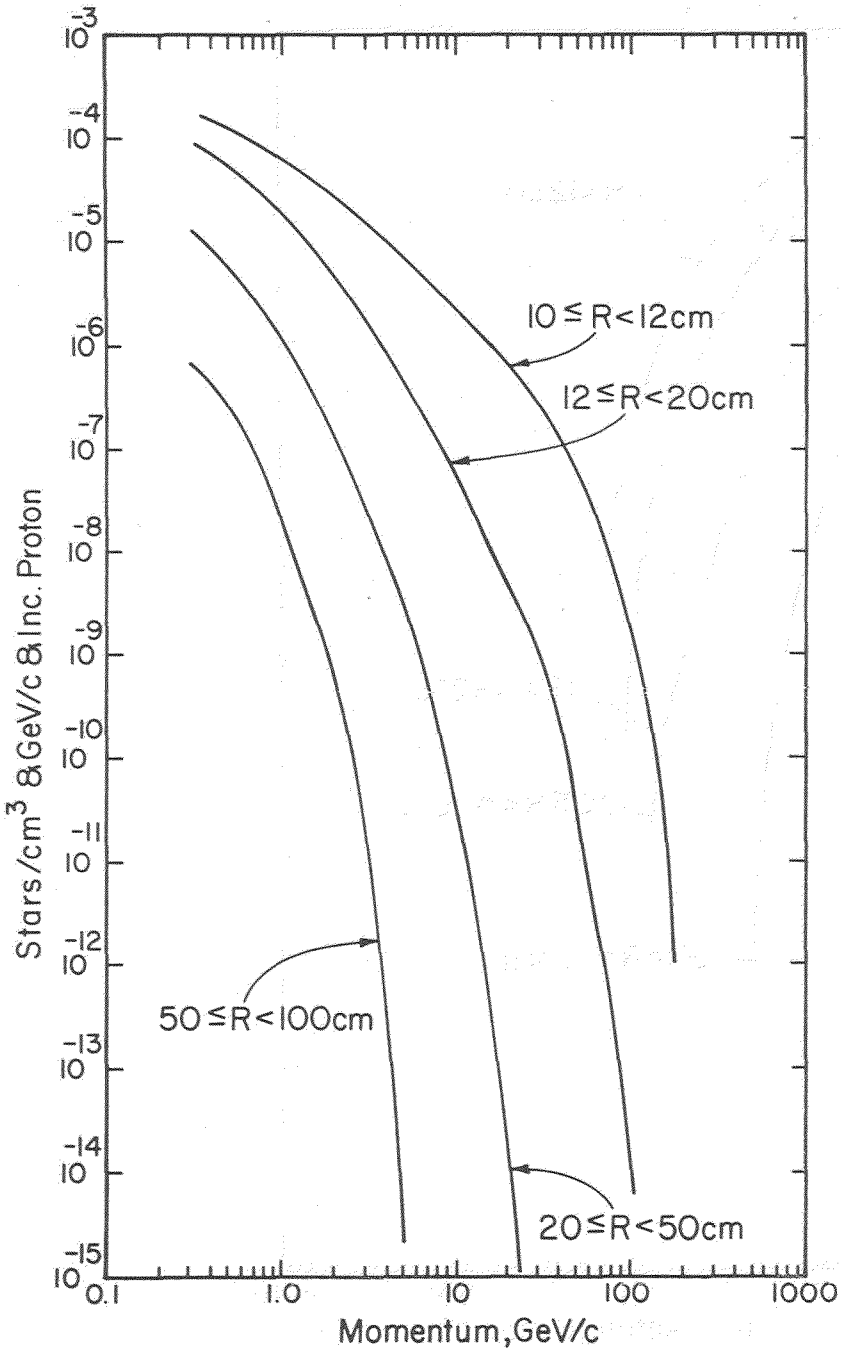

Fig. VIII.73. 300 GeV/c protons incident on a copper target, approximately one interaction length long, placed in an iron pipe. Momentum spectra of interacting hadrons (stars/cm^3 · GeV/c · inc. proton) for four radial regions and for depths between 200 cm and 900 cm. The spectra are not calculated below 0.3 GeV/c momentum.

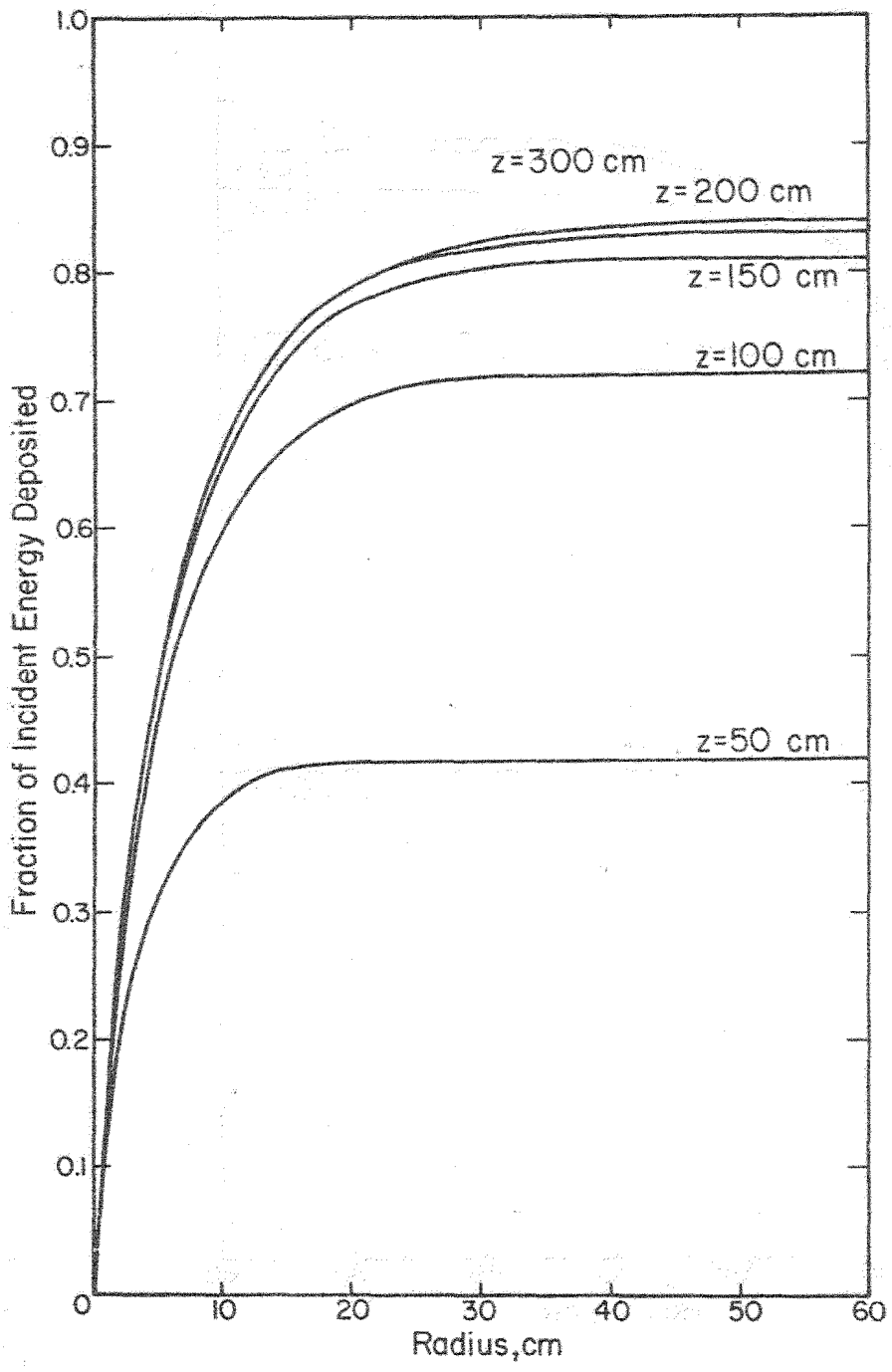

Fig. VIII.74. 30 GeV/c protons incident on a solid iron cylinder. Fraction of the incident kinetic energy deposited as ionization, plotted as a function of radius for various cylinder lengths. The beam of 0.3 cm × 0.3 cm cross section is centered on the cylinder axis.

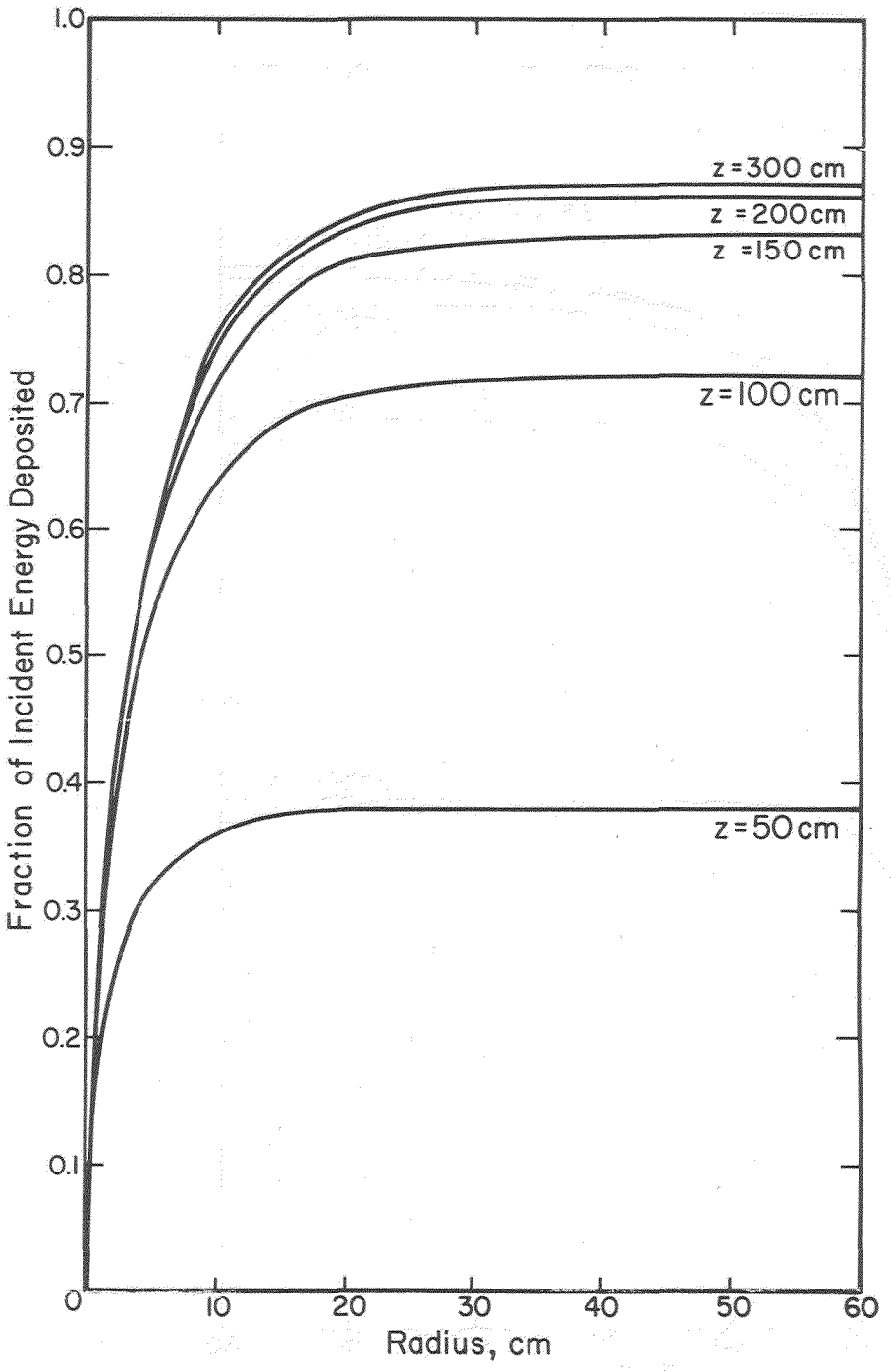

Fig. VIII.75. 100 GeV/c protons incident on a solid iron cylinder. Fraction of the incident kinetic energy deposited as ionization, plotted as a function of radius for various cylinder lengths. The beam of 0.3 cm × 0.3 cm cross section is centered on the cylinder axis.

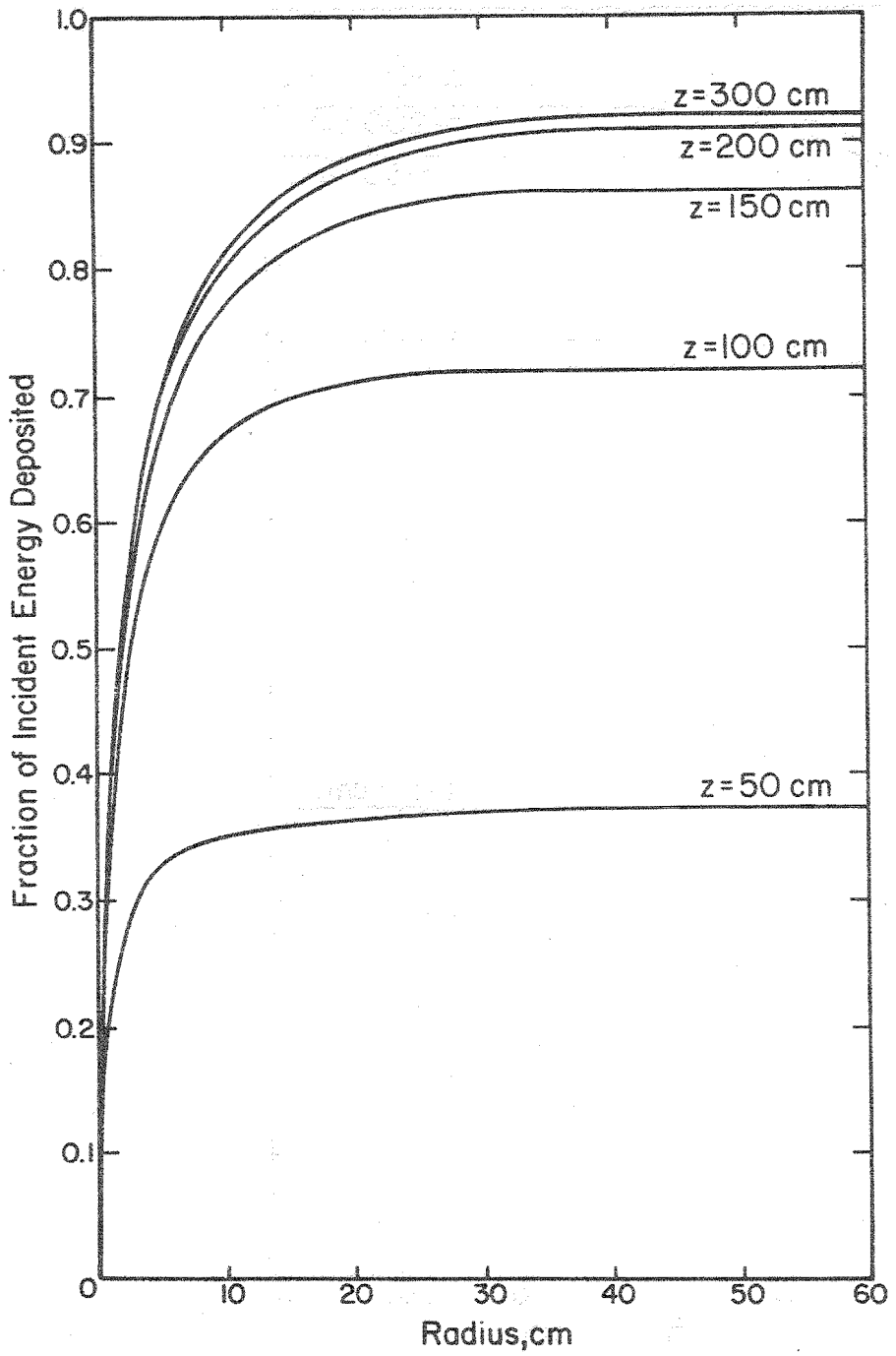

Fig. VIII.76. 300 GeV/c protons incident on a solid iron cylinder. Fraction of the incident kinetic energy deposited as ionization, plotted as a function of radius for various cylinder lengths. The beam of 0.3 cm × 0.3 cm cross section is centered on the cylinder axis.

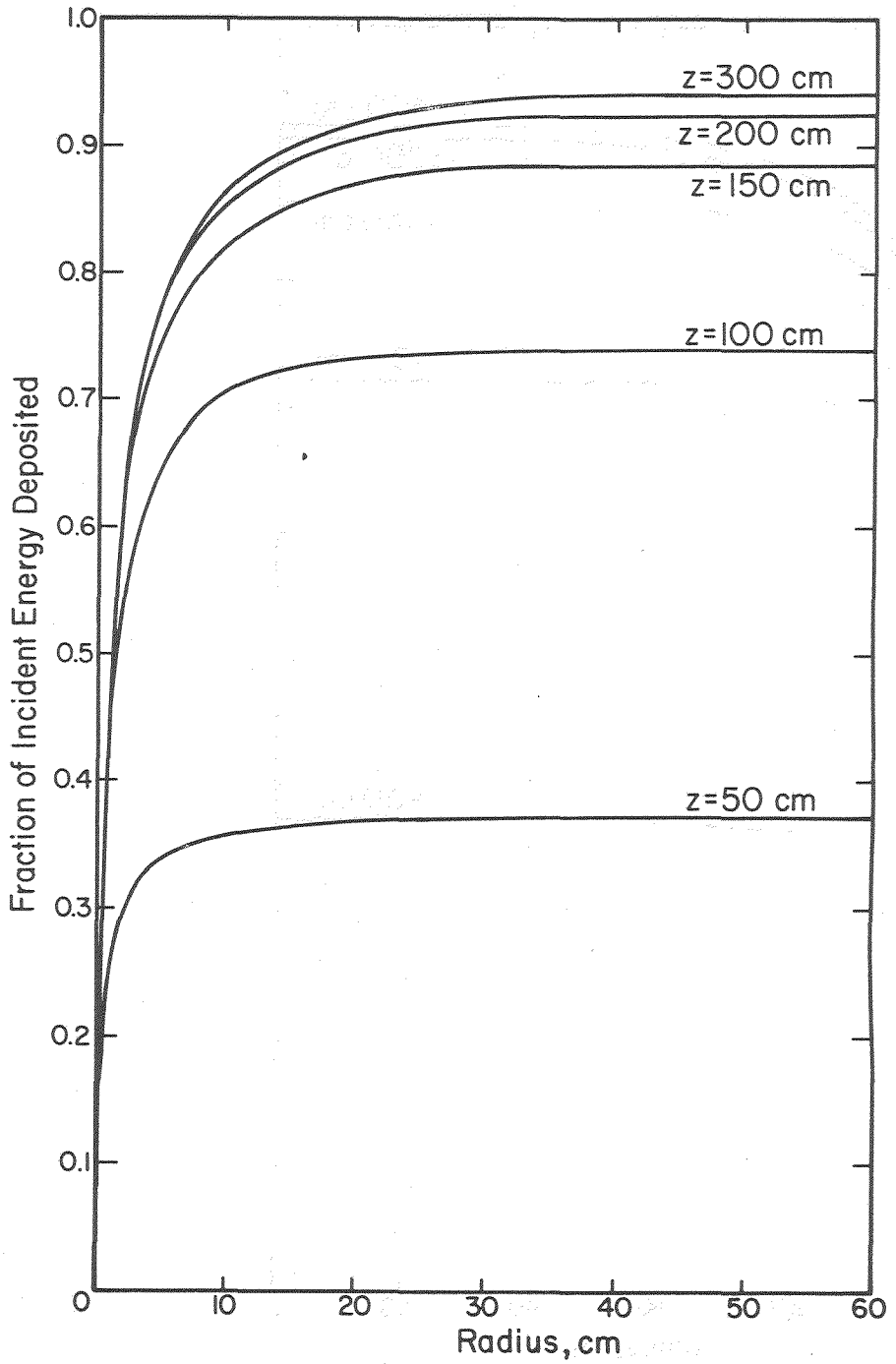

Fig. VIII.77. 1000 GeV/c protons incident on a solid iron cylinder. Fraction of the incident kinetic energy deposited as ionization, plotted as a function of radius for various cylinder lengths. The beam of 0.3 cm × 0.3 cm cross section is centered on the cylinder axis.

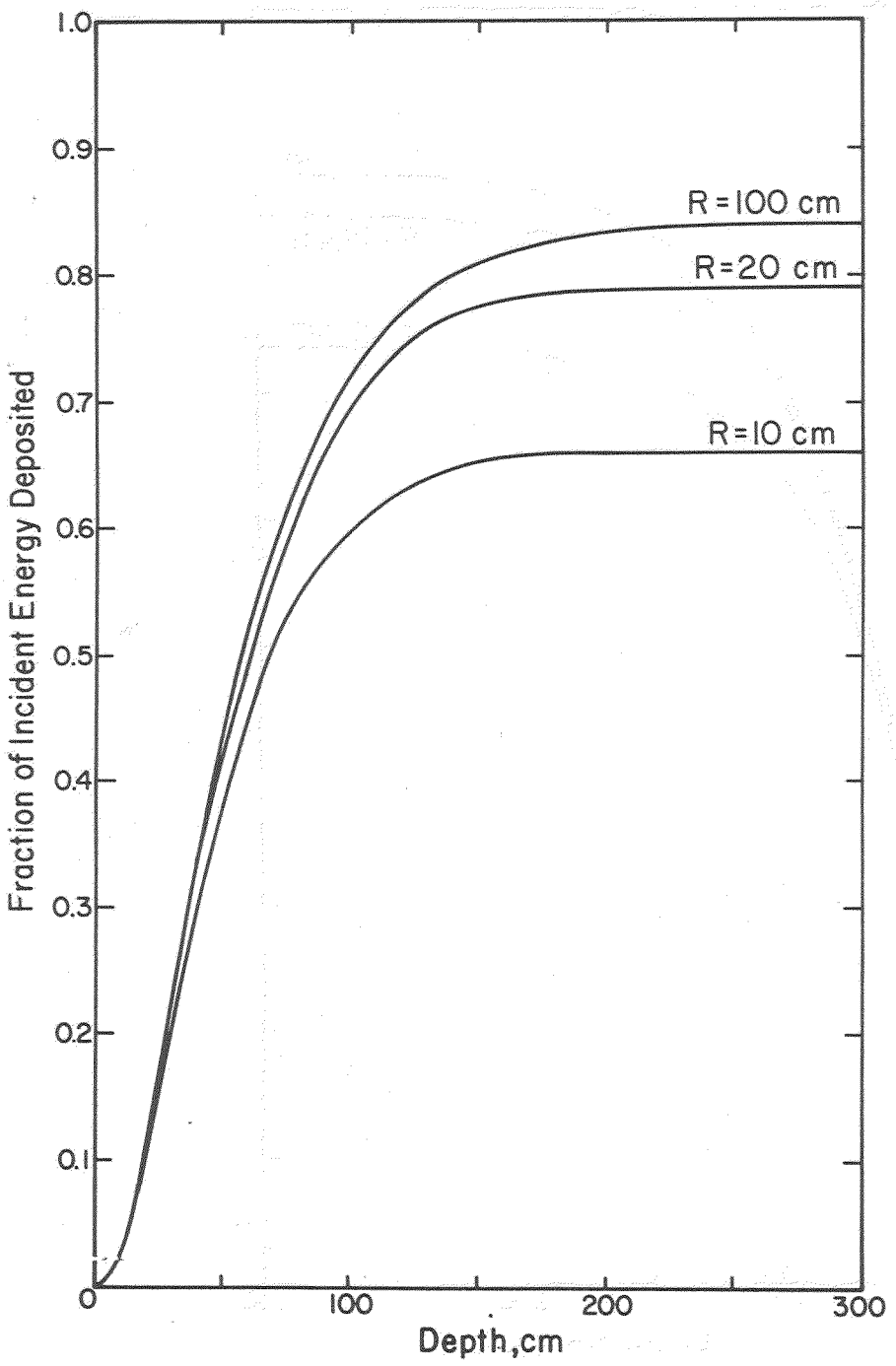

Fig. VIII.78. 30 GeV/c protons incident on a solid iron cylinder. Fraction of the incident energy deposited as ionization plotted as a function of length for various cylinder radii. The beam of 0.3 cm × 0.3 cm cross section is centered on the cylinder axis.

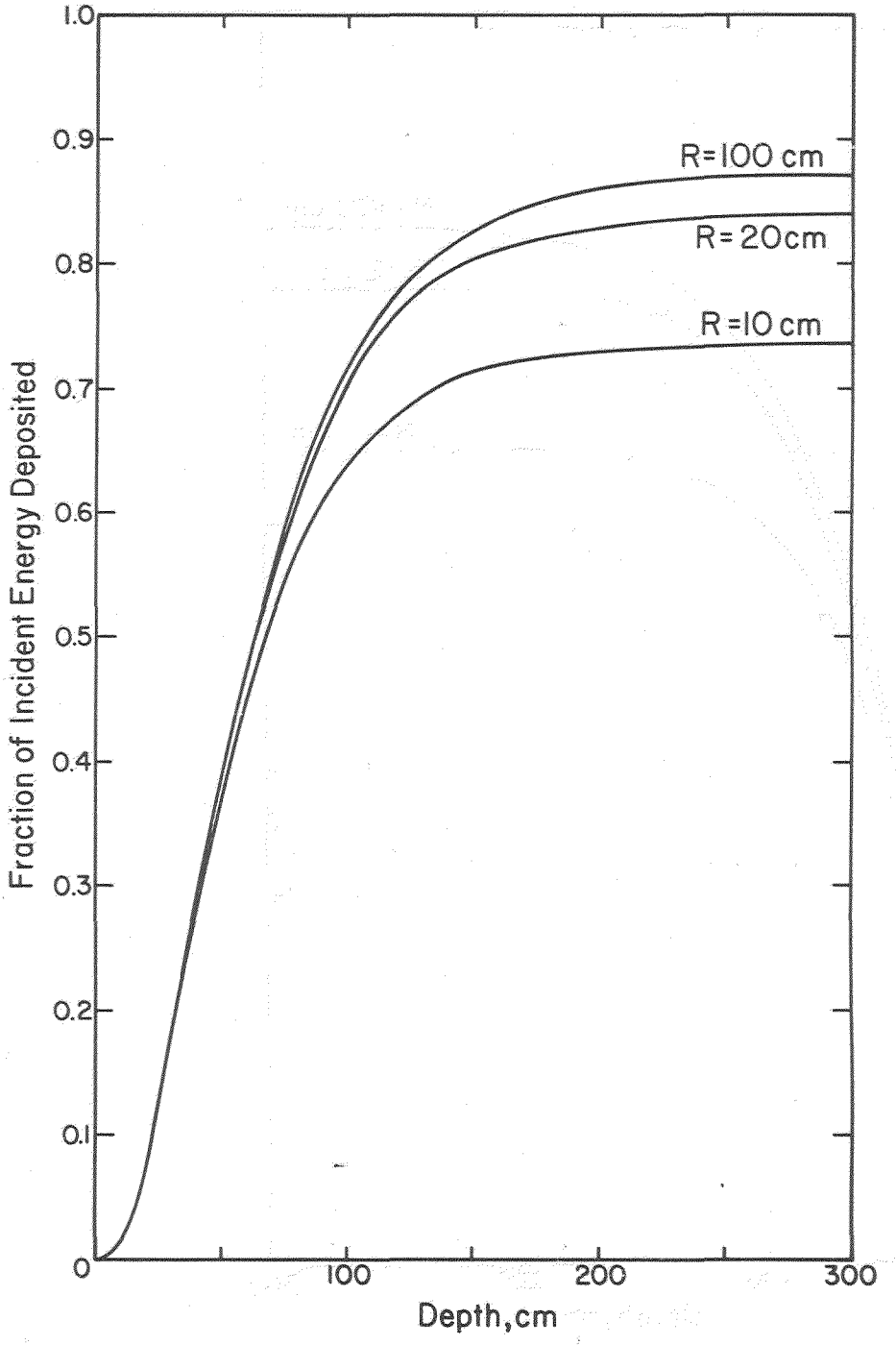

Fig. VIII.79. 100 GeV/c protons incident on a solid iron cylinder. Fraction of the incident energy deposited as ionization plotted as a function of length for various cylinder radii. The beam of 0.3 cm × 0.3 cm cross section is centered on the cylinder axis.

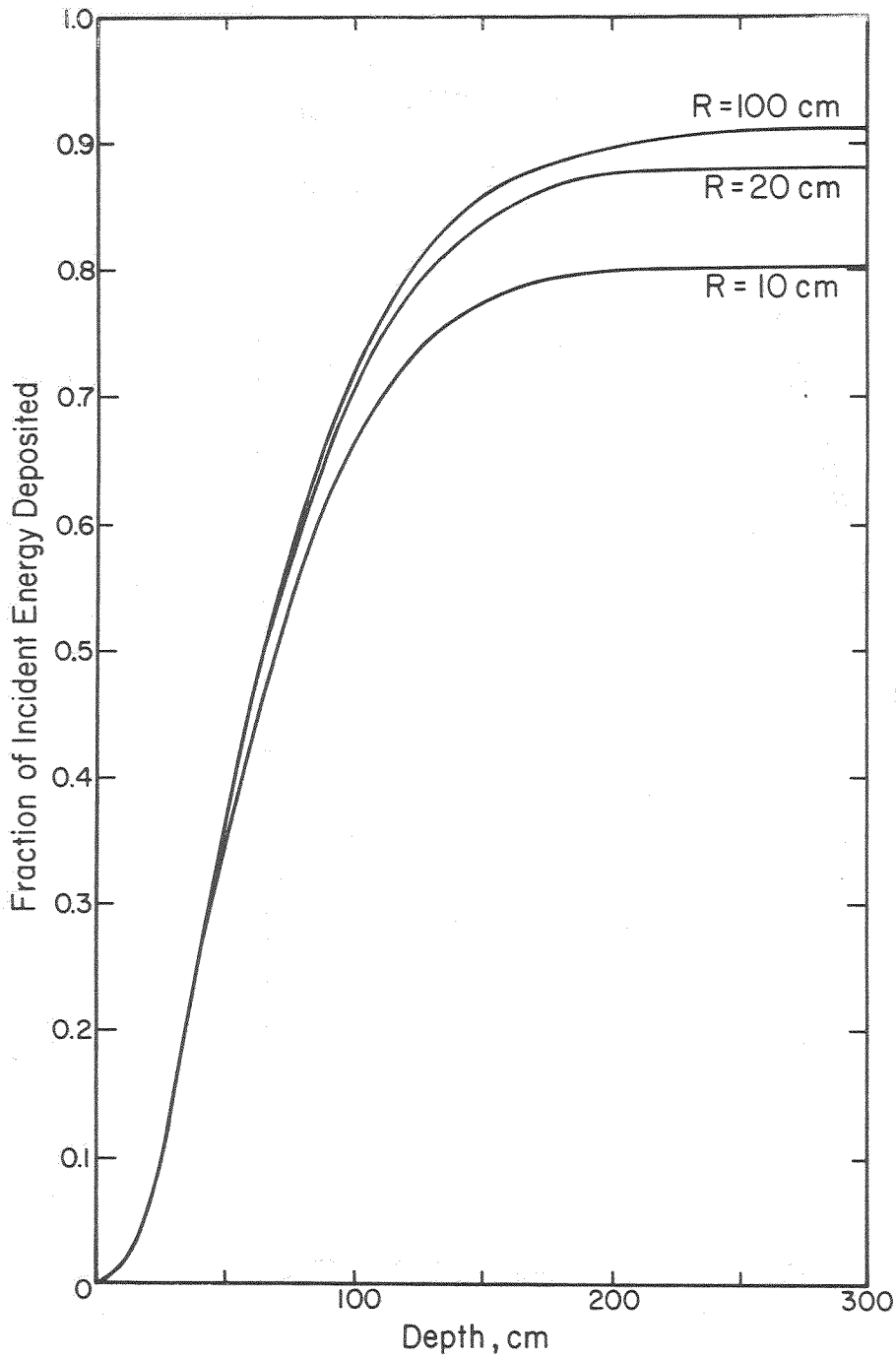

Fig. VIII.80. 300 GeV/c protons incident on a solid iron cylinder. Fraction of the incident kinetic energy deposited as ionization plotted as a function of length for various cylinder radii. The beam of 0.3 cm × 0.3 cm cross section is centered on the cylinder axis.

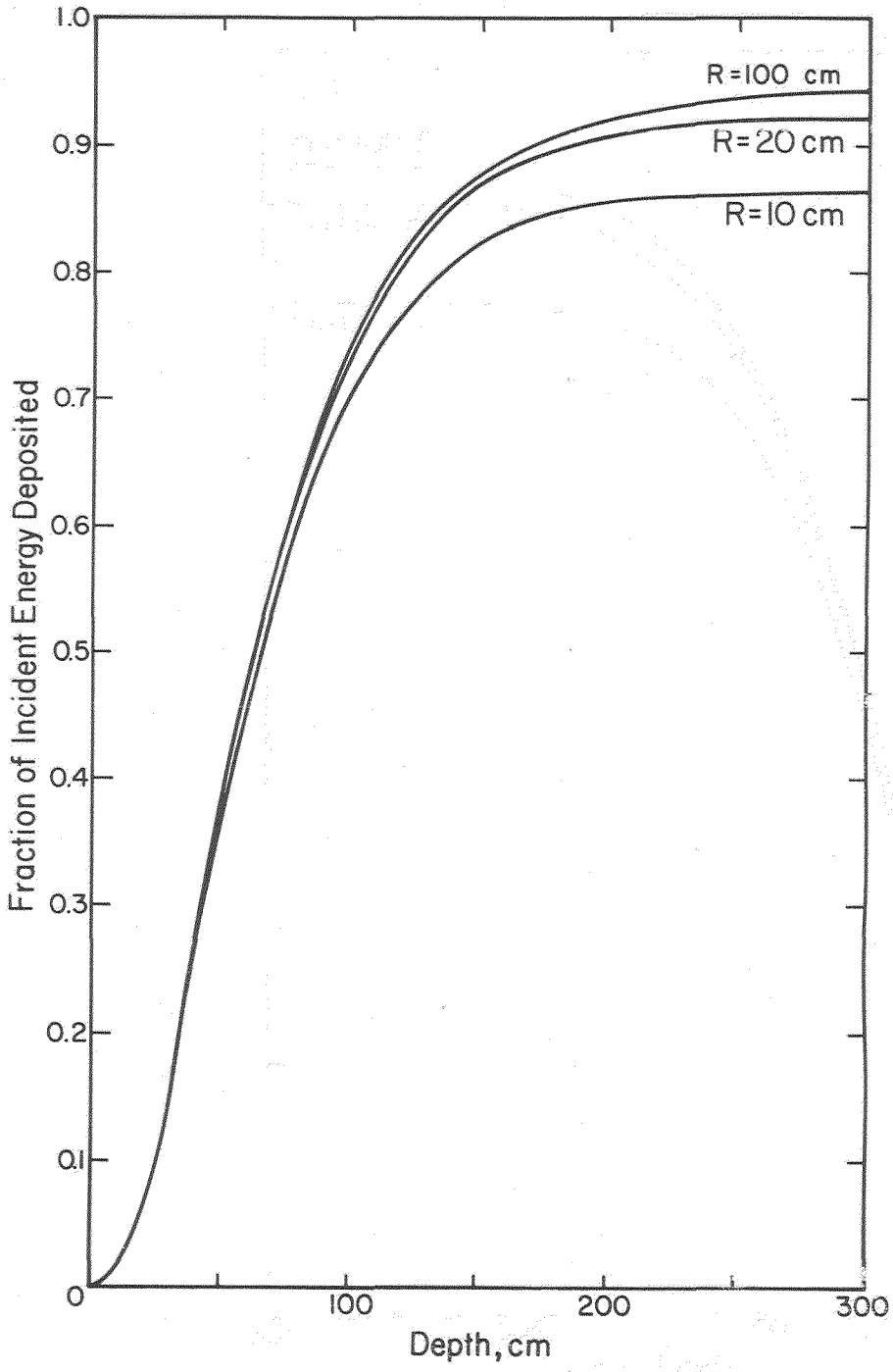

Fig. VIII.81. 1000 GeV/c protons incident on a solid iron cylinder. Fraction of the incident kinetic energy deposited as ionization plotted as a function of length for various cylinder radii. The beam of 0.3 cm×0.3 cm cross section is centered on the cylinder axis.

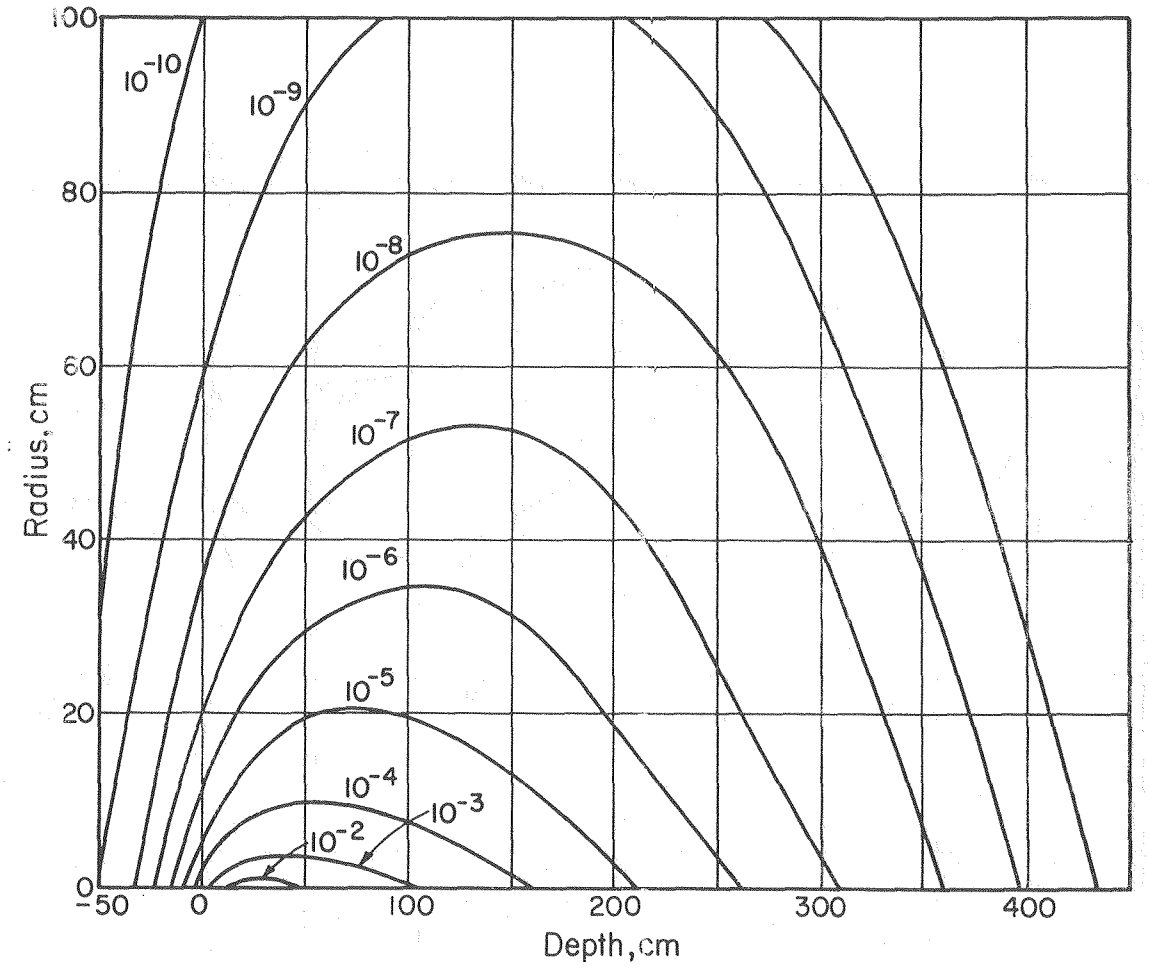

Fig. VIII.82. 30 GeV/c protons incident on a solid iron cylinder. Contours of equal deposited energy density (GeV/cm^3 · inc. proton). The beam of 0.3 cm×0.3 cm cross section is centered on the cylinder axis and starts to interact at zero depth. Contours of higher energy density are not shown for clarity of the plot, those of lower energy density are not included due to statistical uncertainty.

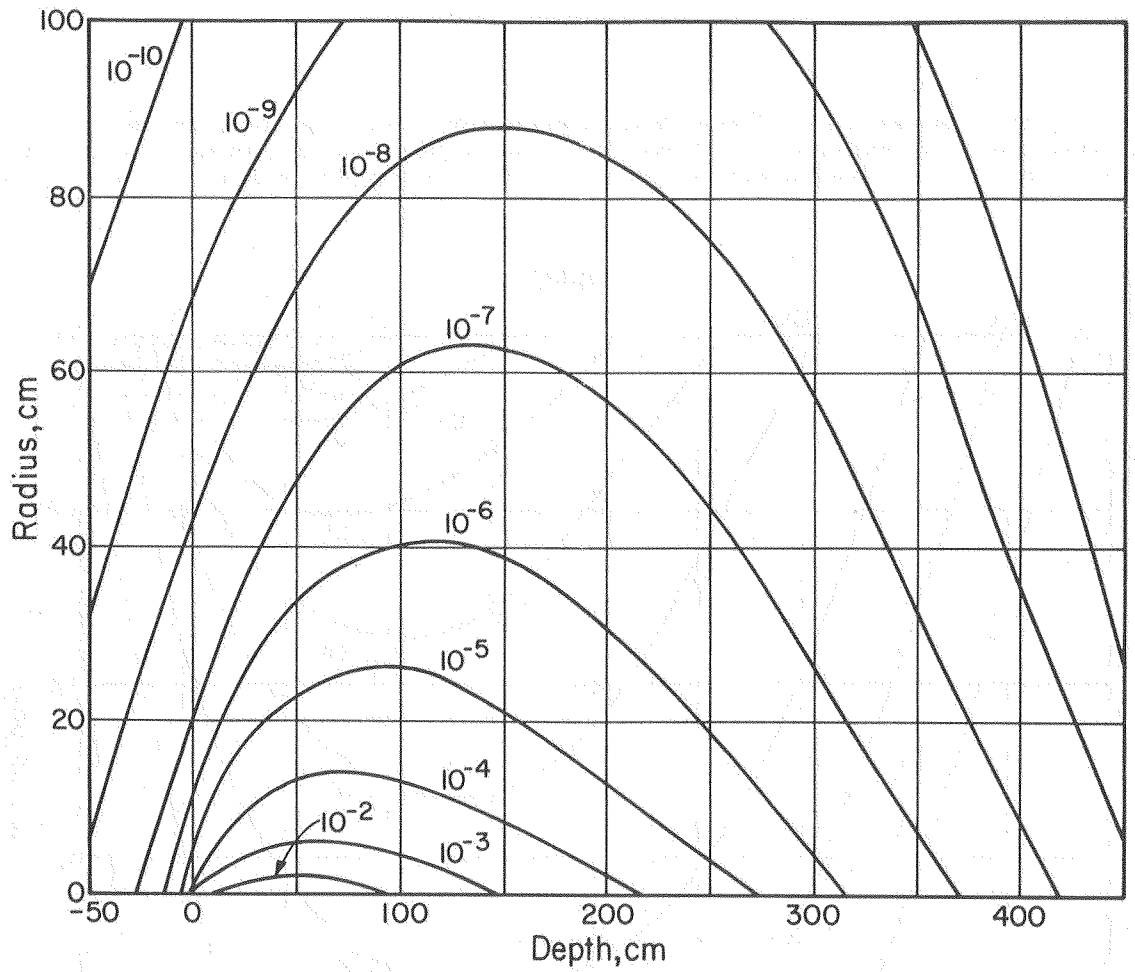

Fig. VIII.83. 100 GeV/c protons incident on a solid iron cylinder. Contours of equal deposited energy density (GeV/cm^3 · inc. proton). The beam of 0.3 cm × 0.3 cm cross section is centered on the cylinder axis and starts to interact at zero depth. Contours of higher energy density are not shown for clarity of the plot, those of lower energy density are not included due to statistical uncertainty.

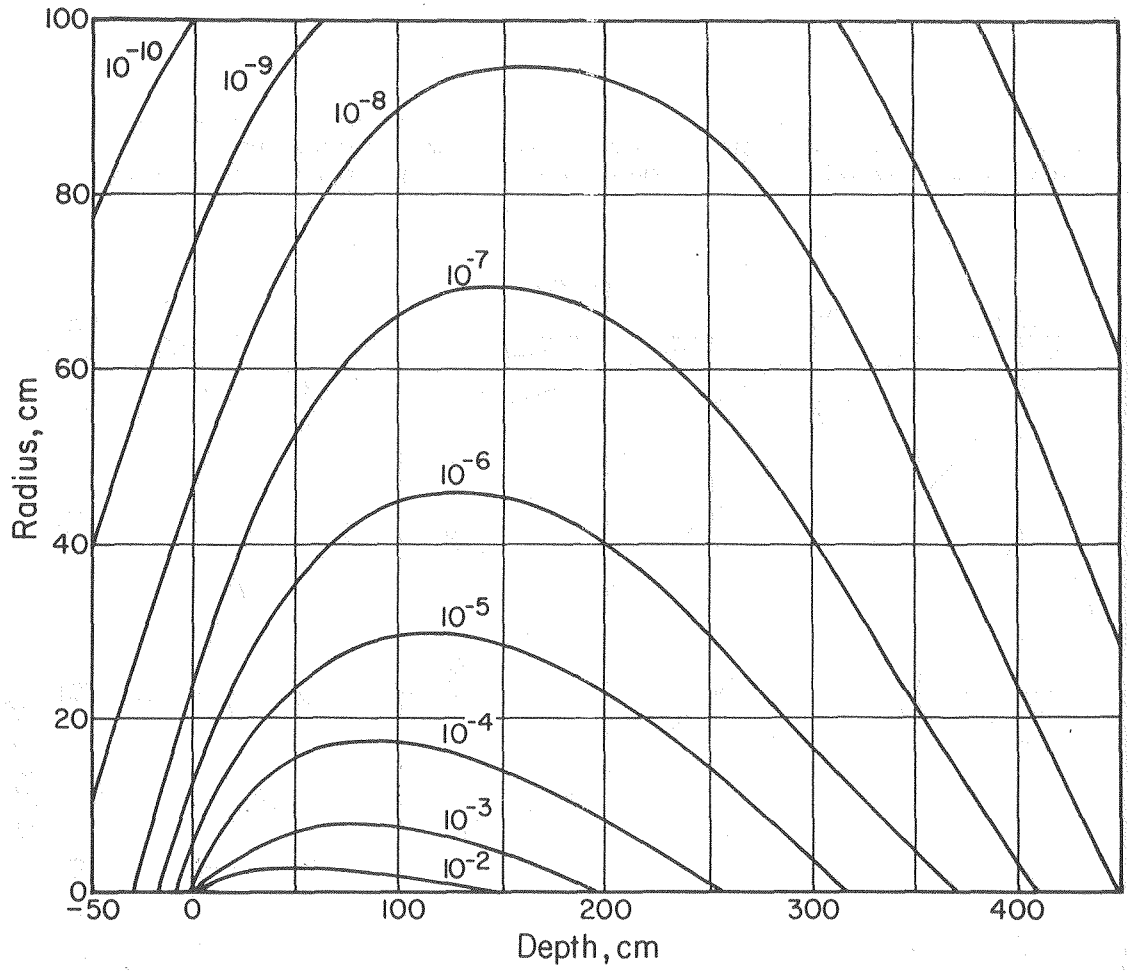

Fig. VIII.84. 300 GeV/c protons incident on a solid iron cylinder. Contours of equal deposited energy density (GeV/cm^3 · inc. proton). The beam of 0.3 cm × 0.3 cm^3 cross section is centered on the cylinder axis and starts to interact at zero depth. Contours of higher energy density are not shown for clarity of the plot, those of lower energy density are not included due to statistical uncertainty.

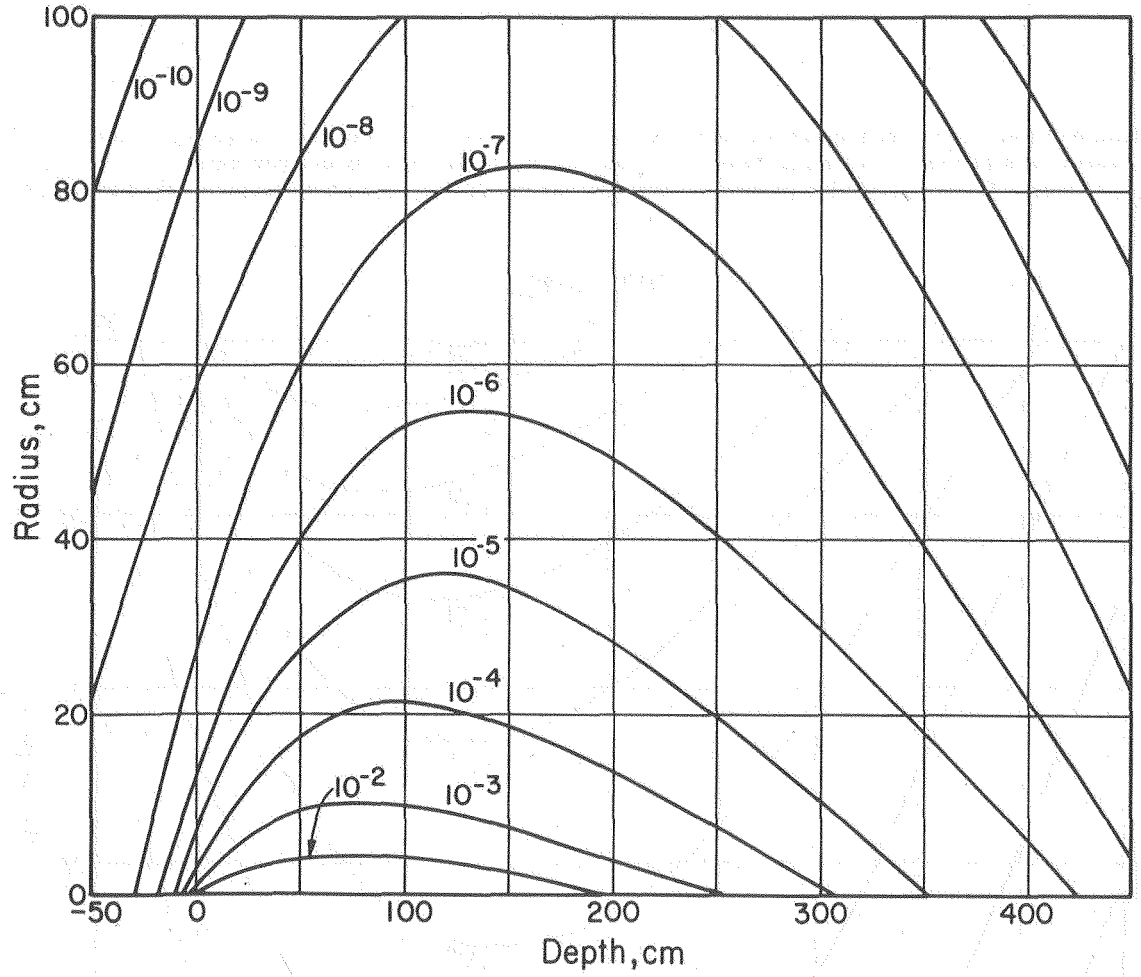

Fig. VIII.85. 1000 GeV/c protons incident on a solid iron cylinder. Contours of equal deposited energy density (GeV/cm^3 · inc. proton). The beam of 0.3 cm × 0.3 cm cross section is centered on the cylinder axis and starts to interact at zero depth. Contours of higher energy density are not shown for clarity of the plot, those of lower energy density are not included due to statistical uncertainty.

APPENDIX

FN-260
1111.200

COMPARISON OF SOME RECENT DATA ON p-NUCLEUS INTERACTIONS WITH THE HAGEDORN-RANFT MODEL PREDICTIONS

A. Van Ginneken

August 6, 1974

I. Introduction

Problems of radiation shielding and the like, i.e., wherever internuclear cascades are important, have for the past year or so been analyzed using the Hagedorn-Ranft (HR) model[1] for particle production[2]. The HR model was chosen after careful consideration. It is presently the only one furnishing extensive predictions on particle yields from p-nucleus collisions and which furthermore could be adapted (albeit in crude fashion) to incident particles other than protons. Because of the important role the particle production model plays in such calculations it is necessary to compare the HR model predictions with experimental data. Recently some results have been reported from emulsion studies and counter experiments. While this sample is too limited to yield definitive conclusions, it is still worthwhile to make these comparisons.

It should be briefly recalled that the HR model explicitly pertains to proton-proton collisions and contains a number of parameters determined by data fitting. Some time later Ranft[3] readjusted these parameters to fit the 19.2 GeV/c p-nucleus data of Allaby et al[4]. It follows from this procedure that particle spectra so generated will retain many features of p-p particle spectra (e.g., symmetry in a p-p center of mass) no longer obeyed in p-nucleus collisions. Likewise specific nuclear effects (e.g., coherent particle production) will not be well represented in the spectra.

A few additions and modifications were made to the HR model before applying it to shielding-type problems. These are briefly listed below and appear in more detail elsewhere[2].

(1) Additional low energy nucleons are added to the HR spectra. Their differential yields were taken from the parametrization of Ranft and Routti[5] of the intranuclear cascade calculations of Bertini[6]. These nucleons have kinetic energies up to a few hundred MeV.

(2) Each inelastic particle-nucleus collision creates a certain amount of nuclear excitation. The dominant excitation mechanism is via emission of low energy ($\lesssim$ 30 MeV) nucleons and nuclear fragments.

(3) Neutrons (not explicitly treated by HR) have the same relative spectra as protons. The total number of nucleons emerging from the collision (belonging to the HR component) is normalized to two. The total number of protons is (1+Z/A).

(4) The pion spectra are normalized so as to conserve energy in the collision (assuming the π^0 production cross-sections are equal to the average of those of π^+ and π^-). The normalization constants so determined are fairly close to unity except at low incident energies.

(5) Particles other than nucleons and pions are presently not included. However, by enforcing energy conservation in the above manner the effects of such particles (e.g., in terms of radiation hazards) are not completely neglected.

The results presented here are obtained using the parameters as they appear in the "Atlas" of Grote, Hagedorn and Ranft[1]. The extra normalization discussed above (depending upon target, incident momentum and particle type) is stated explicitly for each case treated here (see figure captions). This might be of interest when using the HR model to estimate target yields.

Results obtained with hydrogen targets are not included. While they are no doubt of more fundamental importance they are of lesser interest from the applied point of view adopted here.

II. Comparison with Emulsion Studies

Results of a number of emulsion experiments performed at 200 GeV have been reported[7]. These include: average number of "shower tracks", $\langle n_s \rangle$, and the average number of "heavy tracks" $\langle N_h \rangle$, per inelastic event as well as the angular distribution of shower tracks. (Roughly, a proton leaves a shower track in the emulsion above 400 MeV kinetic energy and a charged pion above 50 MeV. Below these values they leave heavy tracks.)

The emulsion data ($\langle A \rangle \approx 70$) are compared with predictions of HR for Cu ($A \approx 64$). The latter are rather insensitive to nuclear mass. It is further assumed that all charged pions and protons contribute to n_s. The comparison of $\langle n_s \rangle$ versus incident momentum is shown in Fig.1. It appears that the HR model underestimates the number of shower tracks produced, more so the higher the incident momentum.

For the average number of heavy tracks the model used in shielding calculations[2] predicts $\langle N_h \rangle \approx 10$ while experimentally $\langle N_h \rangle \approx 7.5$ is observed. Both values remain essentially constant above ~ 5 GeV/c incident momentum.

The comparison of the angular distribution (in the forward direction) of shower particles is presented in Fig.2 in the form of a $dN/d\theta$ vs θ plot. It can be seen that the disagreement is at worst a factor of two, except possibly at very small angles. It should be pointed out that for angles $\lesssim$ 10 mrad the emulsion data suffer somewhat from low event rates and poor experimental resolution. There may also be systematic errors present in this angular region[8].

At high energies the model underestimates the multiplicity of shower tracks rather seriously. The angular distributions, outside the dubious small-angle region, are quite well matched in shape and it appears that the model underestimates the angular distribution of shower tracks about uniformly.

The implications of these results for shielding calculations are rather difficult to assess. The aim of the latter is to predict particle fluxes and momentum spectra of particles

emerging from thick targets. These particles are usually many generations removed from the incident ones. Looking at Fig.1, the HR model together with forced energy conservation will predict fewer energetic particles in the first generation, but since these are more energetic each will produce more particles in the next generation. The key to how well the model will perform in this respect, particularly at high energy, lies in the angular distribution of the energy carried off by cascade propagating particles. Presently, little is known about this.

As Fig.1 shows, the average number of shower tracks predicted is closer to measured value at lower incident momenta. The same appears to hold for their angular distribution. Fig.3 shows the angular distribution for 60 GeV/c π^- on emulsion[9]. Ignoring again the small angle region, the fit is definitely better than for 200 GeV/c protons Presumably around 20 GeV/c, where the model was matched to experiment, the fit can be expected to be better yet.

III. Comparison with data of Baker et al.

Baker et al[10] measured particle yields at 3.6 mr from a beryllium target (1/8" x 1/8" and 12" long) both for 200 GeV/c and 300 GeV/c incident protons. Of the various particles measured p,π^+ and π^- are of interest here. Since a target of this length (about one interaction length) is quite commonly used, it is worthwhile to calculate specifically the effect of finite target length. This was performed using the program CASIM[2] and keeping a separate tally of secondaries and of all higher generations. (The yield of secondaries only could equally well be calculated from the differential yield per nucleus with straightforward corrections for absorption). Figures 4 and 5 show the comparisons. The data points carry errors in excess of 30%, mainly overall normalization. Because the calculations essentially lump all particles other than nucleons into the pion spectra the sums of π's and K's of like charge are also shown. Apart

from measurements very near the incident momentum (say above ~ 170 GeV/c at 200 GeV/c), the largest deviation occurs for π^- of ~ 35 GeV/c where the calculation overestimates the yield by a factor of ~ 2.5. Generally the fits are quite good.

The sharp peak in the proton spectra near the incident momentum at 200 GeV/c (Fig. 4a) is likely associated with (quasi) elastic scattering and diffractive excitation off initially bound target nucleons. From the way the HR model for p-nucleus collisions is obtained it cannot be expected to fit this feature.

The calculation also underestimates the high momenta π^- yield (Fig. 4c). This is again not surprising in view of the rather cursory treatment of the kinematical cut-off in the HR model[11]. Effects of finite step size in the numerical integration also become apparent.

Neither of the discrepancies occuring at high momenta are likely to have significant effects on the outcome of shielding calculations. The comparisons as plotted in Figures 3 and 4 actually show the equivalent of the energy carried off by the particles as a function of momentum. The discrepancy of π^- can be seen to occur where this quantity is down by more than two orders of magnitude from the broad peak at ~ 50 GeV/c. The effects of the protons in the high momentum peak are not much different from the incident protons themselves and their omission should not have any serious consequences.

IV. Comparison with data of Cronin et al.

Cronin et al[12] measured particle yields at 77 mr from targets of beryllium (3.14" long x 1/4" diam.) and titanium (2.23" x 1/4") for 300 GeV/c incident protons, and from tungsten (0.85" x 1/4") at 200, 300 and 400 GeV/c. (The angle of 77 mr corresponds roughly to $\pi/2$ radians in a nucleon-nucleon center of mass frame at these energies.) The comparisons with the HR model are shown in Figs. 5 through 9

for the particle yields of interest here (p, π^+, π^-). The ordinates have been chosen to be $p \frac{dN}{d\Omega dp}$ since this is more convenient for the present purpose. The data points carry an overall scale uncertainty of 50% in addition to statistical and other known systematic errors. The measurements actually extend to higher values than are reproduced here (70 GeV/c for Be and Ti, 120 GeV/c for W).

It is obvious that the calculation underestimates the experimental values at high momenta by a wide margin. Thick target effects appear also appreciable although it is difficult to state this with certainty since the HR model diviates so much at the high momenta it cannot be relied on to estimate this effect. (Cronin et al. used also a 2.0" x 1/8" tungsten target. For this longer and thinner target the spectrometer accepts a large faction of the particles from the side of the target, which reduces thick target effects. Because of variations in beam conditions etc. no reliable differences between targets could be observed). The consequences for shielding calculations from these comparisons must be found at the rather low momenta and here the comparisons are more satisfactory. Typically, below about 20 GeV/c, the calculation overestimates proton yields and underestimates π^- yields while π^+ yields are reproduced fairly accurately. The plots show that truly large deviations begin to occur only at levels involving on the order of 1% of the energy carried off by the different particles. This is unlikely to cause great difficulties for shielding calculations.

In view of the large scale uncertainty and the lack of data points below 10 GeV/c it is difficult to state whether this comparison corroborates the result of the comparisons with emulsion work viz., that of an underestimate (by a factor of ~ 2 at 77 mr) of the total number of shower particles.

Acknowledgment

I wish to thank Drs. M. Awschalom, W. F. Baker, J. W. Cronin, P. J. Gollon and J. Hébert for helpful information and for discussions.

References

1. R. Hagedorn, Suppl. Nuovo Cim. 3, 147 (1965); R. Hagedorn and J. Ranft, Suppl. Nuovo Cim. 6, 196 (1968); H. Grote, R. Hagedorn and J. Ranft, "Atlas of Particle Spectra", CERN, Geneva (1970).
2. A. Van Ginneken and M. Awschalom, "High Energy Shielding Manual I. Hadrons", to be published.
3. J. Ranft, "Secondary Particle Spectra According to the Thermodynamical Model. A Fit to Data Measured in p-Nucleus Collisions", TUL36, Karl Marx Univ., DDR (1970).
4. J. V. Allaby et al., "High Energy Particle Spectra from Proton Interactions at 19.2 GeV/c", CERN-70-12 (1970).
5. J. Ranft and J. T. Routti, "Hadron Cascade Calculations of Angular Distribution of Secondary Particle Fluxes from External Targets and Description of Program FLUKU", CERN-II-RA/72-8 (1972).
6. H. Bertini, Phys. Rev. 188, 1711 (1969).
7. J. Babecki et al., Phys. Lett. B47, 268 (1973); J. Hébert et al., Phys. Lett. B48, 467 (1974); A. Gurtu et al., "Multiplicity in Proton-Nucleus Collisions at 200 GeV/c and Models of Multiparticle Production", Tata Inst., Bombay, preprint TIFR-BC-74-6 (1974).
8. J. Hébert, private communication. Efforts are presently under way to provide a better angular distribution at small angles.
9. J. Gierula et al., Acta Physica Academia Scientarum Hungaricae 29, Suppl. 3, 157 (1970).
10. W. Baker et al., "Measurement of $\pi^{\pm}$, $K^{\pm}$, p and $\bar{p}$ Production by 200 and 300 GeV/c Protons", NAL-Pub-74/13-EXP (1974).

11. J. Ranft, Phys. Lett. 31B, 529 (1970).

12. J. W. Cronin et al., "Production of Hadrons with Large Transverse Momentum at 200,300 and 400 GeV", paper submitted to the XVII Int. Conf. on High Energy Physics, Imperial College, 1-10 July 1974; J. W. Cronin et al., "Atomic Number Dependence of Hadron Production at Large Transverse Momentum in 300 GeV Proton-Nucleus Collisions", ibid.

13. A. Dar and J. Vary, Phys. Rev. D6, 2412 (1972); A. S. Goldhaber, Phys. Rev. D7, 765 (1973); P. M. Fishbane, J. L. Newmeyer and J. S. Trefil, Phys. Rev. D7, 3324 (1973); K. Gottfried, "Coherent and Incoherent Multiple Production in Nuclei", CERN-Th-1735 (1973).

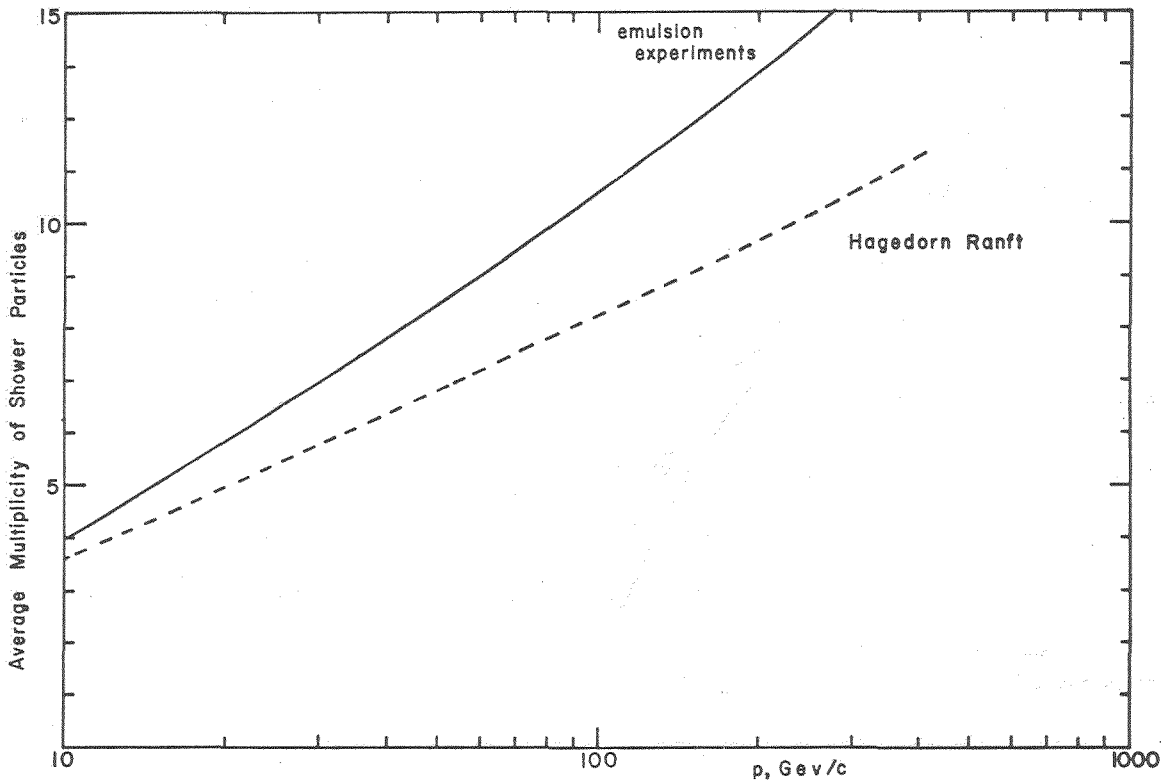

Fig.1 Average multiplicity of shower particles versus incident proton momentum.

—— emulsion studies

--- Hagedorn - Ranft (as used in shielding programs)

The extra normalization constants (see text) which multiply the HR predictions range from N_p=1.56, N_π=1.28 at 10 GeV/c to N_p=0.94, N_π=1.06 at 300 GeV/c.

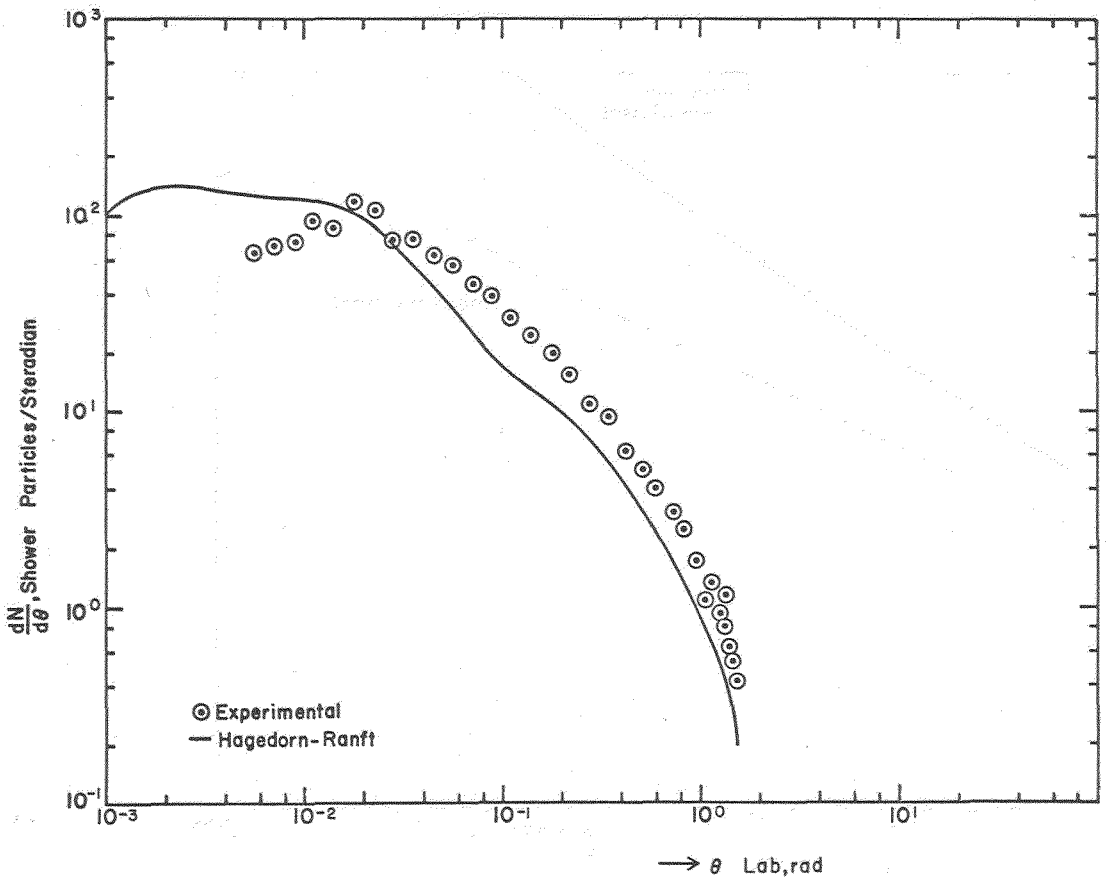

Fig.2 Angular distribution of shower particles produced by 200 GeV/c protons in emulsion.

O Hébert et al. (Ref 7)

— Hagedorn - Ranft (N_p=0.98, N_π=1.12)

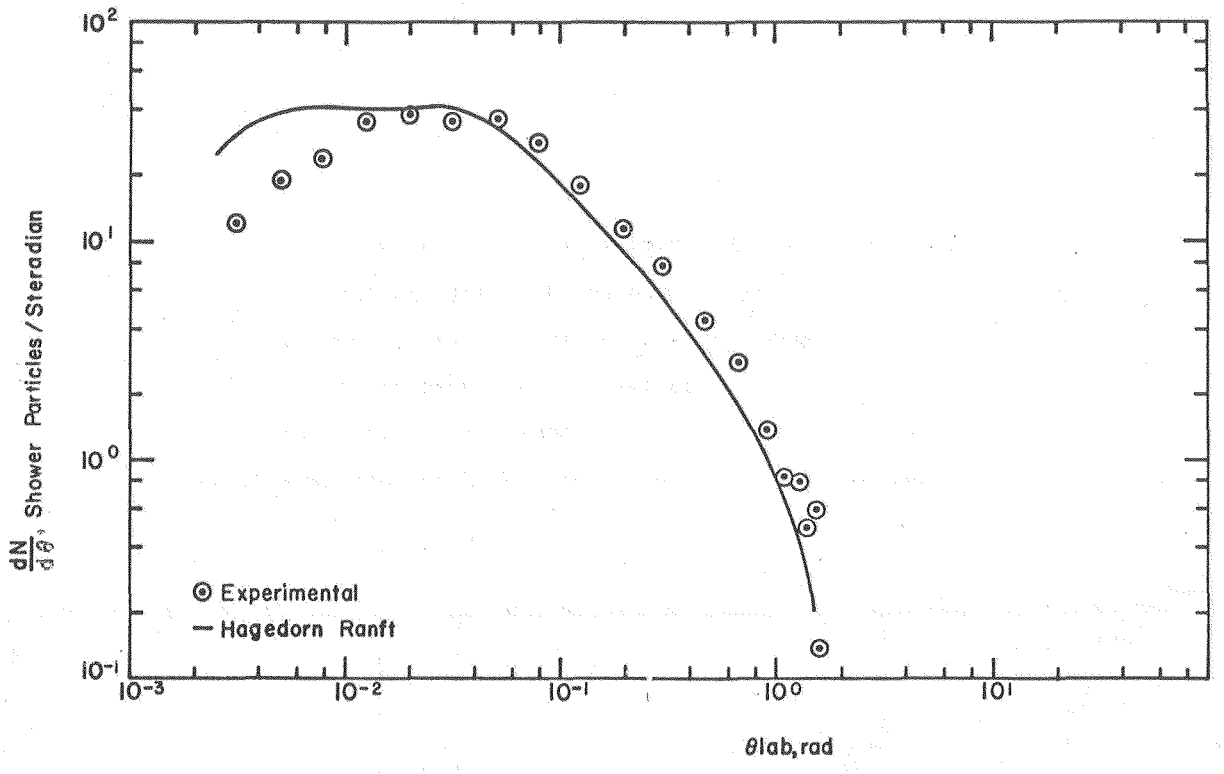

Fig.3 Angular distribution of shower particles produced by 60 GeV/c π^- in emulsion.

⊙ Gierula et al. (Ref 9)

— Hagedorn - Ranft (N_p=1.06, N_π=1.27)

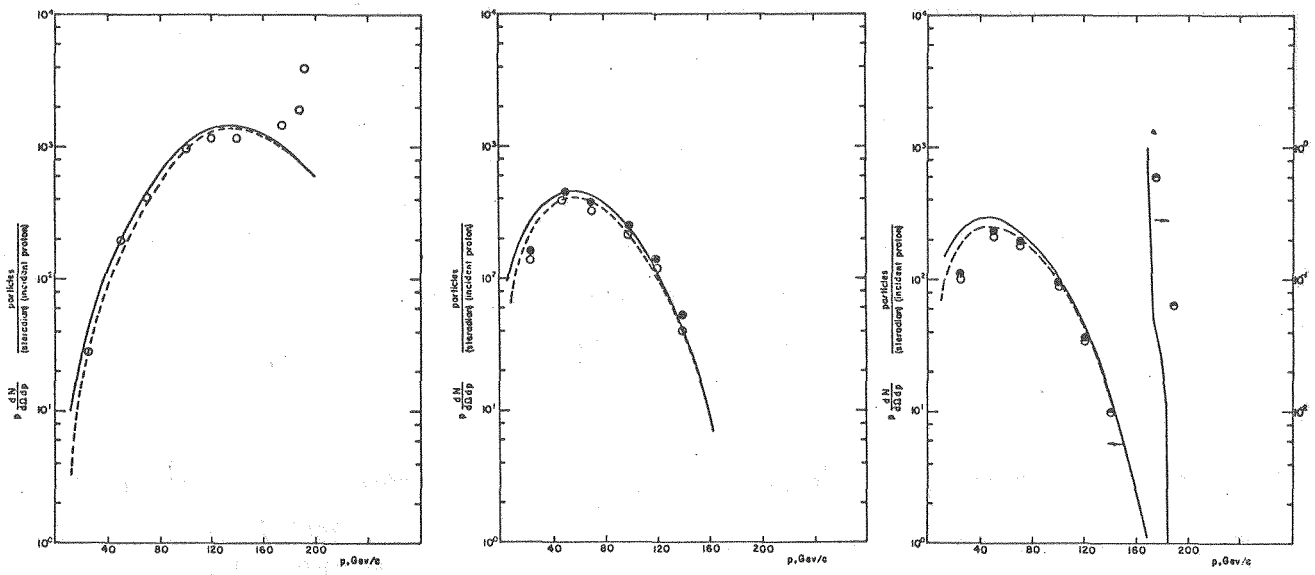

Fig.4 Particle yields at 3.6 mr for 200 GeV/c protons incident on a beryllium target (a) protons (b) π^+ (c) π^-.

O data of Baker et al. (Ref 10)

● data of Baker et al. with $K^+(K^-)$ added to $\pi^+(\pi^-)$

--- secondaries only, Hagedorn - Ranft

—— total yield of thick target (N_p=0.84, N_π=1.01)

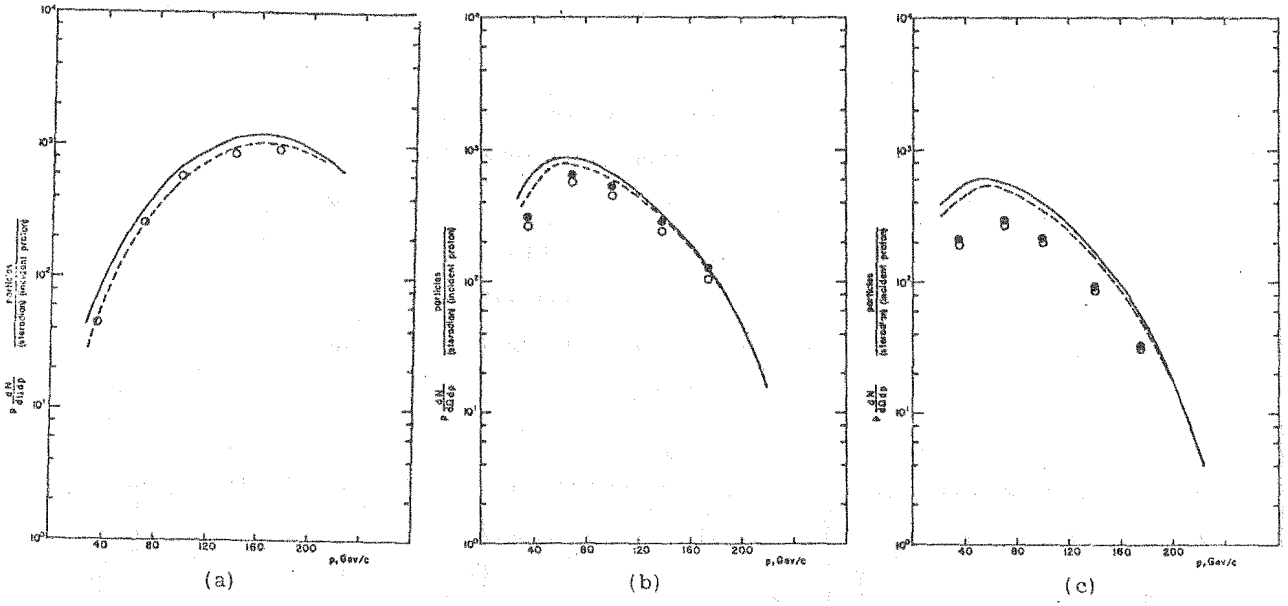

Fig.5 Same as Fig.3, for 300 GeV/c incident protons

(N_p=0.81, N_π=0.96).

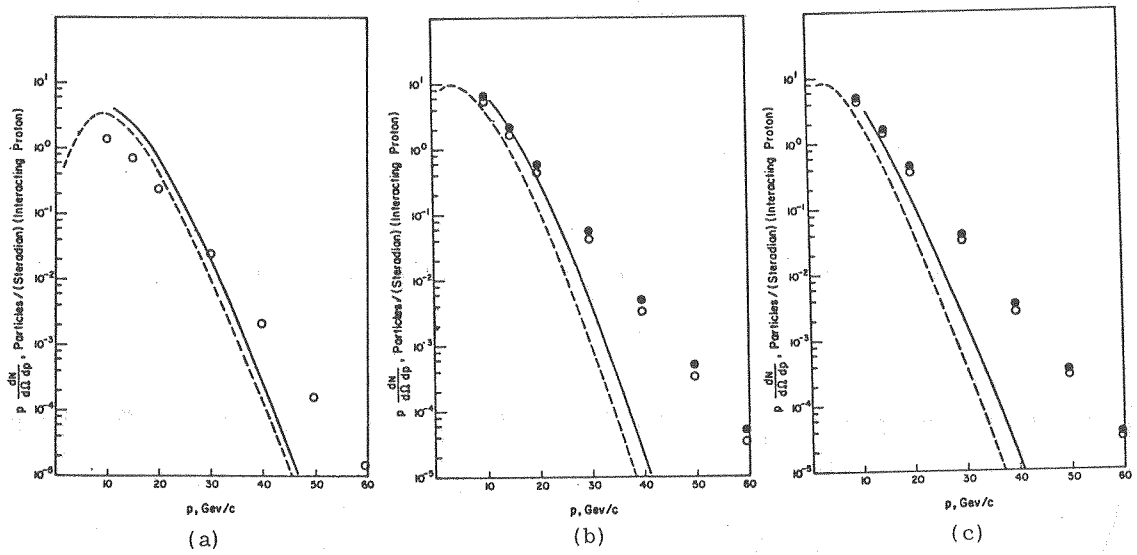

Fig.6 Particle yields at 77 mr for 300 GeV/c protons incident on a beryllium target (a) protons (b) π^+ (c) π^-.

O data of Cronin et al. (Ref.12)

● data of Cronin et al. with $K^+(K^-)$ added to $\pi^+(\pi^-)$.

--- secondaries only, Hagedorn - Ranft

—— total yield of thick target (N_p=0.81, N_π=0.96)

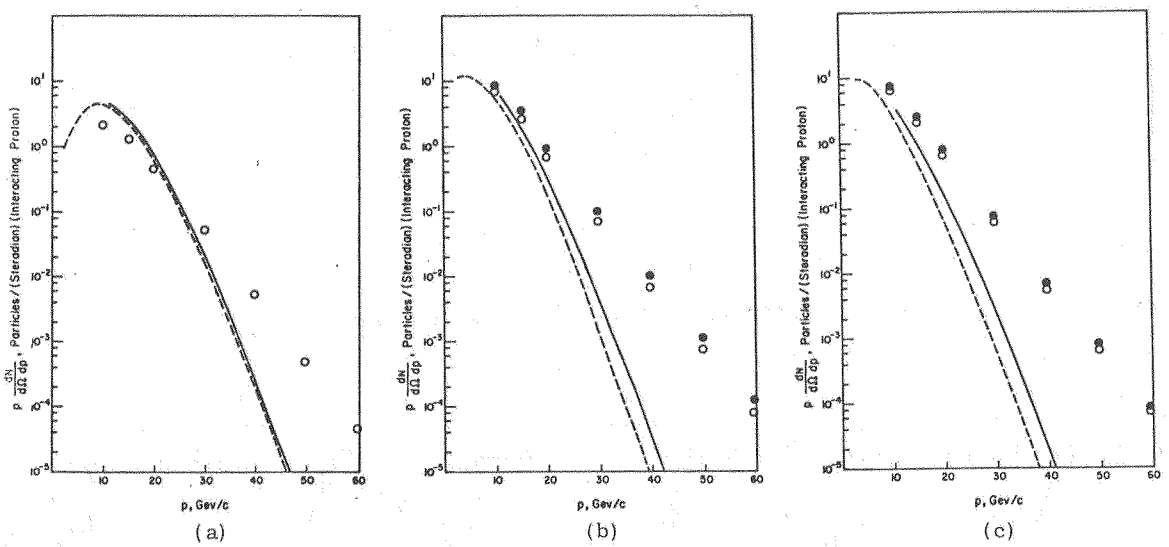

Fig.7 Same as Fig.6. 300 GeV/c p on Ti.

(N_p=0.90, N_π=1.04).

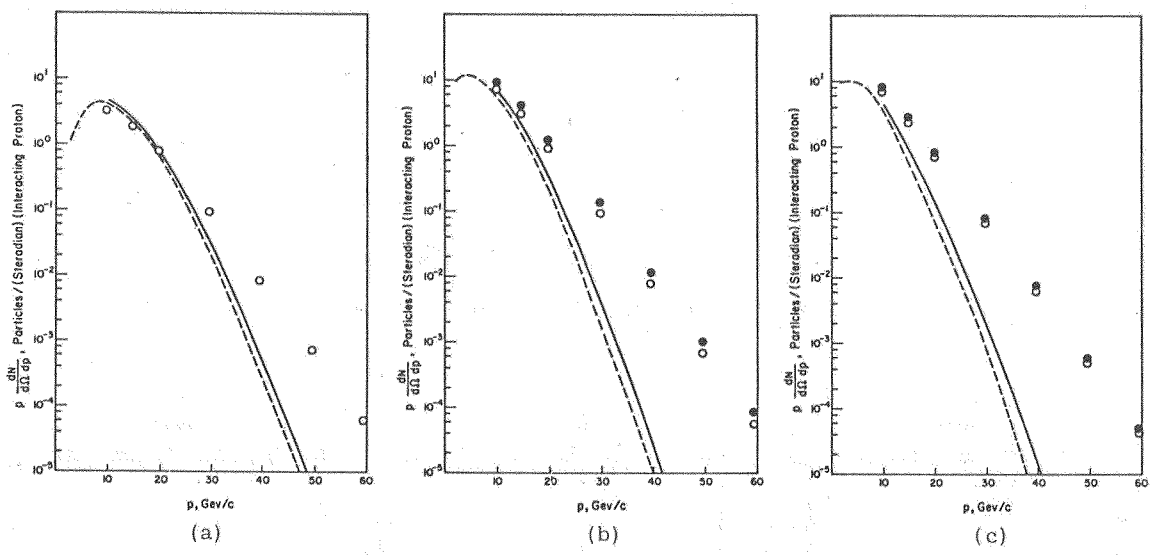

Fig.8 Same as Fig.6. 200 GeV/c p on W.

(N_p=1.06, N_π=1.22).

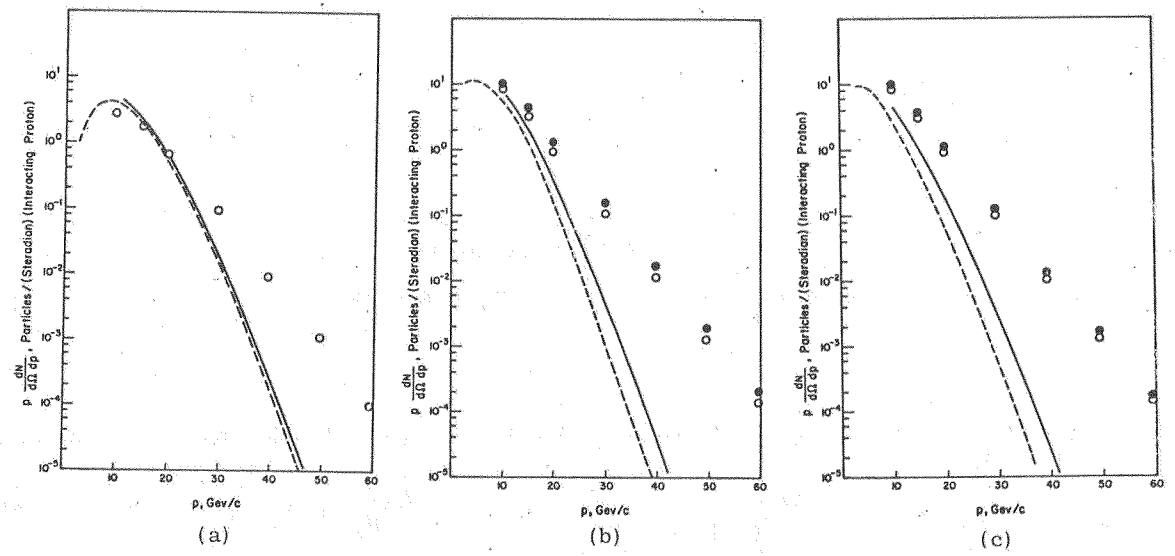

Fig.9 Same as Fig.6. 300 GeV/c p on W.

(N_p=1.03, N_π=1.16).

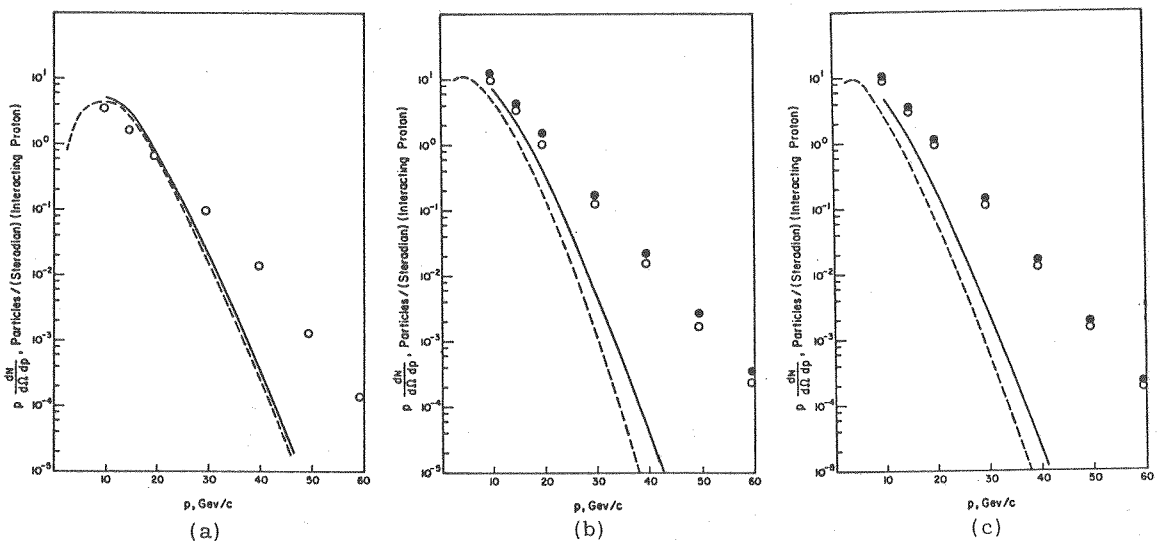

Fig.10 Same as Fig.6. 400 GeV/c p on W.

(N_p=1.02, N_π=1.12).